

# **Processing, microstructure and mechanical behavior of bulk nanostructured Mg alloy**

**Dikai Guan**

**Department of Materials Science and Engineering**

**The University of Sheffield**



Thesis submitted for the degree of Doctor of Philosophy

September 2015

## **Abstract**

Due to lightweight and high specific strength, the research and development of magnesium-based alloys has been widely expanded. New magnesium alloys and novel processing technology also have been developed to satisfy the need for applications in the automotive, communications and aerospace industries. In particular, ultrafine grain sized (UFG) and even nanostructured (NS) magnesium alloys fabricated via severe plastic deformation have attracted most of researchers' attention because of impressive mechanical properties compared to micro sized Mg alloys. With a UFG, NS or a mixed microstructure, exceptional high strength with good ductility could be achieved.

A combination of cryomilling and spark plasma sintering (SPS) was employed in this project to fabricate a NS magnesium alloy. Nanocrystalline (NC) AZ31 powders were produced by cryomilling. A minimum average grain size of approximately 26 nm was obtained when the cryomilling time was extended to 6 hours or longer. Cold welding played a dominant role in the early stage of cryomilling, while fracture took place in the late stage and surpassed cold welding. The former increased while the latter decreased the particle size. The highest hardness of around 160 HV was obtained after 6 hours cryomilling.

This cryomilled NC powder showed excellent thermal stability during annealing at elevated temperatures. There were two separate growth stages with a transition point around 400 °C. More specifically, between 350 and 400 °C, NC Mg grains stabilized around 32 nm,

even after 1h heating. At 450 °C, the nano grains grew to 37 nm in the first 5 minutes and grew quickly to approximately 60 nm after 15 minutes. Nevertheless, the average grain size was still less than 100 nm even after 60 minutes annealing at 450 °C.

Bulk nanostructured (NS) Mg AZ31 alloy was produced by spark plasma. The bulk samples consolidated at 400 °C with an average grain size of 45 nm showed exceptional average true compressive yield strength of 408.7 MPa and true ultimate compressive strength of 504.0 MPa. These values were superior to published results for most of conventional Mg alloys. Higher sintering temperature (425-450 °C) improved compressive strain at the sacrifice of strength, while samples consolidated at 350 °C displayed brittle behavior with low strength. However, true compressive strains of these four samples were all less than 0.06 at true ultimate compressive strength.

To enhance the ductility of bulk NS Mg AZ31 alloy in this study, a facile strategy, *in situ* powder casting during SPS, was introduced. Different amounts of eutectic Mg-Zn alloy powders with low melting temperature approximately 350 °C were mixed with cryomilled powder. During SPS at 400 °C, the low melting temperature eutectic alloy particles melted, and flowed along cryomilled powder particle boundaries and partly dissolved into the Mg matrix. The compressive strain was improved by *in situ* powder casting during SPS without loss of strength, especially when 20 % (wt. %) of eutectic alloy powder was added. Compared to samples sintered by pure cryomilled powder, its compressive strain was extended from 3.6% to 6.6%. The reason for this was *in situ* powder casting can simultaneously significantly remove

the artifacts such as porosity, enhance the inter-particle bounding between nanostructured Mg particles and introduce very small dense precipitates into bulk NS Mg alloy.

# Contents

Abstract.....	i
Acknowledgements.....	viii
Introduction.....	1
1 Literature Review .....	4
1.1 Introduction to magnesium .....	4
1.1.1 Brief history of magnesium.....	4
1.1.2 Basic physical properties of magnesium.....	5
1.1.3 Magnesium alloys classifications.....	5
1.2 Crystallography and Deformation Modes.....	6
1.2.1 Four-axis coordinates system.....	6
1.2.2 Slip systems .....	8
1.2.3 Critical Resolved Shear Stress (CRSS) and Schmid Factor.....	10
1.3 Magnesium alloys development.....	12
1.4 Synthesis of bulk nanostructured metals and alloys .....	13
1.4.1 Motivation and concept of bulk nanostructured materials .....	13
1.4.2 Processing methods of bulk nanostructured materials .....	14
1.5 Microstructure of bulk nanostructured metals .....	35
1.5.1 Dislocation density.....	36
1.5.2 Grain boundary misorientations.....	36
1.5.3 Non-equilibrium grain boundaries .....	37
1.6 Deformation mechanisms of bulk NS metals.....	37
1.6.1 Grain boundary sliding/grain rotation.....	38

1.6.2 Dislocation emission from grain boundaries.....	39
1.6.3 Deformation twinning.....	39
1.6.4 Stress-coupled grain boundary migration .....	40
1.7 Mechanical behavior of bulk nanostructured metals .....	40
1.7.1 Strength.....	41
1.7.2 Ductility .....	42
1.7.3 Approaches to improve ductility of bulk NS metals and alloys.....	43
2 Effect of cryomilling time on microstructure evolution and hardness of cryomilled AZ31 powders.....	46
2.1 Introduction.....	46
2.2 Experimental .....	47
2.2.1 Mg alloy powder .....	47
2.2.2 Cryomilling .....	48
2.2.3 X-Ray Diffraction (XRD).....	49
2.2.4 Microstructure characterization .....	49
2.2.5 Chemical analysis .....	50
2.6 Micro hardness test .....	50
2.3 Results and discussion .....	51
2.3.1 Particle morphologies evolution during cryomilling .....	51
2.3.2 Micro hardness results .....	52
2.3.3 Crystallite Size Measurement by XRD.....	54
2.3.4 Grain size measurement by combination of OM, SEM and TEM .....	59
2.3.5 Chemistry.....	66
2.4 Conclusions.....	67
3 Thermal stability of cryomilled powder.....	68
3.1 Introduction.....	68
3.2 Experimental.....	69

3.2.1 Annealing treatment .....	69
3.2.2 Micro hardness test .....	70
3.2.3 Transmission Electron Microscopy (TEM).....	70
3.3 Results and discussion .....	70
3.3.1 Micro hardness results .....	70
3.3.2 Grain size characterization.....	72
3.4 Conclusions.....	86
4 Synthesis of high strength, bulk nanostructured Mg–3Al–Zn alloy .....	87
4.1 Introduction.....	87
4.2 Experimental.....	90
4.2.1 SPS processing.....	90
4.2.2 Density measurement.....	91
4.2.3 Optical Microscopy.....	91
4.2.4 Scanning electron microscope (SEM).....	91
4.2.5 Transmission Electron Microscopy (TEM).....	91
4.2.6 Micro hardness test .....	92
4.2.7 Compression test.....	92
4.2.8 Compression test compliance correction[214].....	93
4.3 Results and discussion .....	94
4.3.1 SPS processing curves .....	94
4.3.2 Morphologies of bulk SPSed samples.....	98
4.3.3 Micro hardness results of bulk SPSed samples.....	105
4.3.4 Compression testing behavior of bulk SPSed samples .....	106
4.4 Conclusions.....	120
Chapter 5 A facile strategy to improve compressive strain of bulk nanostructured Mg alloy without loss of strength .....	122

5.1 Introduction.....	122
5.2 Experimental.....	125
5.2.1 Mg-Zn eutectic alloy powder preparation.....	125
5.2.2 Thermogravimetric analysis (TGA).....	127
5.2.3 Powders mixing.....	128
5.2.4 Scanning electron microscope (SEM).....	128
5.3 Results and discussion.....	128
5.3.1 Characterization of eutectic alloy powder.....	128
5.3.2 SPS processing curves.....	131
5.3.3 Mechanical behavior of bulk SPSed samples.....	133
5.3.4 Morphologies of bulk SPSed samples.....	138
5.4 Conclusions.....	151
6 Conclusions.....	153
7 Future work.....	153
8 References.....	158

# Acknowledgements

First and foremost, I want to express my deepest gratitude to my first supervisor, Prof. Mark Rainforth, for all of the encouragement, support and continuous guidance he has given me during my PhD in the University of Sheffield. Second, special appreciation is deserved for my second supervisor, Prof. Iain Todd, for his supervision and equipment support for my PhD project.

I am grateful to the University of Sheffield, CSC (China Scholarship Council) and Mercury Centre for the funding and equipment for my PhD research project.

I have been very pleased to work in the Advanced Metallic research group for the last 4 years. Appreciations go particularly to all those who I have cooperated with in room H6 for creating a harmonious atmosphere to make me constantly focus on my work. I have also learnt a lot of skills from them and made some great friends. Junheng Gao and Zhilun Lu are my close friends and always willing to help me do some experiment which I am not familiar with.

I am very thankful to Dr. Andrew Williams. He played a very important role in the initiation of my research projects, especially sample preparation for microstructure investigation.

Special thanks must go to Dr Nogiwa Valdez, who helped me to set up cryomill, glovebox and trained me how to use SPS machine, and to Dr Amit Rana who is always ready

for helping me. I am also grateful to Dr Joanna Sharp for doing the HRTEM experiments for me.

I am grateful for all of the trainings and assistance from technical staff in my department and experimental officers in the Sorby Centre.

Final thanks must go to my parents for their deepest love and endless support. I am also indebted to my sisters since she has been the only person to look after my parents during the past years. The most important person I would like to thank is my precious wife for her love, understanding and support. In addition, my little son is the source of my strongest enthusiasm and greatest happiness.

# Introduction

## 1 Background

Bulk NS materials, with structural features less than 100 nm in at least one dimension, can be obtained by either a “one-step” method such as severe plastic deformation, or a “two-step” approach such as powder consolidation. The former strategy can produce defect-free bulk NS material with greater ductility than these fabricated by the latter method. Nonetheless, these NS materials with exceptionally high strength usually exhibit poorly low ductility. Recently, several strategies have reported to increase ductility of bulk UFG and NS materials. Introducing a bimodal or multi-grain size distribution, pre-existing nanoscale twins, and engineering nanoscale precipitates into matrix have widely studied and reported. Nevertheless, most of these strategies either sacrificed some of the strength of the bulk UFG or NS materials strength or were only used in the “one-step” approach. The most frustrating issue for bulk NS materials fabricated by the “two-step” approach is those materials often have artifacts such as porosity and cracks, which plays a detrimental role in causing very low ductility (defined as less than 5% elongation to failure).

Due to lightweight and high specific strength, the research and development of magnesium-based alloys has been widely expanded. New magnesium alloys and novel processing technology also have been developed to satisfy the need for applications in the automotive, communications and aerospace industries. In particular, ultrafine grain sized (UFG)

and even nanostructured (NS) magnesium alloys fabricated via severe plastic deformation have attracted most of researchers' attention because of impressive mechanical properties compared to micro sized Mg alloys. With a UFG, NS or a mixed microstructure, exceptional high strength with good ductility could be achieved.

## **2 Main Techniques Used**

The main method we employed to produce bulk nanocrystalline Mg AZ31 alloy was the combination of cryomilling and Spark Plasma Sintering consolidation.

For microstructure characterization, optical microscope, SEM, TEM and XRD were used to investigate the internal microstructure.

We also used conventional compression testing to evaluate sample's mechanical properties.

### **3 Main Objectives**

1. To find out whether cryomilling can be extended to produce NC microstructure in a magnesium AZ31 alloy with much lower alloying content
2. To study the effect of short annealing time on the grain size of cryomilled AZ31 powder and provide a guidance to optimize SPS consolidation parameters
3. To investigate the response of grain growth and mechanical behaviour, when samples were sintered at various temperatures, especially at elevated temperatures (e.g., 450 °C, 0.78 Tm)
4. To develop a novel process for improving the ductility of bulk NS Mg alloy without loss of high strength.
5. To gain a greater understanding of the mechanism of enhanced ductility in bulk NS Mg alloy.

# 1 Literature Review

## 1.1 Introduction to magnesium

### 1.1.1 Brief history of magnesium

Magnesium was discovered in the year of 1774 and is regarded as the 6th most abundant element in the world, comprising 2% of the total mass of the earth's crust. Magnesium can be only found in the form of compounds in nature instead of the elemental state because it is located in the alkaline earth metals group. Magnesium can be mainly refined from minerals, such as magnesite  $\text{MgCO}_3$  (27% Mg), dolomite  $\text{MgCO}_3 \cdot \text{CaCO}_3$  (13% Mg), and carnallite  $\text{KCl} \cdot \text{MgCl}_2 \cdot 6\text{H}_2\text{O}$  (8% Mg). In addition, sea water consists of 0.13% Mg or 1.1 kg mg per  $\text{m}^3$ , the third most abundant dissolved minerals in the sea. Electrolysis of molten anhydrous  $\text{MgCl}_2$ , thermal reduction of dolomite and extraction of magnesium oxide from sea water are the major three routes to recovery magnesium [1,2]. The US geological survey in January 2010 reported the total worldwide production of magnesium in 2008 was 671,000 tonnes and 570,000 tonnes estimated in 2009. Historically, a great deal of magnesium was used as an alloying additive for aluminum [3].

With an approximate density of  $1.738 \text{ g/cm}^3$  at room temperature, magnesium is the lightest structural metal in common use. With a high specific stiffness and strength, magnesium is an outstanding candidate for weight critical structural applications. The past twenty years

have seen increasingly rapid advances in the field of magnesium alloy research and development, especially in areas of automotive, aerospace and transportable equipment, because low weight components are most cost-effective for these applications [4].

### **1.1.2 Basic physical properties of magnesium**

Pure magnesium forms a hexagonal close packed (hcp) crystal structure with a melting temperature of 650°C [1,2]. Its atomic number is 12. The lattice parameters are as follows:

$$a = 0.32092 \text{ nm [1,2]}$$

$$c = 0.52105 \text{ nm [1,2]}$$

The crystal lattice parameters give a  $c/a$  1.6236 that is almost identical to the ideal close packed ratio of 1.633. Therefore, pure magnesium can be regarded as perfectly close packed [2]. In addition, its atomic diameter is about 0.32 nm, which makes it favorable to form solid solutions with a majority of elements within a size range of  $\pm 15\%$  according to the law of Hume-Rothery and Raynor [5]. Figure 1.1 gives the major properties of pure magnesium.

### **1.1.3 Magnesium alloys classifications**

The international magnesium alloys designation is based on the American Society for Testing and Materials (ASTM). Generally, the alloys are named with two letters indicating the main alloying elements followed by two numbers illustrating the nearest nominal weight percent of each of the two additions. A third letter may be needed to indicate a specific variation in the composition. Table 1.1 shows the key letters representing major alloying elements used in magnesium alloys. In addition, a fabrication code (e. g.: F: as-cast, T4: solution heat treated)

is added to indicate the condition of the alloy. Heat treatment designation used in magnesium alloys shares the same identification system with aluminum alloys, as shown in table 1.2. For instance, AZ31 T4 is a 3wt % aluminum, 1wt % zinc alloy which has been solution heat treated.

<b>Crystal Structure .....</b>	<b>hcp</b>
<b>Density .....</b>	<b>1,738 g/cm<sup>3</sup> at RT</b>
<b>.....</b>	<b>1,584 g/cm<sup>3</sup> at T<sub>m</sub></b>
<b>Young's Modulus .....</b>	<b>45 GPa</b>
<b>Ultimate Tensile Strength .....</b>	<b>80-180 MPa</b>
<b>Fracture Elongation .....</b>	<b>1-12 %</b>
<b>Melting Point.....</b>	<b>650 +/- 0,5°C</b>
<b>Boiling Point .....</b>	<b>1090°C</b>
<b>Specific Heat Capacity.....</b>	<b>1,05 kJ/(kg K)</b>
<b>Fusion Heat.....</b>	<b>195 kJ/kg</b>
<b>Heat Conductivity .....</b>	<b>156 W/(m·K) (RT)</b>
<b>Linear Expansion Coefficient.....</b>	<b>26·10<sup>-6</sup> K<sup>-1</sup> (RT)</b>
<b>Shrinkage (solid-liquid) .....</b>	<b>4,2 %</b>
<b>Shrinkage (T<sub>s</sub>-RT) .....</b>	<b>ca. 5%</b>
<b>Specific Electrical Conductivity.....</b>	<b>22,4 m/(Ω mm<sup>2</sup>) (RT)</b>
<b>Normal Potential.....</b>	<b>-2,37 V</b>

Figure 1.1 Properties of pure magnesium [1]

## 1.2 Crystallography and Deformation Modes

### 1.2.1 Four-axis coordinates system

The three-figure Miller indices used in other crystal systems cannot clearly illustrate which planes or directions have the equivalent or similar relations. For example, it cannot be easily identified that [1 0 0] has a similar crystal direction with [1 1 0], but it can be directly found that the corresponding four-figure Miller indices crystal directions  $[2\bar{1}10]$  and  $[11\bar{2}0]$  belong to the  $\langle 11\bar{2}0 \rangle$  family. To avoid confusion, the four-figure Miller indices are always used in most publications. Several different directions and planes are depicted in figure 1.2.

**Table 1.1** ASTM alloy designation [6,7]

Alloying element	Abbreviation letter
Aluminum	A
Copper	C
Rare earth	E
Thorium	H
Zirconium	K
Lithium	L
Manganese	M
Silver	Q
Silicon	S
Yttrium	W
Zinc	Z

**Table 1.2** ASTM heat treatment designation [6,7]

Code	Temper
F	As Fabricated
O	Annealed, Recrystallised (wrought)
T1	Cooled and naturally aged
T2	Annealed (cast products)
T3	Solution heat treated, then cold worked
T4	Solution heat treated
T5	Cooled then artificially aged
T6	Solution heat treated and artificially aged
T7	Solution heat treated and stabilised
T8	Solution heat treated, cold worked, artificially aged
T9	Solution heat treated, artificially aged, cold worked
T10	Cooled, artificially aged, cold worked

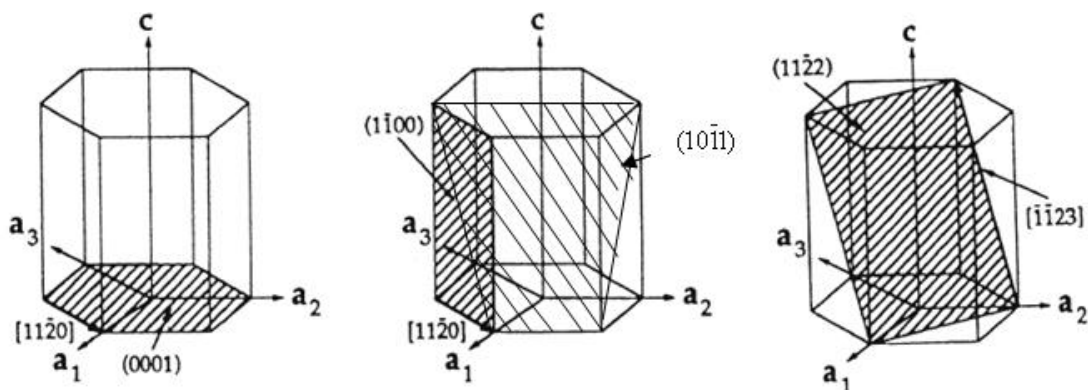


**Figure 1.2** Unit cell and major slip planes and directions in magnesium (adapted from [2])

## 1.2.2 Slip systems

As mentioned above, magnesium has an almost ideal hcp crystal structure. However, this close packed structure restricts the ability of deformation at low temperature (e. g., < 225 °C) and the primary slip occurs along the close packed direction  $\langle 11\bar{2}0 \rangle$  on the close packed basal plane (0001) in these conditions. As von Mises stated, at least five independent slip systems are required to plastically deform uniformly without failure [8]. However, the strain on basal plane produced by the third can be produced by a simple addition of the previous two, so only two independent slip systems are available. Because of inadequate slip systems at room temperature, deformation causes fracture or twinning. Thus, other non-basal slip systems or mechanical twinning need to be activated to facilitate plastic deformation.

As shown in figure 1.2, the prismatic  $\{1\bar{1}00\}$  and first order pyramidal  $\{10\bar{1}1\}$  planes share the same close packed direction  $\langle 11\bar{2}0 \rangle$  with the basal plane. Slip can also be activated on these two planes [9-12]. Because the critical resolved shear stress (CRSS) for prismatic slip at room temperature is about 100 times higher than that of basal slip, while at 300°C only four times higher [13], it indicates twinning readily prefers to be the candidate to enhance the deformation ability at room temperature. When material is subject to an external shear force, it can produce twinning. Some plastic strain is usually accommodated by the rapid formation of mechanical twins, and an increase of the uniform elongation ensues [14-16]. Often mechanical twinning occurs on pyramidal planes  $\{10\bar{1}2\}$  and sometimes it can be observed on  $\{10\bar{1}1\}$  and  $\{10\bar{1}3\}$  planes.  $\{10\bar{1}2\}$  twinning allows strain under c-axis “tension” [14,17]. In addition, double twinning is activated for compression along the c-axis, which can reorientate the basal

plane for slip. The double twins consist of the primary planes with the secondary planes, including  $\{10\bar{1}1\}$  -  $\{10\bar{1}2\}$  and  $\{10\bar{1}3\}$  -  $\{10\bar{1}2\}$  double twins. Because double twinning assists slip on basal plane, it results in work softening and strain localization leading to failure in both Mg single crystals and polycrystals [18,19]. However, twinning only gives shear strain in one direction instead of the three from dislocation slip, so it cannot be treated as an independent mechanism of deformation [20]. Once the temperature is higher than 200°C (the temperature varies with different alloy composition), non-basal slip systems, including prismatic  $\{1\bar{1}00\}$  and first order pyramidal  $\{10\bar{1}1\}$ , are activated and substitute for mechanical twinning [1,2]. Only 2 more independent slip systems can be added on the prismatic  $\{1\bar{1}00\}$  and primary pyramidal  $\{10\bar{1}1\}$  planes along  $\langle 11\bar{2}0 \rangle$  direction. Some researchers reported [12,21-24] that a further  $\langle c+a \rangle$  slip system, slip on the second order pyramidal  $\{11\bar{2}2\}$  in the direction of  $\langle \bar{1}\bar{1}23 \rangle$ , can be triggered in hcp metals to provide the remaining slip system for full plasticity. It is named  $\langle c+a \rangle$  slip, because a Burgers vector of dislocation is composed of both the c and a directions. To sum up, a schematic of the five slip systems is presented in figure 1.2 and table 1.3, respectively.

**Table 1.3** Slip systems for magnesium and its alloys at room and elevated temperature

Temperature range	Slip plane	Slip direction	Number of independent slip systems
Room temperature	$\{0001\}$	$\langle 11\bar{2}0 \rangle$	2
	$\{1\bar{1}00\}$	$\langle 11\bar{2}0 \rangle$	2
Elevated Temperature	$\{10\bar{1}1\}$	$\langle 11\bar{2}0 \rangle$	0
	$\{11\bar{2}2\}$	$\langle \bar{1}\bar{1}23 \rangle$	1

### 1.2.3 Critical Resolved Shear Stress (CRSS) and Schmid Factor [25]

The understanding of slip arises from single crystals, which is then extended to polycrystalline materials. During deformation, edge, screw, and mixed dislocations move along a slip plane and in a slip direction responding to the applied shear stress. The relevant stress acting on dislocations is the applied stress resolved onto the activated slip systems. These stresses are termed resolved shear stresses, which depend not only on the applied stress, but also on the orientation of both the slip plane and direction. Figure 1.3 shows the geometrical relationship between the tensile axes, slip plane and slip direction. The angle between the normal to the slip plane and the applied stress  $\sigma$  direction is defined as  $\phi$ , and  $\lambda$  the angle between the slip and stress directions. Therefore, the resolved shear stress  $\tau_R$  can be calculated using equation 1-1

$$\tau_R = \sigma \cos \phi \cos \lambda \quad (1-1)$$

A single crystal needs at least five different slip systems to be activated to deform permanently. In general, the resolved shear stress of every slip system is different because of the various orientations of each relative to the stress axis. There is one slip system which owns a favorable orientation. In other words, it has the biggest resolved shear stress,  $\tau_R(\max)$

$$\tau_R(\max) = \sigma (\cos \phi \cos \lambda)_{\max} \quad (1-2)$$

To move dislocations on a specific slip system, slip in a single crystal starts on the most favorably oriented slip system when the resolved shear stress reaches a critical value, called

the critical resolved shear stress (CRSS)  $\tau_{crss}$ . The plastic deformation commences when  $\tau_R(\max)$  equals  $\tau_{crss}$ .

$$\sigma_y = \frac{\tau_{crss}}{\cos \phi \cos \lambda} \quad (1-3)$$

$\cos \phi \cos \lambda$  is defined as the Schmid factor, and it normally ranges from 0 to 0.5. When  $\phi = \lambda = 45^\circ$ , the Schmid factor is 0.5. Therefore, yielding occurs at a minimum stress.

$$\sigma_y = 2\tau_{crss} \quad (1-4)$$

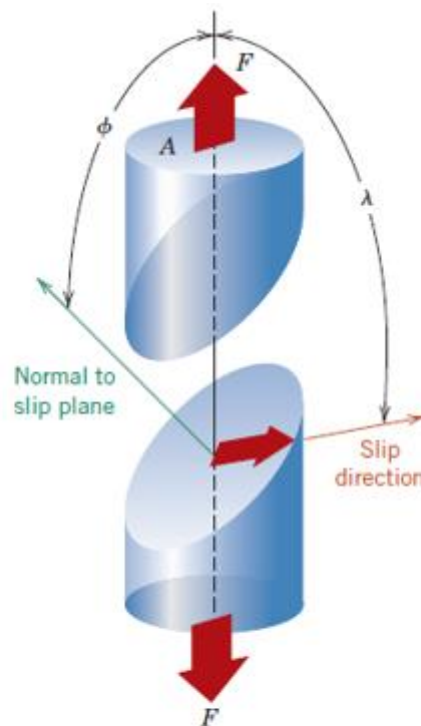


**Figure 1.3** Geometrical relationships between the tensile axis, slip plane, and slip direction used in calculating the resolved shear stress for a single crystal [25]

### 1.3 Magnesium alloys development

The high demand of automobile and other large-scale potential users of magnesium have speeded its alloy development and its alloy exploration and development has extended significantly during the past two decades [4,26]. The advantages of magnesium have been mentioned previously, especially low density, which encourage relevant companies to substitute heavier materials including Fe, Ti, Cu and Al alloys with Mg alloys [3,27]. Figure 1.4 summarizes the different trends of die cast, sand cast and wrought Mg alloys [27]. In addition, Polmear listed nominal composition, typical tensile properties and characteristics of most casting and wrought magnesium alloys in his book [3]. The most widely studied in the literature and commonly used commercially magnesium alloys are as follows:

AZ31 [9,10,12,14,15,17,20,28-36]: Mg-3Al-1Zn-0.3Mn (wt. %)

It is commonly used for wrought applications because of reasonable ductility, room temperature strength, cost, weld ability and good formability.

WE43 [37-41]: Mg-4Y-3RE (wt. %)

It owns good mechanical properties at high temperatures. It can be stable for long term exposure up to 250 °C. In addition, WE43 is more isotropic than other alloys.

ZK60 [42-44]: Mg-6Zn-0.4Zr (wt. %)

It is generally used for wrought applications. The strength is increased by artificial aging. It exhibits the best comprehensive properties at room temperature.

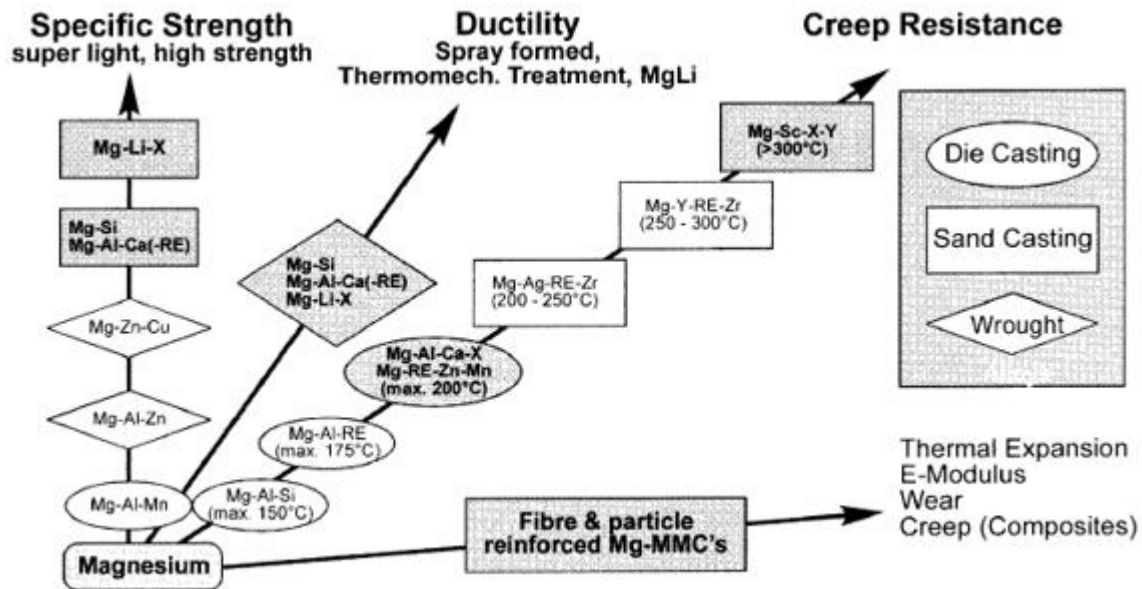


Figure 1.4 Directions of magnesium alloy development [27]

## 1.4 Synthesis of bulk nanostructured metals and alloys

### 1.4.1 Motivation and concept of bulk nanostructured materials

As Taylor [45] indicated in 1938, a smaller grain size augments the strength of a metal because of the greater grain boundary area to impede dislocations motion. The relationship between yield stress and grain size of a metal can be described by the well-known Hall-Petch relationship. Therefore, to improve the mechanical properties, several researches have focused on optimizing grain refinement processing routes to obtain UFG materials. UFG materials are classified as polycrystals with average grain sizes 0.1-1  $\mu\text{m}$ . For bulk UFG materials, quite

homogeneous and reasonably equiaxed microstructures and a majority of grain boundaries with high angles of misorientation are required to achieve superior and unique properties [46,47]. Furthermore since the 1980s, bulk nanostructured (NS) metals have developed with exclusive mechanical properties and potential applications [48-50]. By definition, bulk NS materials consist of microstructures (e.g., grains, subgrains and twins within grains, etc.) which are characterized with at least one dimension less than 100 nm [51-54]. For bulk NS metals and alloys, the amount of GBs is considerably higher than those of coarse grained materials, which can significantly improve the strength. Grain size can be determined by the rate of solidification from the liquid phase, and also by plastic deformation followed by an appropriate heat treatment. Rapid solidification process (RSP) and severe plastic deformation (SPD) are two favorable processing techniques to effectively reduce the grain size.

#### **1.4.2 Processing methods of bulk nanostructured materials**

To date, numerous methods have been developed to produce UFG and NS metals and alloys. One classification is defined based on the number of stages involved to produce NS materials. Bulk NS metals and alloys can be obtained by either a “one-step” or a “two-step” approach. A consolidation is not necessary for the one-step approach. By contrast, in the two-step approach, an extra route is required to consolidate individual particles, agglomerates or clusters produced firstly. Typical one-step approaches include electrodeposition and some of severe plastic deformation (SPD) methods, which are high pressure torsion (HPT), equal channel angular pressing (ECAP), and multi-directional forging (MDF). The significant advantage of the one-step approach is it can usually produce bulk dense NS materials without

internal defects, such as cracks and pores. On the other hand, typical two-step approaches employ inert gas condensation, mechanical milling or cryomilling to produce nanostructured particles or agglomerates. Several consolidation methods, such as cold/hot isostatic pressing (CIP/HIP), quasi-isostatic pressing, and spark plasma sintering (SPS). In addition, SPD techniques, including ECAP and HPT, can also be employed to consolidate precursor powders. Compared with the one-step approach, defect including pores, insufficient bonding and impurities often exist in materials synthesized by the “two-step” method. Nevertheless, it is widely used because it can fabricate samples with large dimensions thereby extending engineering applications.

In this section of this thesis, general information related to commonly used routes will be presented for producing bulk NS and UFG materials. The combination of spark plasma sintering and cryomilling will be used to fabricate bulk NS Mg alloy and will also be described in detail in later sections.

### **1.4.2.1 One-step approaches**

#### **1.4.2.1.1 Electrodeposition**

Electrodeposition was reported to produce film of NS materials including Cu [55,56], Ni [57] and its alloys [58]. It yields grain sizes in the range between 20-40 nm with depth of 100  $\mu\text{m}$  or more [58]. The major advantages of the electrodeposition method are as follows: (1) potential of fabricating a great many of nanostructured materials (e.g., pure metals, alloys and composite systems), (2) cost-effective with a high production rates, (3) not equipment-intensive,

and (4) high probability of extending its application to existing electroplating and electroforming industries[58].

#### **1.4.2.1.2 Severe plastic deformation**

Over the past several decades, substantial attention has been concentrated on the use of SPD to work on metals. It evolved from heavy deformations (e.g., cold rolling, drawing) resulting in considerable refinement of microstructure [59]. Valiev et al. [60] summarized the mechanisms and applications of SPD and concluded that the grain sizes of bulk metals can be refined to the scale of sub-micrometer or even nanometer via SPD techniques. Consequently, SPD processing is one possibility of enhancing the advantage of superior mechanical properties associated with high strength at room temperature and a capability of super plastic forming operations at elevated temperatures. Additionally, SPD methods can address a number of issues which cannot be effectively avoided by other processing methods, such as residual pores in consolidated samples, trace contamination introduced by milling, etc.

To obtain ultrafine microstructures in bulk metals via heavy deformation, several requirements need to be considered. Valiev and co-workers [47,60,61] summarized requirements as follows:

- a) It is critical to obtain ultra-fine grained structures with dominant high-angle grain boundaries, because only in this way can a qualitative improvement in properties of materials occur.

- b) In order to provide stable properties, it is essential to obtain ultrafine microstructures homogeneously distributed in the matrix.
- c) The processed materials also cannot yield to any mechanical damage or cracks, even though they are subjected to severe plastic deformation.

Conventional routes of large deformation, including rolling, drawing and extrusion are not capable of meeting the above principles. Nevertheless, special techniques were established and applied for meeting these requirements. These techniques mainly include equal ECAP, HPT and MDF [60]. It was well established that SPD techniques are able to successfully produce bulk NS metals and alloys containing some commercial alloys.

#### (1) Equal channel angular pressing (ECAP)

ECAP, where a billet with shapes of a rod or bar, is pressed through a die constrained within a channel bent through a very abrupt angle, is also known as equal channel angular extrusion (ECAE) [62,63]. Figure 1.5 shows a schematic of a typical ECAP unit [64]. It has been attracting a great many researcher's attention in the field of materials science since 1990s due to related work done by Valiev and co-workers [61,65]. They investigated that submicron-grained microstructure can be formed after ECAP. In reference [61] a Mg-1.5Mn-0.3Ce alloy with grain sizes as small as 300 nm can be produced using ECAP. Compared with traditional metal-working methods, ECAP has a number of advantages. One of the most significant is that extra-large, strictly homogeneous and monodirectional deformations could be achieved with comparatively low loading force for relatively large samples [62].

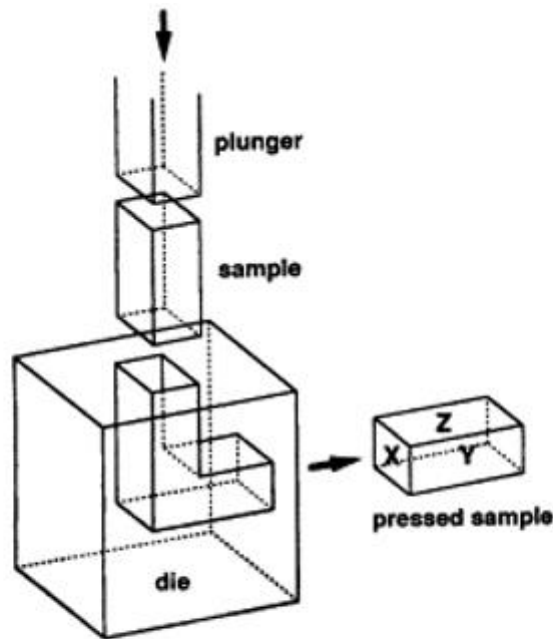


**Figure 1.5** Schematic illustration of a typical ECAP facility: the X, Y and Z planes denote the transverse plane, the flow plane and the longitudinal plane, respectively [64]

Recently, Furui [63] reported a Mg-8Li alloy acquired an exceptionally high elongation of about 1780 % in the Cast + Extrude + ECAP condition at 200 °C. The grain sizes reduced from 60–70  $\mu\text{m}$  in the as-cast condition to 1–7  $\mu\text{m}$  after ECAP. The outstanding yield strength (310 MPa) and ductility (17.2 %) in a ZK60 alloy could be ascribed to the fine grains and favorable texture accelerating basal slip [42]. Ding et al. [66] developed a multiple-temperature ECAP process. Due to grain refinement to 0.37  $\mu\text{m}$ , the 0.2% proof strength of AZ31 was up to 372 MPa with an elongation of 9.7 %.

## (2) High-pressure torsion (HPT)

A device for large plastic torsion strain with high pressure is shown in figure 1.6 [46]. High-pressure torsion (HPT) was originally designed for study of phase transformations under

heavy deformation. As shown in figure 1.6, the sample with a disk shape processed by HPT is placed between anvils and stressed in torsion under the applied pressure ( $P$ ) in the order of GPa. A lower holder rotates and surface friction forces distort the ingot by shear. Due to the disk shape of the sample, the main volume of the material is subjected to a quasi-hydrostatic compression. Therefore, although severe deformation occurs, the deformed disk is not damaged [46,60]. The most important step to treat HPT as a novel technique to produce UFG materials is the successful formation of homogeneous nanostructures with high-angle grain boundaries reported by Valiev and co-workers [65,67]. They indicated that HPT could fabricate UFG metals with outstanding properties (elastic, strength, superplastic, damping and magnetic properties of UFG materials.). HPT can manage to refine grain sizes to approximately 100 nm in a Mg-Mn-Ce alloy [65].

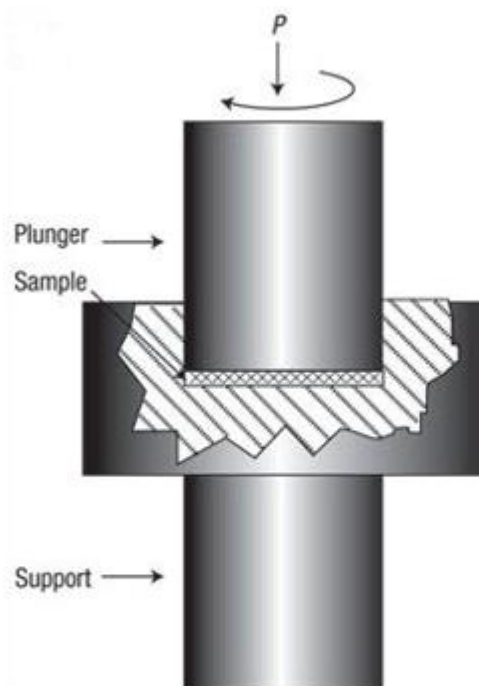


**Figure 1.6** Schematic illustration of a typical HPT device [46]

For magnesium alloys processed by HPT, the properties, including mechanical and corrosion resistance, have been improved compared with conventional methods [68,69]. Kai et al.[69] confirmed the possibility of employing HPT to process Mg-9 wt% Al alloys. The grain sizes after HPT were less than 0.4  $\mu\text{m}$  in their research, which resulted in a maximum elongation of 810% tested at 200 °C with an initial strain rate of  $5.0 \times 10^{-4} \text{ s}^{-1}$  [69]. When HPT was applied to pure magnesium, a bimodal microstructure with an average grain size of  $\sim 1 \mu\text{m}$  was formed, thereby increasing both tensile strength and ductility [70]. The grain size of a commercial Mg AZ31 alloy decreased from the range of 5–45  $\mu\text{m}$  to an average grain size of 0.5  $\mu\text{m}$  after HPT at 180 °C for up to 5 turns, but the deformation process was found to be heterogeneous due to a different refinement mechanism taking place in hcp crystal structure compared to fcc [71,72].

### (3) Multi-directional forging (MDF)

The method of multi-directional forging (MDF) was designed for refinement of microstructures in metallic materials. Figure 1.7 shows a schematic of MDF procedure [73]. Salishchev and co-workers first introduced the concept of MDF in titanium alloys, where sub-microcrystalline structure formed after MDF [74,75]. Compared to ECAP and HPT, MDF can obtain a nanostructure in quite brittle materials as processing activates at high temperatures and specific loads on tooling are relative small [60].

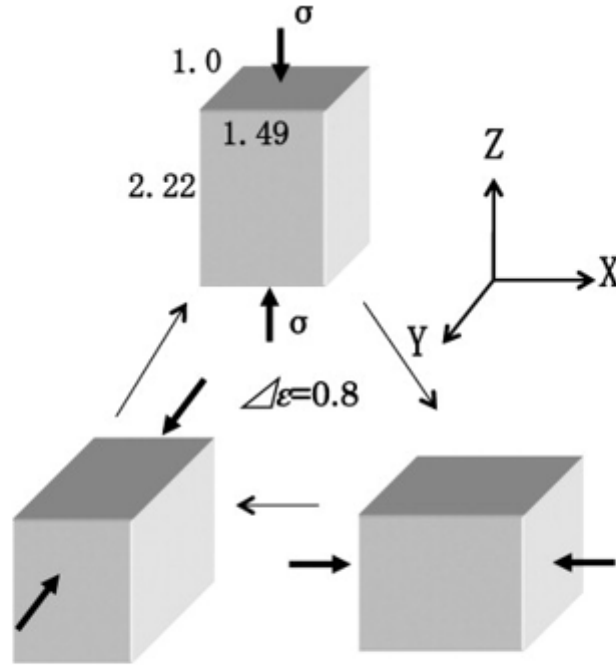


**Figure 1.7** Schematic representation of MDF when a pass strain  $\Delta\epsilon = 0.8$  is employed.

Numbers indicate the aspect ratio of the rectangular shaped sample [73]

A Mg AZ31 alloy after MDF has a good balance of strength and ductility at ambient temperature [76]. Its average grain size was approximately 300 nm, an ultimate tensile strength of 530 MPa and ductility was about 15%. For an AZ61Mg alloy, the average grain size reduced from 56.8  $\mu\text{m}$  to 0.8  $\mu\text{m}$  after MDF, which can be attributed to mechanical twinning, kinking, and continuous dynamic recrystallization. The MDFed sample showed an ultimate tensile strength of 440 MPa and ductility of over 20% [73]. Most recently, Biswas and Suwasn[77] reported they fabricated a Mg–3Al–0.4Mn alloy with UFG microstructure and weak texture in their preliminary experimental. The average grain size was about 400 nm and the texture was rather weak characterized by electron backscattered diffraction (EBSD), which resulted in an increment in yield strength (200 MPa) and ductility (55%) at ambient temperature [77].

## **1.4.2.2 Two-step approaches**

Because cryomilling and SPS are used in this project to produce a bulk NS Mg alloy, those two techniques will be discussed in detail while other commonly used methods will only be simply described.

### **1.4.2.2.1 Synthesis of nanostructure particles**

#### **(1) Inert gas condensation**

This technique was initially reported and studied by Gleiter [51] and Siegel [78]. It is capable of producing large amount of tiny crystallites with dimension of several nanometers. Metal is firstly evaporated in a chamber at evaporation temperature. Afterwards, it is evacuated to high vacuum ( $\sim 10^{-7}$ ) and back filled with a low-pressure inert gas. The evaporated metal is condensed into fine powders via a cooling device [58]. Finally, those deposited powders are scraped off and collected for further compaction.

#### **(2) Mechanical milling**

Mechanical milling processes are widely used to produce NS powders [79,80]. During the milling process, heavy deformation was introduced into the metallic powers due to collisions by milling balls. The grains are refined as the milling time increases. A nanostructured grain size can be obtained for most of metallic materials after abundant processing time, which is strongly related to the specific material and machine used. Large quantities of NS powders can be obtained in a single batch if using appropriate equipment.

Several techniques, including attrition mills, shaker mill and planetary ball mills, have been developed and modified for dry milling, SPEX milling and cryomilling [80]. The evolution of powder particles during milling process usually consists of three steps [81,82], which will be elaborated in the section of cryomilling.

### (3) Cryomilling

#### *Development of cryomilling*

Cryomilling, which can also be classified as a severe plastic deformation technique, evolves from a mechanical milling process but the material is milled with milling balls and a cryogenic liquid instead of a process control agent. In this way, compared with conventional mechanical alloying, cryomilling exhibits several features including relatively high strain rates, large accumulative strains, and a cryogenic temperature, which sharply reduce processing time to obtain the satisfied tiny particle size [81,83]. Because of working at a cryogenic temperature, it can effectively suppress powder agglomeration and welding to the milling balls. In addition, contamination by oxygen, nitrogen and iron are reduced due to the lower diffusion coefficients of oxygen and nitrogen under nitrogen atmosphere [84]. More recently, cryomilling has attracted considerable attention because of its ability to produce nanocrystalline and other non-equilibrium structures and bulk materials followed by appropriate consolidation techniques. One of the early literatures on the application of cryomilling was a composite of Al–Al<sub>2</sub>O<sub>3</sub> [85]. Subsequently, cryomilling has been widely used to produce nanostructured materials such as Ni [86,87], Al [88-93], Fe [94], Zn [95] and Ti [84,96] alloys. Considering the advantages of

cryomilling and the process obtained in other alloys systems, cryomilling has been used to fabricate and successfully synthesize nanostructured bulk magnesium based alloys [83,97]. Because grain size reduction of Mg and its alloys to NC scale by conventional routes are not able to fully suppress dynamic recovery and recrystallization [98], cryomilling provides another facile method to produce NS materials.

### *Apparatus and processing*

As indicated by Herrick et al. [85], the first cryomilling apparatus was modified based on a Szegvari attritor mill, which can allow continuous flow of liquid nitrogen into the mill and control the milling temperature. Figure 1.8 gives a schematic design of a typical cryomilling attritor and figure 1.9 demonstrates how the Szegvari attritor is converted to a cryomill [81,99]. The most commonly used cryomilling equipment reported in the publications are from Union Process laboratory mills. As shown in figures 1.8 and 1.9, the milling atmosphere contains the powder, milling media and continuous flowing liquid N<sub>2</sub> [81,100]. To prevent overpressure, evaporated nitrogen flows into a blower coupled with a particle filter to seize any powder particles within the gas flow. A temperature controller is applied to switch on and off valves in order to control liquid nitrogen flow speed to keep the temperature of the mill under setting values [81,99].

### *Microstructure evolution of cryomilled powder*

As indicated previously, cryomilling is mainly distinguished from mechanical milling in two aspects: First, cryomilling can be regarded as mechanical milling that runs in a bath of liquid nitrogen. Secondly, a lower-energy milling level is employed. Due to the cryogenic milling temperature, suppression of dislocation recovery in the material is significant, which plays a positive role to reduce the milling time to obtain nanocrystallites [101]. Therefore, the mechanism of nanostructure formation during cryomilling is similar to mechanically milling process. Fecht[82] stated there are mainly three stages of microstructure mechanically milling process. Firstly, localized deformation occurs in shear bands consisting of high density dislocation arrays; secondly, because these dislocation arrays are not stable and dislocation annihilation and recombination of dislocations then ensue, this results in the formation of nano-sized subgrains; finally, this sub-grain structure transforms to completely random high-angle grain boundaries between individual grains. Figure 1.10 also illustrates the mechanism of grain refinement during ball milling [81,95].

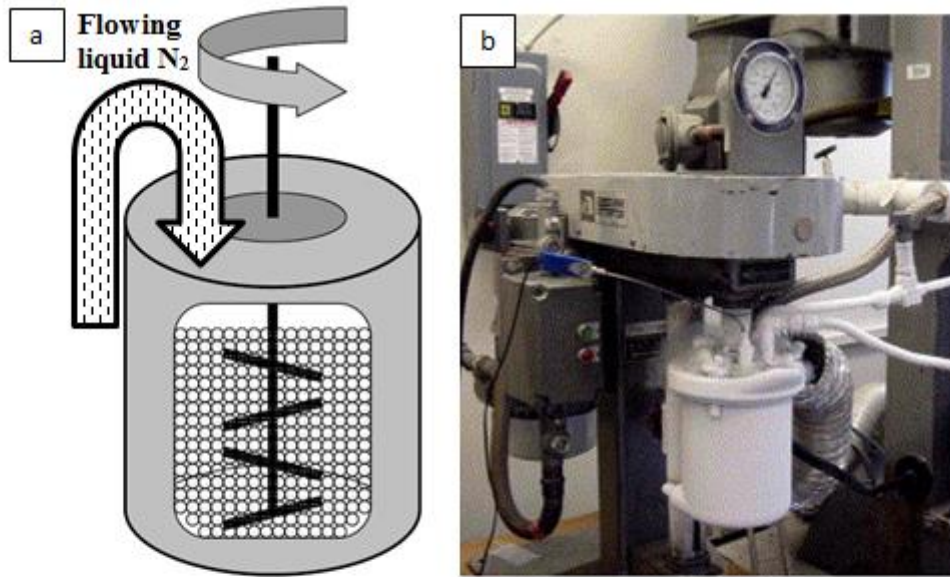


**Figure 1.8** (a) Schematic design of a typical cryomilling attritor mill [99], (b) Photograph of a modified Union Process Szegvari Attritor [81]

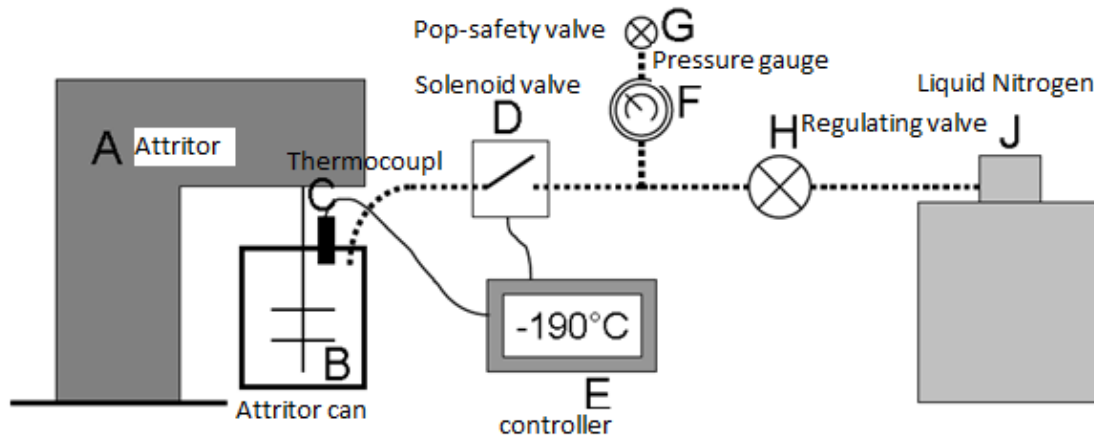


**Figure 1.9** Schematic design of an attritor with cryogenic cooling [99]

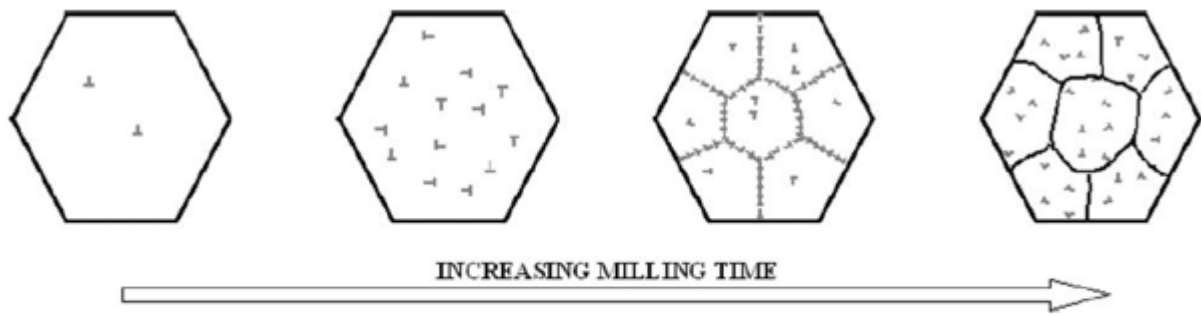


**Figure 1.10** Schematic representation of grain refinement mechanism during ball milling [81,95]

### *Cryomilled magnesium based alloys*

Because magnesium powder is very reactive, cryomilling has rarely been used to synthesize UFG sized magnesium alloys. Most recently, Pozuelo et al. [83] successfully produced nanocrystalline Mg–Al alloy powder via cryomilling. The average grain size of cryomilled powder was about 25 nm. Zheng et al. [100] reported Mg–Al–Zn alloy particles with a size of 30  $\mu\text{m}$  consist of nano-sized grains with a size of approximately 40 nm. In addition, cryomilling has also extended to the application of magnesium hydrogen storage material recently [97,102,103].

#### **1.4.2.2 Consolidation of nanostructure particles**

To transform cryomilled powders into a bulk material, a great many consolidation or sintering methods, such as hot-isostatic-pressing (HIP) and cold-isostatic-pressing (CIP) need to be employed. For my research work, spark plasma sintering (SPS) is the only one consolidation technique and will be illustrated in details in the following sections.

## (1) CIP/HIP

CIP/HIP are commonly used techniques to consolidate NS powder particles [81]. Because of processing at room temperature, CIP generally cannot fully compact powder particles. By contrast, with the combination of high working temperature and stress to densification, satisfactory density can be obtained after HIP. Additionally, samples with large sizes can be produced by HIP. Nevertheless, secondary consolidation techniques such as hot extrusion, ECAP or HPT may be necessary for full densification of NS powder particles [81]. The oxidized film covering around the particle surface or the particle boundaries can be broke down by the large amount of shear, thereby facilitating further densification [88].

## (2) Spark Plasma Sintering

To produce bulk materials with unique properties, the precondition is that the original nanocrystalline structure in the cryomilled powder can be retained after the consolidation process. However, due to high working temperature, conventional consolidation methods of cryomilled powder always lead to a significant grain growth [88,104]. SPS has been proved to effectively sinter powder with nanocrystalline structure into a dense disk with rapid rates at low temperatures, both of which enable the preservation of the nanostructured microstructure [89].

## *History of SPS*

SPS consolidates powders via a combination of the use of electrical current and uniaxial mechanical pressure. SPS has been widely used since 1970s based on the fabulous increasing number of publications related to SPS processes [105]. The fast development of SPS can be contributed to its own unique characteristics compared with other conventional consolidation techniques including pressureless sintering, hot press, etc. Its main advantages are in the following: quicker heating rate, lower sintering temperature, shorter sintering time, consolidation of difficult-to-sinter-powders, and no need of sintering aids cold compaction, and less sensitivity to initial powders characteristics [105,106]. Particularly, lower sintering temperature and shorter sintering time can make SPS manage to produce large bulk nanocrystalline materials with near theoretical density [105-107]. In these publications, SPS was called as field-assisted sintering technique (FAST) [108], electric pulse assisted consolidation (EPAC) [109], pulsed electric-current sintering (PECS) [110], plasma-assisted sintering (PAS) [111] and a new name current-activated, pressure-assisted densification (CAPAD) [107]. Irrespective of the different names, the core of this technique is considerable electric currents and uniaxial pressure are loaded at the same time. In most publications, there is little persuasive evidence for the existence of sparks or plasma during the SPS process [112]. On the other hand, there are lots of convincing reports of the dominance of current activated sintering [113-116]. Due to the historical reason, spark plasma sintering (SPS) is most frequently used although plasma was proved to be absent in SPS processing [117,118]. For this thesis, spark plasma sintering is used through the whole context to avoid confusion.

### *Apparatus and processing*

Most of SPS systems using electric current and pressure to consolidate materials are DC and pulsed DC machines in the world. Two primary suppliers are companies such as SPS Syntex (Japan, formerly Sumitomo) [83] and FCT Systeme GmBH (Germany) [119]. Figure 1.11a is a photograph of a FCT Systeme GmBH SPS system after loading a sample and figure 1.11b is a schematic illustrating the main components of a SPS apparatus [107]. A typical system comprises of a vacuum chamber, electrodes for both current and load delivery, and a power supply capable of delivering high electric currents at relatively low voltages. The current capacity of typical SPS units ranges from 1000 A to 10,000 A at 10–15 V maximum. The force abilities range from 50 kN to 250 kN[107]. For example, the FCT Systeme GmBH SPS system used in this project can apply a force between 12.5 and 4000 kN at maximum temperature of 2400 °C. A component with diameter of 30 cm can be fabricated in a short time. These features offer a novel route to producing a lot of materials with excellent properties, such as nanomaterials, functionally graded materials (FGM), composite materials, innovative cemented carbide materials, metallic alloys and intermetallics structural and functional ceramics. As shown in figure 1.11, the sample (initially powder) is sintered inside a die which is fixed by top and bottom copper spacers connecting with electrodes. Due to brilliant strength at elevated temperature, good thermal and electrical conductivity, the most commonly used die and plunger are made of graphite with high purity and high-density [105-107].

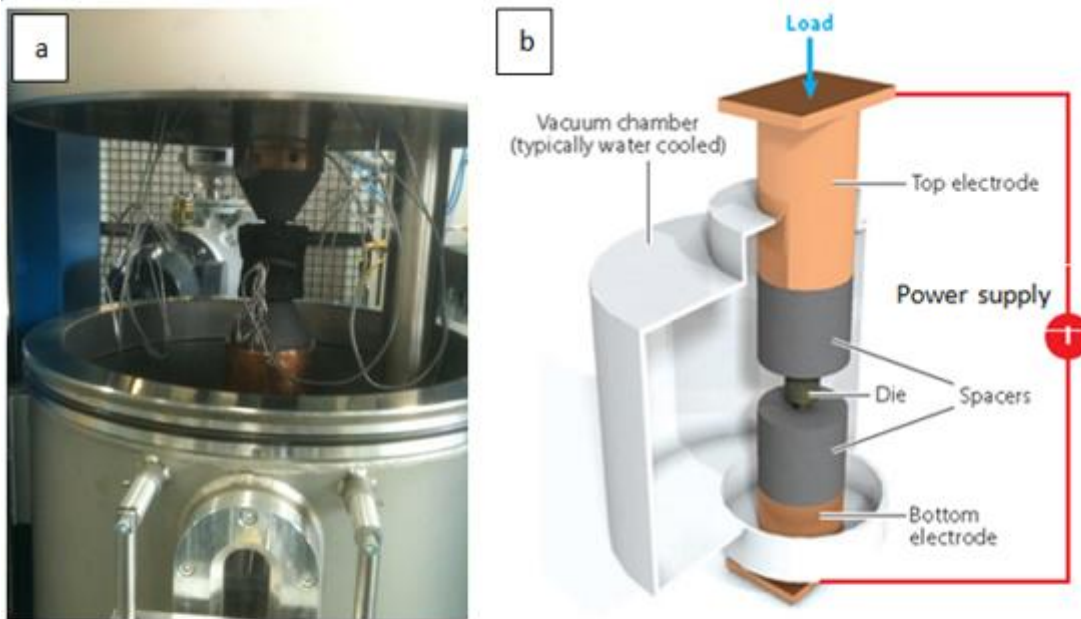


**Figure 1.11** (a) A picture of a FCT Systeme GmbH SPS System after loading a sample. This unit was installed at the University of Sheffield. (b) A schematic depicting the key components in the chamber [107]

The SPS process is also depicted in figure 1.11 (b). It simultaneously applies an electric current and a uniaxial pressure to consolidate powders. The applied electric current and mechanical load can be persistent throughout the whole sintering cycle or may vary during different densification stages. The current can be controlled by a coupled thermocouple so that an expected temperature cycle can be designed. Most machines are equipped with real-time data acquisition systems, which record temperature, current, voltage and displacement. Figure 1.12 schematically shows a SPS mould with powder inside the chamber. It is not only used for densification but also simultaneously produce reactive powders [105-107].

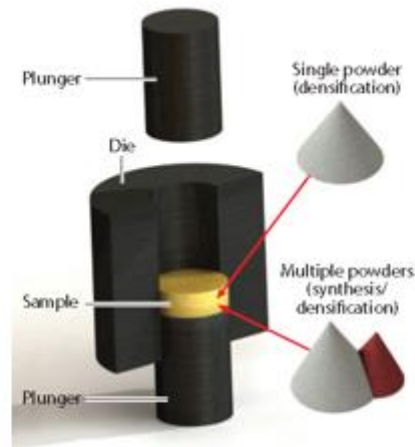


**Figure 1.12** A schematic of a die, plungers, and powder. Pure densification or simultaneous synthesis and densification can be realized via SPS [107]

The mechanism of SPS densification is still a controversial issue in the research area. In particular, it is not clear whether a plasma is generated or is totally absent during SPS processing, which was mentioned in the previous section. One mechanism was proposed by Knor et al. [112] as schematically shown in figure 1.13.

### *Magnesium based alloys fabricated by SPS*

Rapidly solidified AZ91 alloy ribbons prepared by melt–spinning were processed by SPS at 400 °C for 300 s after being crushed into fine powders [120]. The pre-formed compacts consolidated by extrusion after heat treatment showed high tensile strength of 350 MPa, which can be partially attributed to the retention of fine grains during SPS. Porous magnesium based materials can be synthesized via SPS using Mg alloy chips as starting materials [121]. It indicated that the high density materials where the particles are well bonded consist of low melting Mg-Al intermetallic and wide semi-solid temperature range, since its non-equilibrium

solidified compound is remelted during SPS. In addition, dense bulk metallic glass ( $\text{Mg}_{55}\text{Cu}_{30}\text{Gd}_{15}$  and  $\text{Mg}_{55}\text{Cu}_{30}\text{Y}_{15}$ ) were successfully prepared by spark plasma sintering at 125 °C [122]. Ayman et al. [123,124] reported the tensile strength of consolidated Mg–Al–Zn–Ca–La and Mg–Al–Mn–Ca billets were processed via SPS was improved due to good bonding between particles as well as hindered grain growth compared to conventional sintering. Recently, Straffelini et al.[125] showed that a high relative density of AZ91 alloy can be produced. Nevertheless, the sintering degree of the materials was not excellent. Muhammad et al. [126] systematically studied the optimized SPS processing parameters for pure magnesium and AZ31 alloy. They stated a maximum tensile strength of 120 MPa for Mg and 160 MPa for AZ31 alloy were attained at 585 °C and 552 °C, respectively. In addition, Mg–SiC and AZ31–SiC composites were also successfully synthesized based on the conditions of monolithic Mg and AZ31 alloy. The SiC reinforced particles improved the tensile strength of corresponding monolithic Mg and AZ31 alloy to 140 MPa and 170 MPa, respectively [126].

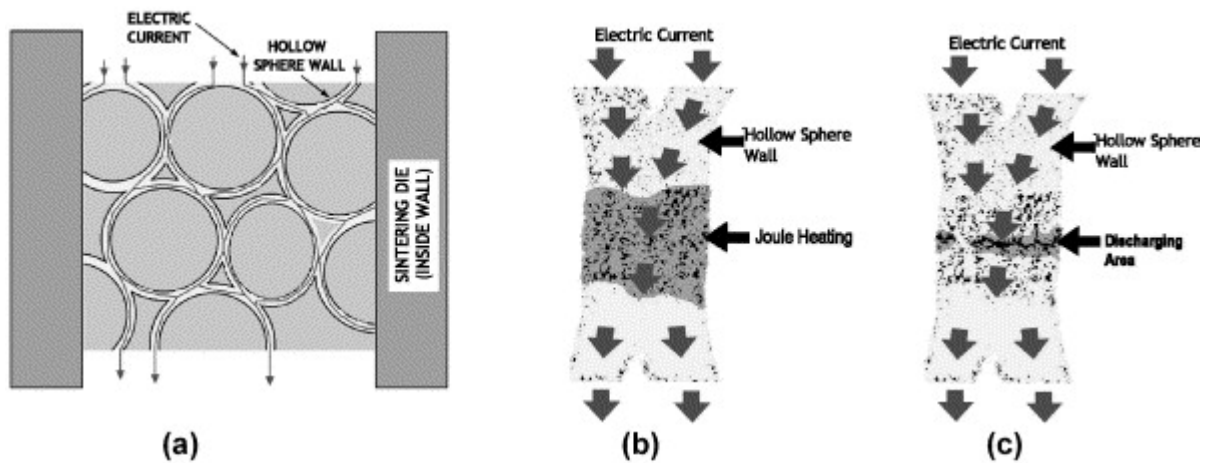


**Figure 1.13** (a) Current flows through the randomly hollow sphere (RHS) ball wall of stainless steel 316L during SPS, (b) extra Joule heating helps to eliminate micro-pores, (c) spark plasma generated at fissure or mass gap results in the evaporation–condensation mass transferring [112]

The strength of bulk NS metals is higher than those of micro sized metals, even corresponding alloys [50]. However, the quite low ductility at room temperature limits its application as structural materials. Recently, as shown in figure 1.14, Wang et al. [49] successfully obtained a nanostructured Cu with a bimodal grain size distribution (with micrometre-sized grains embedded inside a matrix of nanocrystalline and ultrafine (<300 nm) grains). This bimodal microstructure rendered high strength exceeding 400 MPa and high tensile ductility-65% elongation to failure.

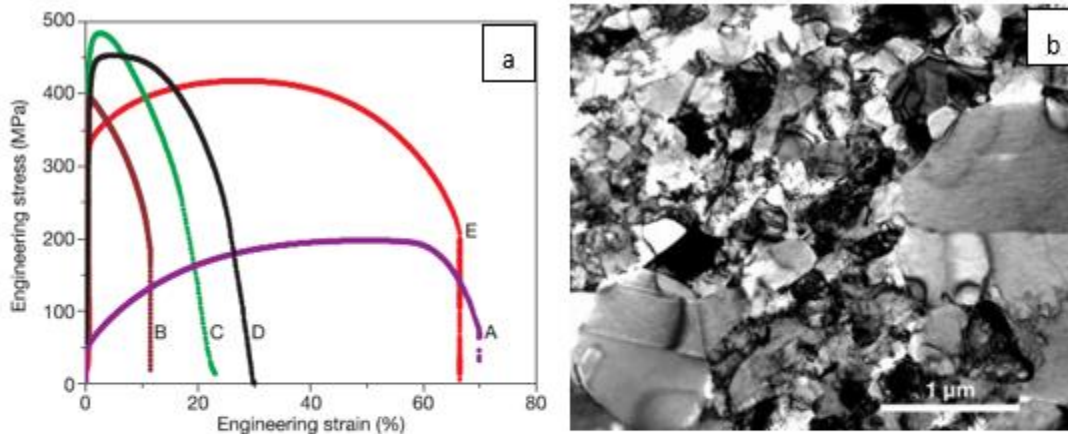


**Figure 1.14** (a) Engineering stress–strain curves for pure Cu. Curve A, annealed, coarse grained Cu; E, 93% Cold work + 200 °C, 3 min. (b) TEM image of the sample used to obtain curve E. (Adapted from ref. [49])

SPS can retain the grain sizes of nanocrystalline starting powders during consolidation. Much recent work has focused on using this to obtain bulk NS materials with a bimodal microstructure, especially in the field of aluminum and its alloys [89,127-130]. Such a bimodal microstructure imparts an excellent balance of strength and ductility. For magnesium based alloys, Pozuelo et al.[83] successfully consolidated a cryomilled  $Mg_{70}Al_{30}$  powder to produce a dense bulk nanocrystalline material via SPS. A bimodal grain size distribution was also observed. 0.5  $\mu m$  coarse grains were surrounded by NC grains with a mean grain size of approximately 50 nm [83].

## 1.5 Microstructure of bulk nanostructured metals

Due to various compositions, processing methods and parameters, different bulk NS materials may exhibit significant difference in terms of microstructures[58,131], which include grain size, grain boundary structure, dislocation structure, presence of precipitate, second phases, nano-twins and solute atom content [132,133]. However, the microstructures of different bulk NS metals and alloys have several features in common, which are described and summarized as follows:

### **1.5.1 Dislocation density**

Bulk NS metals and alloys have various dislocation densities, which depends on the specific processing route. SPD methods usually introduce very high dislocation density (e.g.,  $10^{15}$ - $10^{16}$   $m^{-2}$ ) [134]. Electrodeposition generally induces a relatively high dislocation density (e.g.,  $10^{14}$ - $10^{15}$   $m^{-2}$ ) [135]. Particles with nano-sized microstructure produced by inert gas condensation, later consolidation leads to low dislocation density in bulk NS materials. For instance, cryomilling promotes the formation of dislocation and its density can reach on the order of  $10^{16}$   $m^{-2}$  in NS particles. Nevertheless, after consolidation by HIP or SPS, significant reduction of dislocation density to the order of  $10^{14}$  -  $10^{15}$   $m^{-2}$  takes place [136].

### **1.5.2 Grain boundary misorientations**

Grain boundaries (GBs) can be divided into high-angle GBs ( $> 15^\circ$ ) and low-angle GBs ( $2$ - $15^\circ$ ). The specific volume fraction of these two GBs strongly relates to processing technologies. A high fraction of high-angle GBs usually could be produced via electrodeposition [137]. For SPD methods like ECAP and HPT, the fraction of high-angle GBs

was determined by the imposed strain, processing parameters and processing routes [47,60]. During initial stages of deformation, a great many GBs exist with low-angle misorientations. However, with increasing strain, low-angle GBs are transformed into high-angle GBs. Generally, bulk NS materials produced by two-step approaches own higher fraction of high-angle GBs due to potential recrystallization during consolidation [81].

### **1.5.3 Non-equilibrium grain boundaries**

This concept was first proposed in the 1970-80s based on studies regarding to interactions of lattice dislocations with GBs[138]. A non-equilibrium GB is defined by excess GB energy and the existence of long range elastic stresses. GBs in bulk NS materials processed by SPD routes have been reported to be essentially non-equilibrium GBs, because these GBs are in the form of a curved and wavy configuration [60]. By contrast, NS materials processed by two-step methods generally own equilibrium GBs, even though the precursor NS particles (e.g., cryomilled powder) own non-equilibrium GBs [81]. This can be attributed to the elevated working temperature applied during consolidation, which is beneficial for the annihilation of some dislocations and also stimulates dissipation of excess GB energy.

## **1.6 Deformation mechanisms of bulk NS metals**

For typical coarse grained (CG) metals, deformation is attributed to the lattice dislocations movement, which are generally formed within grain interiors or around GBs. However, for the counterpart bulk NS metals and alloys, very limited space in grains is

available to accumulate dislocations. Therefore, the deformation mechanisms are quite different compared to those of CG metals. Several deformation mechanisms have been investigated and disclosed, which will be discussed below in detail.

### **1.6.1 Grain boundary sliding/grain rotation**

Plastic deformation in CG metals is mainly achieved via continuous nucleation of dislocations from Frank–Read sources within grains and the slip motion of dislocations through internal crystal lattice [139]. Obviously, the size of the sources is restricted to the size of corresponding grains. Because the stress required to trigger a Frank–Read source is inversely proportional to its size, this mechanism can only be valid to a minimum grain size of  $\sim 1 \mu\text{m}$ [140]. With further reduction in grain size, finally all dislocation nucleation terminates and is replaced by the GB-based processes including GB sliding, migration, diffusion and grain rotation [141-143].

Molecular-dynamics simulations of a bulk NS Ni sample with a mean grain size of 12 nm indicated GB sliding was the main deformation mechanism during a tension test at room temperature. The GB sliding is prompted and enabled by uncorrelated atomic shuffling and stress-assisted diffusion at some degree [144,145]. By contrast, molecular dynamics simulations of bulk NS Pd materials with symmetric grains and Non-equilibrium GBs revealed GB sliding was strongly related to enhance GB diffusion at elevated temperature, which was similar to Coble creep [143]. Theoretical analytical models reported grain rotation behaviour can be regarded as a sliding issue along the boundary of the grains [146-148].

## 1.6.2 Dislocation emission from grain boundaries

When grains are too small to provide a good source of dislocation nucleation, grain boundary takes over and acts as the main source for dislocation emission. Because *in situ* TEM is normally performed with low resolution, it is not able to distinguish partial dislocations from perfect dislocations. However, partial dislocation emissions from GBs were widely detected by MD simulations [149-152], and were confirmed by *ex situ* HREM investigations [153]. In addition, in some special circumstances, dislocations with high density are possible and can be obtained in bulk NS metals and alloys. For instance, a large amount of dislocations were observed inside the grains of bulk NS Ni after constrained cryorolling [154].

## 1.6.3 Deformation twinning

Because the stress required for a twin to nucleate increases rather quickly compared to the full dislocation slip, deformation twinning in NS Mg is not energetically preferred [155,156]. For instance, the stress for twin nucleation increases substantially with nano-sized grains [157,158]. For CG Mg and its alloys, profuse deformation twinning takes place during tension or compression tests [14,15,157,159]. These deformation twins are dependent on working temperature [157,160], strain rate [160], and grain size [156,161-164]. It has been reported bigger grain sizes were more favourable for twin nucleation [156,161-164]. With decreasing grain size, the Hall–Petch slope constant for deformation twinning is much bigger than that for dislocation slip [160,163]. Therefore, deformation twinning will be retarded with a smaller grain size if critical stress to stimulate the twin is not reached. Nevertheless,

deformation twins were discovered in cryomilled Mg based alloys powder [83,100,165-167]. Based on experimental observations and MD simulation results, Zhu [156] summarized seven deformation twinning mechanisms in nanostructured materials, namely, overlapping of stacking fault ribbons, partial emission from grain boundaries, twinning with low macroscopic strain, grain boundary splitting and migration, sequential twinning mechanism, partial multiplication at twin boundaries and dislocation rebound mechanism.

#### **1.6.4 Stress-coupled grain boundary migration**

Theoretical studies [168,169] proposed that when a shear stress is imposed on a GB, normal motion of the GB can be prompted as well as the tangential displacement of grains along the GB. This mechanism is generally designated as stress-coupled GB migration. It has been demonstrated experimentally NS Al films [170,171], whereas the grain size where stress-coupled GB migration took place was about 100 nm, which was much larger than that simulated by molecular dynamics.

### **1.7 Mechanical behavior of bulk nanostructured metals**

Strength and ductility are often commonly used to evaluate mechanical properties of metals and alloys. Generally, strength and ductility are normally mutual exclusive in bulk NS metals and alloys [48-50,53,172]. In the following part, the study of mechanical behaviour is focused on strength and ductility in bulk nanostructured materials.

## **1.7.1 Strength**

### **1.7.1.1 Hall-Petch relation**

Grain refinement plays an important role in improving mechanical behaviour, especially increasing yield strength. For conventional CG metals, the relationships between yield strength and grain size are well illustrated and concluded to follow the Hall-Petch equation. For UFG metals and alloys with grain size in the range of 100 nm and 1  $\mu\text{m}$ , the Hall-Petch equation is still validate to evaluate mechanical properties [131]. However, with further grain refinement down to smaller than 100 nm, break-down of Hall-Petch equation was extensively reported [131].

### **1.7.1.2 Deviation from Hall-Petch relation**

When internal grain size is less than 100 nm, a deviation from the Hall-Petch relationship often takes place [58,131]. When the grain size is in the range of 20 to 100 nm, the changes of yield strength still obeys the Hall-Petch relationship, but it should be noted the Hall-Petch equation slope was substantially decreased. At some point, the strength increment saturates and shows no further increase. This could be fully elucidated by the change of the deformation mechanism as mentioned above. The prerequisite for the Hall-Petch relationship is dislocation pile-ups must be accumulated near the GBs [173]. When the grain size is between 20 and 100 nm, the nucleation and glide of dislocations (full or partial dislocations) still dominates the deformation mechanism. Nevertheless, dislocation pile-ups cannot be accumulated near the GBs due to the very limited area inside the grains [58,150]. While the

grain size is further decreased to around 10-20 nm, GB-based deformation mechanism governs the plastic deformation, and dislocation-based mechanisms become insignificant.

## **1.7.2 Ductility**

The ductility of most CG ductile metals can be as high as 50-60%. By contrast, their correspondent bulk NS metals and alloys have relatively low ductility, usually less than 5%, which is the critical ductility required for many structural applications [58,133]. Currently, the low ductility of bulk NS metals and alloys has largely limited their use as structural materials. The poor ductility could be attributed to the following two reasons: extrinsic processing defects and intrinsic microstructures/deformation mechanisms [174,175]. Processing defects, such as porosity and cracks, can be easily found in bulk materials fabricated by “two-step” approach. These defects are the main reasons for premature failure during mechanical experiments before noticeable plastic deformation takes place, sometimes failure even occurs before the onset of yielding [58]. To avoid these defects, bulk defect free NS metals and alloys are produced by the “one-step” approach. The ductility is governed by intrinsic deformation mechanism. Nevertheless, those materials typically have poor ductility. The poor ductility of defect free bulk NS materials can be partially attributed to their low strain hardening [50]. Work hardening strongly depends on the accumulation of dislocations, which makes further deformation more difficult [175]. Conversely, in nanostructured metals and alloys, dislocation accumulation rarely occurs due to small grain sizes [176]. Dislocations are generated from one GB segment and quickly disappear at another without dislocations piling up inside the grains.

Indeed, zero work hardening was found experimentally in most nanostructured metals [177]. The poor work hardening rate leads to early necking instability, thereby causing poor ductility.

### **1.7.3 Approaches to increase ductility of bulk NS metals and alloys**

Based on the above deformation mechanisms for low ductility of bulk NS materials, several strategies were designed for enhancing the ductility, which are classified into two catalogues, namely extrinsic and intrinsic strategies.

#### **1.7.3.1 Extrinsic strategies**

To increase ductility of bulk NS metals and alloys produced via using “two-step” methods, it is important to decrease processing defects to minimize the negative effect of extrinsic detrimental factors. For instance, contamination introduced during processing needs to be minimized, and proper processing windows must be established to eliminate porosity and enhance bonding between particles. An extra extrusion after consolidation was often used to further break down the oxide film covering metallic powders, remove the internal pores and improve the bonding between particles [165].

#### **1.7.3.2 Intrinsic strategies**

Intrinsically, improving working hardening is crucial to increase the ductility of bulk NS metals and alloys. Hence, the main principle for improving ductility by intrinsic methods

is to maximize the dislocation accumulation inside grains during deformation. Several specific and effective strategies have been reported to meet this purpose, which will be described below in detail.

#### **1.7.3.2.1 Bimodal/multimodal grain size distribution**

The fundamental mechanism for bimodal grain size distribution is combining the high strength of nanocrystalline grains and the better work hardening of coarse grains to gain relatively high strength and enhanced ductility simultaneously. A good combination of strength and ductility could usually be obtained by this strategy and has been reported [174,178]. Nevertheless, except in some exceptional examples in which high strength and good ductility are simultaneously achieved [49,179], significant improvement in ductility usually comes with a sacrifice in strength due to the low strength of the CG constituent. Recently, multimodal grain size distribution, ranging from nanometers to microns, produces a better combination of strength and ductility, i.e., minimizing the loss in strength while sustaining approximately equivalent improvement in ductility [175]. Zhao reported [179] the yield strength of multimodal Ni is about 50% higher than that of bimodal Ni, while the two samples have similar ductility.

#### **1.7.3.2.2 Nanoscale twins**

Pre-existing nano-twins, either growth [132,180] or deformation twins [181], can significantly improve ductility while preserving high strength. For example, due to a relatively dense growth nano-twins in the ultrafine grains, nanotwinned Cu has equal strength compared

to NS Cu, but its ductility was substantially extended [132,180]. Twin boundaries can act as effective barriers to hinder dislocations movement, which cause strengthening similar to the role of GBs. Furthermore, large numbers of dislocations can be piled up at twin boundaries, thereby improving high strain hardening.

#### **1.7.3.2.3 Other strategies**

Besides these two most important and commonly used intrinsic strategies, other methods have also been established to expand ductility of bulk NS metals and alloys, such as a low dislocation density, lowering GB misorientation angle, introducing precipitates and phase transformation. For example, an UFG Cu with low dislocation density produced by HPT followed by cold rolling exhibited a greater tensile uniform elongation than another UFG Cu with high dislocation density treated only by ECAP [182]. The low dislocation density material was able to offer more space for dislocations pile-ups during mechanical testing. Numerous ultrafine grains linked with low misorientation angle grain boundaries constituted a lamellar band [183]. This structure permitted dislocations to slide through low misorientation angle grain boundaries and to gather within the band, thereby improving the uniform deformation ductility without loss of strength [183]. In addition, nano-sized precipitates dispersed in grains can act as pins to accumulate and store dislocations, which can enhance work hardening of bulk NS metals and alloys [133]. Another method is to induce phase transformation during mechanical tests. For instance, an UFG steel, processed by cold rolling followed by annealing, presented a good combination of high strength and ductility because of strain-induced martensitic transformation at room temperature [184].

## **2 Effect of cryomilling time on microstructure evolution and hardness of cryomilled AZ31 powders**

### **Abstract**

In this section, the synthesis of nanocrystalline AZ31 powder by cryomilling was studied. The microstructural evolution during cryomilling, including the changes of particle morphology and internal grain size, was characterized via optical microscopy, SEM, TEM and XRD. Observations during the cryomilling produced four main findings. Firstly, minimum average grain size of about 30 nm was reached when the cryomilling time was extended to 6 hours or longer. Secondly, cold welding played a dominant role in the early stage of cryomilling, while fracture took place in the late stage and surpassed cold welding. The former led to a particle size increase while the latter decreased the particle size. The minimum average particle size after 6 hours cryomilling was approximately 26 $\mu$ m. Thirdly, a few particles were agglomerated with other particles and could not be processed by cryomilling due to cold welding. Finally, with the cryomilling time increasing, the hardness reached around 160 HV after 6 hours cryomilling.

### **2.1 Introduction**

Recently, cryomilling has attracted considerable attention because of its ability to produce nanocrystalline and other non-equilibrium structures and bulk materials followed by appropriate consolidation. One of the early literatures presented the application of cryomilling was a composite Al–Al<sub>2</sub>O<sub>3</sub> [85]. Afterwards, cryomilling has been widely used to produce nanostructured materials such as Ni [86,87], Al [88-93], Fe [94], Zn [95], and Ti [84,96] alloys.

Considering the advantages of cryomilling and the process obtained in other alloys system, cryomilling starts to fabricate and successfully synthesized nanostructured bulk magnesium based alloys [83,97]. Grain size reduction of Mg and its alloys to NC scale by conventional routes is prevented by dynamic recovery and recrystallization [98]. In contrast, cryomilling provides a facile method to produce NS materials.

For commercially pure Mg and alloys such as AZ31 with low alloying content, it is a challenge to produce even a UFG microstructure, let alone a NC microstructure, due to the rapid growth kinetics of the single-phase grains. In just the past two years, the combination of cryomilling and SPS was successfully applied and proved to fabricate NS Mg-30Al and AZ80 alloys [83,100,185].

The primary two objectives of this chapter are as follows. First, to find out whether cryomilling can be extended to produce NC microstructure in a magnesium AZ31 alloy with much lower alloying content than Mg-30Al and AZ80 alloys? Second, it can provide guidance to subsequent chapters where the investigations focused on bulk samples consolidated by SPS.

## **2.2 Experimental**

### **2.2.1 Mg alloy powder**

The as-received powder of this study was 200 mesh ( $-75\ \mu\text{m}$ ) helium gas atomized AZ31 powder provided by Magnesium Elektron Ltd, USA. Due to cold welding and repetitive fracturing, the powder morphology was changed significantly during cryomilling. Small particles can be either introduced by the as-received powder or formed by repetitive fracturing during cryomilling. In order to distinguish the source of small particles, particles smaller than  $38\ \mu\text{m}$  were removed by a sieve (400 meshes) before cryomilling. Therefore, its particle size of precursor powder is distributed in the range of  $38\text{--}75\ \mu\text{m}$ .

## 2.2.2 Cryomilling

A cryomill with an integrated cooling system (Retsch, Germany) was employed in this project. The grinding jar was continually cooled with liquid nitrogen during the whole grinding process. Liquid nitrogen circulated through the system and was continually replenished from an autofill system to keep the temperature at  $-196\text{ }^{\circ}\text{C}$  and avoid direct contact with liquid nitrogen. A schematic depicting of the cryomiller and its corresponding cooling system are presented in Figure 2.1.

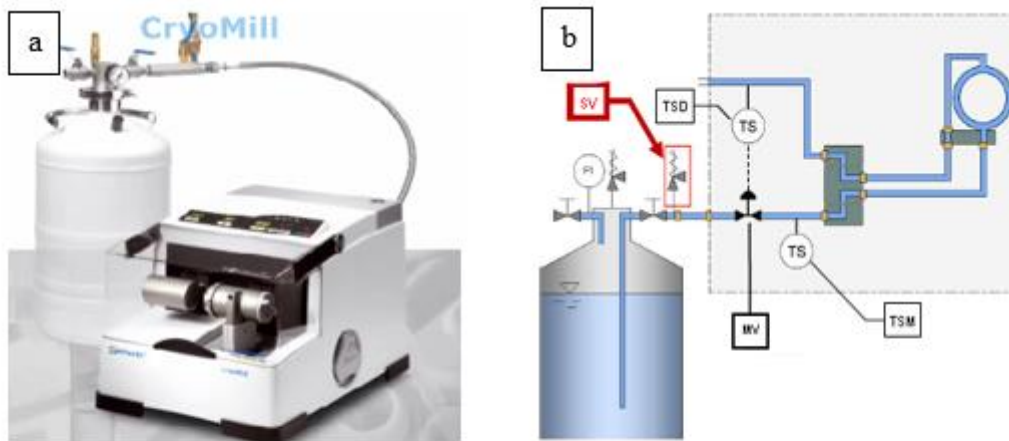


**Figure 2.1** (a) A picture of a Restch cryomill, (b) A schematic depicting the circuit of liquid nitrogen cooling system

6 grams of AZ31 powders and a stainless steel  $\varnothing$  25 mm grinding ball were loaded into the stainless steel 50 ml grinding jar in an argon atmosphere glovebox (Mbraun, Germany). One cycle of the cryomilling process involved precooling, grinding and intermediate cooling. Detailed experimental parameters are shown in Table 2.1. The powders were cryomilled for various time intervals: from 15 minutes to 8 hours, corresponding to from 3 to 96 cycles.

**Table 2.1** Cryomilling process parameters during one cycle

Precooling		Grinding		Intermediate cooling	
Frequency(Hz)	Time(min)	Frequency(Hz)	Time(min)	Frequency(Hz)	Time(min)
5	18	22	5	5	3

### 2.2.3 X-Ray Diffraction (XRD)

A Siemens X-Ray Diffractometer D5000 using Cu K $\alpha$  ( $\lambda = 0.15406$  nm) radiation was employed to study the cryomilled powders. The diffractometer has a programmable divergence slit with a 0.02 rad Soller and a 1 degree divergence slit on the Cu K $\alpha$  x-ray source. The detector was set to read from 30° to 80° at 2.4 s/step with a step size of 0.02°. Fully annealed as-received AZ31 powder was used as a standard to subtract instrumental broadening. XRD peak profiles were fitted by Pearson VII function, and FWHM was used as a measure of peak broadening. The pure sample peak broadening  $B$  was calculated using

$$B = \sqrt{B_{obs}^2 - B_{inst}^2}$$
, where  $B_{obs}$  is the observed peak broadening, and  $B_{inst}$  is the instrumental broadening.

### 2.2.4 Microstructure characterization

#### 2.2.4.1 Optical Microscopy

Optical microscopy was carried out on a Nikon (Eclipse LV150) microscope. Images were taken at various magnifications to study the microstructure and grain size. Samples were cold mounted and ground with SiC paper from 800 to 4000 grit. To minimize oxidation exposure to water, samples were polished with alcohol based diamond suspensions of 1 and

0.25 $\mu$ m. Some samples were etched using an acetic-picral solution (4.2g picric acid, 10ml acetic acid, 70ml ethanol and 10ml water) for 1 s.

#### **2.2.4.2 Scanning electron microscope (SEM)**

The sample preparation procedure for SEM was the same to that of optical microscopy, but etching was not necessary in some cases. A FEGSEM (Inspect F, FEI) was employed to investigate morphology of powders.

#### **2.2.4.3 Transmission Electron Microscopy (TEM)**

TEM samples were prepared by grinding using a mortar and pestle and suspended in isopropanol, followed by ultrasonic dispersion and then deposition onto a 200 mesh Cu grid with holey carbon film. A FEI Tecnai 20, operating at 200 kV, was used for conventional TEM characterization.

#### **2.2.5 Chemical analysis**

Chemical analysis was conducted in an institution (London & Scandinavian Metallurgical Co Limited, Sheffield, UK). Elemental analysis was requested and results reports were returned, for oxygen, nitrogen and iron, because these species are expected to be the main impurity species in cryomilled powders during the cryomilling process.

### **2.6 Micro hardness test**

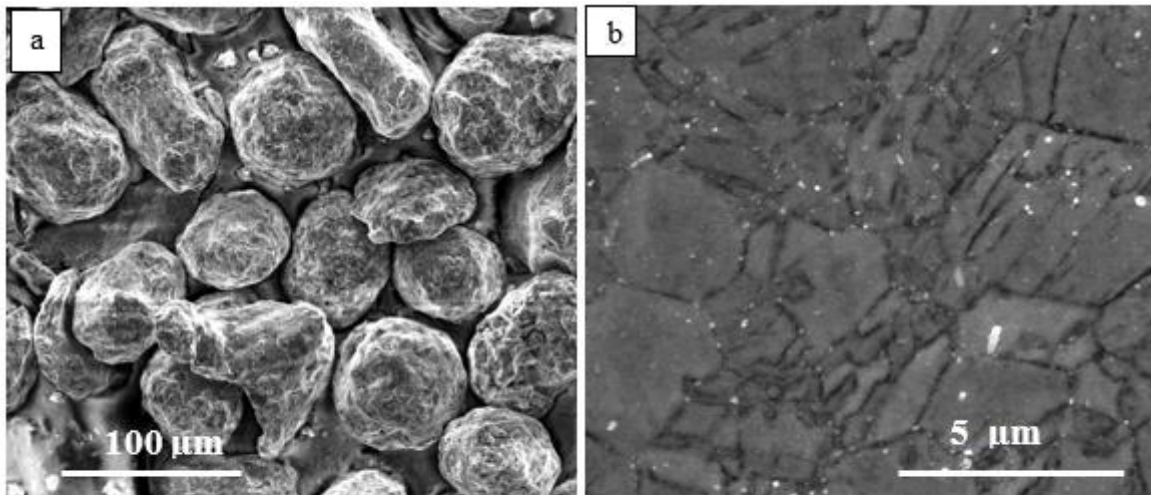
To obtain a flat surface for hardness test, the cold mounted powder samples were ground with 800, 1200, 2500, 4000 grade SiC papers and finally polished by 1  $\mu$ m and 1/4  $\mu$ m alcohol based diamond suspension. A Vickers hardness tester (Akashi Corporation Sagami Plant, model

HM-101) was used to perform hardness tests with a load of 50 grams and a dwell time of 15 s. At least 11 indents were collected for each sample to obtain accurate hardness results.

## 2.3 Results and discussion

### 2.3.1 Particles morphologies evolution during cryomilling

Figure 2.2(a) shows particle size and morphology of the as-received AZ31 powder. After careful grinding, polishing and etching, Fig. 2.2(b) shows the particle has an average internal grain size of  $2.03\pm 0.47\mu\text{m}$ .



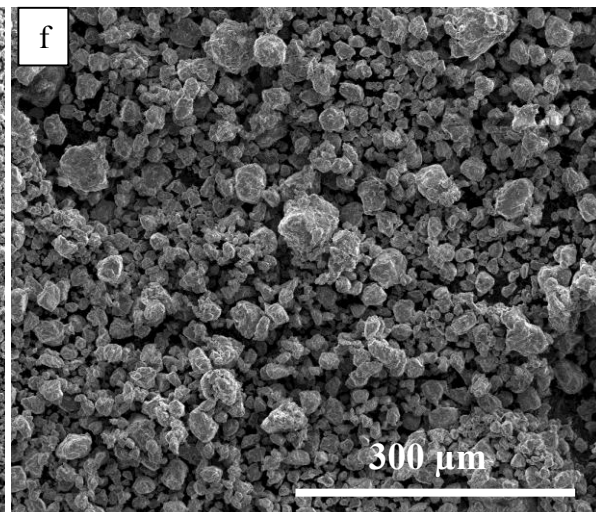
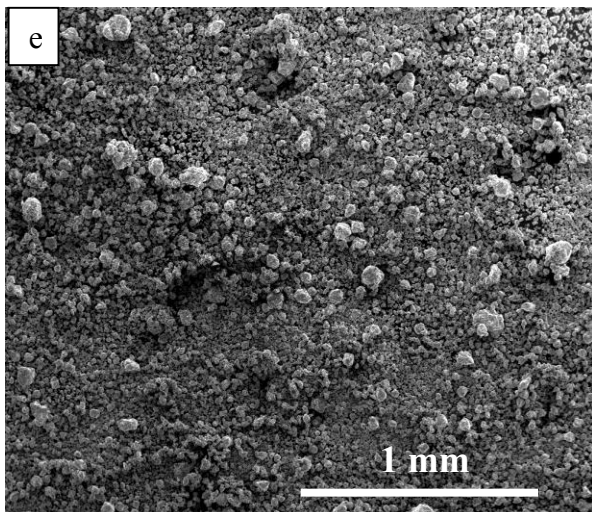
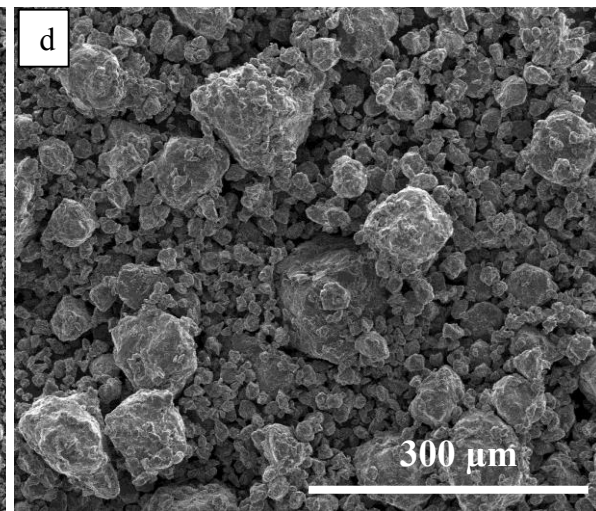
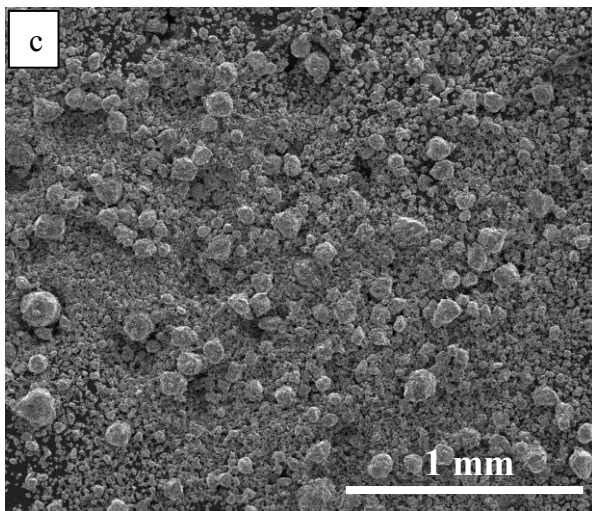
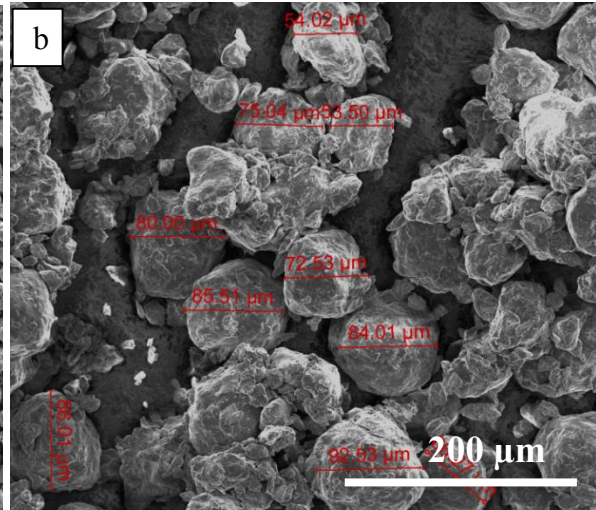
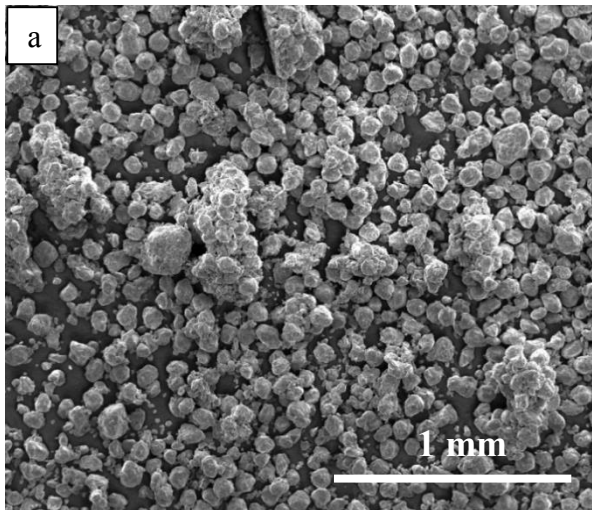
**Figure 2.2** Typical SEM images showing the morphology of (a) as-received AZ31 powder, (b) internal grains

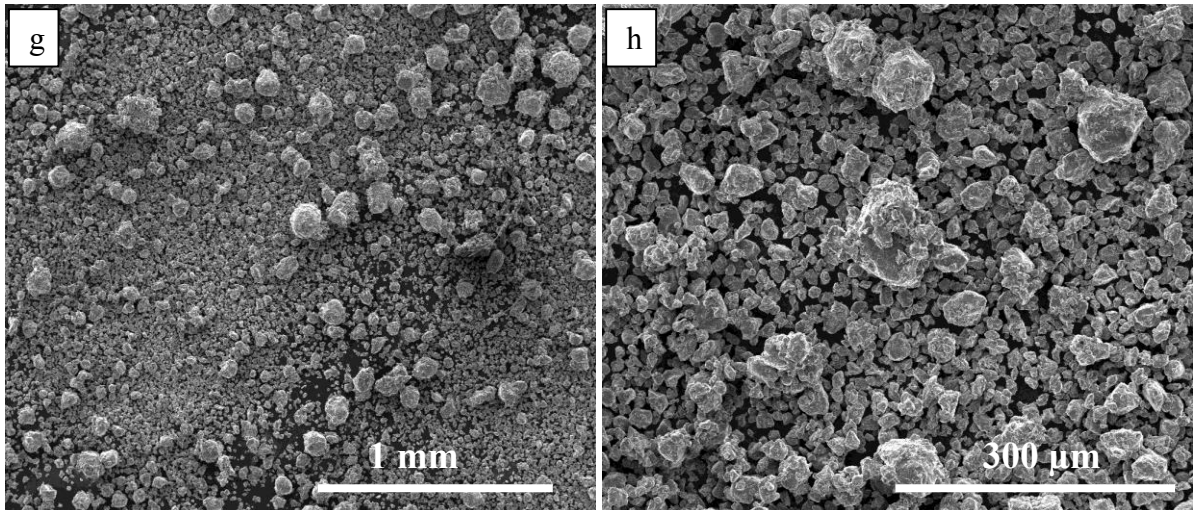
Figure 2.3 shows the particle morphology after different cryomilling times. It should be noted that only 1h, 5h, 6h and 8h cryomilled powders were selected here which were regarded as sufficient to show the particle morphology evolution. As shown in Figure 2.3(a, b), it can be clearly seen that most of the 1h cryomilled particles were larger than the as-received particle size ( $\sim 75\mu\text{m}$ ) and some particles were also agglomerated. However, with increasing the cryomilling time to 5h, approximately half particles were evidently reduced in size due to the

milling. After 6h cryomilling, more coarse particles were crushed into fine particles with an average size of 26  $\mu\text{m}$ . Finally, no significant change in particle size was observed after 8h cryomilling compared to the 6h cryomilled powders. Therefore, there was no point in extending the cryomilling time further. The evolution in particle morphology can be explained by cold welding and fracture occurring during the whole of the cryomilling process [80,81,84,186]. The grinding ball with a high shaking frequency plastically deforms the particles resulting in work hardening and fracture. The fractured fresh surface assists the deformed particle to weld together leading to increase particle size. However, with continued severe cold deformation, fracture plays a dominant role over cold welding and reduces the particles size. Finally, cold welding and fracture reach a balance and the particle size does not change. Although the particle size is not evidently changed, the internal structure of the particles is increasingly refined due to continued high energy impact of grinding ball, which is discussed below.

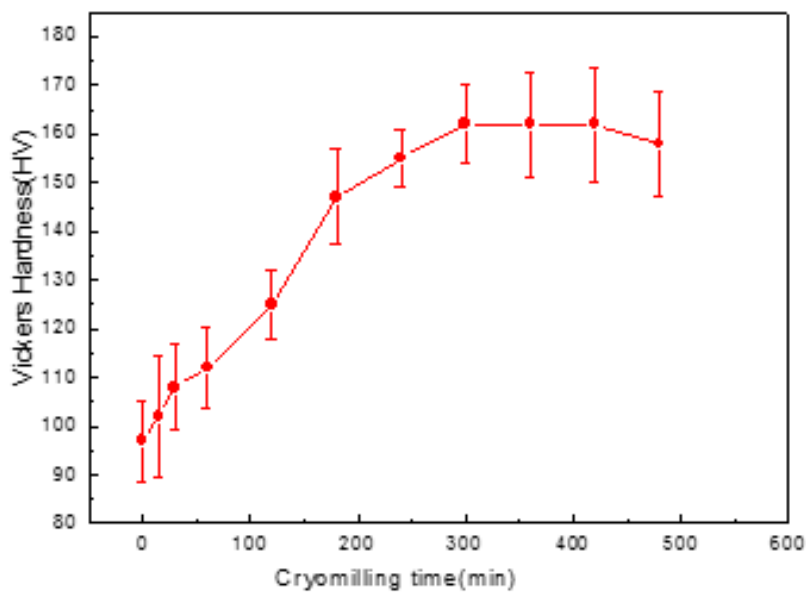
### **2.3.2 Micro hardness results**

Figure 2.4 presents average Vickers micro hardness results of all cryomilled powders. Due to grain refinement after cryomilling, the hardness is expected to increase. As shown in Figure 2.4, the hardness increased substantially in the first 3 hours. The rate of increase in hardness slowed down when the powder was further cryomilled to 4 and 5 hours. It reached a plateau during cryomilling between 5 and 7 hours with the highest average Vickers micro hardness of  $162 \pm 10.7 \text{ HV}$ , which is by far the highest value reported for an AZ31 alloy. Finally, it slightly dropped after cryomilling for 7 hours, although this change is not statistically significant.





**Figure 2.3** Typical Secondary electron SEM images showing particles morphology of cryomilled powders after (a-b)1 h, (c-d) 5 h, (e-f) 6 h, (g-h) 8 h



**Figure 2.4** Micro hardness results of cryomilled powders

### 2.3.3 Crystallite Size Measurement by XRD

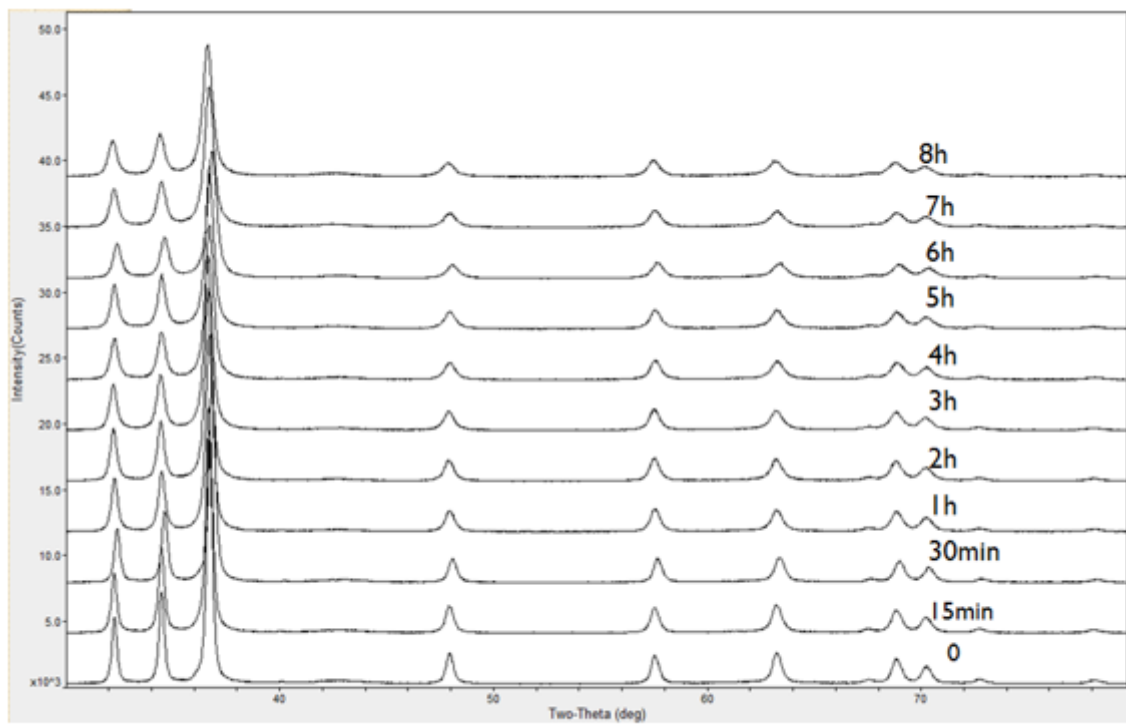
The concept of a crystallite is different from a grain. A crystallite is the smallest un-faulted portion of the crystal while grains can be treated as the area of a polycrystalline material with the same crystallographic orientation and structure [187]. In some cases, grain size

matches crystallite size obtained from TEM and XRD analysis, especially in nanocrystalline materials. The terminology crystallite is often used in XRD.

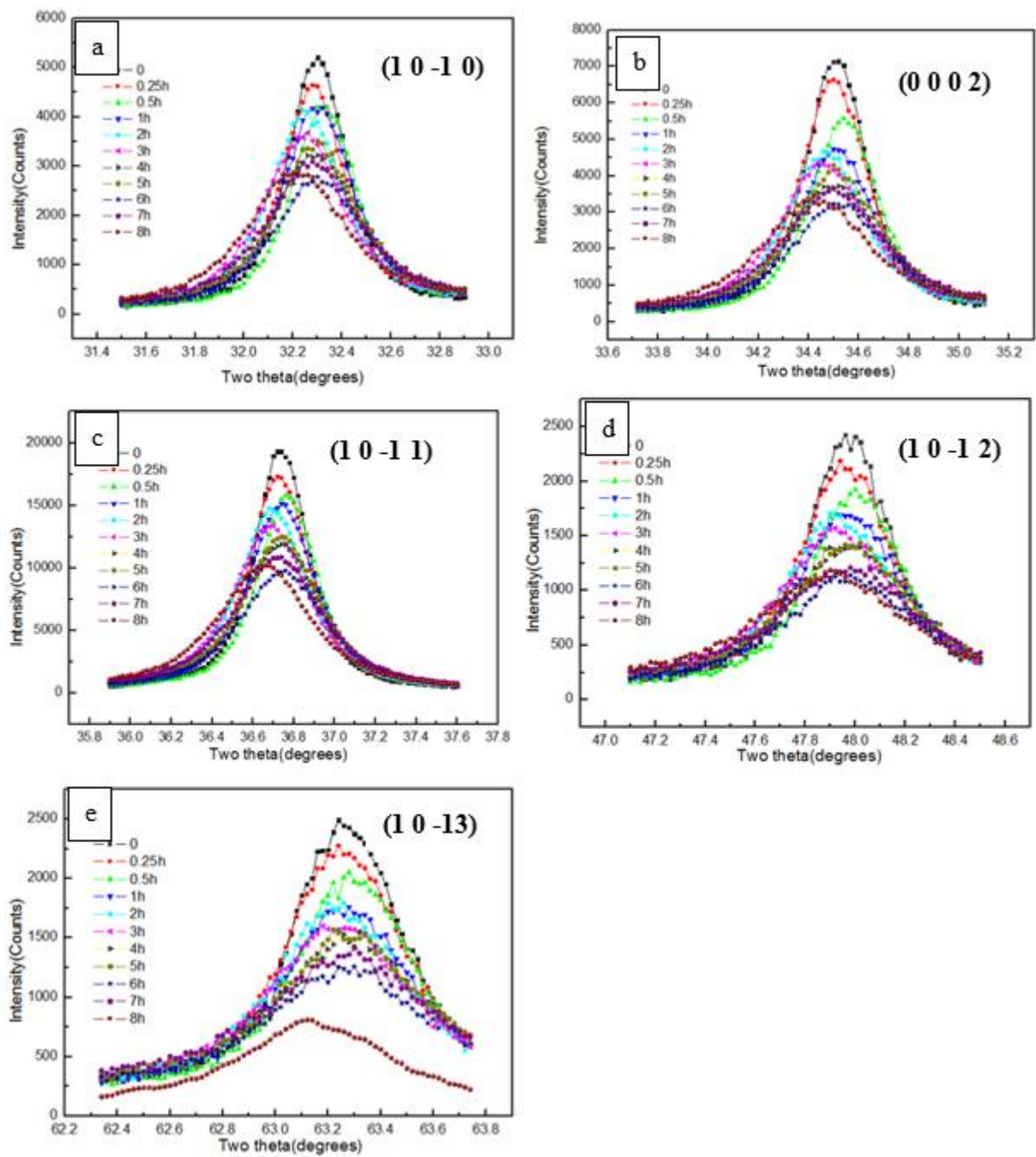
Figure 2.5 shows XRD patterns of as-received AZ31 and cryomilled powders. Compared to the as-received powder, significant peak broadening was evident after cryomilling for 4h. To further observe the broadening effect, five of the highest intensity peaks of magnesium were extracted and plotted in Figure 2.6. Due to severe plastic deformation and very limited recovery and recrystallization during cryomilling, this peak broadening can be attributed to the ultra-fine crystallite size and high internal micro strain. Approximating the crystallite size and micro strain broadening profiles by a Cauchy function, the relationship between crystallite size ( $d$ ) and the internal micro strain  $\varepsilon$  can be fitted using Williamson-Hull plot (equation 2.1):

$$B \times \cos(\theta) = \frac{K \times \lambda}{D} + 4 \times \varepsilon \times \sin(\theta) \quad (\text{Equation 2.1})$$

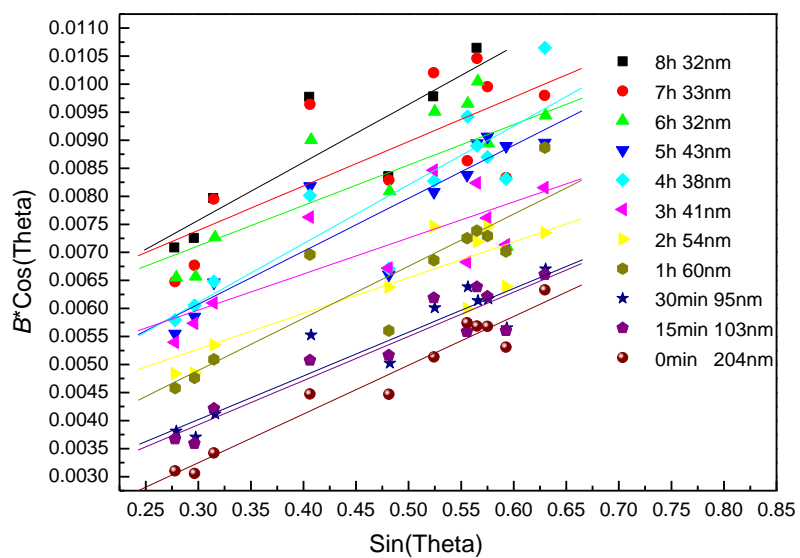
where  $B$  is the sample diffraction FWHM breadth (as defined in section 3.6),  $\theta$  is the position of the peak maximum,  $K$  is a constant as 0.94,  $\lambda$  is the wavelength of the X-ray radiation (Cu, 0.154056 nm),  $D$  is the average crystallite size and  $\varepsilon$  is the micro strain. By performing a least squares fit to  $B \cos(\theta)$  against  $\sin(\theta)$  for all of the measured peaks of a sample, the average crystallite size was estimated to be 32 nm for AZ31 powder after 6-8 h cryomilling based on the intercept  $K\lambda/D$ , as shown in Figure 2.7 and 2.8. It is obvious the crystallite size was rapidly reduced in the first 3 hours and the minimum crystallite size after cryomilling was 32 nm in this study.



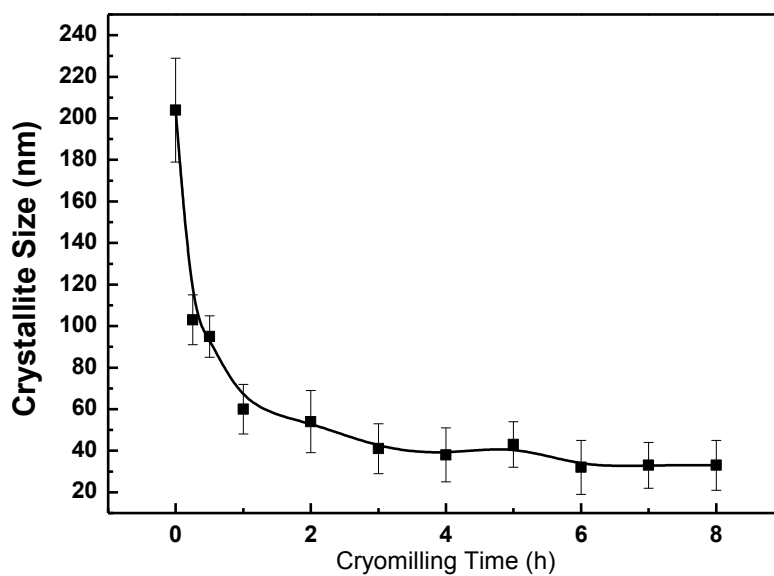
**Figure 2.5** The XRD pattern of as-received and cryomilled Mg AZ31 powders



**Figure 2.6** Single intensive peak of as-received and cryomilled Mg AZ31 powders



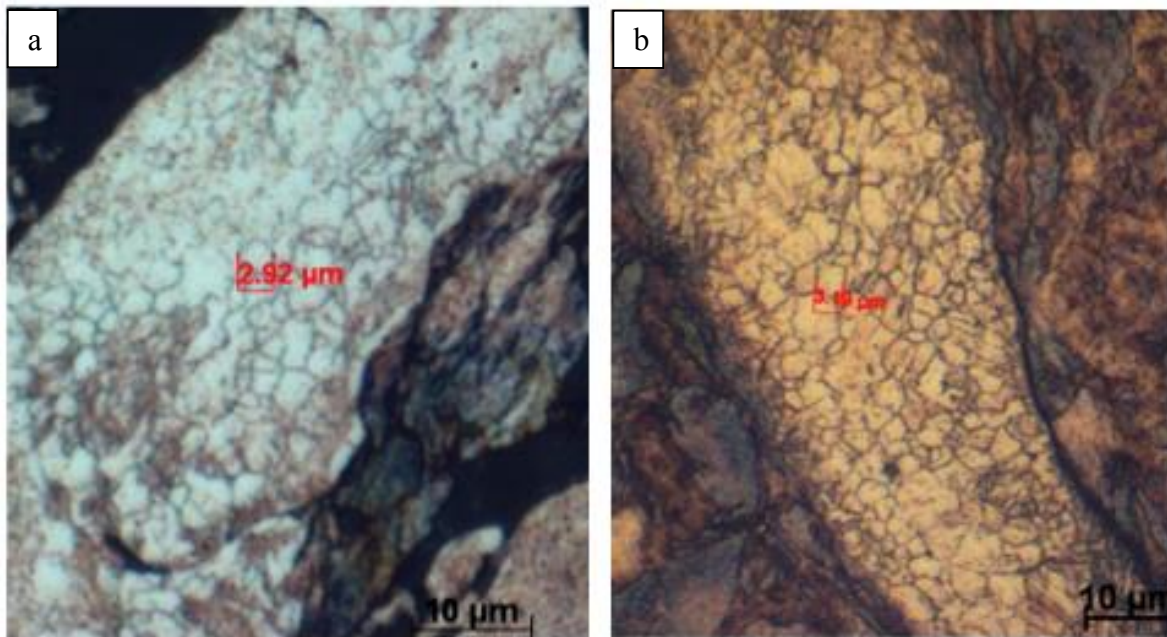
**Figure 2.7** Crystallite size fitting curves of cryomilled powders at various cryomilling time



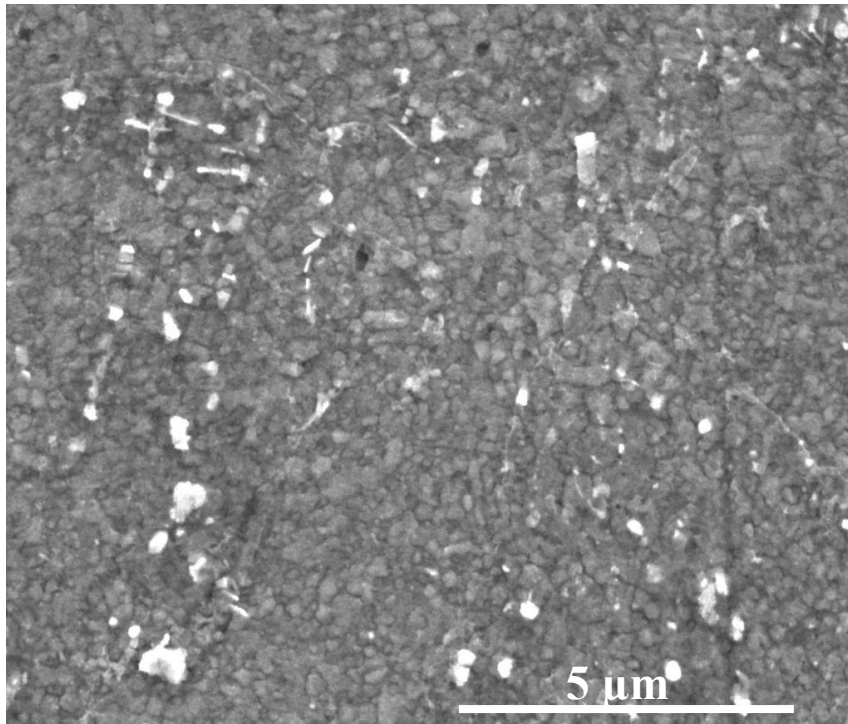
**Figure 2.8** Crystallite sizes of cryomilled powders vs. cryomilling time

### 2.3.4 Grain size measurement by combination of OM, SEM and TEM

Figure 2.9 shows grain distributions for 15 min and 30 min cryomilled powders. The grain size in most of particles was in the range of 1-5  $\mu\text{m}$  and was not changed significantly compared to the as-received powder (Figure 2.2). However, very few particles of 30 min cryomilled powder consisted of ultra-fine grains observed by SEM, as shown in Figure 2.10, which indicated grain refining started due to cryomilling.



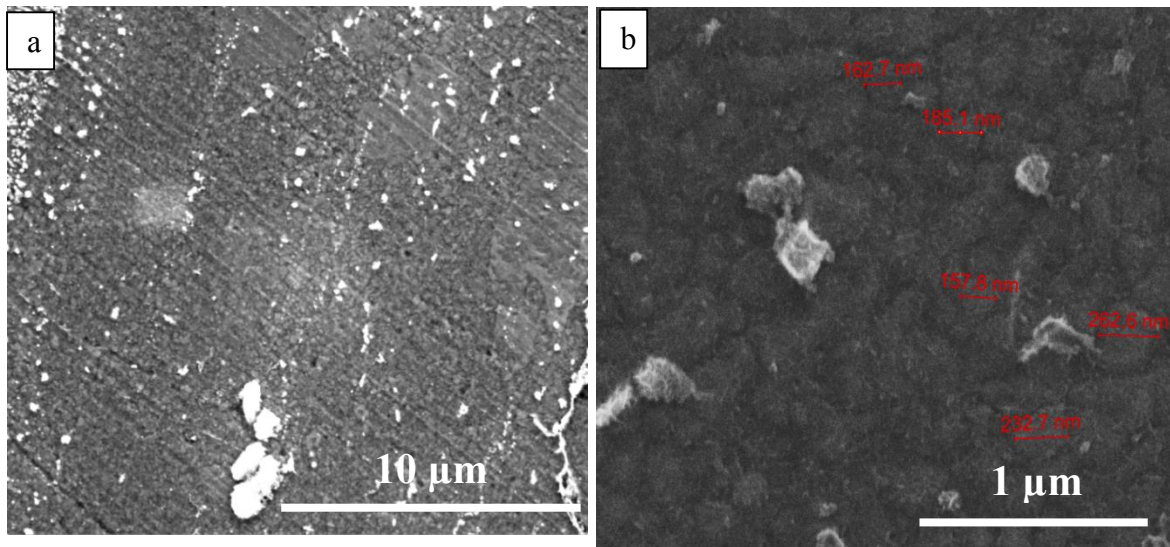
**Figure 2.9** Typical OM images of etched cryomilled powders after (a)15 min, (b) 30 min



**Figure 2.10** A secondary electron SEM image of Ultra-fine grains in a cryomilled 30 min particle

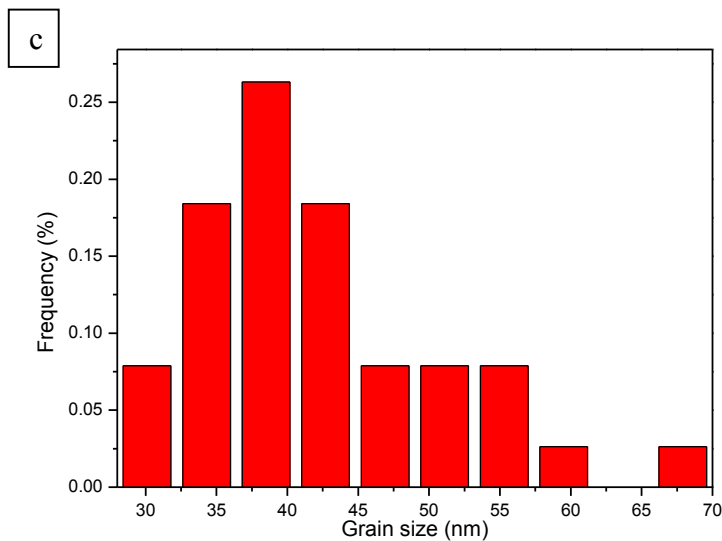
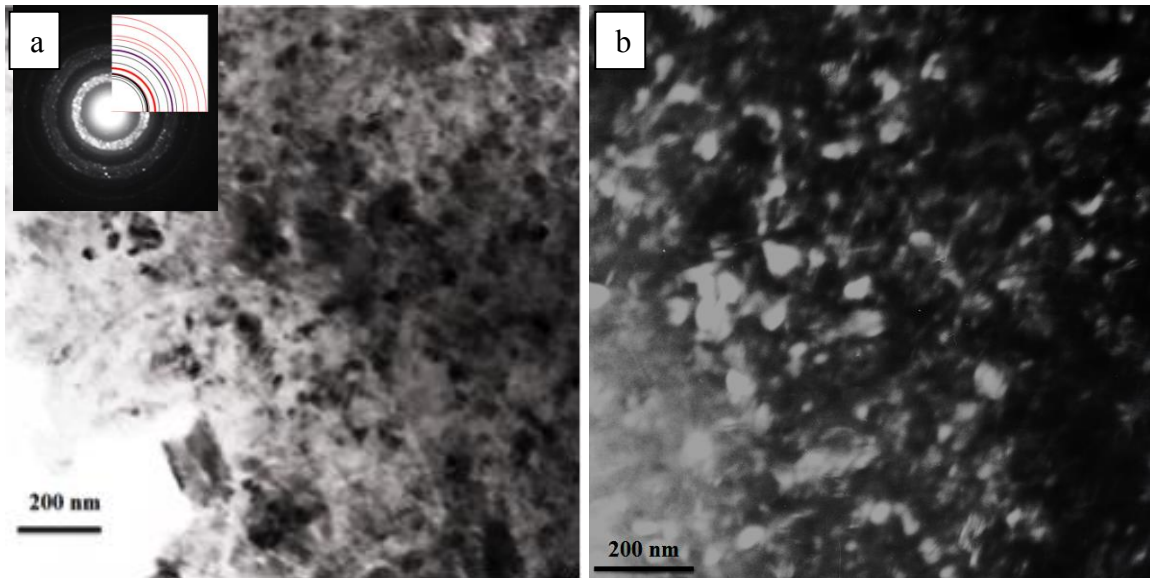
Figure 2.11 shows a low and corresponding high magnification of 1h cryomilled powder. The size of some individual grains was measured and marked on the image. Furthermore, its average grain size was calculated to be approximately 190 nm using linear intercept method.

Grains are expected to be further refined with increasing cryomilling time. The resultant grain size exceeds the resolving power of the SEM and TEM was employed to observe these nanostructures. Because oxidation could not be avoided in the cryomilled magnesium powders while preparing TEM samples, a very thin film of MgO film was always present on the surface and was responsible for additional diffraction ring pattern. To identify Mg and MgO diffraction patterns in the same diffraction pattern, a simulation of diffraction rings of Mg and MgO was plotted and used to distinguish MgO diffraction rings from Mg. Only 3h, 6h and 8h cryomilled powders were selected to show the grains refining process.



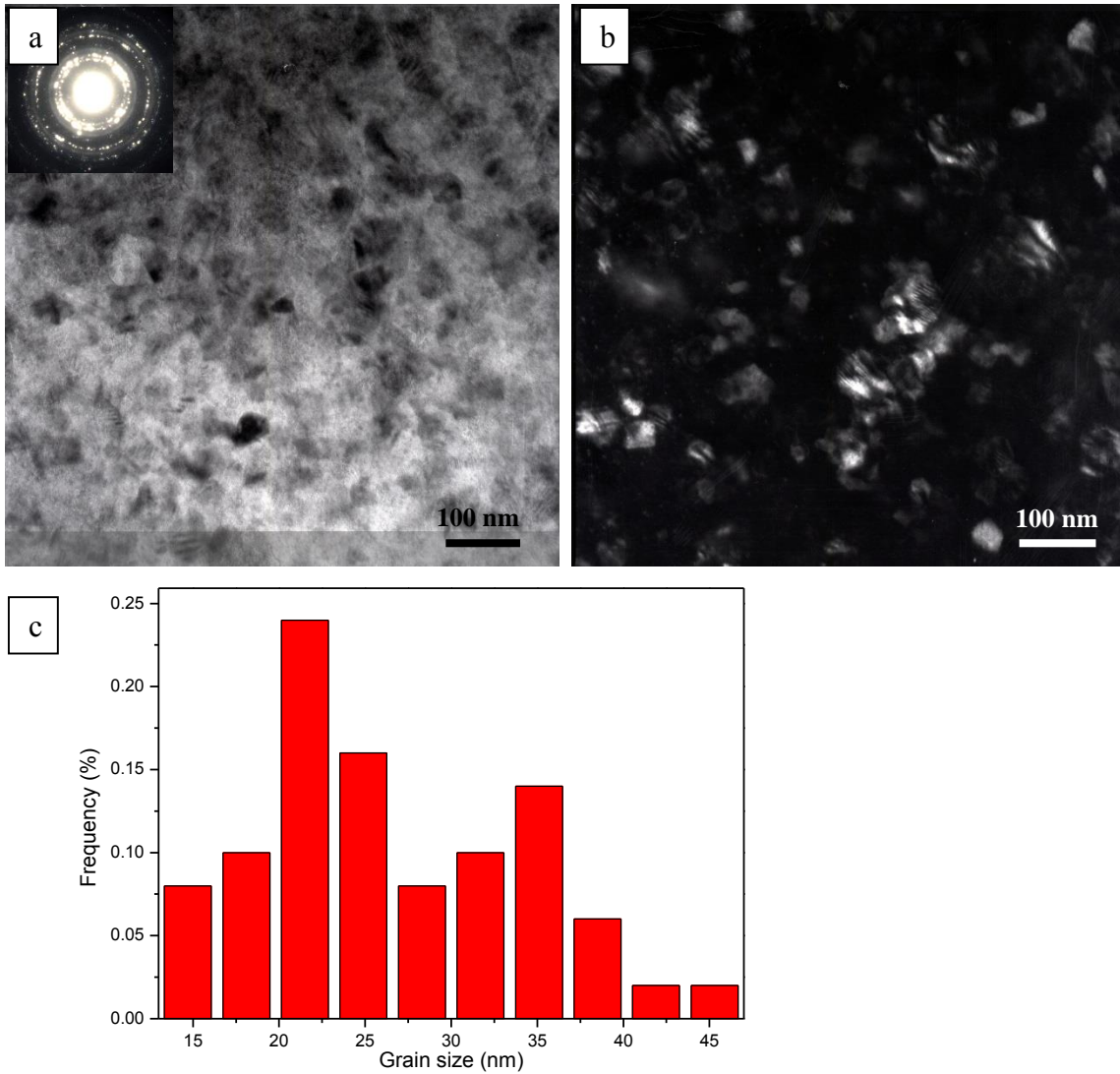
**Figure 2.11** Typical secondary electron SEM images of 1h cryomilled powder showing ultra-fine grains

Figure 2.12(a) shows selected area diffraction (SAD) pattern and BF images of 3h cryomilled powder. The red rings shown in Figure 2.12(a) represent standard MgO diffraction rings while black rings correspond to Mg diffraction rings. The purple ring is the overlap diffraction ring of Mg ( $1\ 0\ \bar{1}\ 3$ ) and MgO ( $2\ 2\ 0$ ) crystal planes. The large number of diffraction spots, spread out in a complete ring for most planes indicated that most of grains were in the nano grain size regime with a random orientation. Figure 2.12(b) is a dark field image, where fine crystallites can be clearly observed. The average grain size calculated was  $42.4 \pm 12.2$  nm based on well-defined grain boundaries. Figure 2.12(c) displays the grain size distribution of the 3h cryomilled powder (determined from 50 grains measured). It should be noted that very small grains were not included in determining the grain size distribution, since these small grains cannot effectively be distinguished from MgO dispersions, which will be discussed in the following chapter.



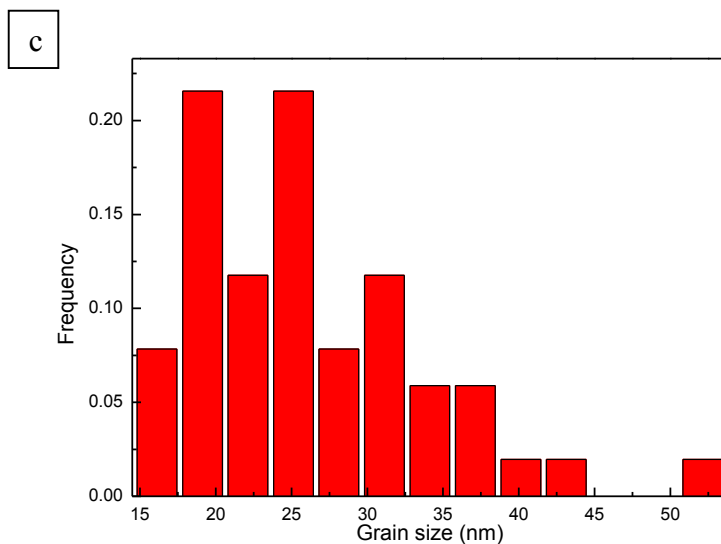
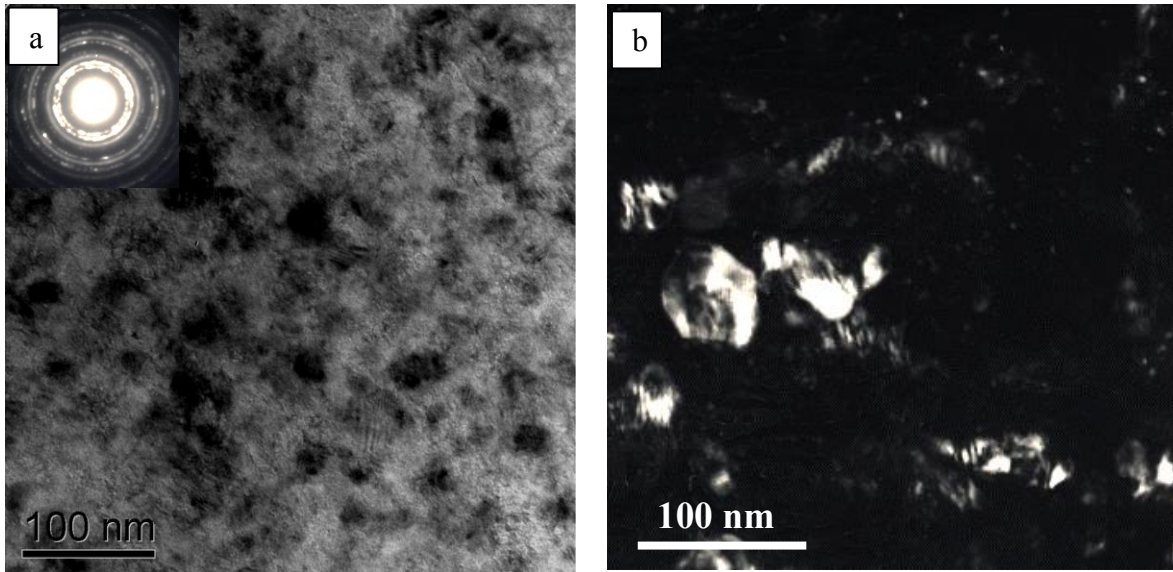
**Figure 2.12** TEM image of 3h cryomilled powder: (a) Typical BF image and SAD pattern, (b) DF image and (c) grain size distribution histogram calculated from the TEM images

Figure 2.13 shows TEM images of 6h cryomilled powder. The BF and DF images exhibited a greater degree of fine microstructure was obtained after cryomilling for 6h. The average grain size was further decreased. Figure 2.13(c) displays the grain size distribution of the 6h cryomilled powder (determined from 50 grains measure) and its average size is  $26.2 \pm 7.9$  nm.



**Figure 2.13** TEM image of 6h cryomilled powder: (a) Typical BF image and SAD pattern, (b) DF image and (c) grain size distribution histogram calculated from the TEM images

Figure 2.14 presents TEM images of 8h cryomilled powder. The BF and DF images showed that the grain size was not changed significantly compared to the 6h cryomilled powder. Figure 2.14(c) displays the grain size distribution of the 8h cryomilled powder (determined from 50 grains measure) and its average size is  $26.1 \pm 7.2$  nm, which is very similar to that of 6h cryomilled powder.



**Figure 2.14** TEM image of 8h cryomilled powder: (a) Typical BF image and SAD pattern, (b) DF image and (c) grain size distribution histogram calculated from the TEM images

Because the main difference between cryomilling and mechanical milling is the working temperature, the mechanism of nanostructure formation during cryomilling can be considered as a mechanical milling process [81]. Due to the cryogenic milling temperature, suppression of the recovery in the material was significant, which plays a positive role in reducing the milling time to obtain nanocrystallites [101]. Fecht stated [82] there are mainly three stages of microstructure mechanically milling process. Firstly, localized deformation

occurs in shear bands consisting of high density dislocation arrays; secondly, because these dislocation arrays are not stable and dislocation annihilation and recombination and annihilation of dislocations then ensues, this results in the formation of nano-sized subgrains; with further deformation, the subgrains with LAGB transform to small grains with HAGB by the annihilation and recombination of more dislocations into the boundaries or accompanying subgrains rotation during collision. Finally, this LAGB structure is able to change to completely random HAGB between individual grains. Figure 2.15 also presents grain refinement mechanisms during mechanical milling [81,95].

During the initial stage of cryomilling, the crystallite size measured by XRD was generally finer than corresponding grain size determined by OM, SEM and TEM methods. The reason for this is because XRD determines coherent diffraction domains including dislocation cells and subgrains[136]. After cryomilling for around 3 hours, the crystallites size measured by XRD was similar to grain size investigated by TEM. This indicated dislocations as well as subgrains started to transform into nano grains with HAGB, as shown by the diffraction rings patterns of cryomilled powders (Figure 2.12-2.14).

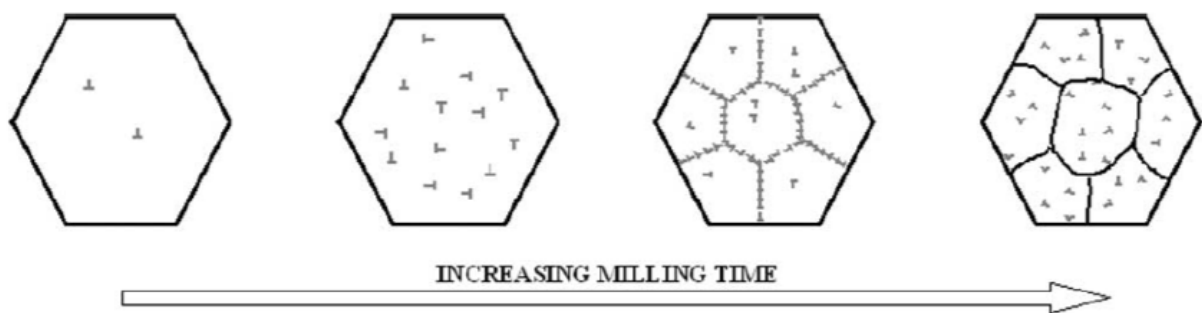


**Figure 2.15** Schematic representation of grain refinement mechanism during ball milling [81,95]

The minimum grain size ( $d_{min}$ ) in this study was reached after 6 hours based on crystallite size determined by XRD and TEM. No significant grain refining occurred when

further extending the cryomilling time. Furthermore, combining the results of particle size evolution and micro hardness, it can be concluded that the shortest cryomilling time to obtain  $d_{\min}$  should be only 6 hours.

### 2.3.5 Chemistry

Based on the investigations above, as-received and 6h cryomilled powders were chosen for chemical analysis to determine the composition changes after cryomilling, especially the impurity content. Results were listed in table 2.2. It shows that the final chemistry of the powders was not changed significantly after 6 hours cryomilling, particularly when compared to other studies relating to cryomilling [188,189]. Ertorer reported the content of N was increased from 0.017% to 2.03% and O from 0.19% to 0.263% after cryomilling [26]. Wen also stated the content of N and O in cryomilled powder was 0.26% and 0.512% respectively [27]. In general, powder contamination can be introduced either from milling or handling environment. Because neither process control agent (PCA) nor liquid N<sub>2</sub> slurry was mixed with the processed powder, N level was only slightly increased compared to other reported researches [188,189]. In contrast, O level was dropped to an undetectable volume after cryomilling. For the as-received powder, there was a thick layer of MgO covering the particle surface, which was easy to detect. However after cryomilling, the MgO film was completely broken-up and scattered uniformly as nano particles in the internal matrix, which resulted in the low detectable volume of O level. In addition, Fe level was also not noticeably changed.

**Table 2.2** Chemical analysis results for AZ31 powders (wt%)

Powder type	Mg	Al	Zn	Mn	N	O	Fe
As-received	96.15	3.02	0.80	<0.25	0.013	0.014	<0.25
CM6h	96.28	2.87	0.79	<0.25	0.060	<0.005	<0.25

## 2.4 Conclusions

In summary, nanocrystalline AZ31 powder was produced by cryomilling in this study. The particles undergo cold welding and fracture and its average size dropped to approximately 26  $\mu\text{m}$  after cryomilling 6 hours. The chemical analysis results indicated contamination introduced from cryomilling was not significant. The levels of contamination were small compared to other studies relating to cryomilling. A minimum average grain size of about 26 nm for the powder can be reached for a cryomilling time of 6 hours or longer. The corresponding hardness of the 6 hours cryomilled powder had a highest value of approximately 160 HV among all the cryomilled powders from 0.5 hours to 8 hours. Therefore, it can be concluded that 6 hours cryomilling can reach the minimum grain size in this study based on the investigations of XRD and TEM. It also should be noted a few particles were agglomerated by other particles and cannot be processed by cryomilling due to cold welding.

## 3 Thermal stability of cryomilled powder

Abstract:

In this short chapter, the thermal stability of cryomilled NC AZ31 powder was evaluated by annealing at elevated temperature ranging from 350 °C to 450 °C (0.675-0.783  $T_m$ ,  $T_m$  represents melting temperature). Because this part was only designed to optimize the SPS consolidation process, the annealing time was only investigated between 5 and 60 minutes.

### 3.1 Introduction

The thermal stability of the cryomilled powders relating to the grain growth is vital to develop an inexpensive process for producing bulk NS materials. The driving force for grain growth is related to grain boundary energy. As grains grow, the total boundary area reduces, providing a reduction in the total energy [25]. The total grain boundary area increases with reducing grain size. In addition, NS materials are in a non-equilibrium thermodynamic state. Consequently, a huge driving force towards equilibrium takes place during annealing at elevated temperatures to reduce the total energy, which results in internal relaxation and grain growth [93,95]. In general, the mechanism of grain growth in most NS materials is related to grain boundary diffusion because its activation energy is closer to grain boundary (GB) diffusion than to that of lattice diffusion [190]. The main factors affecting GB mobility in NS materials include pore drag [191], GB segregation [192], second phase (Zener) drag [193], solute (impurity) drag [194,195], nano twins [178,196] and chemical ordering [197]. Those factors could also change NC grain growth kinetics.

It has been reported that cryomilled NS materials typically possess a higher thermal stability than that of NS materials produced by other routes (e.g., HPT, MDF, ECAP)[198-201]. For example, a cryomilled 5083 Al alloy processed via HIP and extrusion exhibited an excellent thermal stability after creep tests at 300 °C and 350 °C [199]. The cryomilled Al powder had an average grain size of 200 nm. After approximately 1000 h exposure at 300 °C and 350 °C (0.61–0.66T<sub>m</sub>), only slight grain growth occurred. This can be ascribed to the formation of supersaturated solid solution during mechanically alloying and also to nanoscale dispersions that arise because of unavoidable trace impurity elements (O, N, C, Fe, Cr, etc.). These factors provide solute drag and Zener pinning, which significantly reduced the grain boundary mobility and act as barriers to stabilize the microstructure.

The main goal of this chapter was to investigate the effect of short annealing time on grain growth of cryomilled AZ31 powder and provide guidance to optimize SPS consolidation parameters, especially to determine the optimal sintering temperature. Sintering at the optimum temperature cannot only enhance sufficient densification and inter-particle bonding, but also limit the grain growth simultaneously. Consequently, this section will not study details of thermal analysis but describe the key mechanisms introduced by cryomilling process.

## **3.2 Experimental**

### **3.2.1 Annealing treatment**

Cryomilled powders were annealed for times ranging from 5 to 60 minutes at three temperatures (350, 400 and 450 °C). A tube furnace with flowing argon gas was employed for

annealing treatment. The AZ31 powder samples were sealed in Al pans and heated to the proposed temperature with a heating rate of 5 °C/min, then annealed and finally cooled by air.

### **3.2.2 Micro hardness test**

To obtain a flat surface for hardness test, the hot mounted powder samples were ground with 800, 1200, 2500, 4000 grade SiC papers and finally polished by 1 µm and 1/4 µm alcohol based diamond suspension. A micro Vickers hardness tester (Akashi Corporation Sagami Plant, model HM-101) was used to perform hardness tests with a load of 50 grams and a dwell time of 15 s. At least 11 indents were collected for each sample to obtain accurate hardness results.

### **3.2.3 Transmission Electron Microscopy (TEM)**

TEM samples of the cryomilled powders after annealing were prepared by grinding using a pestle and mortar and suspended in isopropanol, followed by ultrasonic dispersion and then deposition onto a 200 mesh Cu grid with holey carbon film. A FEI Tecnai 20, operating at 200 kV, was used for conventional TEM characterizations. HAADF STEM was performed on a JEOL 2010F microscope operated at 200 kV.

## **3.3 Results and discussion**

### **3.3.1 Micro hardness results**

Figure 3.1 presents the variation of Vickers micro hardness with annealing temperatures for annealing times ranging from 5 to 60 minutes. During the first 5 minutes annealing, the hardness of powders annealed at 350 and 400 °C was decreased from around 160 HV to about 150 HV, but it sharply dropped to around 130 HV when further increasing temperature to

450 °C. The reason for hardness decrease was the internal energy relaxation and grain growth. When the annealing temperature was 350 °C, the micro hardness difference was negligible after annealing for 5 to 60 minutes. For annealing less than 30 minutes at 400 °C, the micro hardness was not changed noticeably compared to annealing at 350 °C. With extending annealing time to 45 and 60 minutes, the hardness started to drop down slightly. With the processing temperature increased to 450 °C, its hardness distinctly decreased to 115 HV as the annealing time extended to 15 minutes. However, when the powder was annealed for a longer time at 450 °C, the change in hardness was quite stable around 115 HV between 15 and 60 minutes.

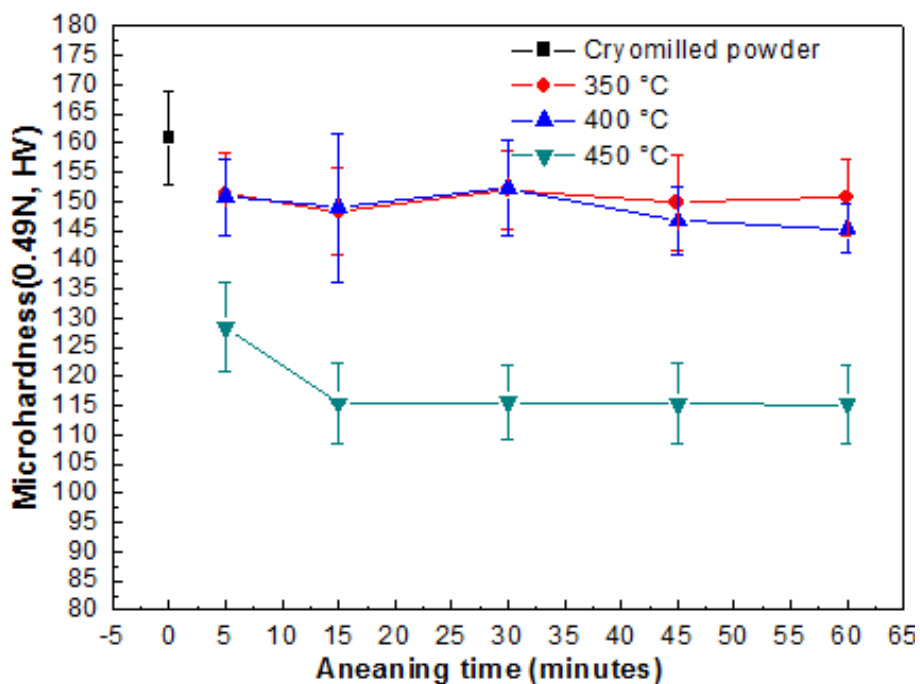


**Figure 3.1** Micro hardness results of cryomilled powders.

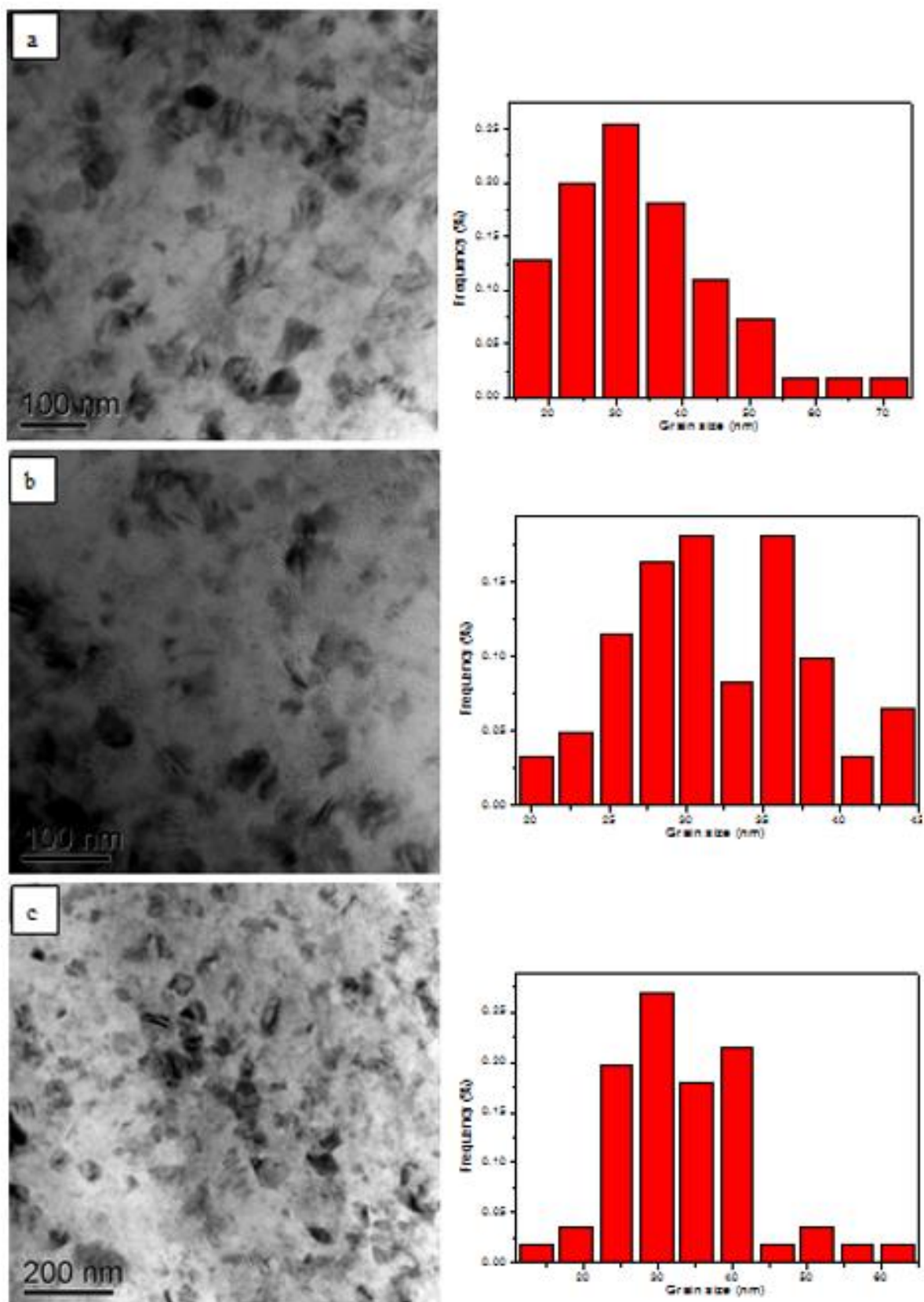
### 3.3.2 Grain size characterization

As mentioned in the previous chapter, the powder after 6 hours cryomilling reached the minimum grain size of about 26 nm. Figure 3.2 shows the TEM images of annealed cryomilled powders at 350 °C and corresponding grain size distribution histograms. For powders annealed at 350 and 400 °C, samples only annealed for 15, 45 and 60 minutes were selected here and sufficient to show the grain growth. Because the hardness decreased substantially during the first 5 minutes, the powder annealed at 450 °C for 5 minutes was added to demonstrate the grain growth at this temperature.

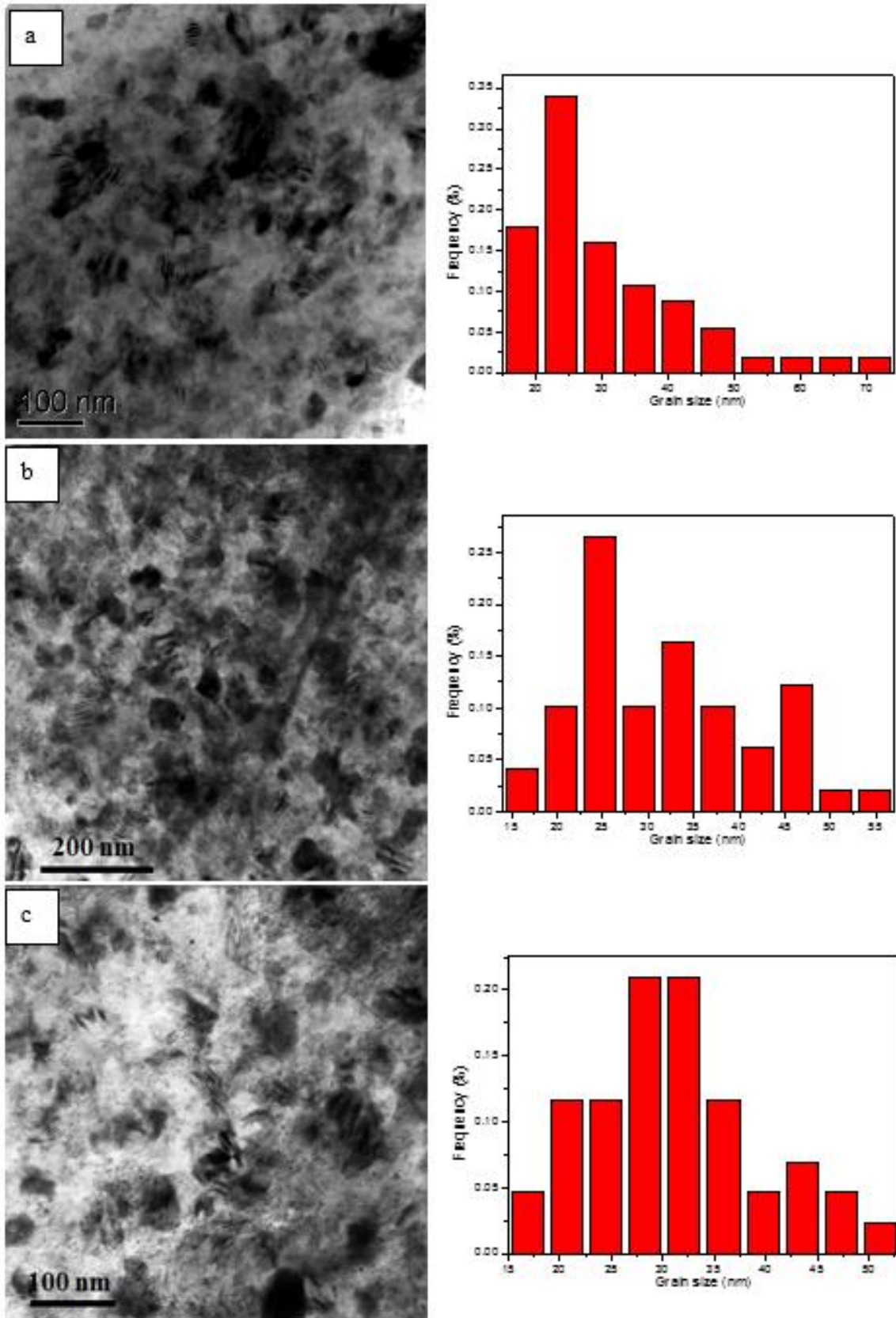
Figures 3.2 and 3.3 present bright field TEM images of cryomilled powders annealed at 350 and 400 °C, and their corresponding grain size distribution diagrams. The average grain sizes of powders after annealing at 350 °C for 15, 45 and 60 minutes were 31.3, 32.1 and 33.9 nm respectively, and the average grain sizes were around 31.9 nm, 32.5 nm and 34.4 nm when annealed at 400 °C. Therefore, during annealing at 350 and 400 °C, the grain size initially increased quickly from 26 to approximately 32 nm, then stabilized and increased very slowly thereafter. These results were consistent with the results of micro hardness results in figure 3.1.

Figure 3.4 shows bright field TEM images of annealed cryomilled powders at 450 °C and corresponding grain size distribution diagrams. The nano grains grew to approximately 37 nm after 5 minutes. With an increase in annealing time to 15 minutes, significant grain growth was observed. However, grain growth was very limited when the annealing time was extended from 15 to 60 minutes. The average grain size of powders was approximately 55 nm, 57nm and 59 nm after annealing for 15, 45 and 60 minutes. It also should be noted some grains grew to

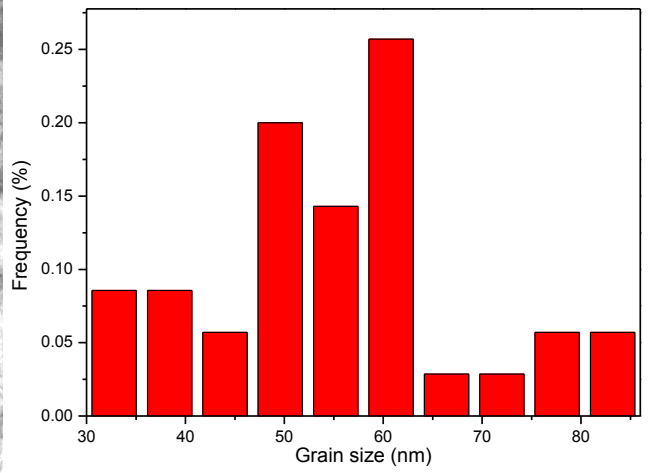
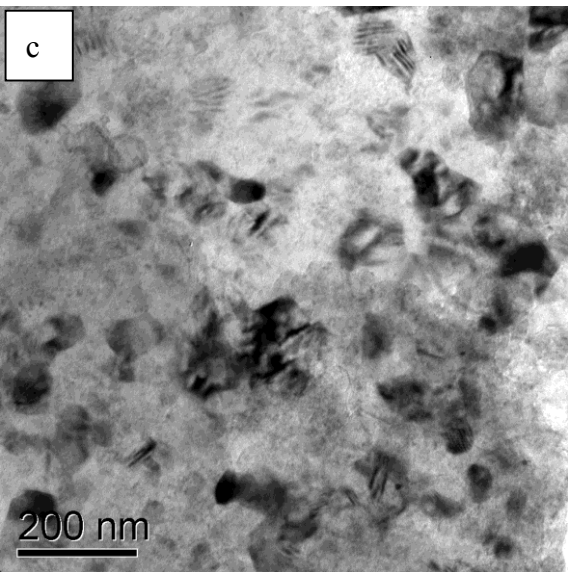
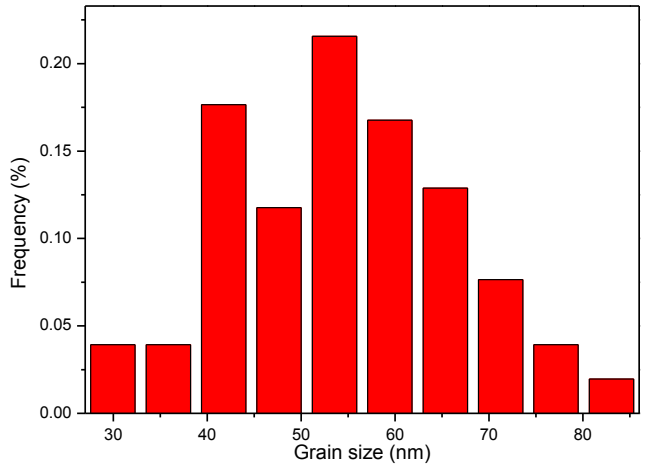
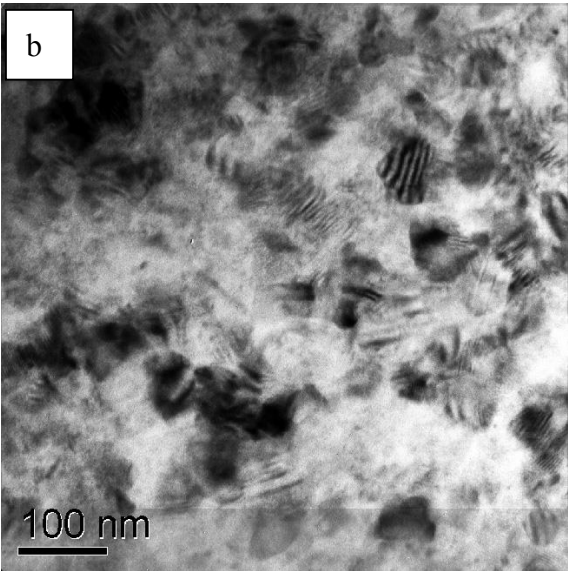
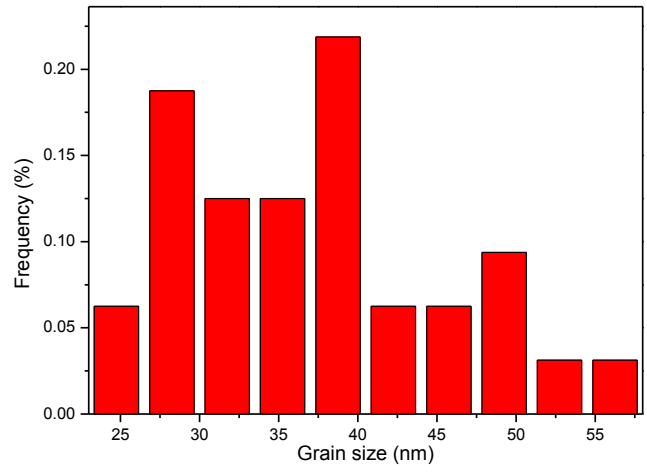
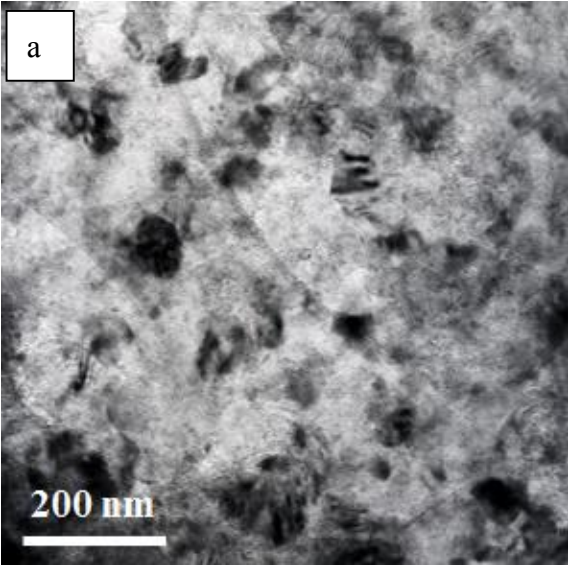
submicrometer size ( $>200$  nm) with a relatively higher rate in some regions (see Fig. 3.5). Nevertheless, the average grain size remained stable at approximately 60 nm even after long anneals at temperatures as high as 450 °C (0.78 T/TM), indicating a high degree of grain size stability.



**Figure 3.2** Representative TEM images and grain size distributions of annealed cryomilled powder at 350 °C: (a) 15 minutes, (b) 45 minutes and (c) 60 minutes.



**Figure 3.3** Representative TEM images and grain size distributions of annealed cryomilled powder at 400 °C: (a) 15 minutes, (b) 45 minutes and (c) 60 minutes.



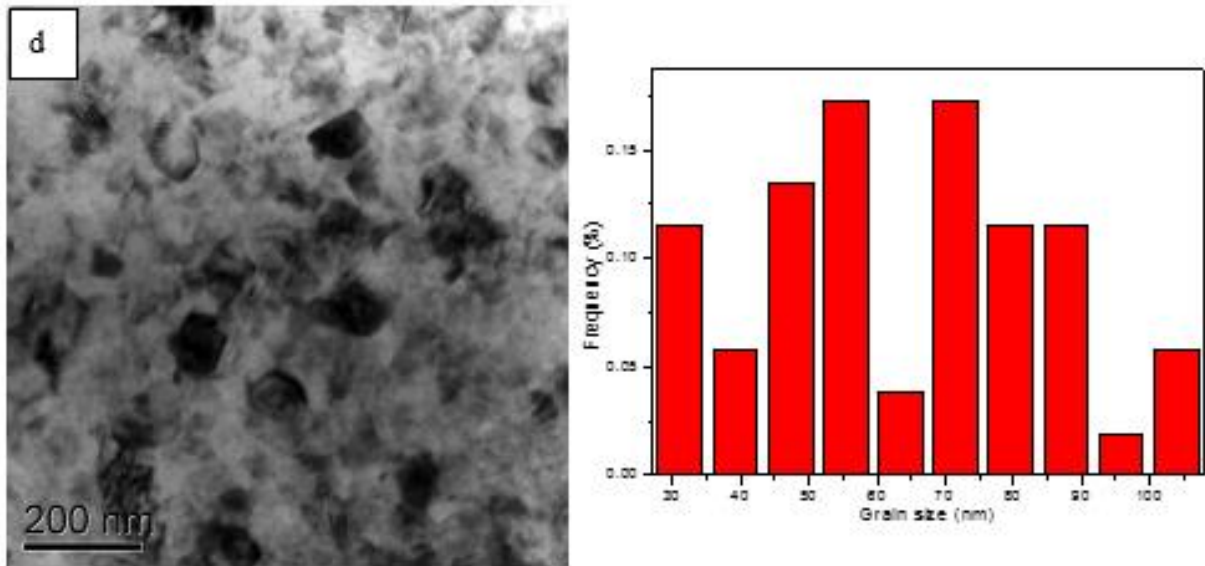


**Figure 3.4** Representative TEM images and grain size distributions of annealed cryomilled powder at 450 °C: (a) 5 minutes, (b) 15 minutes, (c) 45 minutes and (d) 60minutes.

Based on the grain size results mentioned above, it can be concluded there were two separated growth stages with a transition point around 400 °C, i.e. an evident difference existed in the grain growth behavior below and above this temperature. Below this temperature, the grain size difference was insignificant, whereas at higher heating temperatures it became clear. The temperatures of the two growth regimes were found to agree well with the hardness results (Fig. 3.1).

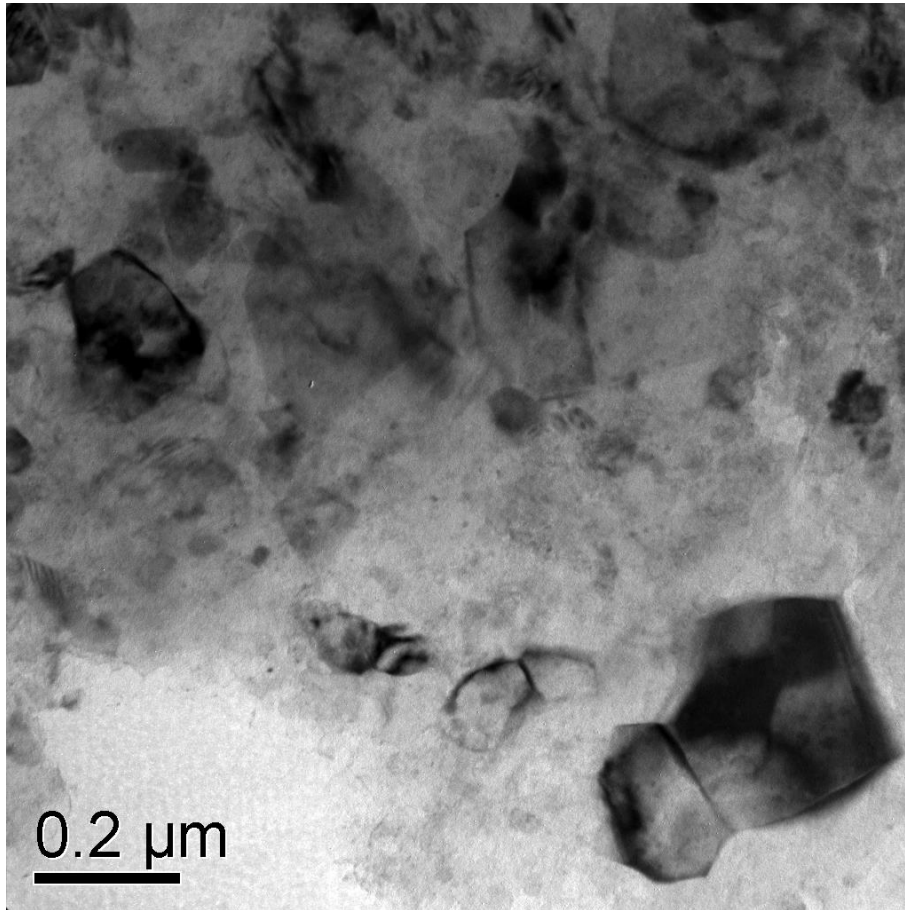


**Figure 3.5** A selected TEM image of powder annealing at 450 °C for 45 minutes showing an area with rapid grain growth rate

The most remarkable observation in this chapter was its excellent thermal stability of cryomilled AZ31 powders. The Mg grains remained nanoscale even after annealing at 350-450 °C (0.675-0.783  $T_m$ ) after 60 minutes. Several mechanisms that impart thermal stability to the nanostructure produced by cryomilling have been proposed, which were reported to include pore drag [191], GB segregation [192], second phase (Zener) drag [193], solute (impurity) drag [194,195] and nano twins [178,196].

During cryomilling, there was an extension in solid solubility at room temperature by this non-equilibrium processing route. The solid solubility limit increased with milling time

due to solute atoms diffusion and extends to a (super)saturation level [80,81,202]. Therefore, powders cryomilled for 6 hours have higher solute levels of Al, Zn and Mn in Mg matrix than in the as-received powders. Besides, large bulk of segregation phases locally distributed in as-received powder were expected to be crushed and redistributed relative uniformly in cryomilled powder. Because newly formed nano-sized grain boundaries had higher internal energy, these became preferential sites for solute segregation. Therefore, the improvement of thermal stability was partly contributed to solute atoms existing at grain boundaries through solute (impurity) drag.

In addition, the outstanding thermal stability of cryomilled powders during subsequent short annealing can be also partly attributed to the in-situ formation of nano sized MgO dispersions that provide Zener pinning. The MgO arises due to the break-up of the MgO film covering the surface of the as-received powder during cryomilling. Figure 3.6 shows a typical dark field TEM image of cryomilled powder. Some bright nanosized particles can be seen distributed in one cryomilled Mg particle. Figure 3.7 clearly demonstrates some lower atomic number (dark contrast) particles were located at a grain boundary. These particles were expected to be MgO. To further confirm this, a series of advanced electron microscopy techniques were used. Figure 3.8 presents a diffraction pattern image under EDS mode. It clearly presents two sets of Kikuchi bands and they were two individual grains with different orientations. The area between was a grain boundary. Electron energy loss spectroscopy (EELS) was employed to identify possible phases on grain boundaries. Figure 3.9 (a) shows the EELS image collected from red point in Figure 3.8 and Figure 3.9 (b) shows a reference spectrum of

MgO from Gatan EELS Atlas. The peaks in Figure 3.8(a) matched well with the peaks in Figure 3.8(b). Hence, it can be concluded the cracked MgO particles can be found and were embedded in the grain boundaries.

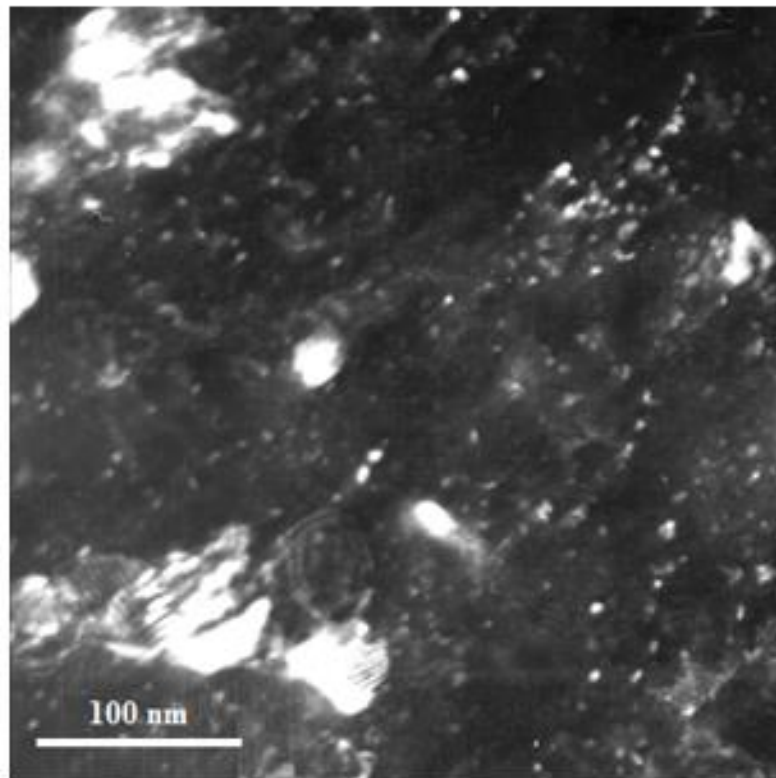


**Figure 3.6** Representative dark field TEM images of cryomilled powder showing the distribution of oxides

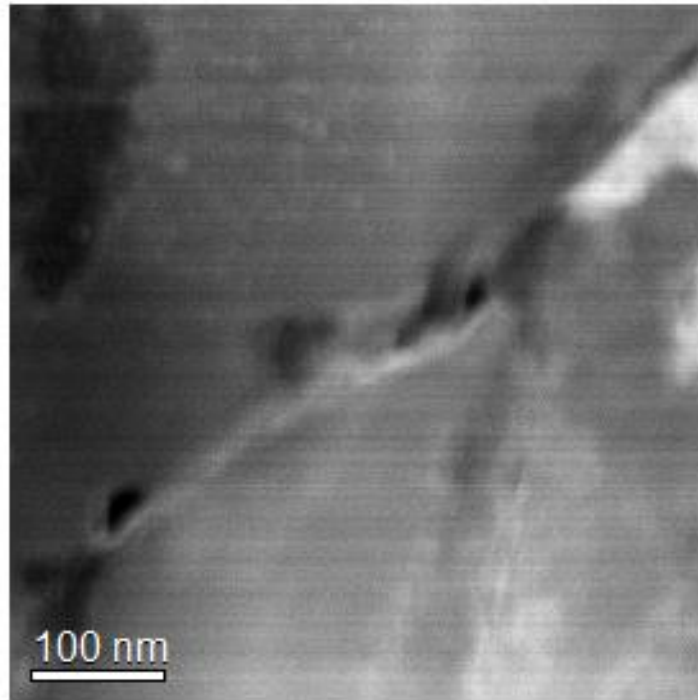


**Figure 3.7** Representative high angle annular dark field (HAADF) TEM images of bulk cryomilled sample after SPS consolidation showing the oxides residing at a grain boundary

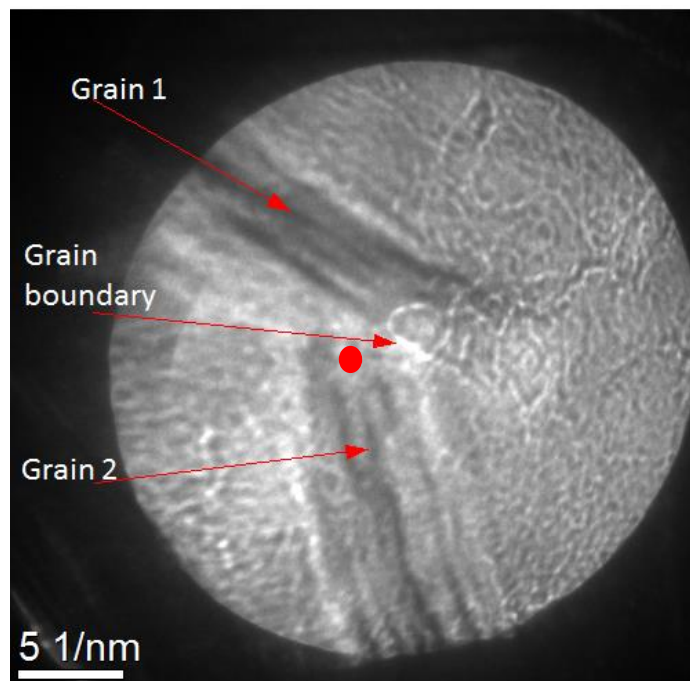


**Figure 3.8** A diffraction pattern image under EDS mode: different Kikuchi bands means grains with different orientations

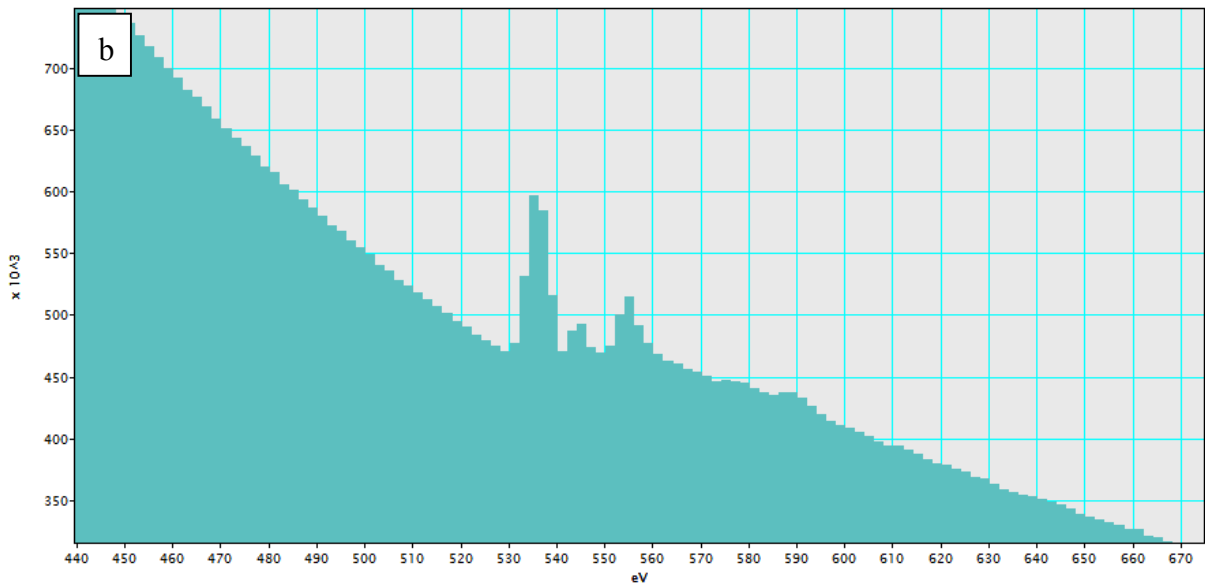
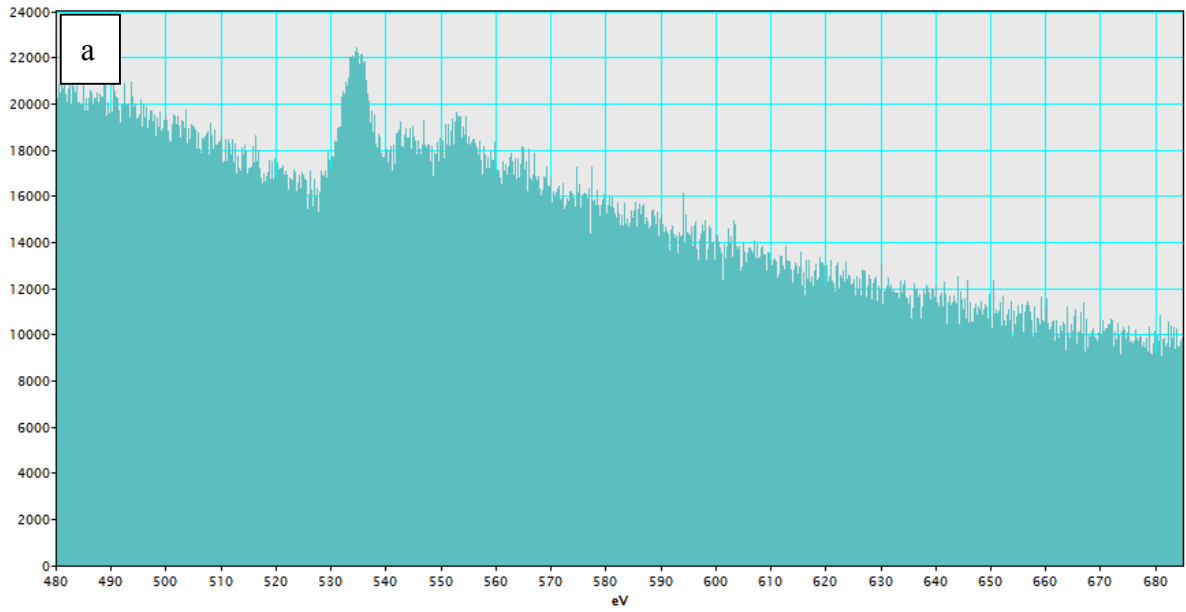


**Figure 3.9** (a) Electron energy loss spectroscopy (EELS) spectrum collected from the grain boundary and (b) a reference spectrum of MgO

In addition, HRTEM images show the distribution of those MgO particles, as presented in figure 3.10. Figure 3.10 (b) gives the corresponding diffraction pattern consisting of

diffraction spots and rings. Extra scattered diffraction spots located at the d spacing for MgO with random orientation (hence forming a diffraction ring) were from nano-sized oxides after cryomilling. These extra spots were chosen to obtain a series of Inverse FFT (IFFT) images. Figure 3.11 shows the positions of nano-sized MgO particles by IFFT processing. It could be clearly observe the locations and sizes of these MgO particles from these two images. They were distributed on or near the grain boundary with a size of 5 nm. The oxides residing at the grain boundaries can play a positive role in pinning grains and suppressing the grain growth [95].

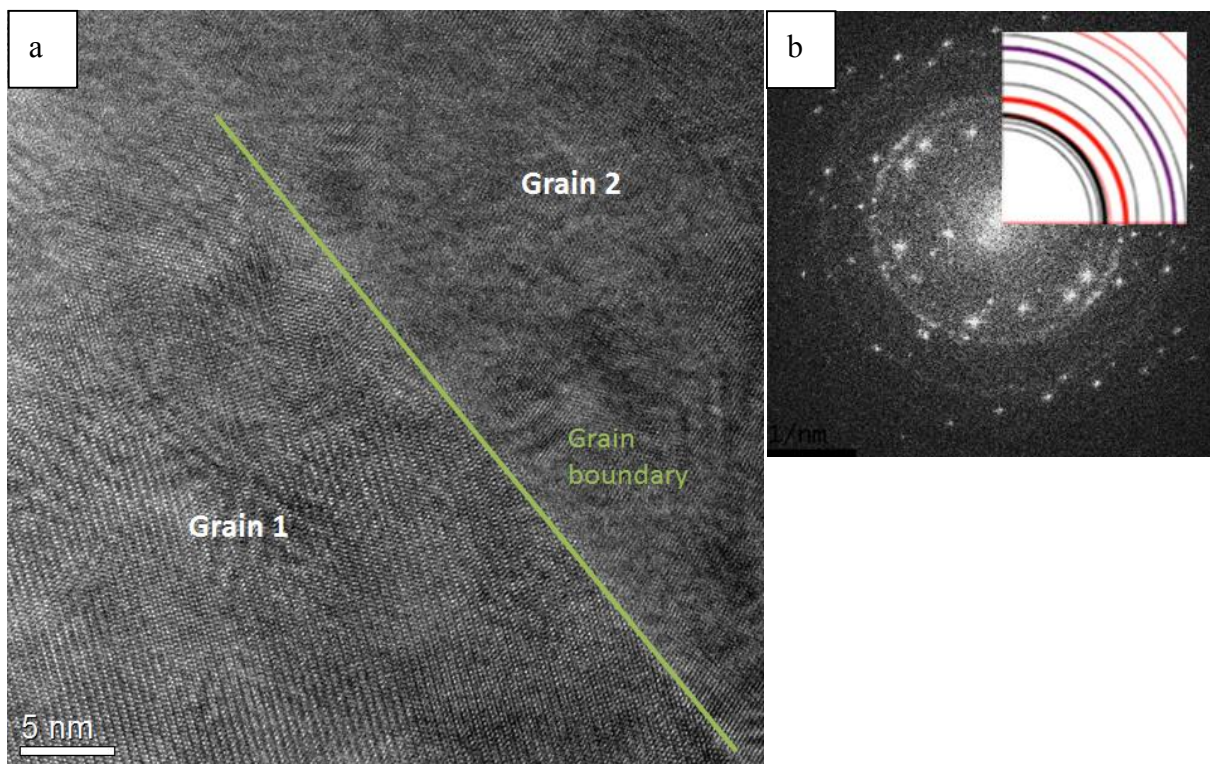


**Figure 3.10** (a) HRTEM image and (b) corresponding FFT diffraction pattern

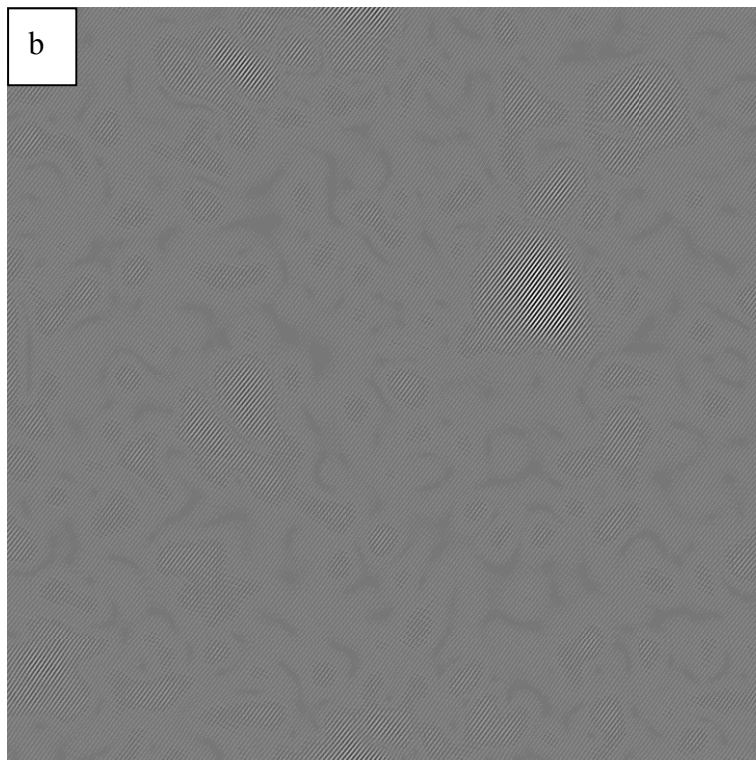
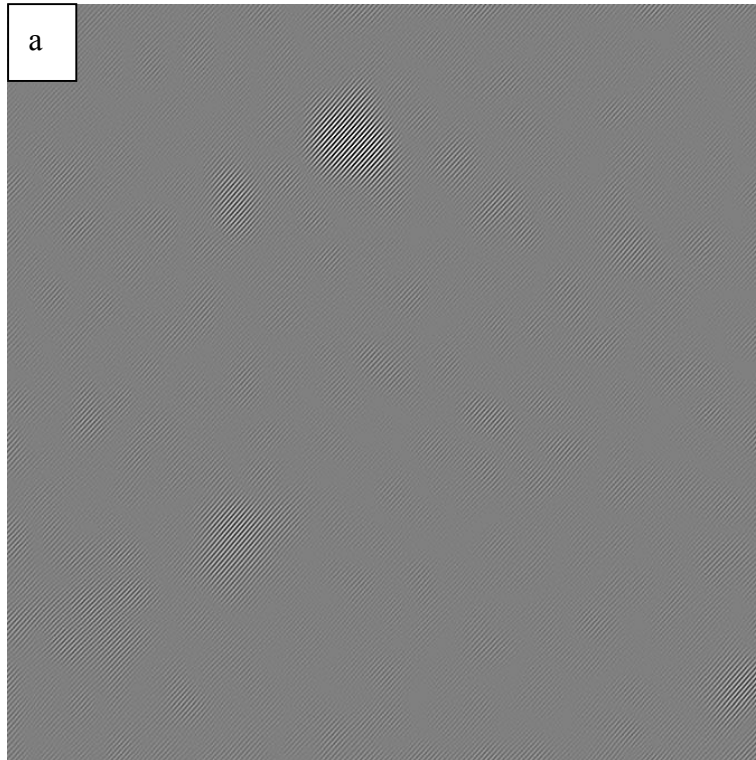


**Figure 3.11** Inverse FFT images showing the size and distribution of tiny MgO particles

It also should be considered that the influence of micro cavities that existed in the cryomilled powders on the thermal stability. Figure 3.12 presents an SEM image of a cryomilled particle. Several micro cavities can be observed in this particle. In addition, it can be concluded that this particle was actually cold welded to two additional particles, as a particle boundary can be easily discovered (see the red arrow). As mentioned in the previous chapter, the repeated powder fracturing and cold welding during cryomilling would introduce partly closed welding interfaces, which produce micro porosity. These micro voids can act as “blocks” of the diffusion channels and significantly decrease the rate of mass diffusion. As a result, the mobility of grain boundaries would be restricted due to lack of mass diffusion [95,191].

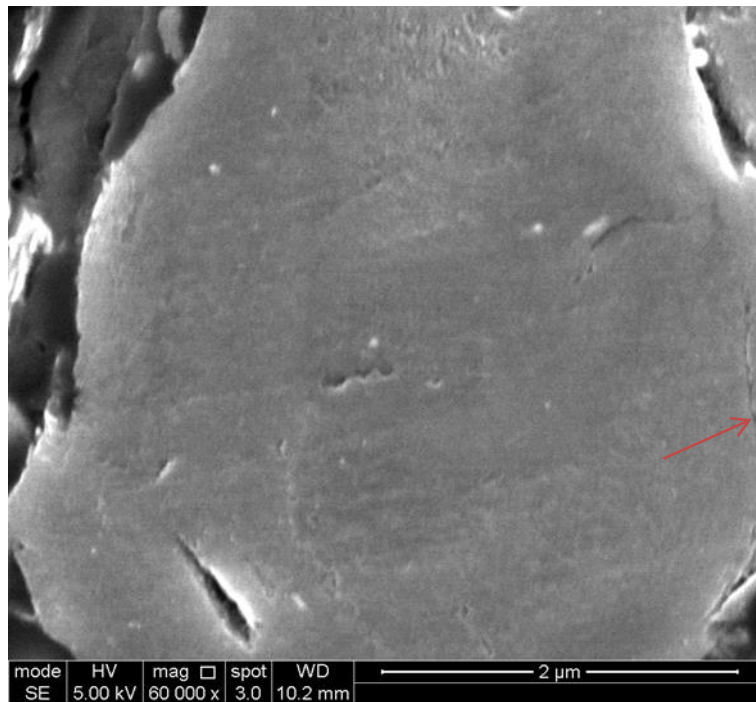


**Figure 3.12** A Representative secondary electron SEM image of cryomilled powder showing micro cavities formed during cryomilling due to repeated fracturing and cold welding.

### 3.4 Conclusions

The NC AZ31 powder prepared by cryomilling exhibits excellent thermal stability during short anneals at 350-450°C. There were two separate growth stages with a transition point at around 400 °C. More specifically, between 350 and 400 °C, NC Mg grains were stable at approximately 32 nm, even after 1h annealing. At 450 °C, the nano grains grew to 37 nm in the first 5 minutes and grew quickly to approximately 60 nm after 15 minutes. However, the grain growth was limited when the annealing time was increased to 60 minutes. Some submicrometer scale (>200 nm) particles can be also observed in some areas when the powder was annealed at 450 °C. Nevertheless, the average grain size remained stable less than approximately 60 nm even after long anneals at temperatures as high as 450 °C(0.78 T/TM), indicating an outstanding degree of grain size stability. This excellent thermal stability can be attributed to solute drag, Zener pinning, and micro porosity. In addition, the results of micro hardness of these annealed powders agreed fairly well with the grain size changes.

# **4 Synthesis of high strength, bulk nanostructured Mg– 3Al–Zn alloy**

Abstract:

Bulk nanostructured (NS) Mg AZ31 alloy has been produced spark plasma sintering (SPS) at four different temperatures from 350 to 450 °C. The effect of sintering temperature on microstructural evolution and compressive behavior was studied in detail. It can be concluded that the sample consolidated at 400 °C exhibited the highest strength. Higher sintering temperature (425-450 °C) improved compressive strain of the bulk sample but at the sacrifice of strength. However, samples consolidated at 350 °C displayed brittle behavior with low strength. All consolidated samples had a bimodal microstructure with nanocrystalline and coarse grains at various temperatures. The nanocrystalline microstructure formed by cryomilling was retained after consolidation and a maximum microhardness was approximately 150 HV. The bulk samples consolidated at 400 °C with an average grain size of 45 nm showed exceptional average true compressive yield strength of 408.7 MPa, true ultimate compressive strength of 504.0 MPa, which was superior to published results for most of conventional Mg alloys. However, nanostructured materials usually have high strength but poor ductility. True compressive strains were all less than 0.06 at true ultimate compressive strength in this study.

## **4.1 Introduction**

Due to its low density, magnesium, with a high specific stiffness as well as strength, is an outstanding candidate for weight critical structural applications [4]. However, the low

ductility due to hcp structure and relatively poor mechanical strength compared to most light Al alloys limit the application of Mg alloys[2]. According to the Hall-Petch effect [173], grain refinement is a very effective route to improve the strength and ductility of materials. This is particularly true for Mg, having a hexagonal structure, which exhibits a higher Hall–Petch coefficient than face centred cubic metals, such as Al (Mg:  $k_y=279 \text{ MPa } \mu\text{m}^{-1/2}$  and Al:  $k_y=68 \text{ MPa } \mu\text{m}^{-1/2}$ ) [139].

Previous chapters detailed how severe plastic deformation (SPD) methods (e.g. equal channel angular pressing, high-pressure torsion, multi-directional forging and mechanical milling) have been applied to effectively reduce grain size of Mg alloys [42,63,66,69,71-73,76,77,203]. Recently in the field of UFG AZ31 alloy, Kim et al. [33,204] reported an exceptionally strong AZ31 alloy produced by high-ratio differential speed rolling. With an average grain size of  $0.6 \mu\text{m}$ , the yield stress reached 382 MPa. Razavia et al. [4] suggested the grain size of the AZ31 produced by ECAP was refined to 350 nm. This alloy possessed a high yield strength of 385 MPa and ultimate tensile strength of 455 MPa with 13% ductility, which has the highest reported combined strength and ductility for an AZ31 alloy. Lee, Morisada and co-authors [205,206] found that an UFG or NC microstructure could be obtained in precipitate-hardened Mg alloys via SPD processes due to the combined high deformation and significant pinning effect from precipitates. In contrast, when the alloying content is low, such as in commercially pure Mg and alloys such as AZ31, it is a challenge to achieve even a UFG microstructure, let alone a NC microstructure due to the rapid growth kinetics of the single-phase grains. Nevertheless, Chang et al.[207] reported that they managed to produce nano grained microstructure in AZ31 alloy with an average grain size of 85 nm via using two-pass friction stir processing under rapid heat sink based on their previous study [208]. The mean hardness of this alloy was around 150 HV, but other mechanical properties were not included in their published papers. In addition, Sun et al.[209] reported a NC bulk AZ31 with an average

grain size of 48 nm by powder metallurgy assisted hydriding–dehydriding and its hardness was about 89 HV, and also no resulting mechanical properties was reported.

Very recently, a novel manufacturing technology, a combination of cryomilling and Spark Plasma Sintering (SPS), has been successfully applied to fabricate NS Mg-10Al, Mg-30Al and AZ80 alloys [83,100,165,185]. The NS AZ80 exhibited a high compressive yield stress of 442 MPa and ultimate compressive strength of 546 MPa with an average compressive strain to failure of 3.7%. The NS Mg-10Al displayed yield strength of 550 MPa, and ultimate strength of 580 MPa, but the compressive strain was less than 2.5%. The exceptional high strength was attributed to the nanocrystalline (NC) grains due to cryomilling. Introduction of cryomilling was elaborated in previous chapters and will not be discussed in this chapter. Retained NC microstructure after consolidation can be mainly attributed to rapid sintering process by using SPS. In the past two decades, a review of the scientific literature reveals that bulk metal or alloys with various compositions have been successfully synthesised by consolidating NC powders via SPS in a short time interval [89,129,136,210-213]. The main features of SPS are as follows: (a) a high heating rate (generally 50-200 °C/min, can reach up to 1000 °C/min), (b) a uniaxial pressure loading (a maximum pressure of around 100 MPa for a graphite die) and (c) effect of the current [105].

Because cryomilled powder yield is very low (only 6 grams for 12 hours cryomilling), several sets of preliminary experiments have been performed using as-received AZ31 gas atomized powder to investigate effects of process parameters (i.e., heating rate, pressure loading mode, dwell time and temperature) on densification and sample mechanical behaviour. Results were adjusted on the basis of some relevant literature and experimental results, and indicated a strong dependence on SPS parameters [105,210]. The results also reached a conclusion: when the highest pressure 80 MPa was applied, sintering temperature played a

dominant role in sample densification, but the effects of various heating rates, long dwell time and different loading modes were found to be insignificant and can be ignored.

Based on the discussions above, the motivations for the work presented in this chapter are twofold. First, to find out whether this novel manufacturing technology can be extended to produce NC microstructure in a magnesium AZ31 alloy with much lower content of alloying elements than Mg-30Al and AZ80 alloys, thereby fabricating high strength nanocrystalline AZ31 alloy. Second, investigate the response of grain growth and mechanical behaviour, when samples were sintered at various temperatures, especially at elevated temperatures (e.g., 450 °C, 0.78 T<sub>m</sub>).

## **4.2 Experimental**

### **4.2.1 SPS processing**

3 grams of cryomilled powder was loaded into a cylindrical graphite die with diameter of 20 mm. To avoid welding and obtain a more uniform current flow, thin graphite foils were placed between powders and the graphite SPS dies surface. Afterwards, the prepressed powder was sintered via an SPS apparatus (FCT Systeme GmBH SPS system, type HP D 1050, Germany) under vacuum. The heating rate 50°C/min, the dwell time 5 minutes and the maximum uniaxial pressure of 80 MPa were applied for sintering based on the results of preliminary experiments. The holding temperatures ranged from 350 to 450°C. The corresponding samples after sintering were designated as CM350, CM400, CM425 and CM450 hereafter. Temperature was monitored by a TC thermocouple inserted into a hole located in the centre of the die close to the sample. To evaluate the improved mechanical behaviour of cryomilled powder and corresponding sintered bulk sample, a bulk sample sintered at 400 °C consisting of as-received powder between 38-75 µm (designated as AR400) was also produced for reference. To avoid oxidation, the powders were loaded into the grinding jar before

cryomilling and the SPS mould in an Ar atmosphere glove box (Mbraun, Germany). The current, temperature, displacement and displacement rate as a function of time were recorded by the software equipped with the SPS apparatus.

#### **4.2.2 Density measurement**

After polishing the surface, the bulk density of the sintered samples was determined by Archimedes method using a balance with accuracy of  $\pm 0.0001$ g (MS104S, Mettler Toledo, Switzerland). At least three measurements were taken for each sample.

#### **4.2.3 Optical Microscopy**

Optical microscopy was carried out on a Nikon microscope. Samples were prepared by grinding with SiC paper from 1200 to 4000 grit. To minimize oxidation exposure to water, samples were polished with alcohol based diamond suspensions of 1 and 0.25 $\mu$ m.

#### **4.2.4 Scanning electron microscope (SEM)**

The sample preparation procedure for SEM is the same to that of optical microscopy, but etching is not necessary in some cases. A FEGSEM (FEI, Inspect F) was employed to investigate morphology of powders and bulk sintered samples. Some samples were etched using an acetic-picric solution (4.2g picric acid, 10ml acetic acid, 70ml ethanol and 10ml water) for 1 s.

#### **4.2.5 Transmission Electron Microscopy (TEM)**

Thin foils samples from bulk SPSed samples were initially mechanically ground to 20-30  $\mu$ m and finally thinned by ion milling coupled with liquid nitrogen cooling system (Fischone

1010, USA). An FEI Tecnai 20, operating at 200 kV, was used for conventional TEM characterisation.

#### **4.2.6 Micro hardness test**

To obtain a flat surface for hardness tests, the hot mounted powder and SPSed samples were ground with 800, 1200, 2500, 4000 grade SiC papers and finally polished by 1  $\mu\text{m}$  and 1/4  $\mu\text{m}$  alcohol based diamond suspension. A Vickers hardness tester (Akashi Corporation Sagami Plant, model HM-101) was used to perform hardness tests with a load of 50 grams and a dwell time of 15 s. At least 11 indents were collected for each sample to obtain accurate hardness results.

#### **4.2.7 Compression test**

Uniaxial compression and tensile tests are the most frequently used methods to evaluate mechanical properties of materials. Considering the relative small scale samples produced by SPS, compressive testing was the only viable method that could be conducted in this project.

Cubic specimens with side size of 4 mm were used for compression test and cut by a high precision saw (IsoMet 5000, Buehler). Figure 4.1a schematically shows where these specimens were cut from. Before tests, all the samples were carefully polished to eliminate oxide layers attached on each surface. A very thin layer of grease was placed on the interface between the sample and the compression cross heads to avoid significant frictional forces. Compression tests were conducted using a Zwick/Roell testing machine at a crosshead speed of 0.06 mm/min until failure. The loading direction for testing was normal to the disk shaped sample surface, as presented in figure 4.1b.

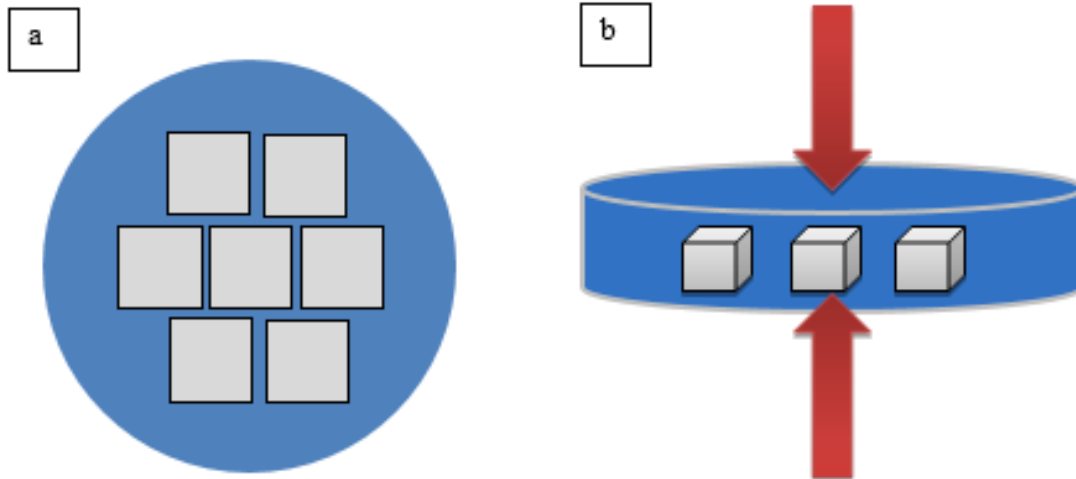


**Figure 4.1** A schematic image showing (a) the specimens position (b) the loading direction of compression test

#### 4.2.8 Compression test compliance correction [214]

Correction for machine compliance is essential to obtain reliable experimental data in many mechanical testing procedures. There are two major drawbacks with compression tests compared with tensile tests: (a) significant frictional forces would exist between the sample and the compression plates if the interface is not appropriately lubricated and (b) measurement of the real deformation from the sample becomes very difficult if the lengths of specimen are too small to use an extensometer.

Kalidindi and co-workers reported three accurate methods to correct machine compliance for simple compression testing [214]. The displacement recorded is treated as the sum of the displacements from the sample and the loading system from the machine, as described in equation 4.1

$$L_R = L_S + L_C \quad \text{(Equation 4.1)}$$

The method “Direct Technique” reported in reference [214] was adopted in this study. In this technique, the load-displacement  $L_C$  for the machine was directly measured without any sample between the compression cross heads. The red line in Figure 4.2 presents the force-

displacement curve of testing machine. Afterwards, a sample was placed between cross heads and the procedure was repeated. The black line in Figure 4.2 shows the corresponding force-displacement curve, and the displacement consists of deformation from both the sample and the testing machine. After fitting these two curves and subtraction, the deformation only from sample can be obtained, as the blue line shown in Figure 4.2.

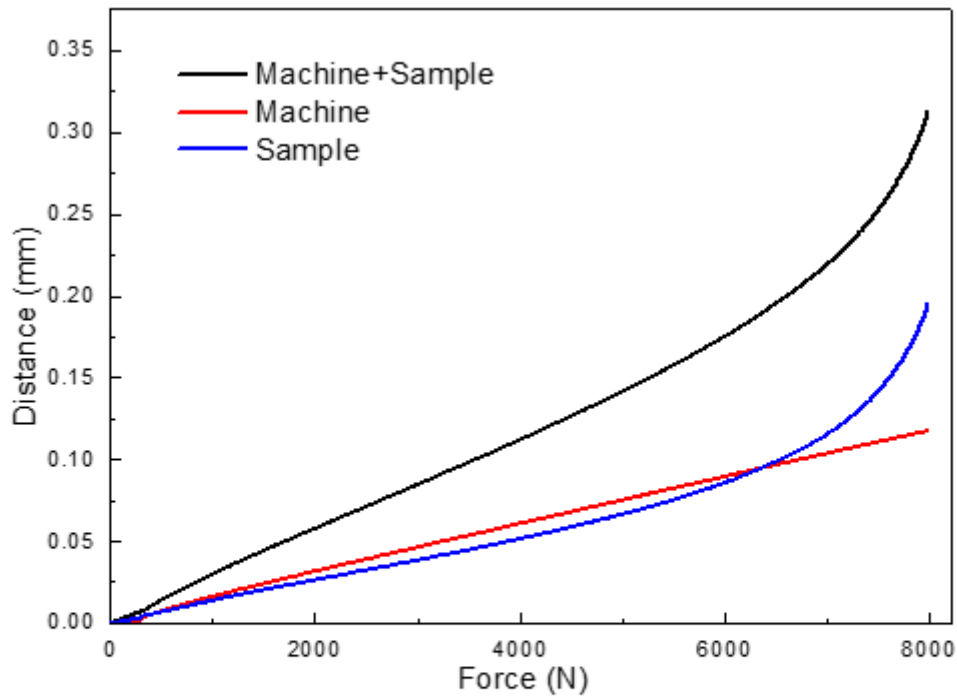


**Figure 4.2** Illustration of the technique for characterizing the machine compliance and obtaining the real deformation from the samples

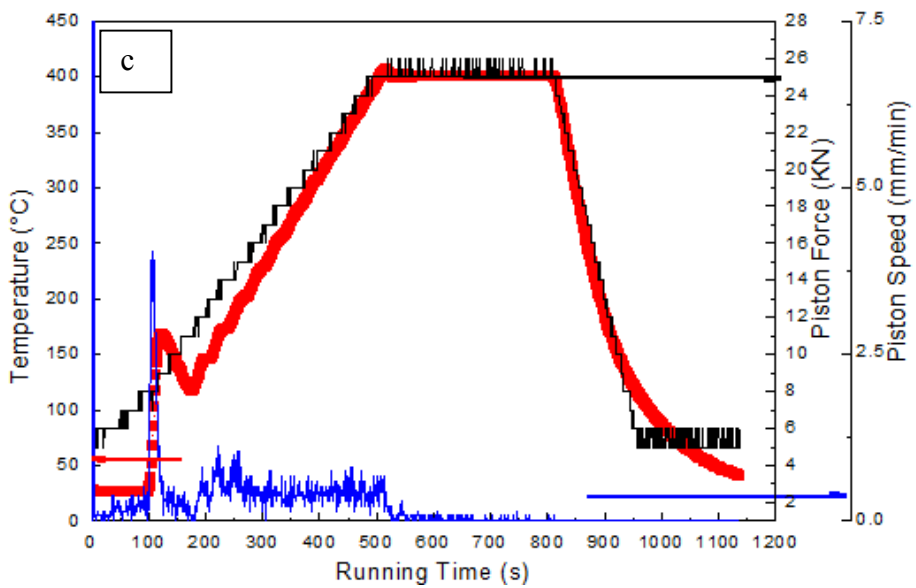
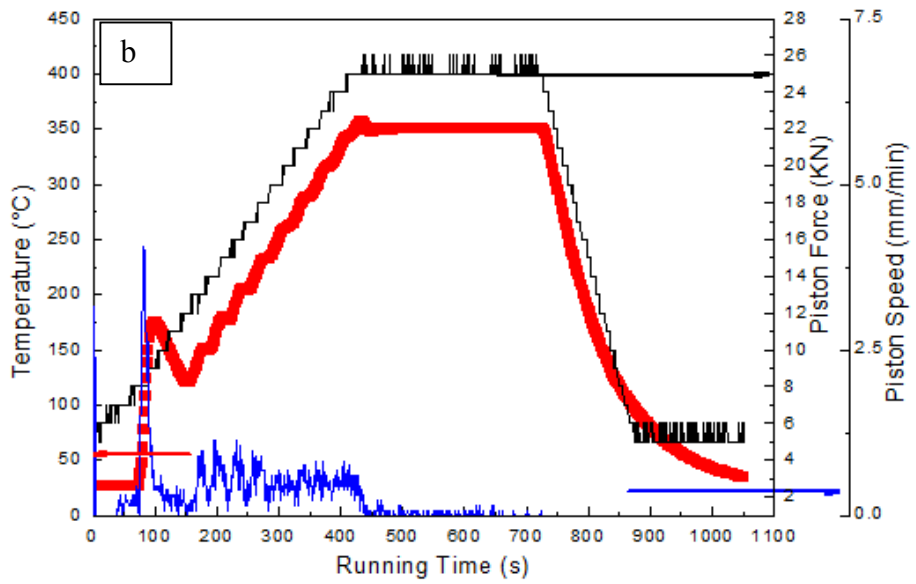
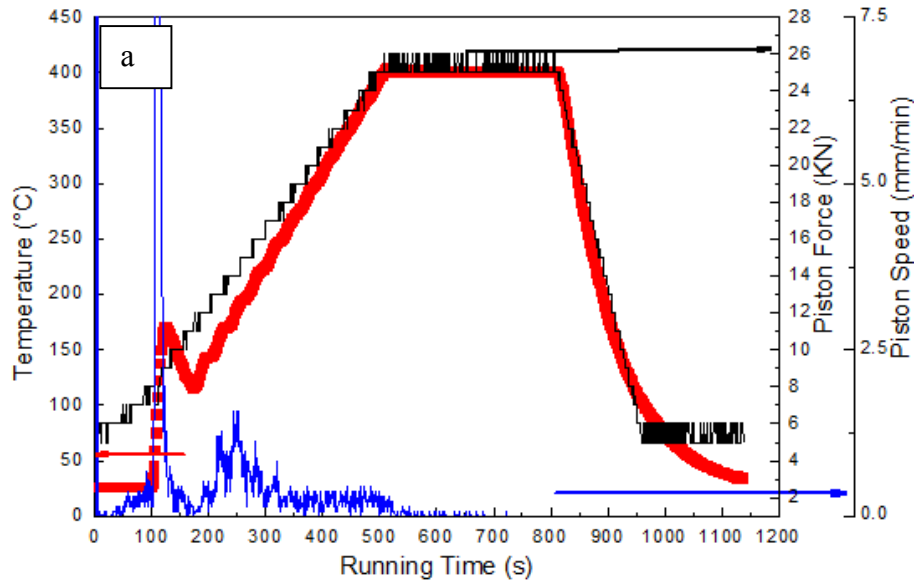
## 4.3 Results and discussion

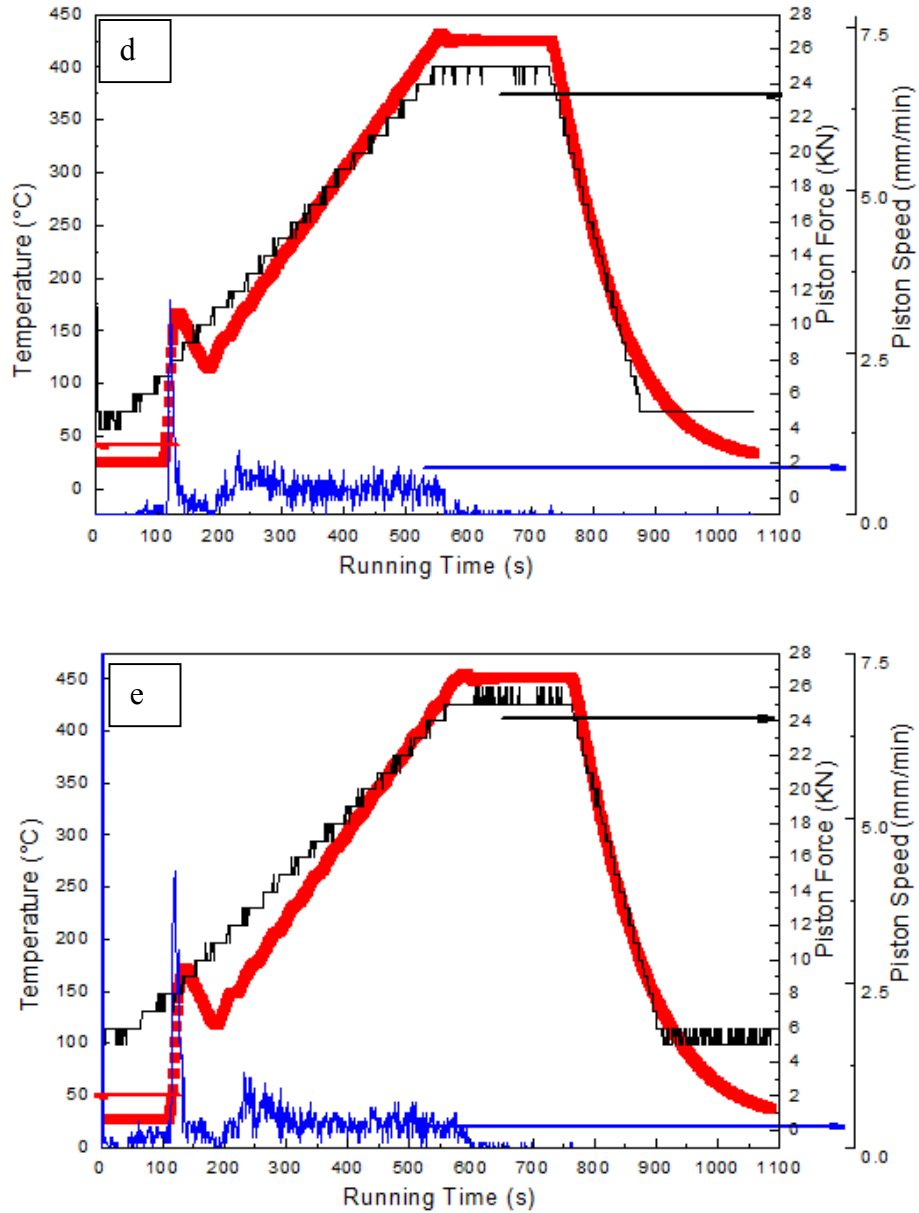
### 4.3.1 SPS processing curves

Figure 4.3 gives the variation of sintering temperature, piston force, and piston speed as a function of running time for different sintering temperature and powders. All these five figures shared some common features. A rapid piston movement occurred when heating and

pressure began to be imposed on the loose powders. Afterwards, the piston moved down continuously with various speeds. When sintering temperature reached the set temperature in each run, the piston speed dropped to zero, especially during the late dwelling stage. This meant that extending the dwell time was not beneficial for densifying samples. To avoid grain growth of NC AZ31 powder at elevated temperature, the dwell time was reduced from 5 minutes to 3 minutes when the sintering temperature was higher than 425 °C. However, it cannot be ignored that the piston still moved down between 500 and 600 s for samples sintered at 425 and 450 °C while the speed was negligible for the other samples. This indicated increasing sintering temperature assisted samples densification process.

Table 4.1 lists density of those five SPSed samples. The error in the data was  $\pm 0.002$ . It can be found that the density was increased with increasing the sintering temperature for the cryomilled powder samples, especially when the sintering temperature changed from 350 to 400 °C. In addition, the density was also significantly improved after cryomilling when compared the density results of CM400 and AR400. To find out the reasons for this difference, microstructural characterization was conducted.





**Figure 4.3** The sintering temperature, piston force, and piston speed as a function of time for bulk samples a) AR400, b) CM350, c) CM400, d) CM425 and e) CM450.

**Table 4.1** Density measurement results for SPSeD samples

Sample	Density (g/cm <sup>3</sup> )
AR400	1.808
CM350	1.802
CM400	1.824
CM425	1.829
CM450	1.835

### 4.3.2 Morphologies of bulk SPSed samples

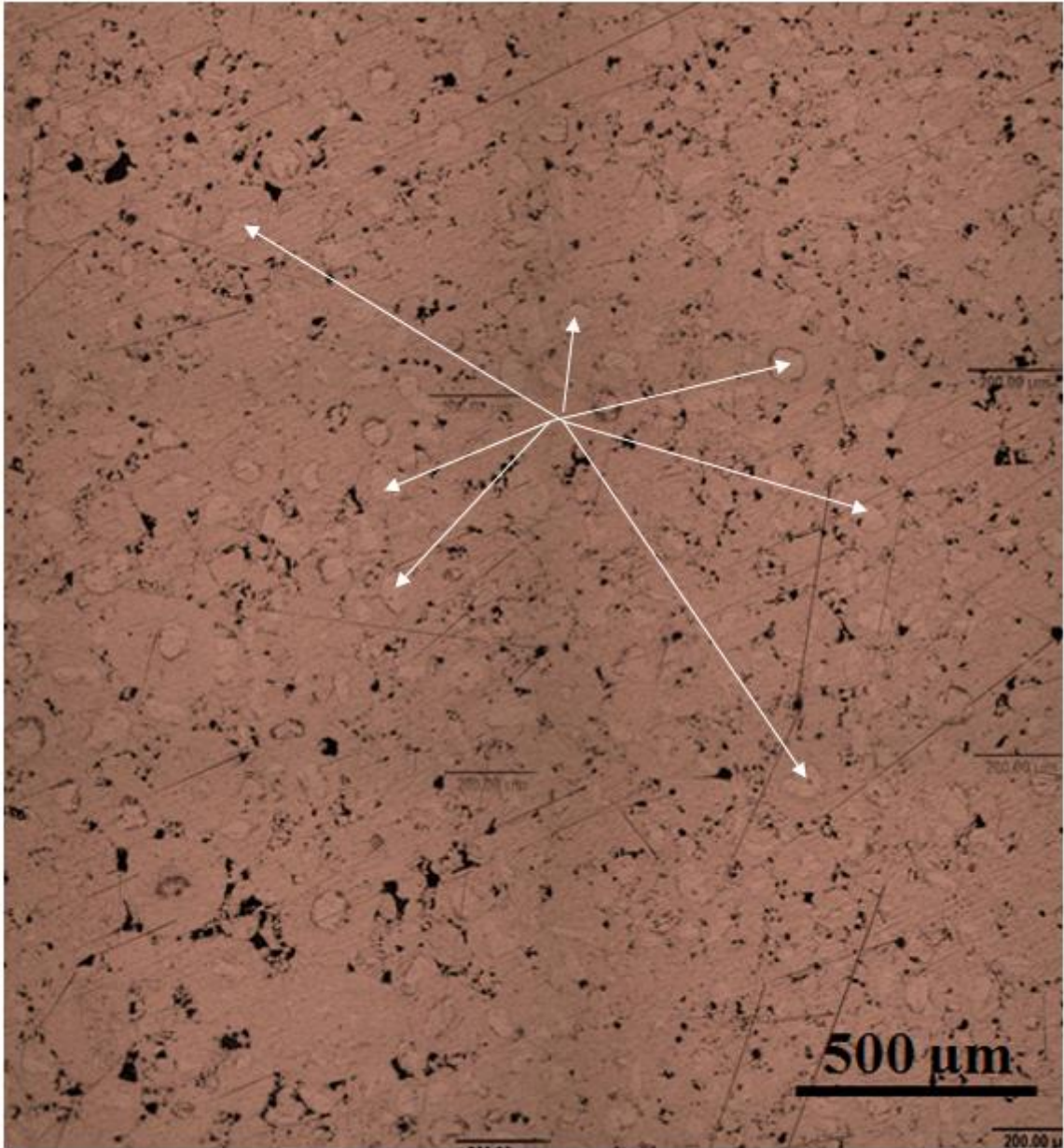
Figure 4.4 shows a large scale optical microscope (OM) image of sample AR400. Considerable porosity can be clearly observed in the image. These pores were arose from insufficient sintering and also occurred due to particle pull out during polishing because of insufficient inter-particle bonding. In addition, a thick layer of Mg oxide film was found to cove each particle, which in itself would have restricted the sintering process.



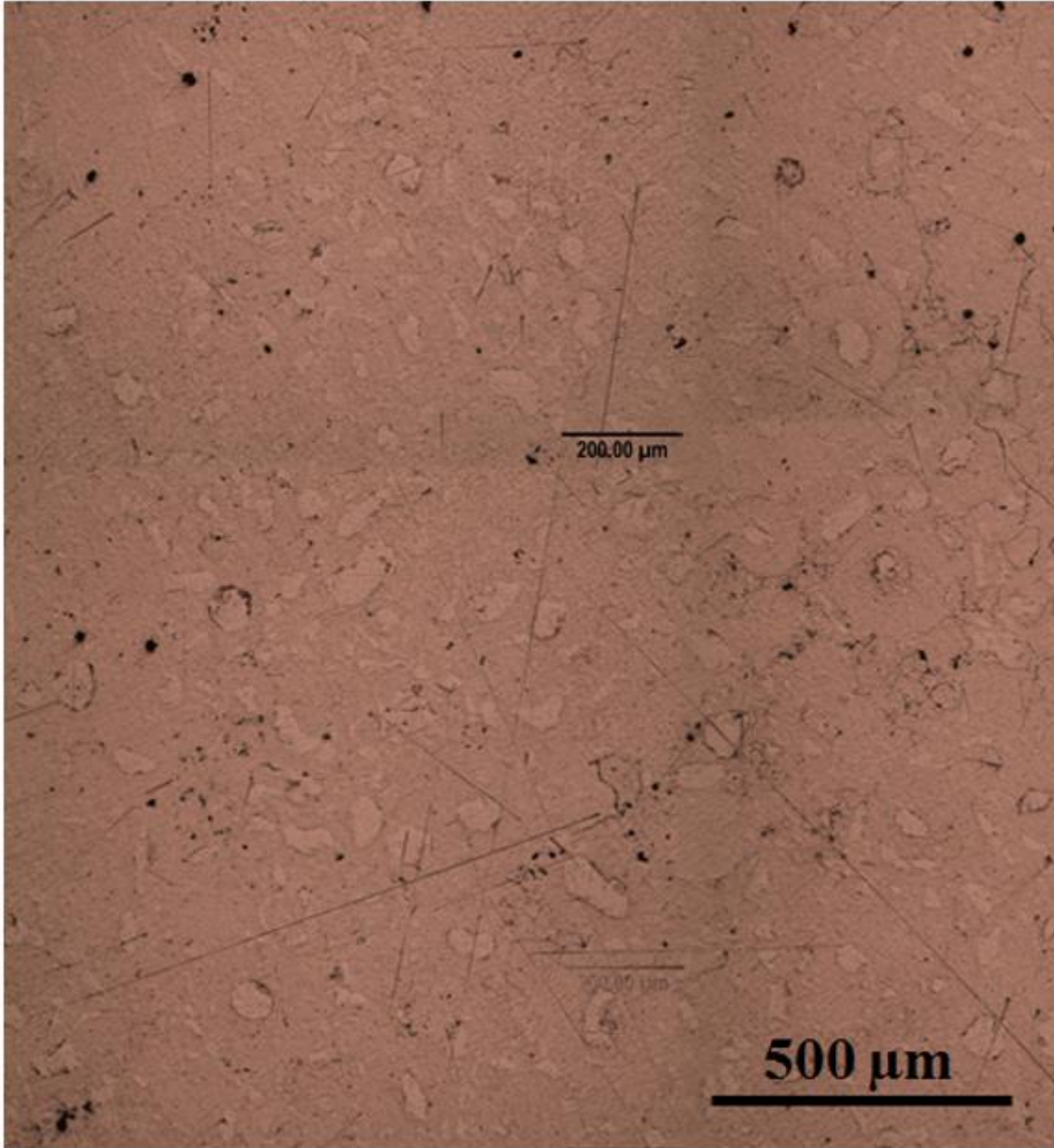
**Figure 4.4** Typical optical microscope image of sample AR400

Figures 4.5-4.8 present the OM images of samples CM350, CM400, CM425 and CM450. The most obvious feature in these images is that the volume fraction of micro pores decreased substantially when the sintering temperature rose from 350 °C to 400 °C. The pores size and quantity was slightly decreased when sintering temperature was further increased, and the pores almost disappeared in most parts of the samples. Therefore, higher sintering temperature played a positive role in assisting sintering samples. In addition, the changing trend of pores agreed well with the results of density listed in table 4.1. The enhancements in density were attributed to the following two factors. First, the strength of the alloy powder drops substantially with increasing temperature. Second, creep flow is the main densification mechanism in the case of pressure-assisted sintering at elevated temperatures and is a diffusion-driven process which strongly relies on temperature [210].

In addition, it was evident that not all the particles in the starting powder had been fully cryomilled. For example, a great many bright particles (exhibiting brighter contrast, arrowed on figure) were distributed among nano grain sized particles in all SPSed cryomilled samples. This is inevitable with mechanical milling, especially without adding process control agent (PCA). The hardness of these particles was only about 70 HV with a mean grain size of 10 μm. Those particles will certainly affect the mechanical properties of this alloy.



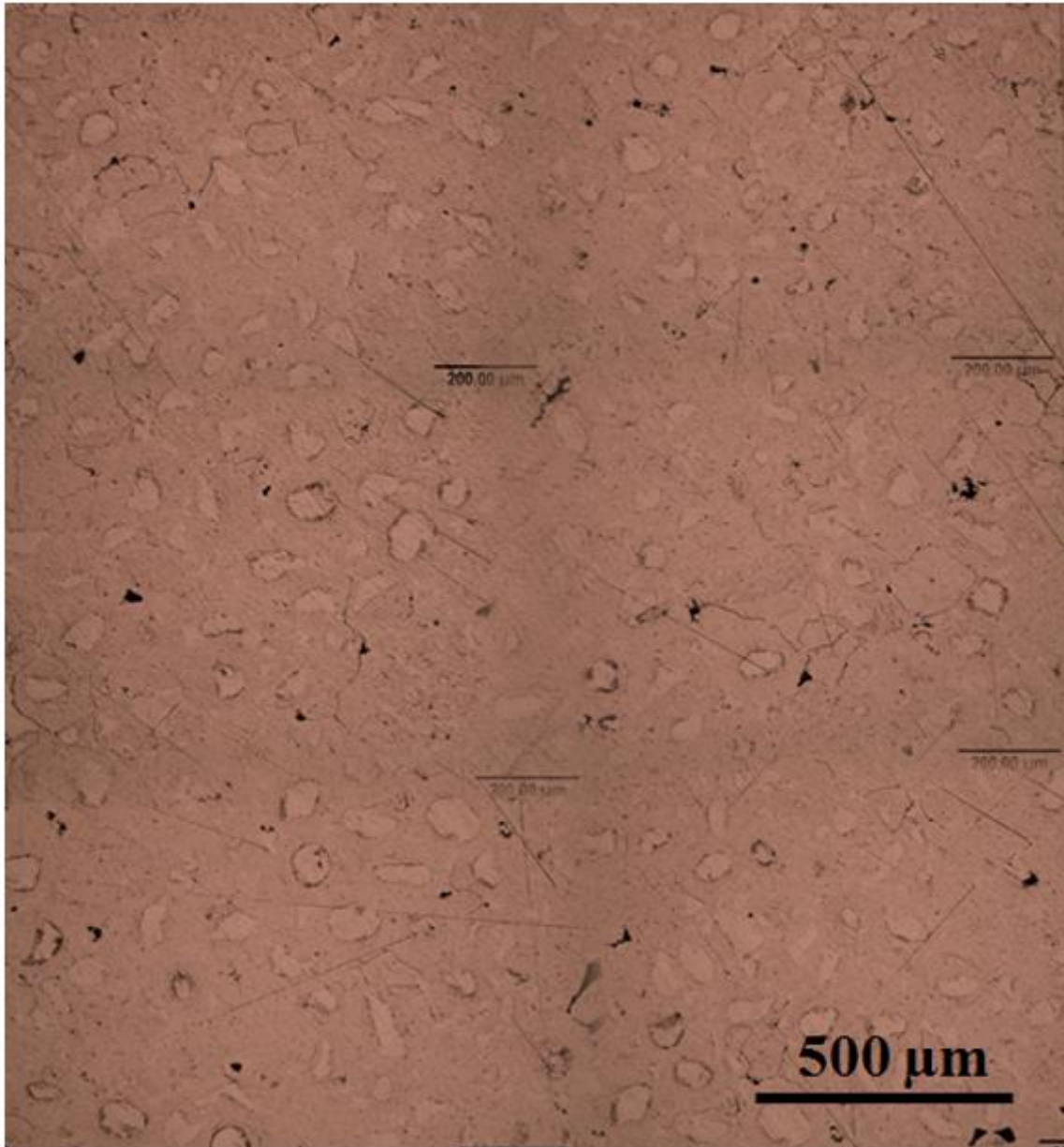
**Figure 4.5** Typical optical microscope image of sample CM350



**Figure 4.6** Typical optical microscope image of sample CM400

Because samples AR400 and CM400 were processed under the same operating parameters, the effect of cryomilling on sample densification can be discussed. SEM was

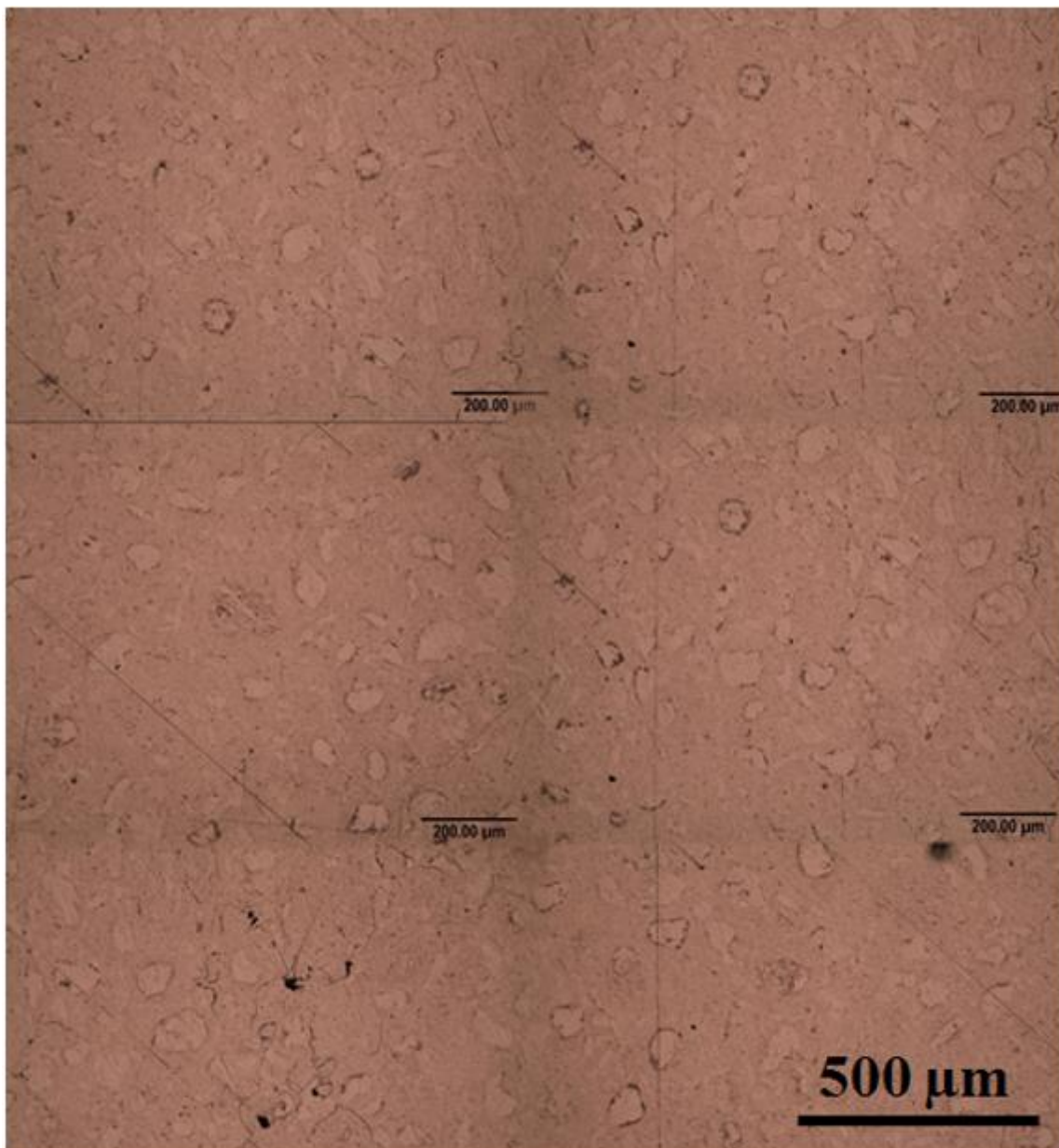
employed to obtain more details of the difference between these two samples. Figure 4.9 shows the back scattered SEM images of AR400 and CM400 samples after SPS.



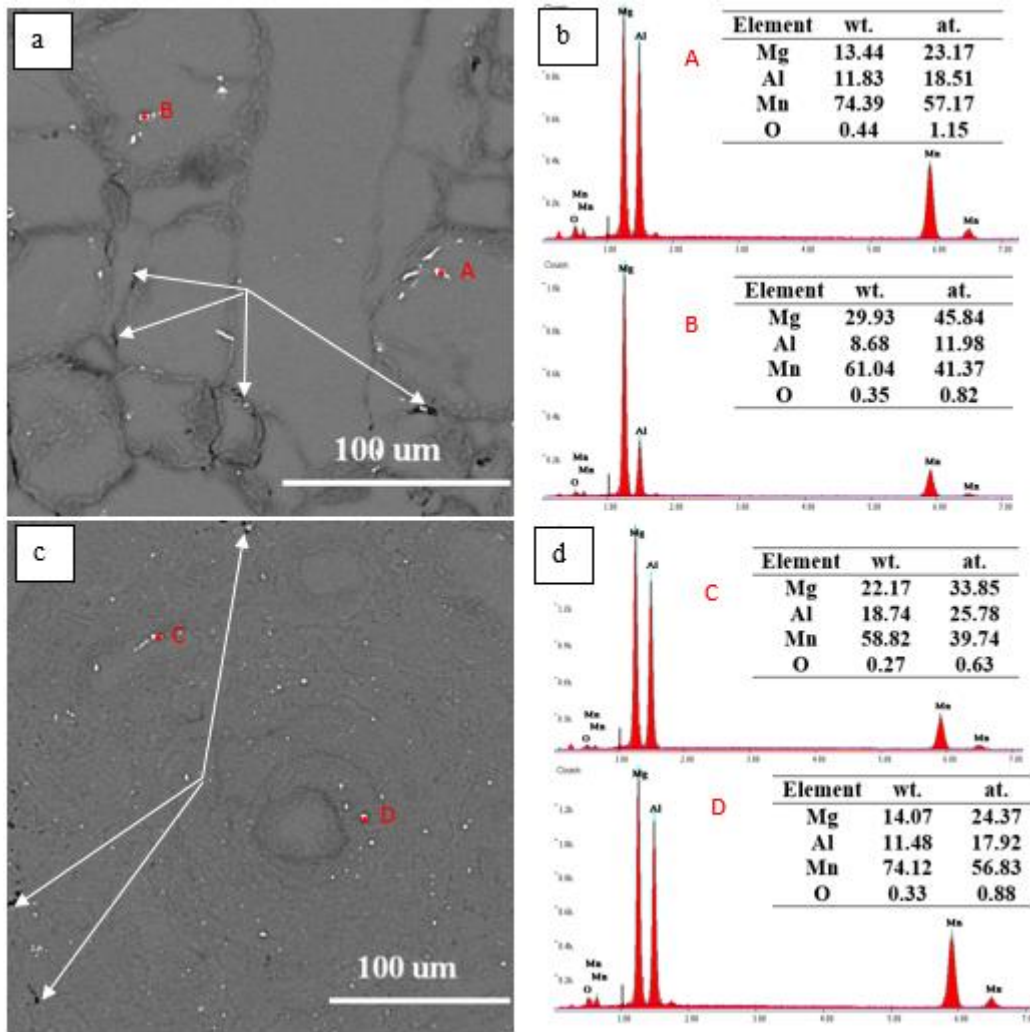
**Figure 4.7** Typical optical microscope image of sample CM425

Pores were observed in both sintered samples between particle boundaries (indicated by the white arrows), but the pores in sample CM400 were smaller and fewer in number than sample AR400. The most prominent difference between these two samples was few particle

boundaries can be found in the nano grain sized area of CM400. The oxide film present on the surface of the magnesium powder had been broken up during cryomilling, such that particle boundaries could only be rarely seen in sample CM400 compared to sample AR400. Clearly, this will be beneficial to decrease the quantity and size of pores and to increase sample relative density. As mentioned in previous chapters, the oxide films appeared to have been broken down to nanosized inclusions and would therefore be expected to act to strengthen the alloy [202].



**Figure 4.8** Typical optical microscope image of sample CM450



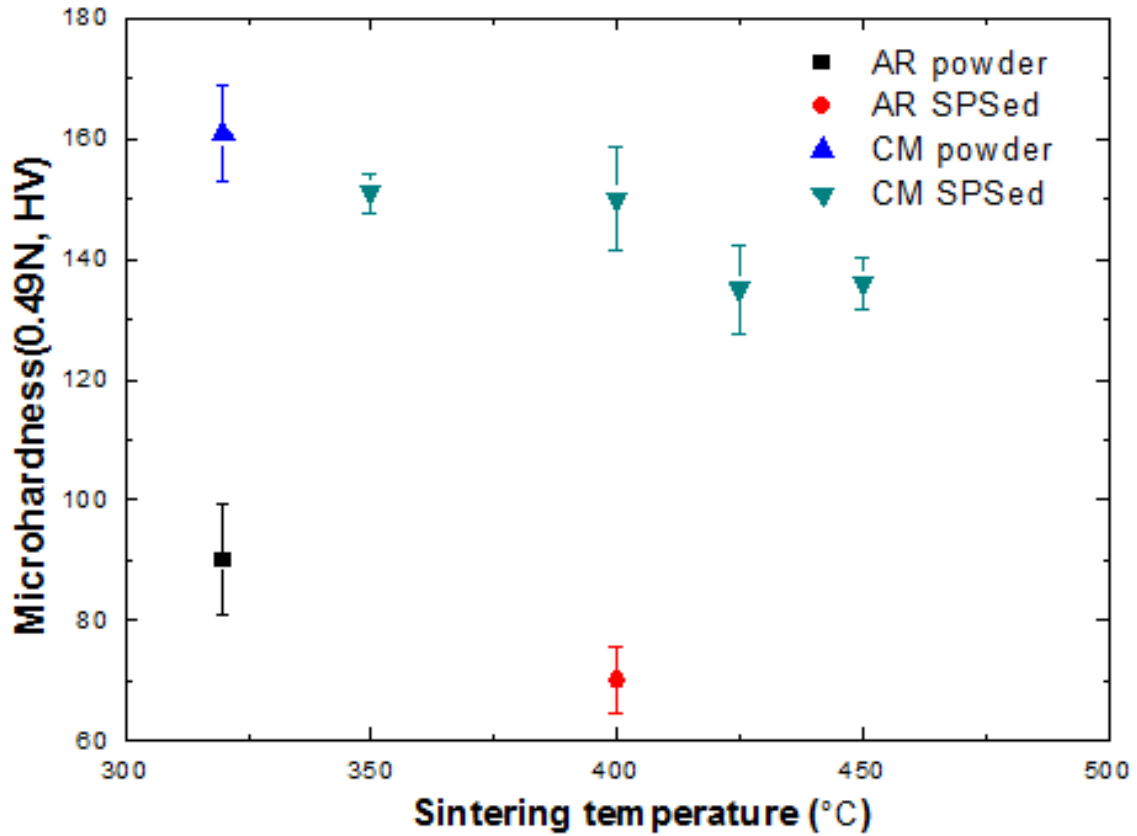
**Figure 4.9** Back scattered electron SEM images of (a) AR400 and (b) corresponding EDX analysis of second phases particles, back scattered electron SEM images of (c)CM400 sample and corresponding EDX analysis of second phases particles

Figure 4.9 (b,d) shows the chemical composition of the second phases exhibiting bright contrast. The EDX point detection resolution is 1  $\mu\text{m} \times 1 \mu\text{m}$ . Therefore, the extra adjacent matrix Mg signal cannot be avoided during the signal collection. As shown in figure 4.9, the Al and Mn rich second phases which were apparent and locally distributed in sample AR400, were broken up and uniformly dispersed in the sample CM400. Although Zn was not automatically detected, small peaks (indicated by the vertical black line) could still be seen and these peaks were located at the position of Zn. However, it cannot be ignored that part of the

second phases were dissolved into the  $\alpha$ -Mg solid solution matrix. This was believed to be due to cryomilling, which increases the equilibrium solubility limit at room temperature, which can also make contribution to increase the strength of the alloy [202].

### **4.3.3 Micro hardness results of bulk SPSed samples**

Figure 4.10 gives the hardness results of the as-received (AR) powder, cryomilled (CM) powder and corresponding bulk SPSed samples sintered from 350 °C to 450 °C. The hardness of the AR powder was  $90\pm 9.2$  HV, which increased to  $162\pm 10.7$  HV after 6h cryomilling. This can be attributed to the fine grain size, extended solid solution ability and the break-up of the oxide film. After SPS consolidation at 400 °C, the hardness of bulk AR400 sample dropped to  $70\pm 5.6$  HV. In contrast, the bulk samples CM350 and CM400 only slightly decreased to approximately 150HV resulting in a material with a hardness more than twice that of bulk AR400 sample. Nevertheless, while the sintering temperatures further extended to 425 and 450°C, the hardness significantly reduced to around 135 HV, although the dwell time was reduced to 3 minutes at these two elevated temperatures. As shown in figure 4.10, there is a transition point at approximately 400 °C. Below this temperature, the decrease of hardness was limited, but beyond this point, sample softness became prominent. These results agreed fairly well with the annealing result of cryomilled powders annealed at 350, 400 and 450 °C discussed in the previous chapter.



**Figure 4.10** Micro hardness results of AR powder, CM powder and corresponding bulk SPSed samples sintered from 350 °C to 450 °C

#### 4.3.4 Compression testing behavior of bulk SPSed samples

To illustrate the influences of cryomilling and sintering temperature on bulk SPSed samples separately, the following part will first focus on the reasons for the exceptional high strength with poor ductility of bulk SPSed samples of the cryomilled powder, and the mechanical behavior response on various sintering temperatures will be discussed afterwards.

Figures 4.11 and 4.12 give true compressive stress-strain curves of samples AR400 and CM400. The corresponding compressive properties are listed in Table 4.2. The measured average true ultimate compressive strength and yield strength (0.2% proof stress) of sample CM400 were 504.0 MPa and 408.7 MPa, respectively. Those values were significantly higher

compared to bulk sample AR400 of 357.6 MPa and 180.5 MPa respectively. Moreover, they also exceed the previously reported highest yield strength of 385 MPa and ultimate strength of 455 MPa in AZ31 alloy [203].

Obviously, grain refinement was the major reason to improve the strength of sample CM6h according to the Hall-Petch effect. In addition, oxide dispersion and solid solution strengthening will also have contributed to this strengthening. Figure 4.13(a) shows a typical secondary electron SEM image of sample AR400 before compression tests and Figure 4.13(b) shows the grain size distribution of sample AR400. The average grain size of the as-received particles increased to approximately 6.5  $\mu\text{m}$ , but grains adjacent to the MgO film boundaries were much finer, which suggested MgO films covering the initial surfaces of powder were an effective barrier to hinder grain growth. Figure 4.14(a) is a TEM BF image of sample CM400. It exhibited a bimodal microstructure with nanocrystalline and coarse micro sized grains. Figures 4.14 (b) and (c) are selected area diffraction patterns (SADP) from nano sized and micro sized grains areas (red circles shown in Fig. 14 (a)), confirming this area consisted of a bimodal microstructure. Figure 4.14 (d) shows the internal average grain size of sample CM400 was around 35 nm (coarse grains bigger than 0.5  $\mu\text{m}$  were not included in this statistics), a result of cryomilling the AZ31 alloy.

Although the average true compressive strain of sample CM400 measured at the ultimate true compressive strength, was only 3.6% which was only about 1/3 of bulk as-received sample and result reported by Razavi et al. [203], it was still acceptable in the field of NC Mg alloys. High strength and poor ductility is the common feature of NC materials [54]. Work hardening is a very important factor related to the ductility of NC materials [50]. Compared to the true stress-strain curves in figure 4.11, evident work hardening effect was observed in bulk AR400 samples, while only limited work hardening occurred in sample CM400. This can be explained by the lack of dislocations accumulation within nanosized

grains and possibly occasional deformation twinning that occurred during the compression tests in bulk CM6h samples. The limited twinning was believed to arise because the stress required for twin nucleation increases substantially with reducing grain size to the nanometre scale [215]. One influence of twinning on the plastic deformation is that unfavorably oriented grains can be adjusted into a more favorable orientation by twinning. The twin boundaries can also impede dislocations movement, thereby increasing working hardening and delaying local necking during deformation. These positive effects have been used to improve the ductility of nanotwinned Cu [180]. Figure 4.15 presents the optical microscope images of both samples after compression tests. Far more deformation twins were produced during compression tests for samples AR400 compared to CM400, where only one twin was observed in a coarse grain. Furthermore, figure 4.16 shows a BF TEM image of nano grained area, and no sign of twins was observed, although nano-twins were reported in other nanostructured Mg alloys with higher contents of alloying elements recently [100,166,167]. In addition, defects introduced from the processing, such as porosity and crack (see Figs. 4.6 and 4.9), could have reduced the low ductility [53,215].

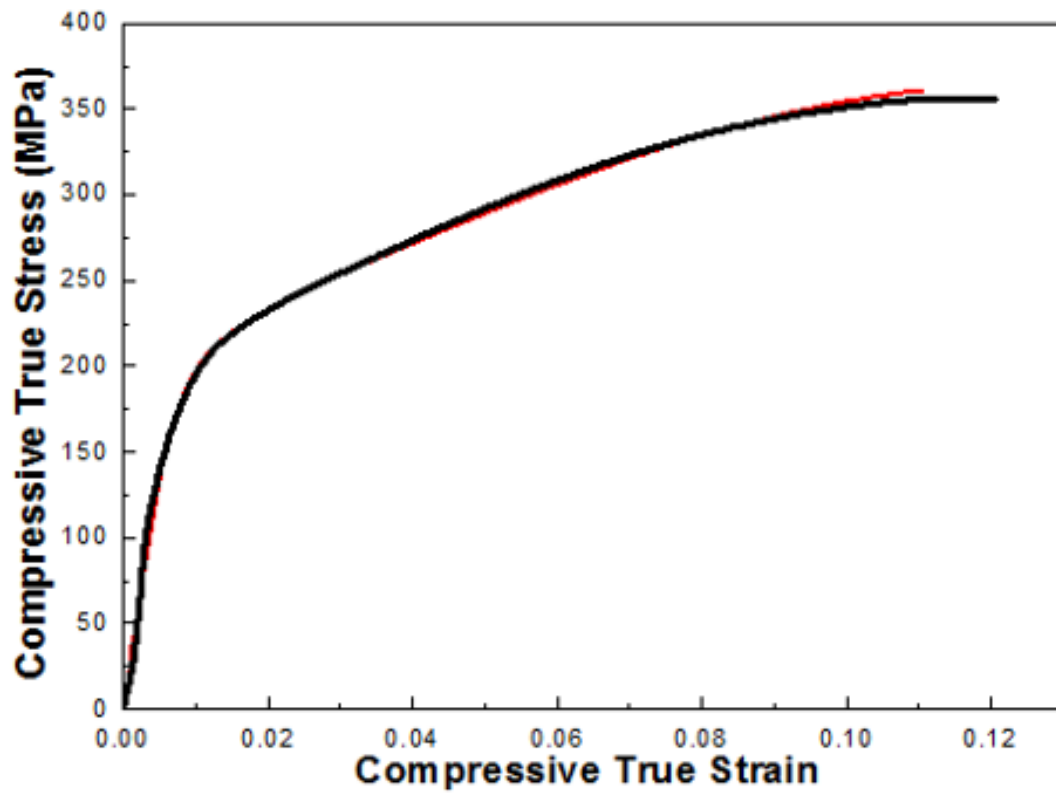


Figure 4.11 Room temperature true stress-strain curves of bulk sample AR400 (two samples)

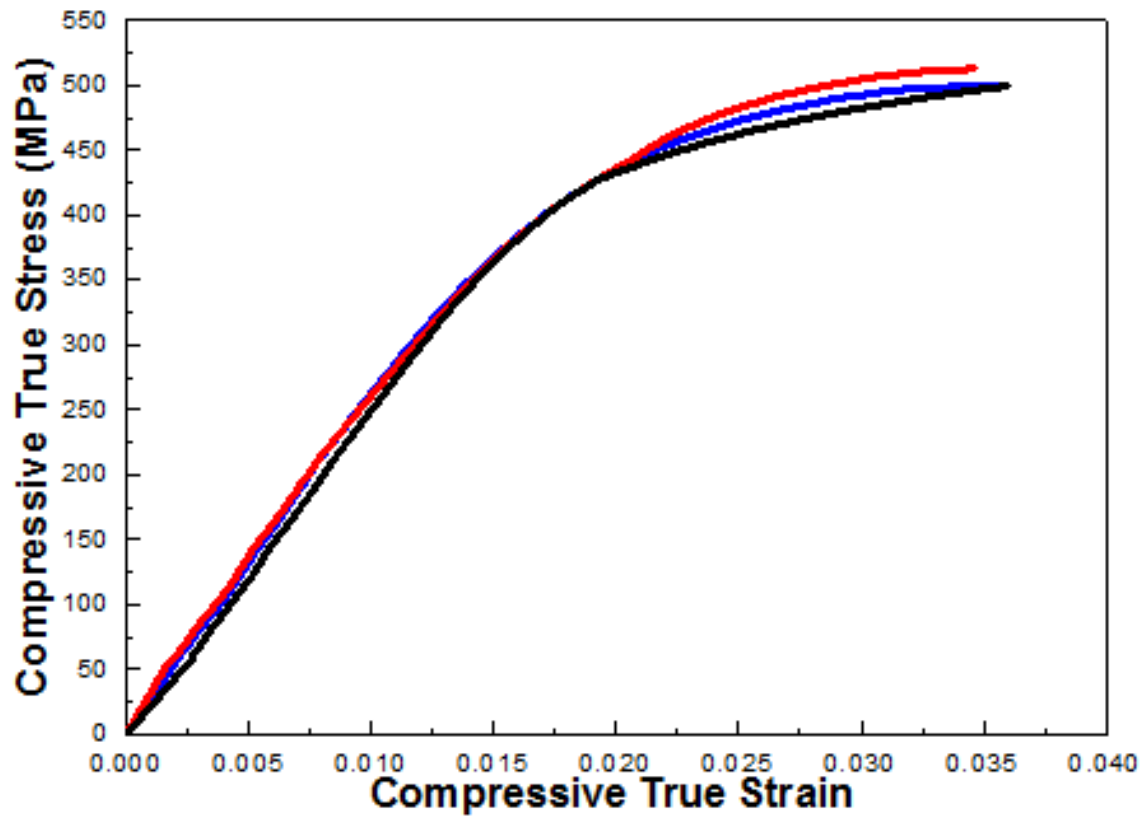
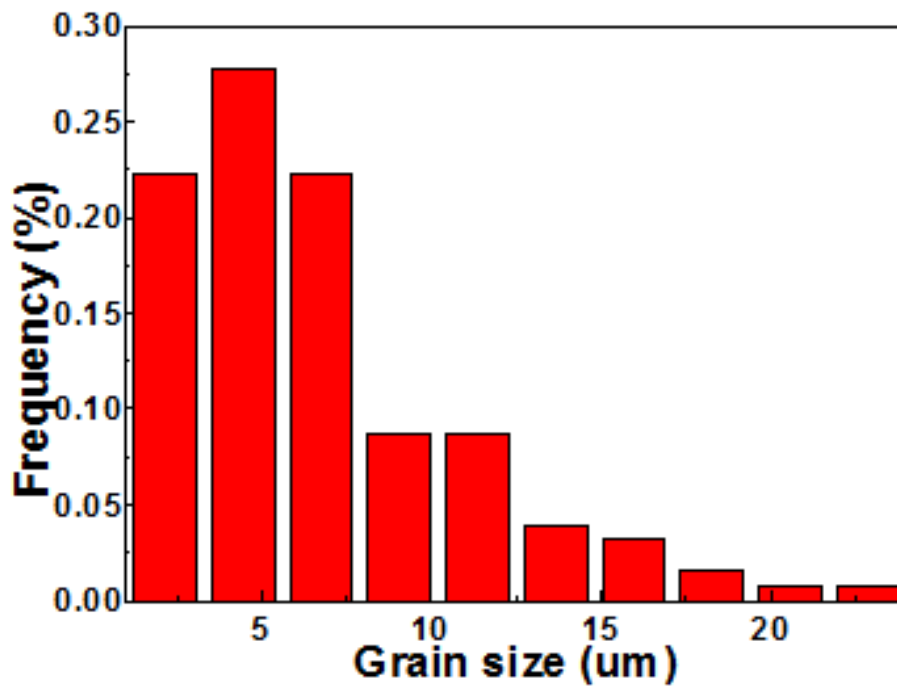
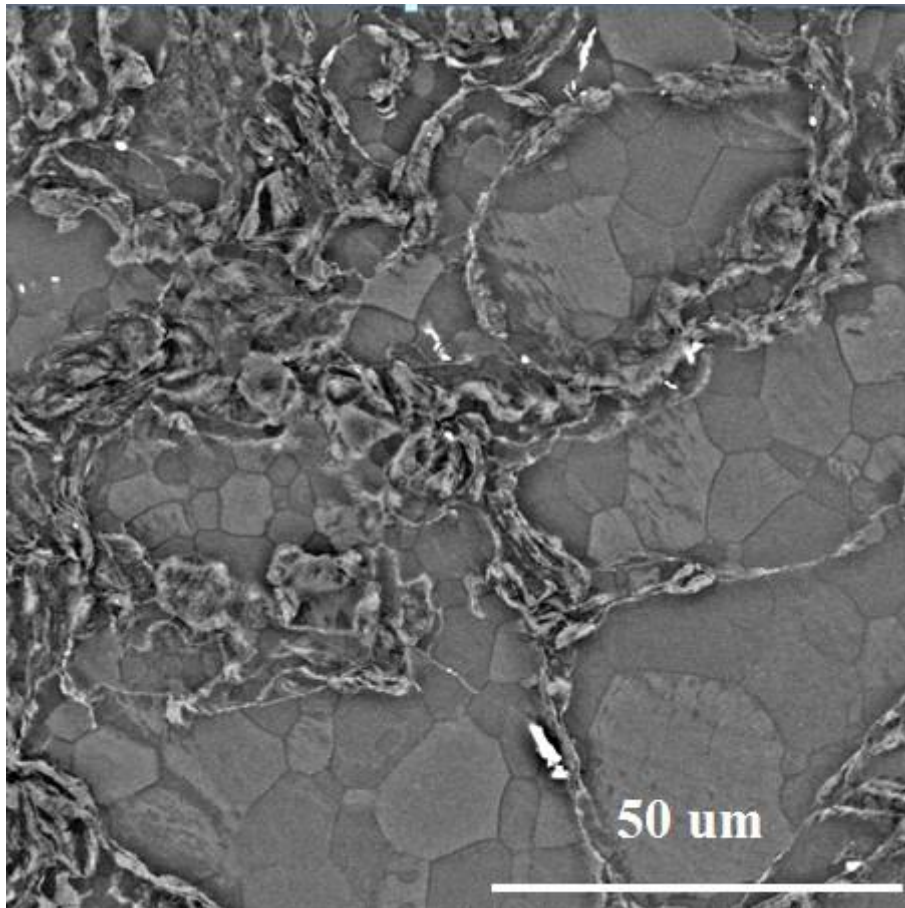


Figure 4.12 Room temperature true stress-strain curves of bulk sample CM400 (3 samples)

Table 4.2 Summary of compressive properties of bulk SPSed samples

Samples	No.	0.2% Proof Stress (MPa)	True Ultimate Strength (MPa)	True strain at ultimate strength
AR400	1	185.7	359.8	0.111
	2	175.3	355.3	0.120
CM400	1	424.8	512.6	0.035
	2	401.2	500.2	0.036
	3	400.2	499.2	0.036



**Figure4.13** A representative secondary electron SEM image and corresponding grain size distributions of sample AR400 before compression tests

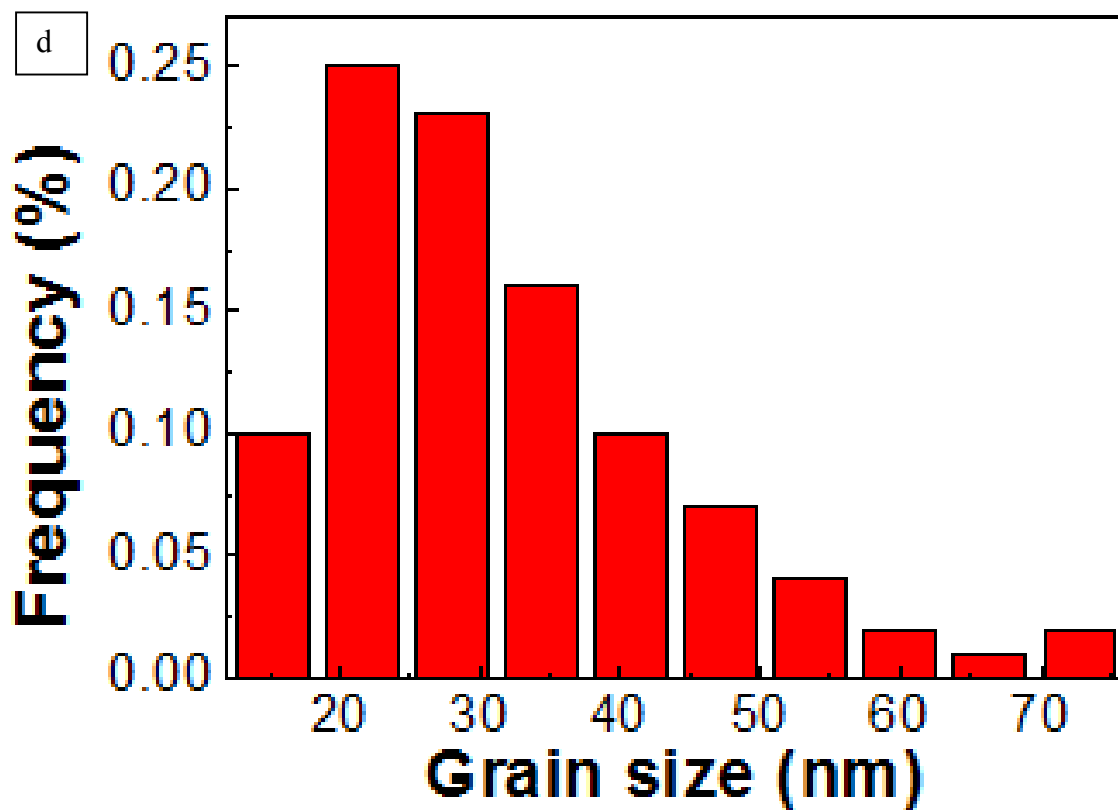
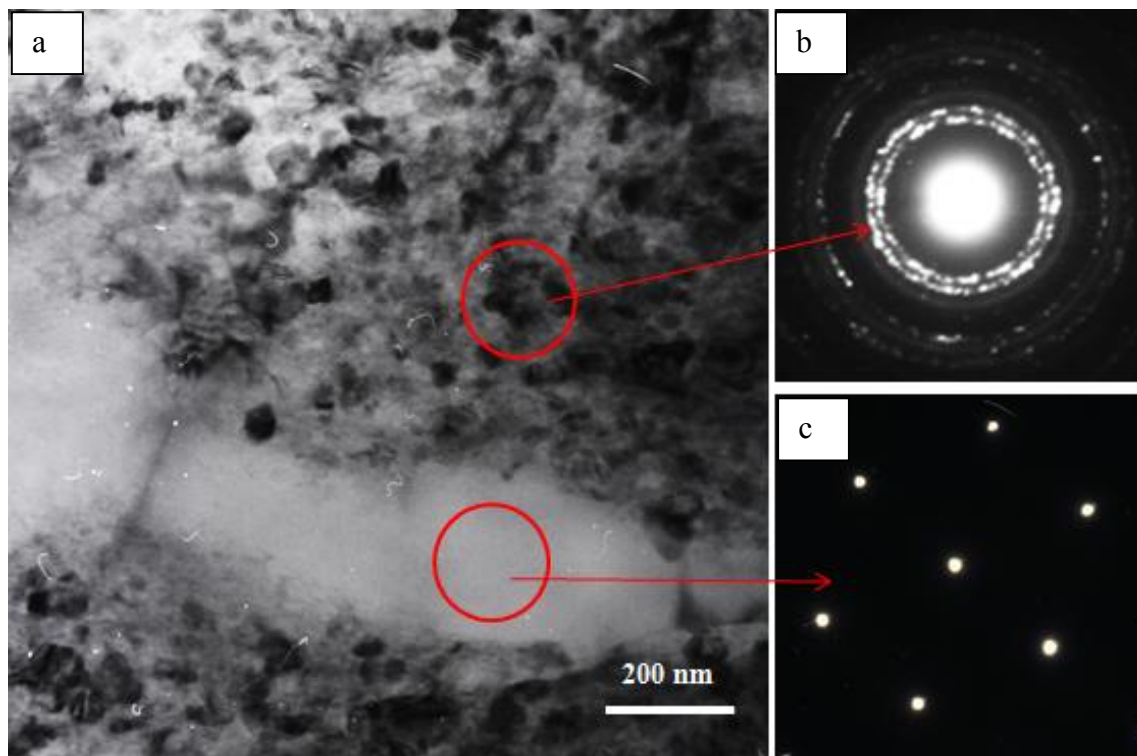
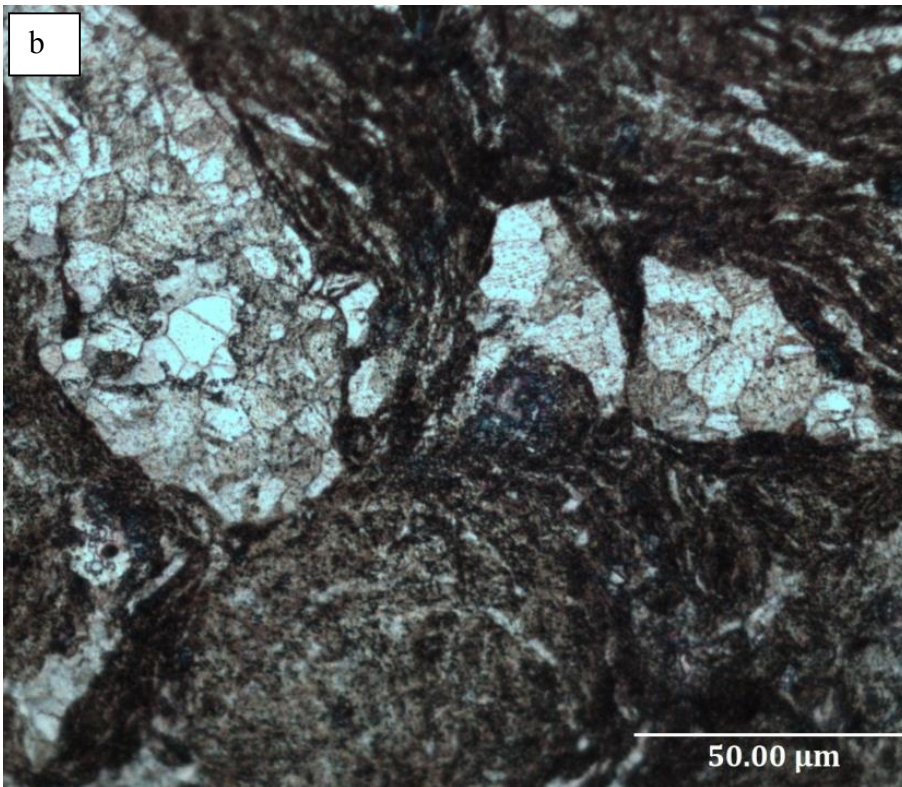
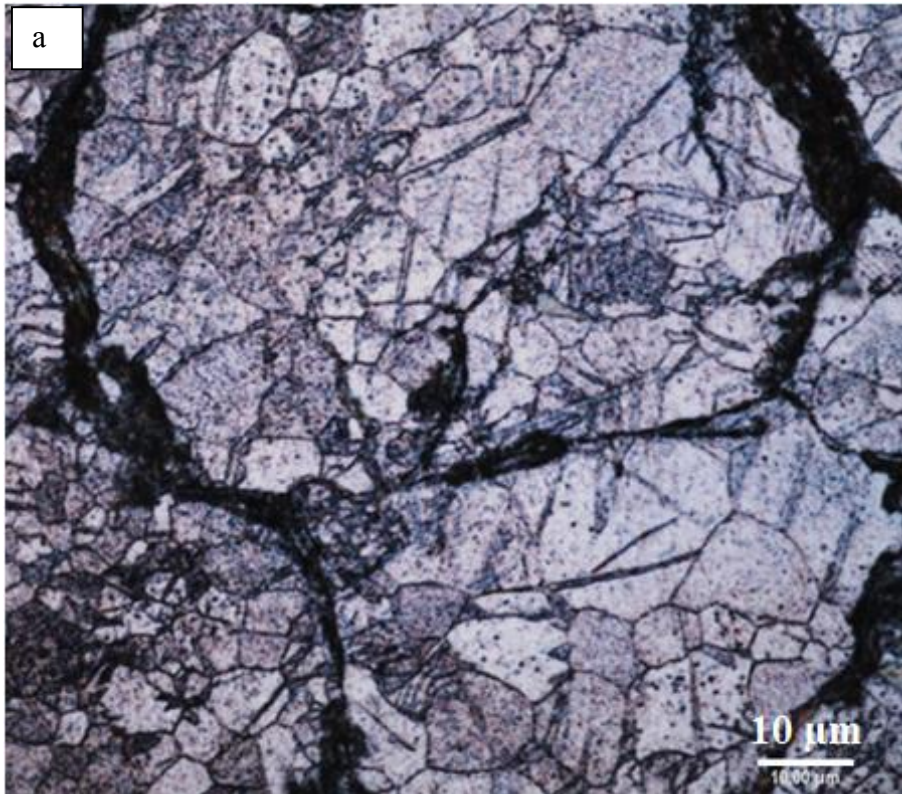
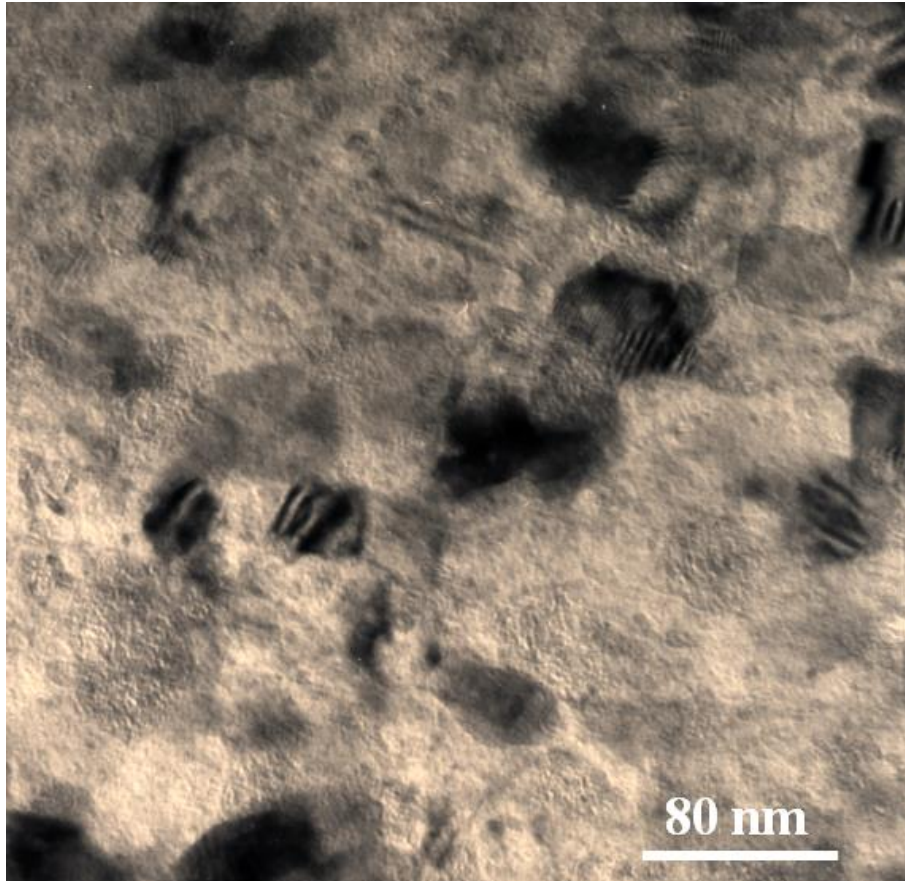


Figure 4.14 TEM images of sample CM400: (a) bright field image, and its correspondent SADP of (b) fine and (c) coarse grain area and (d) grain size distributions before compression tests



**Figure 4.15** Typical OM images of bulk samples (a) AR400 and (b) CM400 after compression tests.



**Figure 4.16** Typical BFTEM image of nano grains area in sample CM400

Figures 4.17-4.19 show true compressive stress-strain curves of samples CM350, CM425 and CM450. The corresponding compressive properties are listed in Table 4.2. For CM350, although it had the highest micro hardness among all the bulk samples (see Fig. 4.10), it had the lowest strength as well as compressive strain. The main reason for this is its porous microstructure and poor density, which caused early failure. Compared to CM400 (see Fig.4.12), the compressive strain of samples CM425 and CM450 sintered at higher temperatures was enhanced owing to the improved density and enhanced inter-particle bonding. However, the loss in both yield and ultimate strength was prominent, as shown in figures 4.17 and 4.18. Related published papers reported that an increase in ductility with a concomitant decrease in strength can result from grain growth at higher temperatures [129,216]. However,

it should be noted that the compressive properties of CM450 were better than that of CM425. For instance, samples CM450 showed an average true ultimate compressive strength and 0.2% proof stress of 483.1 and 372.7 MPa with an average compressive strain of 0.054; whereas sample CM425 only displayed the average true ultimate compressive strength and 0.2% proof stress of 472.1 and 357.9 MPa with an average compressive strain of 0.048. The improved compressive strain can be explained by the higher density and enhanced inter-particle bonding, which can also minimize the early failure. Based on the results of micro hardness (see Fig.4.10), one possible reason of the increase in strength is that the grain size had not increased significantly from sintering temperature 425 to 450 °C. To confirm this, TEM was employed to evaluate the grain size distributions of all three samples here.

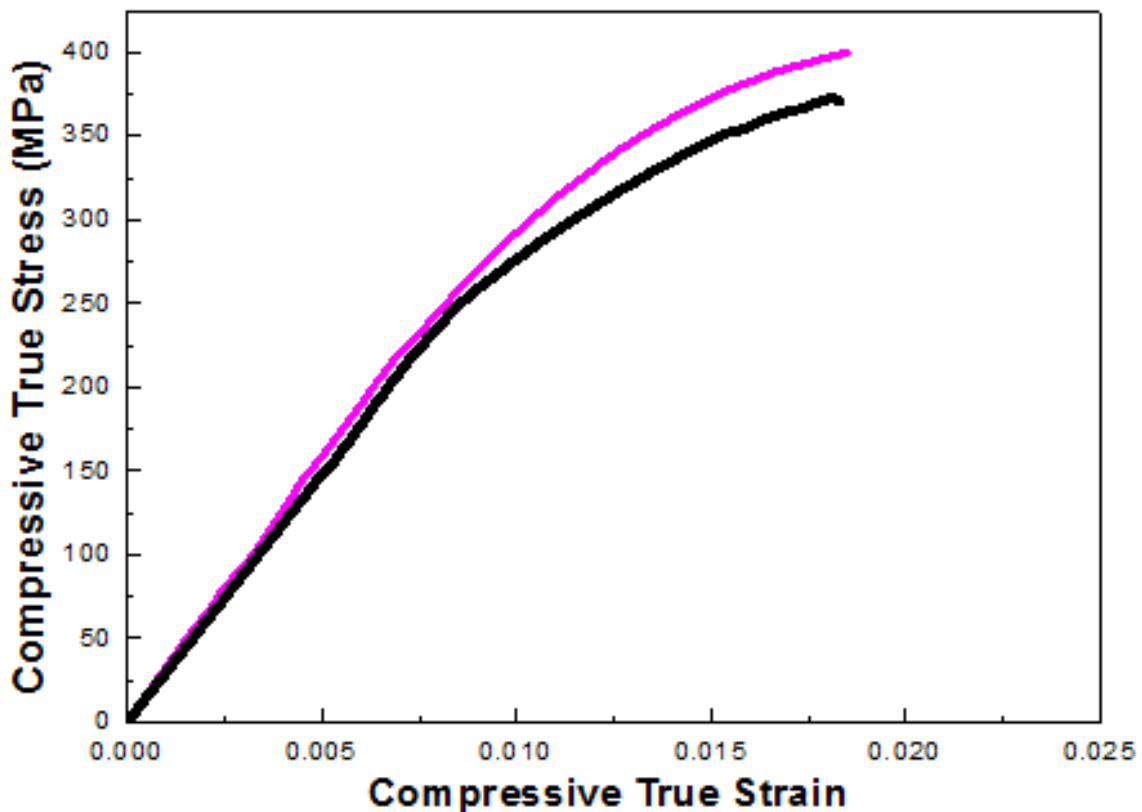


Figure 4.17 Room temperature true stress-strain curves of bulk samples CM350

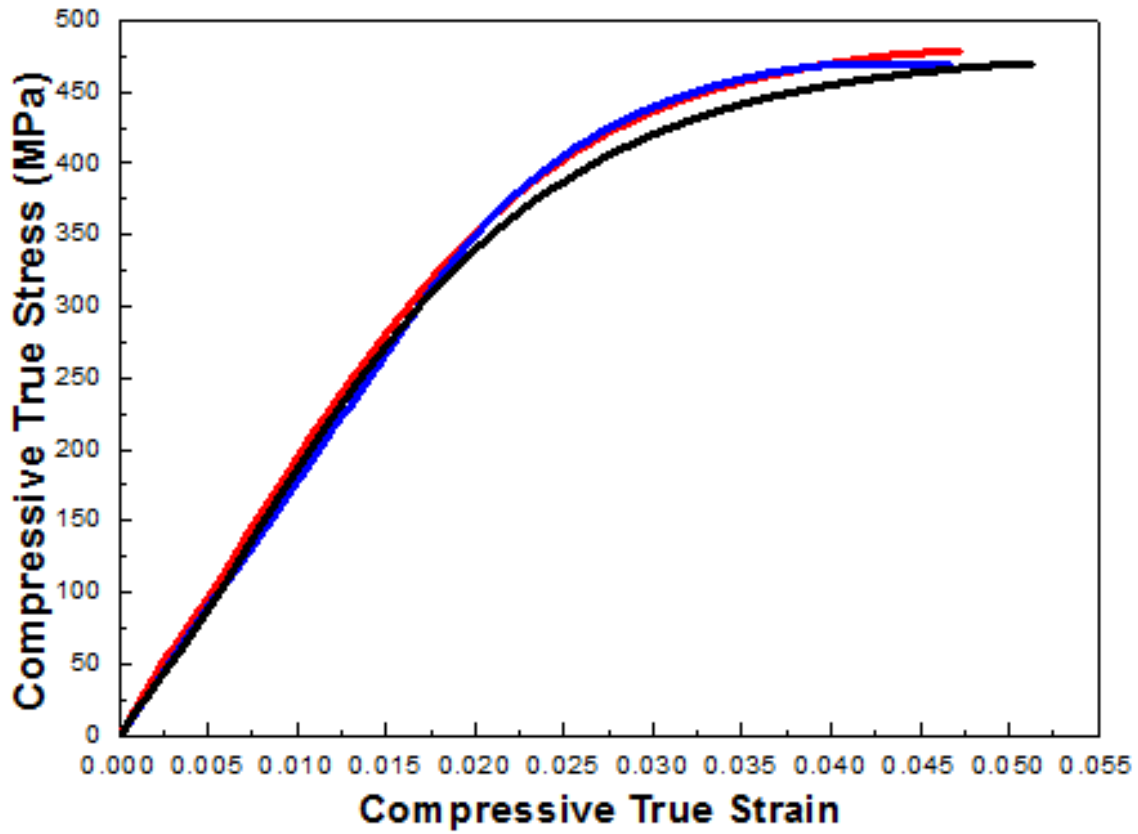


Figure 4.18 Room temperature true stress-strain curves of bulk samples CM425

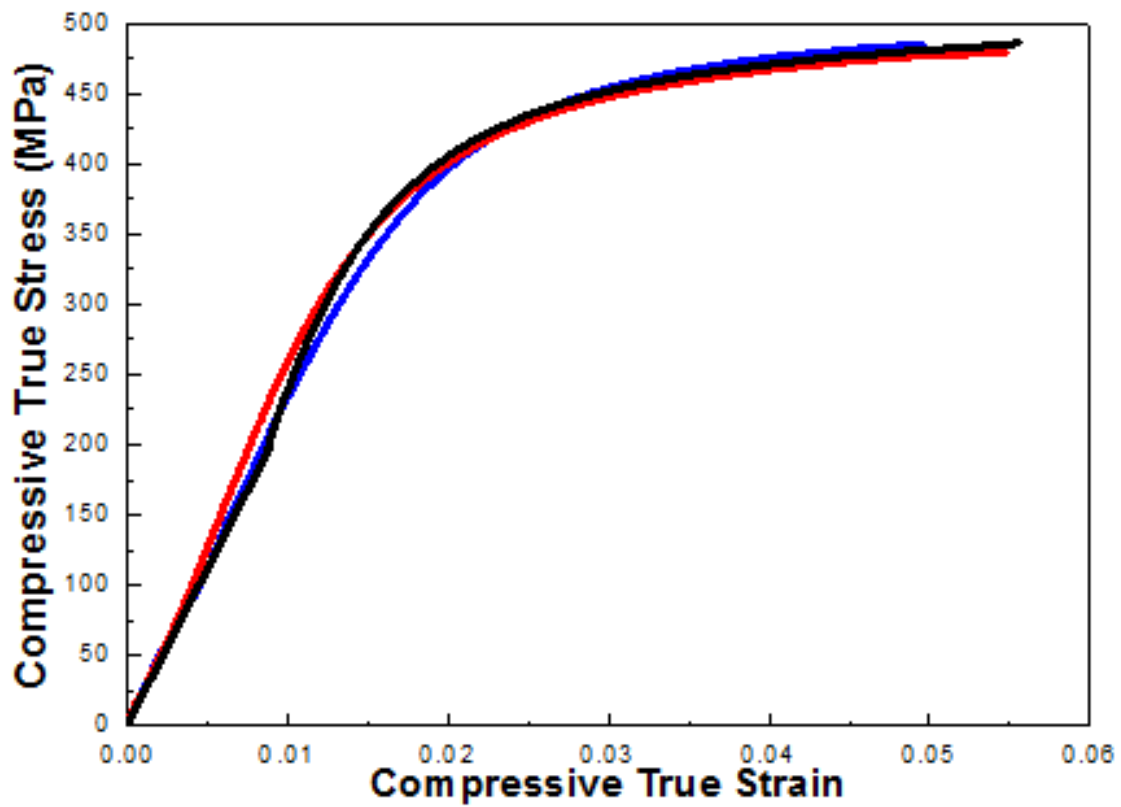


Figure 4.19 Room temperature true stress-strain curves of bulk samples CM450

**Table 4.3** Summary of compressive properties of bulk SPSed samples.

<b>Samples</b>	<b>No</b>	<b>0.2% Proof Stress (MPa)</b>	<b>True Ultimate Strength (MPa)</b>	<b>True strain at ultimate strength</b>
<b>CM350</b>	1	345.2	399.8	0.019
	2	331.3	372.7	0.018
<b>CM425</b>	1	350.4	468.4	0.047
	2	375.2	478.6	0.047
	3	348.2	469.2	0.051
<b>CM450</b>	1	362.3	486.2	0.056
	2	394.7	478.5	0.055
	3	361.2	484.5	0.050

Figures 4.20-4.22 presents BF TEM images of nano grains areas and corresponding SADPs. The histograms of grain size distribution are also given in these three figures. After measurement, the average grain size of sample CM350 was approximately 33 nm, which was slightly smaller than that of sample CM400 (35 nm). However, when the sintering temperature rose to 425 °C, grains grew rapidly to around 59 nm. As the temperature was further increased to 450 °C, the response of grains growth was very weak and the average grain size of CM450 was statistically the same at 60 nm. Therefore, the grain growth in samples sintered from 425 °C to 450 °C can be ignored. It can be confirmed again that the sintering temperature 400 °C was a transition point. Below this temperature, the grain growth during short sintering was limited; but beyond this point, grain growth became prominent even in 3 minutes dwell time. These results agreed fairly well with the micro hardness results and mechanical behavior of CM350, CM400, CM425 and CM450. Overall, CM400 exhibited a balance of compressive strength and

strain. Therefore, this sample will be used as a reference sample in next chapter to design strategies to improve ductility of bulk nanostructured AZ31 with high strength.

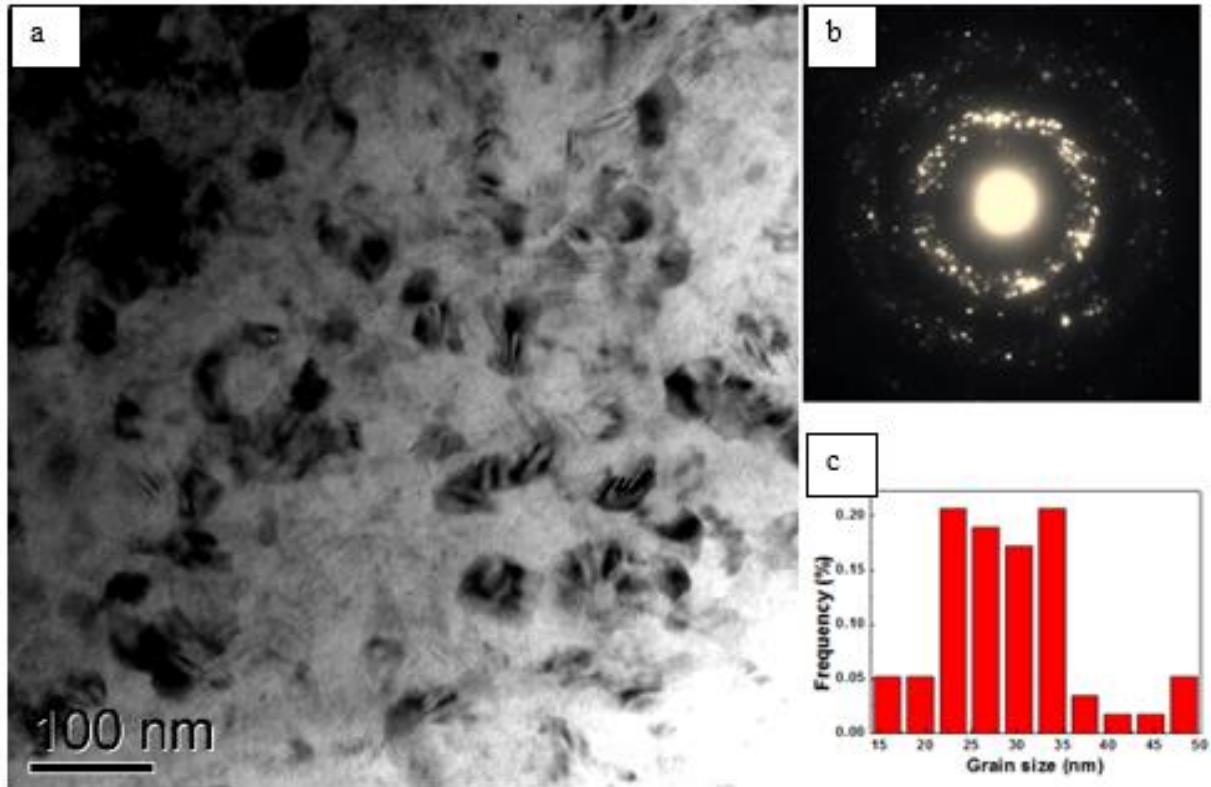


**Figure 4.20** TEM images of sample CM350: (a) bright field image, (b) its correspondent SADP and (c) grain size distributions before compression tests

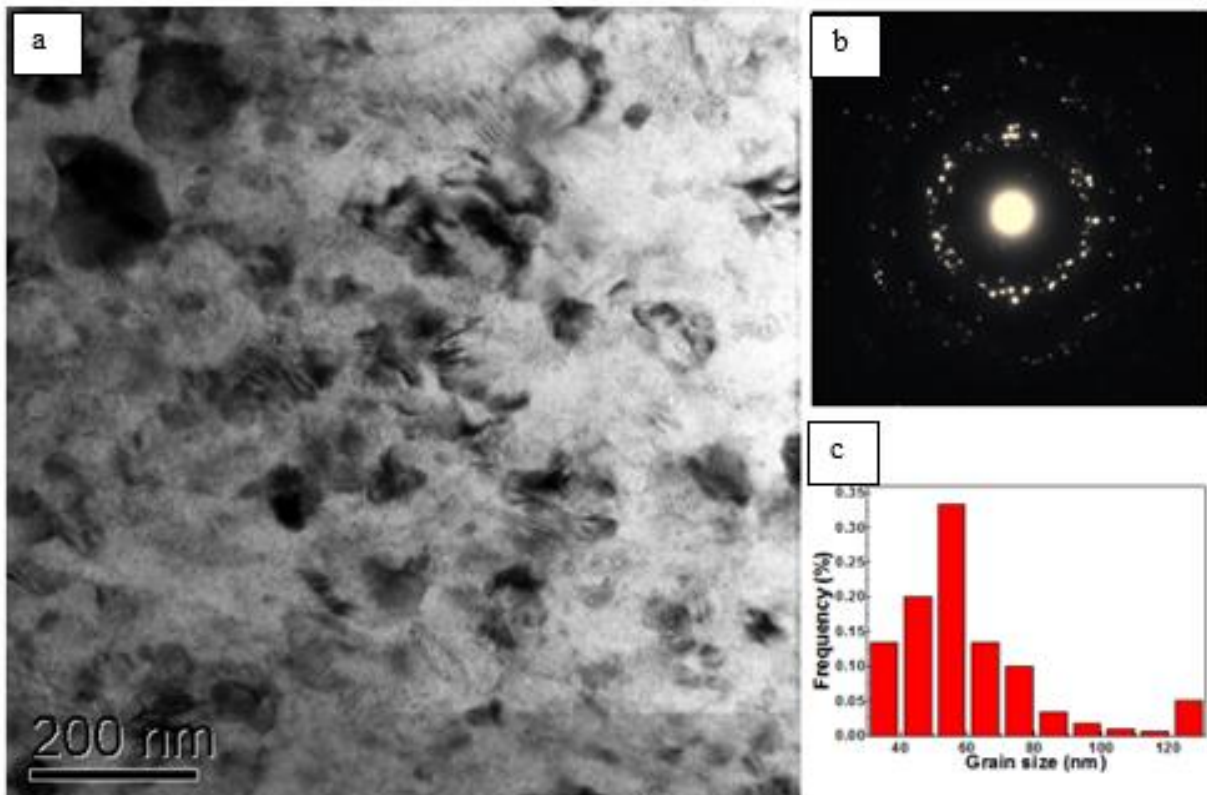


**Figure 4.21** TEM images of sample CM425: (a) bright field image, (b) its correspondent SADP and (c) grain size distributions before compression tests

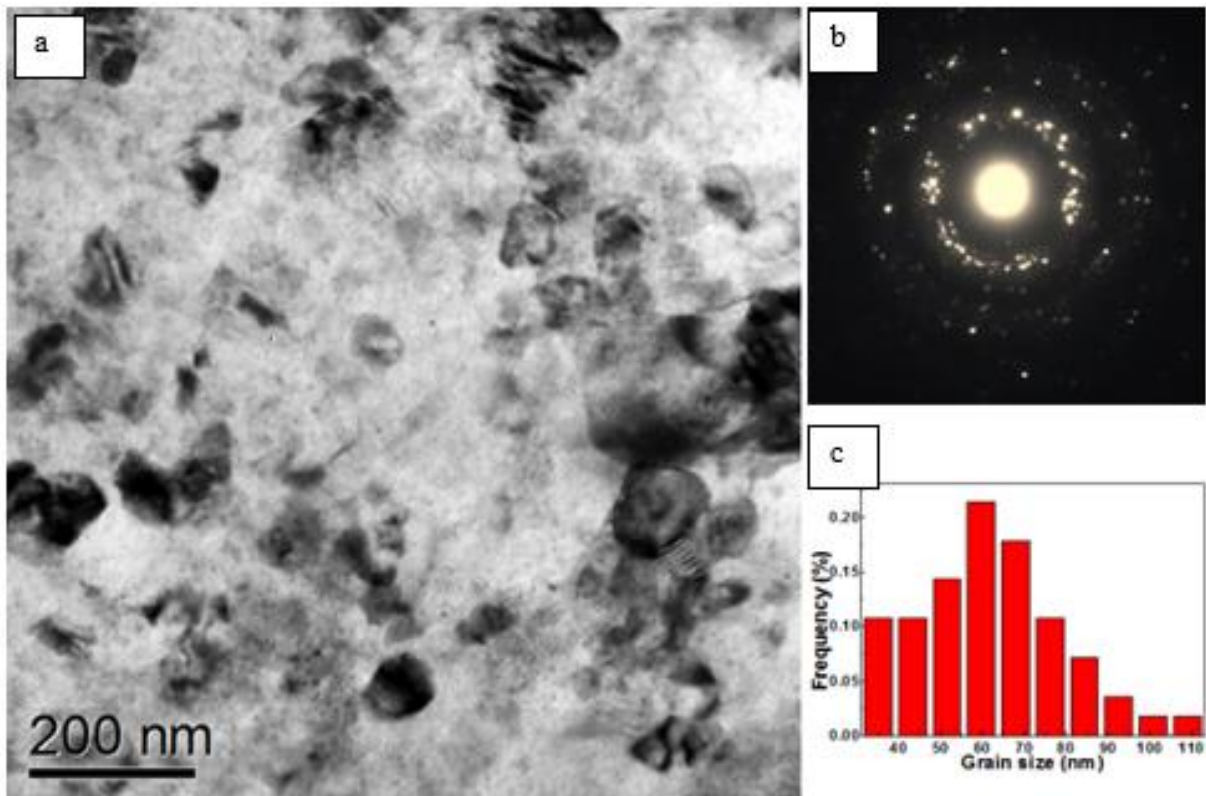


**Figure 4.22** TEM images of sample CM450: (a) bright field image, (b) its correspondent SADP and (c) grain size distributions before compression tests

## 4.4 Conclusions

In summary, a nanocrystalline AZ31 alloy with exceptionally high strength can be fabricated by the combination of cryomilling and SPS. All the bulk samples consolidated from cryomilled powders exhibited a bimodal microstructure. Sample CM400 showed the highest yield strength of 408.7 MPa and ultimate strength of 504.0 MPa with acceptable compressive strain of 0.036. The mean grain size of the material cryomilled for 6h followed by spark plasma sintering consolidation was about 35 nm. The high strength of sample was generally ascribed to the grain refinement strengthening, oxide dispersion and solid solution strengthening. The low compressive strain of this alloy is due to limited work hardening, rare twinning behavior and pores located between particle boundaries.

With regard to the effect of sintering temperature, the density increased with increase in sintering temperature. More specifically, the density was improved significantly from 350 to 400 °C while it was slightly enhanced from 425 to 450 °C. Higher sintering temperature (425-450 °C) improved compressive strain at the sacrifice of strength. In contrast, samples consolidated at 350 °C displayed brittle behaviour with low strength. Generally, bulk NS materials usually have high strength but poor ductility. For example, true compressive strains were all less than 0.06 at true ultimate compressive strength in this study.

Based on the results of micro hardness and grain size distributions, it can be concluded that sintering temperature 400 °C is a transition point. Below this temperature, the grain growth and decrease of hardness during short sintering was limited; but at higher temperature, grain growth and drop of hardness became prominent, even for a 3 minute dwell time. However, the changes between samples sintered at 425 and 450 °C can be ignored. This is the reason that sample CM450 with higher density owned good compressive behavior compared to CM425, although it was sintered at higher temperature.

# **5 A facile strategy to improve compressive strain of bulk nanostructured Mg alloy without loss of strength**

Abstract:

Different amounts of eutectic Mg-Zn alloy powder with a low melting temperature approximately 350 °C were mixed with the cryomilled powder. During SPS at 400 °C, *in situ* powder casting occurred. The low melting temperature eutectic alloy particles melted, flowed around the cryomilled powder particle boundaries and partly dissolved into Mg matrix. The compressive strain of bulk nanostructured (NS) Mg AZ31 alloy was improved by *in situ* powder casting during SPS without loss of strength, especially when 20 % (wt. %) of eutectic alloy powder was added. Compared to samples sintered by pure cryomilled powder, its compressive strain was extended from 3.6% to 6.6%. The reason for this is that this facile process can simultaneously significantly remove the artifacts such as porosity and cracks, enhance the inter-particle bounding between nanostructured Mg particles and introduce very small dense precipitates into bulk NS Mg alloy. Therefore, we were able to improve the ductility of bulk NS Mg alloy without loss of strength.

## **5.1 Introduction**

Strength and ductility are often commonly used to evaluate mechanical properties of metals and alloys. Generally, strength and ductility are normally mutual exclusive in bulk NS metals and alloys [48-50,53,133,172]. Bulk NS materials, with structural features less than 100 nm in at least one dimension [52], can be obtained by either a “one-step” method such as severe

plastic deformation [46], or a “two-step” approach such as powder consolidation [81,83]. The former strategy can produce defect-free bulk NS material with greater ductility than these fabricated by the latter method. Nonetheless, these NS materials with exceptionally high strength usually exhibit poorly low ductility [53]. Recently, several strategies have reported to improve the ductility of bulk UFG and NS materials [175,217]. Introducing a bimodal or multi-grain size distribution [49,179], pre-existing nanoscale twins [55,218], and engineering nanoscale precipitates into matrix [133,219] have widely studied and reported. Nevertheless, most of these strategies either sacrificed some of the strength of the bulk UFG or NS materials or were only used in the “one-step” approach.

The most frustrating issue for bulk NS materials fabricated by the “two-step” approach is those materials often have artifacts such as porosity and cracks, which plays a detrimental role in causing very low ductility (defined as less than 5% elongation to failure)[53]. Because the nanocrystalline powders studied are typically stiff, it is extremely difficult to consolidate nanostructured particles into fully dense samples with complete inter-particle bonding [79]. To soften the nanostructured particles, high processing temperatures have to be employed, which can assist plastic deformation and allow better filling. In addition, material flow by high temperature diffusion is beneficial for eliminating the residual porosity [79]. However, high temperature diffusion also leads to grain coarsening, especially for nanostructured particles [79,220]. Considerable internal energy was stored during powder preparation such as milling, and will be released easily at elevated temperatures, which makes nanoscale grains grow rapidly. Using super high pressures is another option to further compact nanostructured particles, but the mold or die for consolidation usually bears the risk of cracking during consolidation. In a recent study, Koch and co-workers have designed a novel approach and produced full dense bulk NS Cu sphere by *in situ* consolidation [221], which involves the combination of liquid nitrogen and room temperature milling. The bulk NS Cu showed a

uniform tensile elongation of 14% and high yield strength of 790 MPa, but its small scale limits its wide application to some extent.

Despite these impressive and promising results, most the intrinsic nature of the processing limits the material properties. In addition, most of those strategies are applied to bulk NS Cu, Ni, Al, Zn and their alloys, but rarely to Mg and its alloys. The low ductility due to hcp crystal structure [2], not helped by the inhibition of twinning in the nano grain structure [222,223] and its inherent reactive nature severely limits the application of these Mg alloys. In contrast, its low density with a high specific stiffness and strength makes it an outstanding candidate for weight critical structural applications [4].

The aims of this chapter were twofold: Firstly, to develop a novel process for improving the ductility of bulk NS Mg alloy without loss of high strength. Secondly, to investigate the mechanism of enhanced ductility in bulk NS Mg alloy. Very recently, bulk NS AZ80 and Mg-10Al alloys have been successfully fabricated by a combination of cryomilling and spark plasma sintering (SPS) [100,165]. Both NS AZ80 and Mg-10Al exhibited an exceptionally high compressive strength, but the corresponding average compressive strains were only 3.7% and 2.3%. This poor ductility could be ascribed to the internal defect and insufficient inter-particle bonding inside the bulk samples after sintering, since the highest sintering temperature was only 360 °C. The reason why higher sintering temperatures were not adopted in these two papers is that grain coarsen will occur resulting in a loss of strength. To solve this issue, the challenge now is it possible to find a novel process to bypass the dilemmas inherent to the consolidation?

In this chapter we design *in situ* powder casting during SPS with a dwell temperature of 400 °C, by fully mixing various amounts of low melting temperature eutectic Mg-Zn alloy powder with nanostructured Mg particles. Figure 5.1 shows the schematic process. This process can enhance the ductility of bulk NS Mg alloy without loss of strength. Furthermore, our

strategy is also applicable to improve the ductility of other bulk NS metals and alloys produced by “two-step” approach.

## **5.2 Experimental**

The experimental details of cryomilling, SPS consolidation, mechanical test and microstructure characterization have been described in previous chapters and will not be repeated here.

### **5.2.1 Mg-Zn eutectic alloy powder preparation**

9.7 g pure Mg (99.99%) and 10.3 g Zinc (99.99%) ingots were used to produce a eutectic alloy with a composition of Mg<sub>48.7</sub>Zn<sub>51.3</sub> wt. % (Mg<sub>51.04</sub>Zn<sub>19.8</sub> at. %) by using small scale melting. Figure 5.2 presents the Mg-Zn phase diagram, which indicates that this composition has the lowest melting temperature (around 342 °C). Therefore, it will be fully melted when the sintering temperature is 400 °C. After casting, this brittle eutectic ingot was cryomilled for 5 minutes to obtain fine particles.

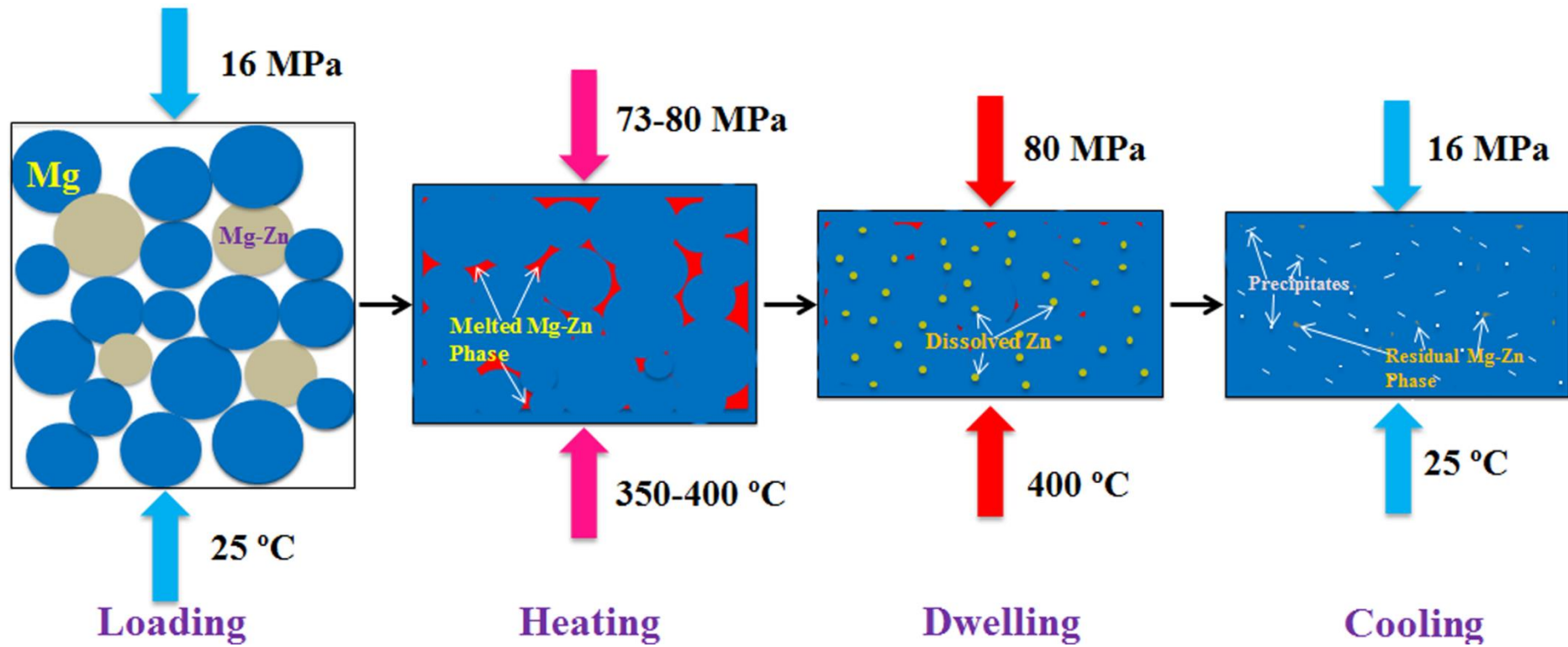
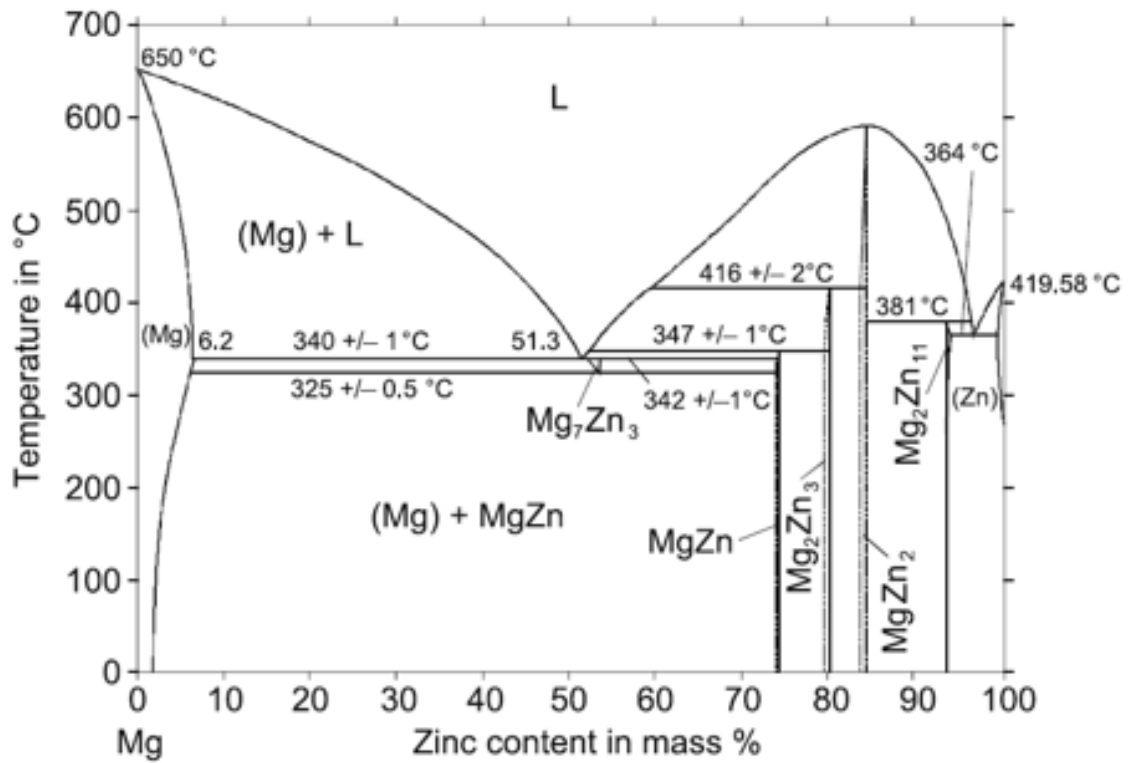


Figure 5.1 Schematics showing the microstructural development due to in situ powder casting during SPS process



**Figure 5.2** Phase diagram of Mg-Zn system [2]. The added Mg-Zn powder was casted with a eutectic composition

### 5.2.2 Thermogravimetric analysis (TGA)

The melting temperature of eutectic alloy powder was measured by using a Pyris 1 TGA Analyzer (PerkinElmer, USA). Approximately 50 mg of eutectic alloy powder was used for analysis. TGA curves were measured from room temperature up to 400 °C in argon with rate of 10K/min.

### **5.2.3 Powders mixing**

0%, 5%, 10% and 20% (wt.%) of eutectic Mg-Zn alloy particles were mixed with cryomilled powder. To achieve a homogeneous mixture, all the selected powders were loaded into grinding jar in glovebox and blended using the cryomiller at room temperature without grinding ball. The grinding jar shakes at frequency of 22 Hz for 1h to fully mix the powders. Afterwards, the prepared powder was consolidated via SPS. Those corresponding samples after sintering were designated as CMEU0 (it is named as CM400 in chapter 4), CMEU5, CMEU10 and CMEU20 hereafter.

### **5.2.4 Scanning electron microscope (SEM)**

Samples were prepared by grinding with SiC paper from 800 to 4000 grit. To minimise oxidation exposure to water, samples were polished with alcohol based diamond suspensions of 1 and 0.25 $\mu$ m. A FEGSEM (FEI Inspect F) was employed to investigate morphology of powders and bulk sintered samples.

## **5.3 Results and discussion**

### **5.3.1 Characterization of eutectic alloy powder**

Figure 5.3 shows a TGA curve from the eutectic alloy powder. An endothermic peak can be seen located at 349.1 °C, indicating its melting temperature is very close to 342 °C. Figure 5.4 shows several long cracks were left on Mg-Zn eutectic ingot after indentation with the loading force of 0.049 N. Figure 5.5 gives the XRD pattern of eutectic alloy powder after 5 minutes cryomilling. It indicated the main phase in this powder is  $Mg_{51.04}Zn_{19.8}$  (at. %) as was designed. Figure 5.6 (a) demonstrates the morphology of this eutectic powder. After calculation, the average particle size after 5 minutes cryomilling was approximately 20  $\mu m$  (Figure 5.6(b)). Figures 5.6(c-d) present elements analyses results collected from areas A and B by electron dispersive spectroscopy (EDS).The results showed the composition from both two particles was very close to the original designing composition of  $Mg_{48.7}Zn_{51.3}$  (wt. %), which agreed fairly well with the results of XRD (Figure 5.5).

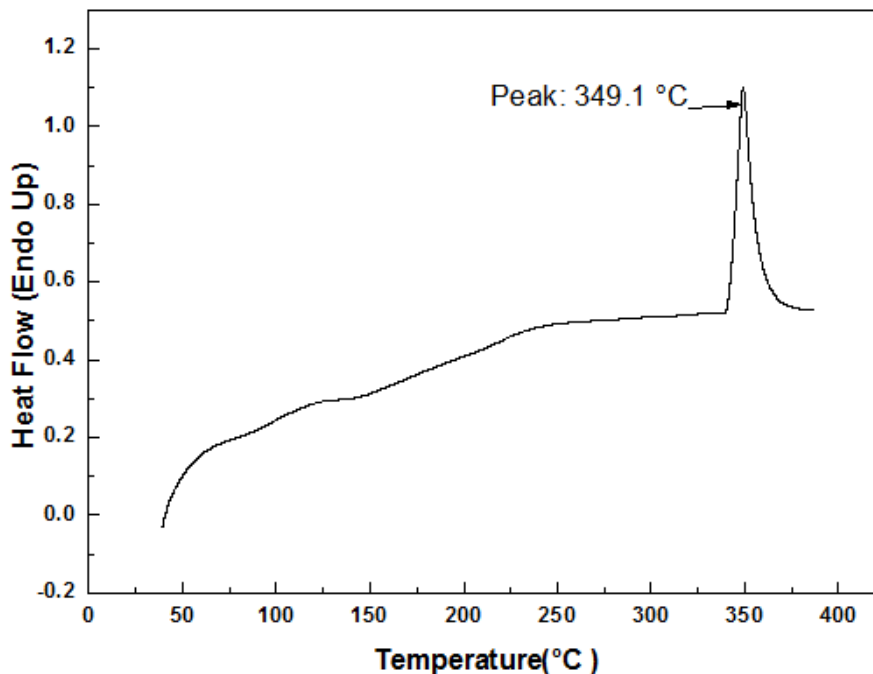


**Figure 5.3** A TGA curve showing the melting temperature of Mg-Zn eutectic alloy powder

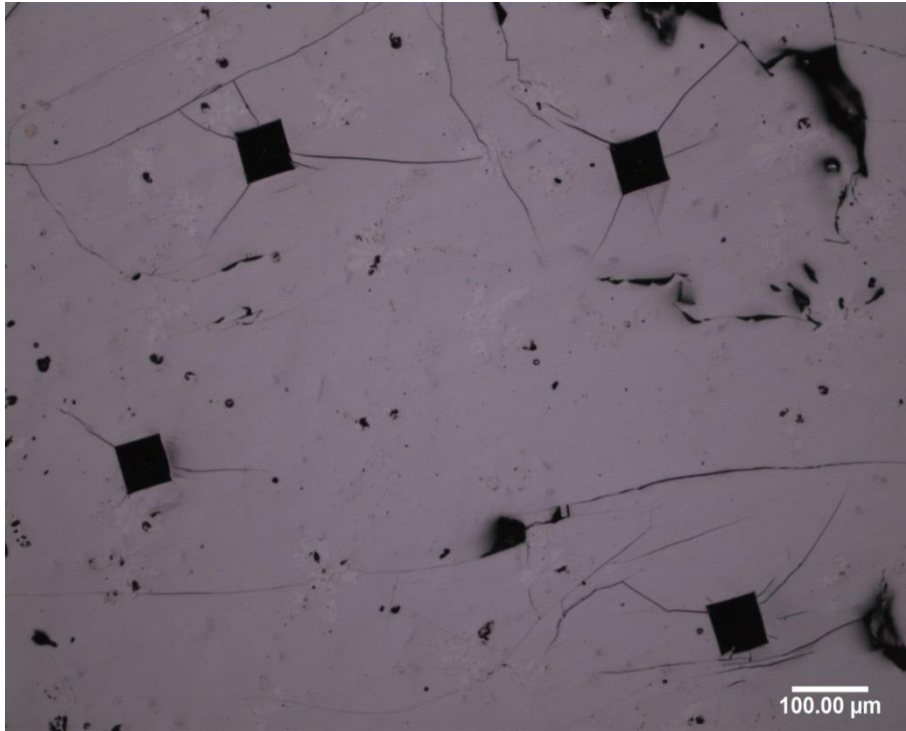


**Figure 5.4** Optical microscope image showing the cracks introduced by indents after micro hardness test

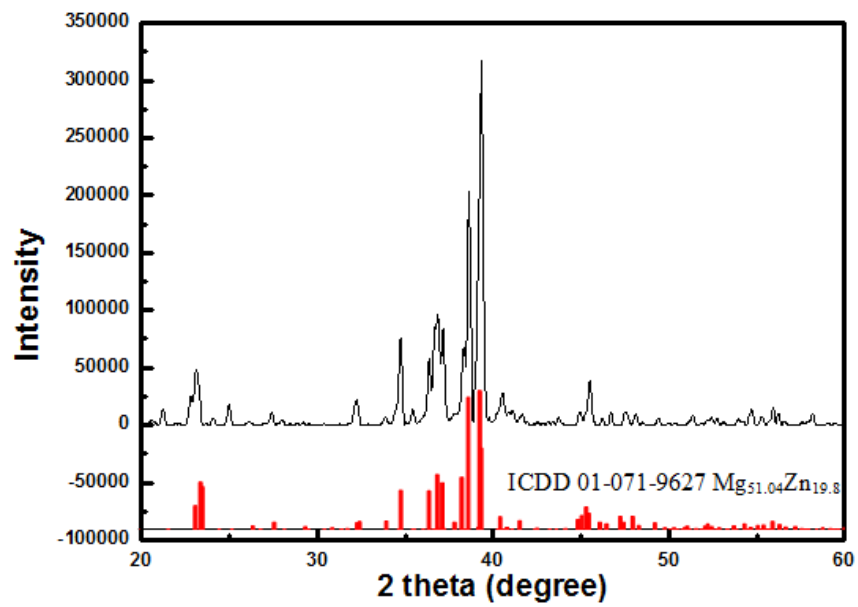


**Figure 5.5** XRD pattern of eutectic Mg-Zn alloy powder

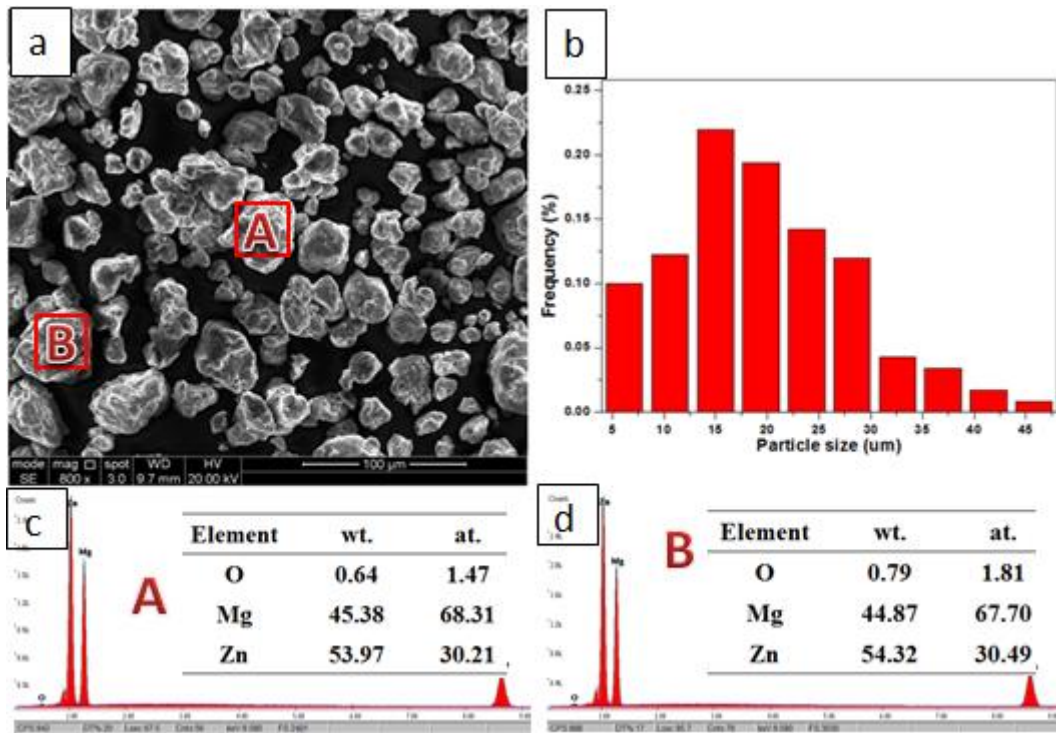
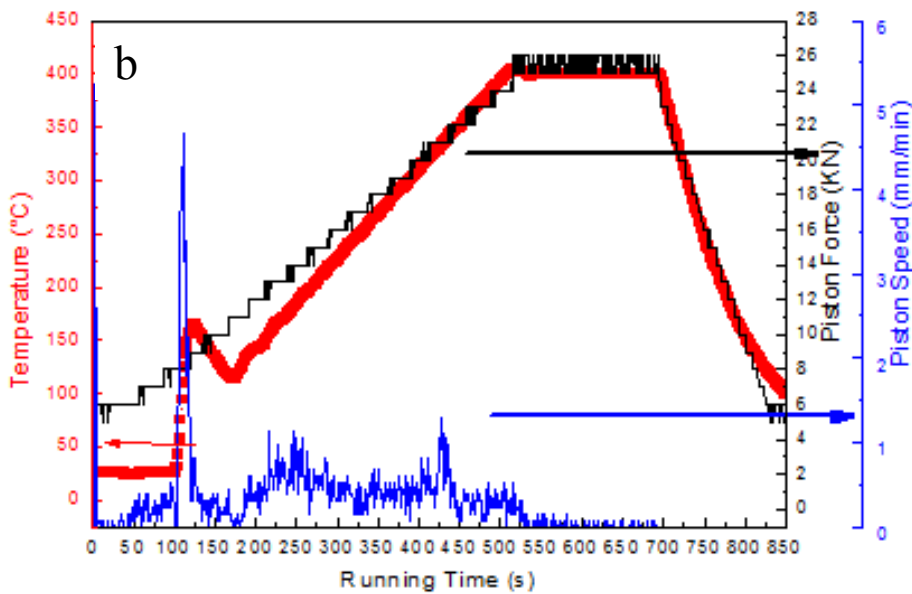
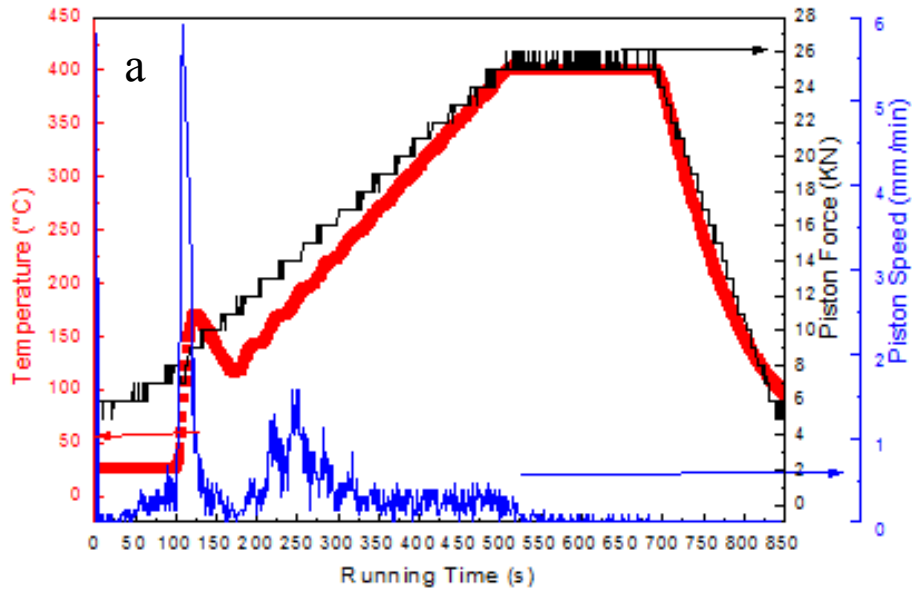


**Figure 5.6** (a) A representative secondary electron SEM image showing the morphology, (b) particle size distribution of Mg-Zn eutectic alloy powder, EDS spectra and quantitative values (inset) from the marked particles (c) A and (d) B.

### 5.3.2 SPS processing curves

Figure 5.7 gives the variation of sintering temperature, piston force and piston speed as a function of running time for different additions of eutectic alloy powder. Compared to sample CMEU5 to CMEU0, a visible rapid piston movement peak appeared when sintering temperature was up to 320-330 °C. It should be noted that the actual temperature in the centre of the SPS die was about 330-350 °C, since the thermal couple which monitors and controls temperature locates in the wall of SPS die. Many experiments suggest the temperature difference between the centre and surface of the SPS die is approximately 10-20 °C in our study. In addition, current density is higher between particles contacting areas due to smaller cross-

sectional areas, which can cause transient higher temperature in local areas [212]. For samples CMEU10 and CMEU20, this peak became more significant when the weight fraction of eutectic alloy was more than 10%. It can be concluded that the appearance of this extra peak can be attributed to the melt of eutectic alloy powder during sintering.



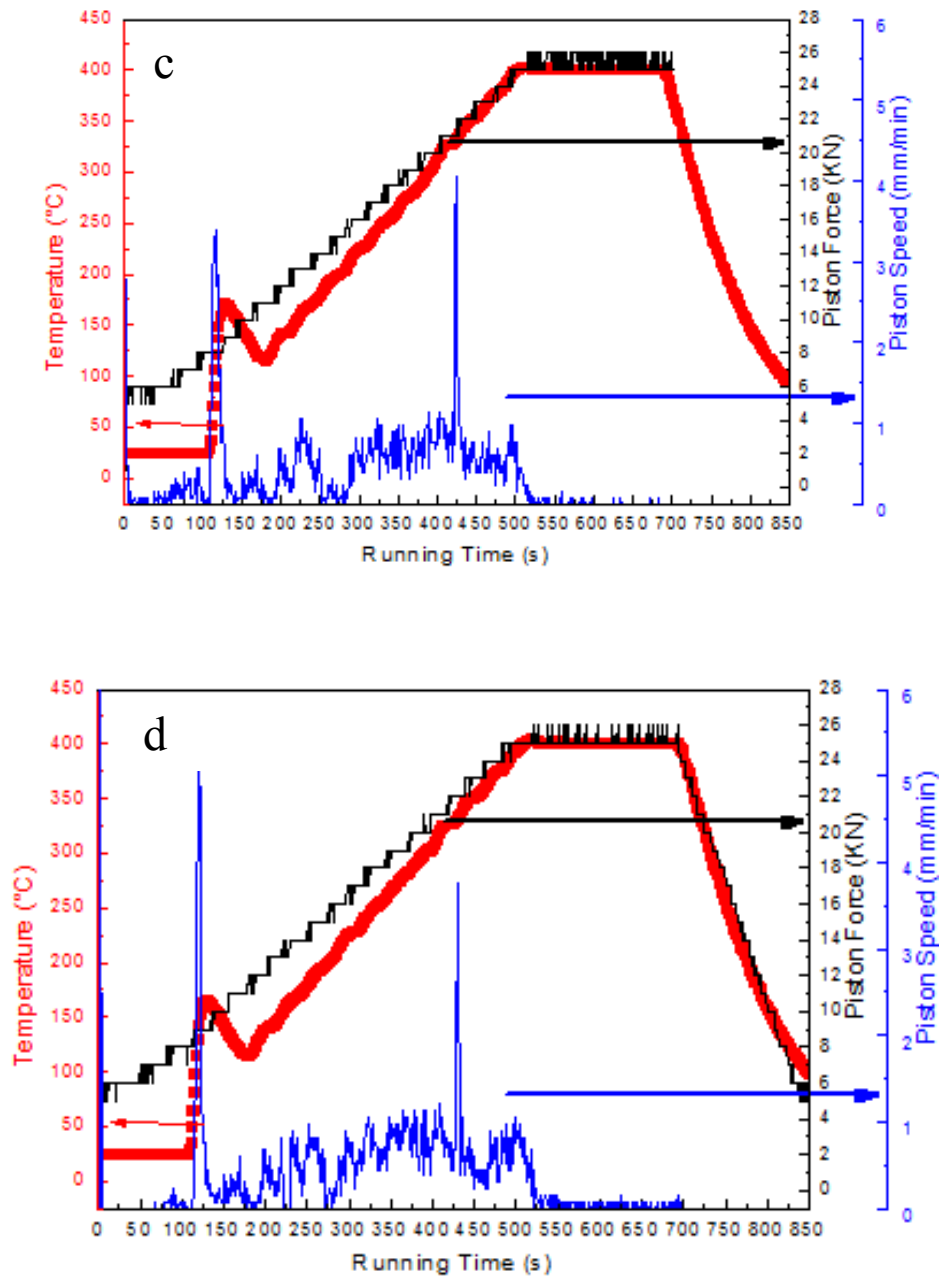
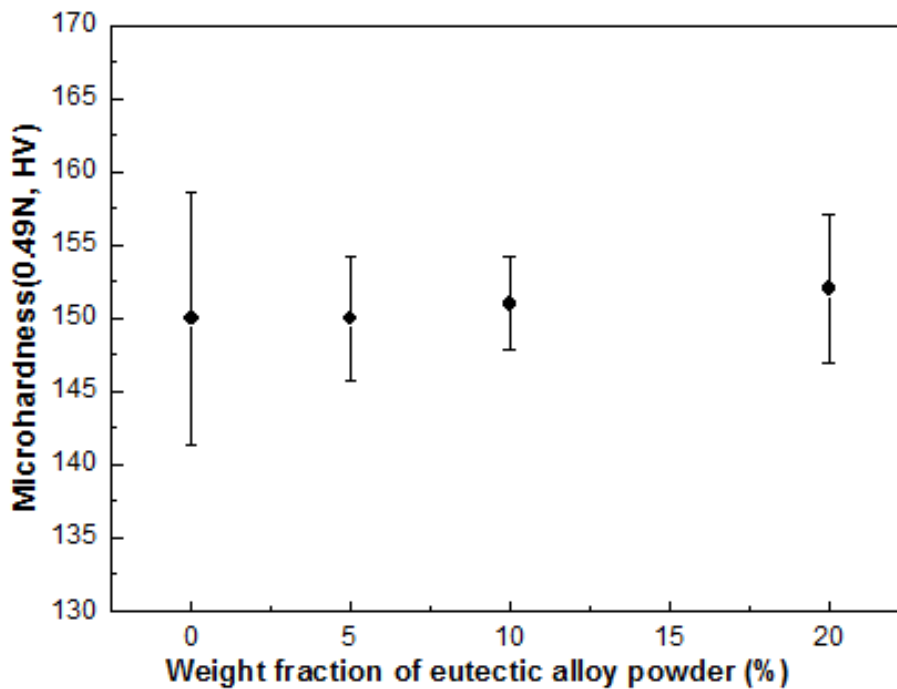


**Figure 5.7** The sintering temperature, piston force, and piston speed as functions of time of bulk samples a) CMEU0, b) CMEU5, c) CMEU10 and d) CMEU20.

### 5.3.3 Mechanical behavior of bulk SPSed samples

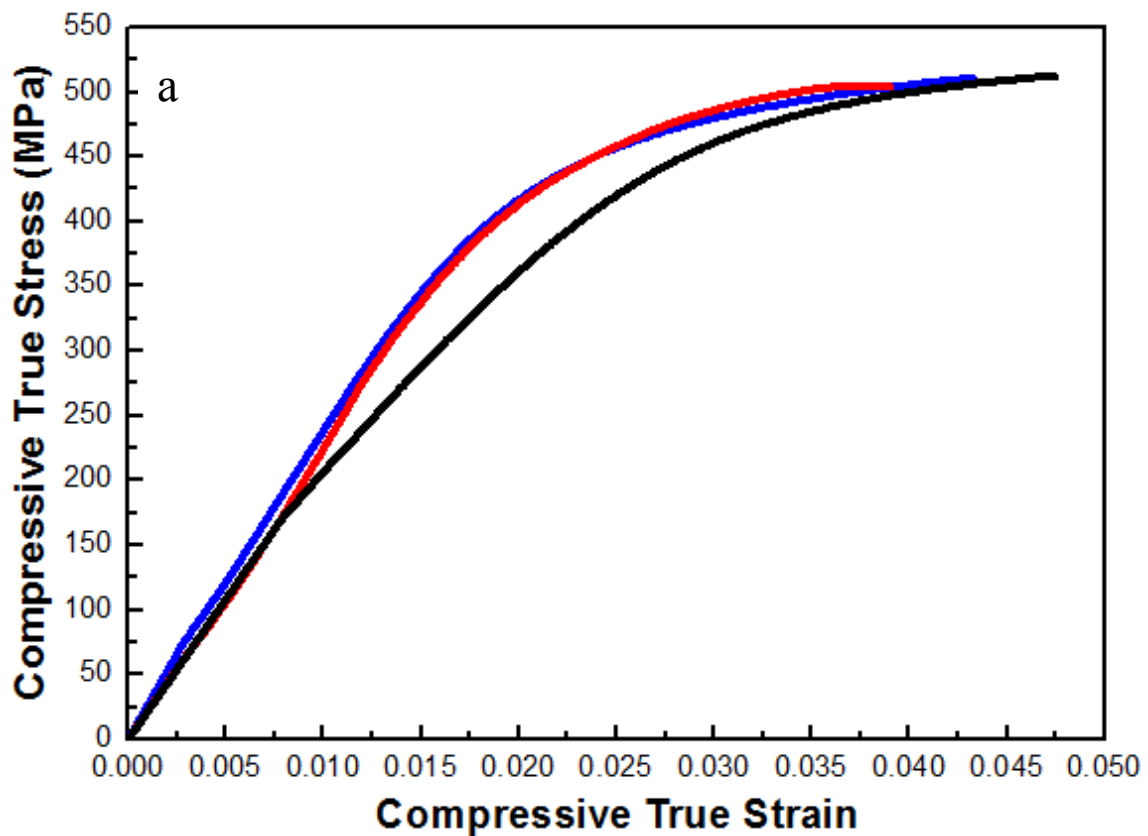
Figure 5.7 shows the micro hardness results of CMEU5, CMEU10, CMEU20 as well as reference sample CMEU0. All the results were collected from indents located on nano grains areas to minimize the error introduced by soft unprocessed particles during cryomilling. Figure 5.8 presents the hardness only slightly increased after adding the eutectic alloy powder.

Figure 5.9 presents the true compressive stress-strain curves of CMEU5, CMEU10, CMEU20 as well as CMEU0 for comparison. The corresponding compressive properties are shown in Table 5.1. The average 0.2% yield compressive strength of CMEU5, CMEU10 and CMEU20 samples were 403 MPa, 404 MPa and 408 MPa, all of which were slightly less than that of CMEU0 mentioned in previous chapter. However, the ultimate compressive strength of CMEU0, CMEU10 and CMEU20 were 509 MPa, 513 MPa and 509 MPa, which was enhanced rather than decreased, compared to sample CMEU0 with strength of 504 MPa.



**Figure 5.8** Micro hardness results of bulk SPSed samples

It is clear that the compressive strain was enhanced after adding Mg-Zn eutectic alloy powder. When the weight fraction of this eutectic alloy powder was only 5%, the mechanical properties were not significantly enhanced. For example, the average compressive strain was only 4.3%. Conversely, when the weight fraction of eutectic alloy powder exceeded 10%, the true compressive strains at the ultimate compressive strength were significantly improved, especially for sample CMEU20. Its compressive strain was extended to 6.6%, which is beyond the critical ductility (5%) required for various structural applications. Therefore, the *in situ* powder casting by introducing low melting temperature eutectic alloy powder improved the ductility of bulk NS sample by 83% without sacrificing the strength. The enhanced ductility of CMEU20sample was attributed to improved strain hardening.



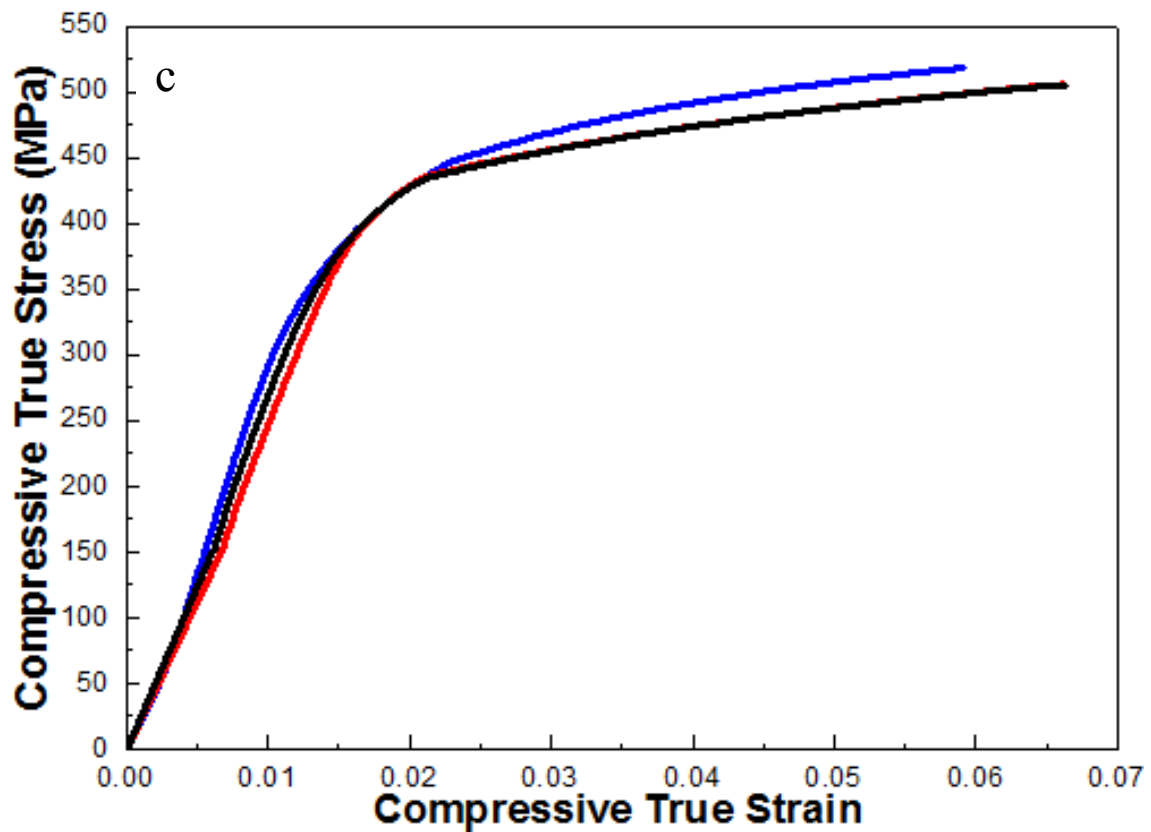
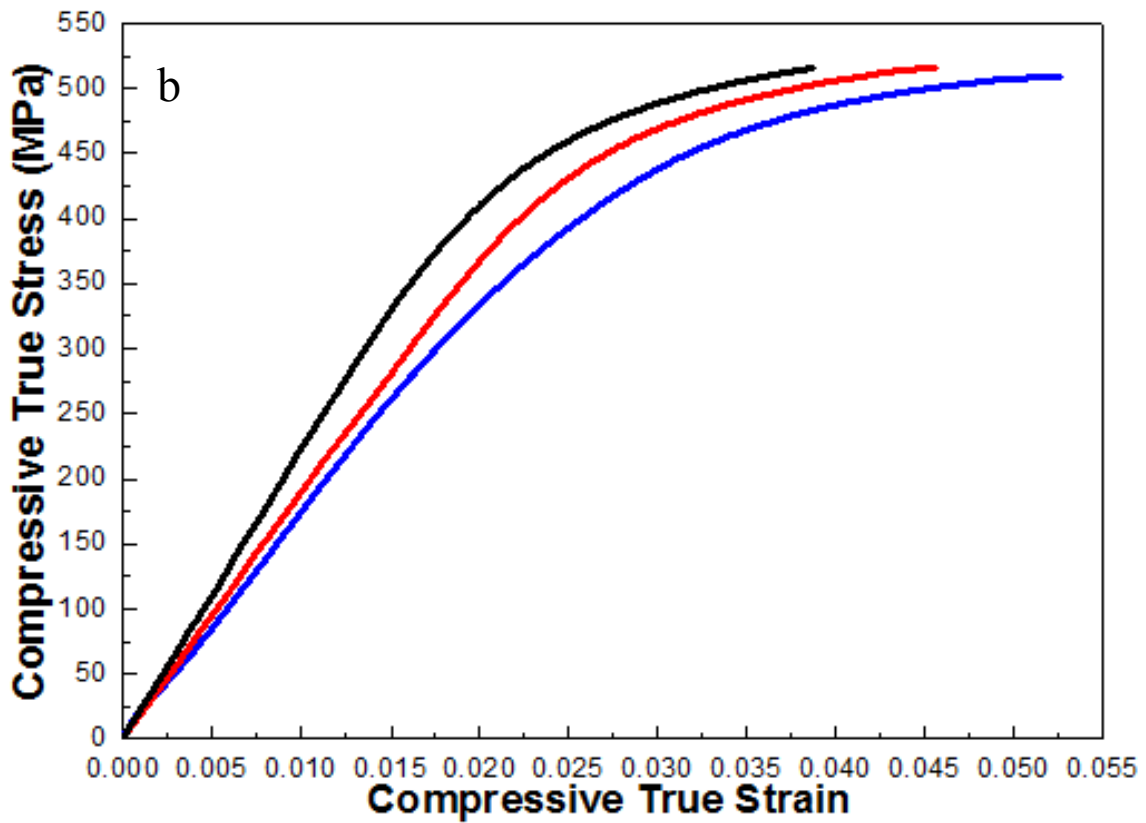


**Figure 5.9** Room temperature true stress-strain curves of bulk samples (a) CMEU5, (b) CMEU10 and (c) CMEU20

Figure 5.10 summarizes the ultimate compressive strength versus strain. The compression test data was collected from published papers related to bulk NS Mg alloys produced by “two step” approach as well as the present results. Most of the published results and present results from CMEU0 and CMEU20 samples were positioned in the red and yellow ovals, showing an inverse relationship between the strength and ductility. In contrast, the result from CMEU20 sample was located in green oval area, indicating a good combination of high strength with improved ductility in the field of bulk NS Mg alloys.

**Table 5.1** Summary of compressive properties of bulk SPSed samples

Samples	No.	0.2% Proof Stress (MPa)	True Ultimate Strength (MPa)	True strain at ultimate strength
CMEU0	1	424.8	512.6	0.035
	2	401.2	500.2	0.036
	3	400.2	499.2	0.036
CMEU5	1	400.0	512.7	0.047
	2	397.5	504.4	0.039
	3	412.6	510.2	0.043
CMEU10	1	420.3	515.2	0.039
	2	372.1	508.7	0.053
	3	419.4	516.4	0.046
CMEU20	1	412.2	517.7	0.059
	2	408.6	505.5	0.066
	3	404.7	504.6	0.066

### 5.3.4 Morphologies of bulk SPSed samples

The mechanical behavior has a strong relationship with the microstructure. In chapter 4, optical microscopy was employed to investigate the internal pore distribution of the bulk SPSed samples sinter at various temperatures. It becomes difficult to still use this method to track the distribution of Mg-Zn phases. Therefore, we used SEM to characterize these bulk SPSed samples with the additions of eutectic alloy powder.

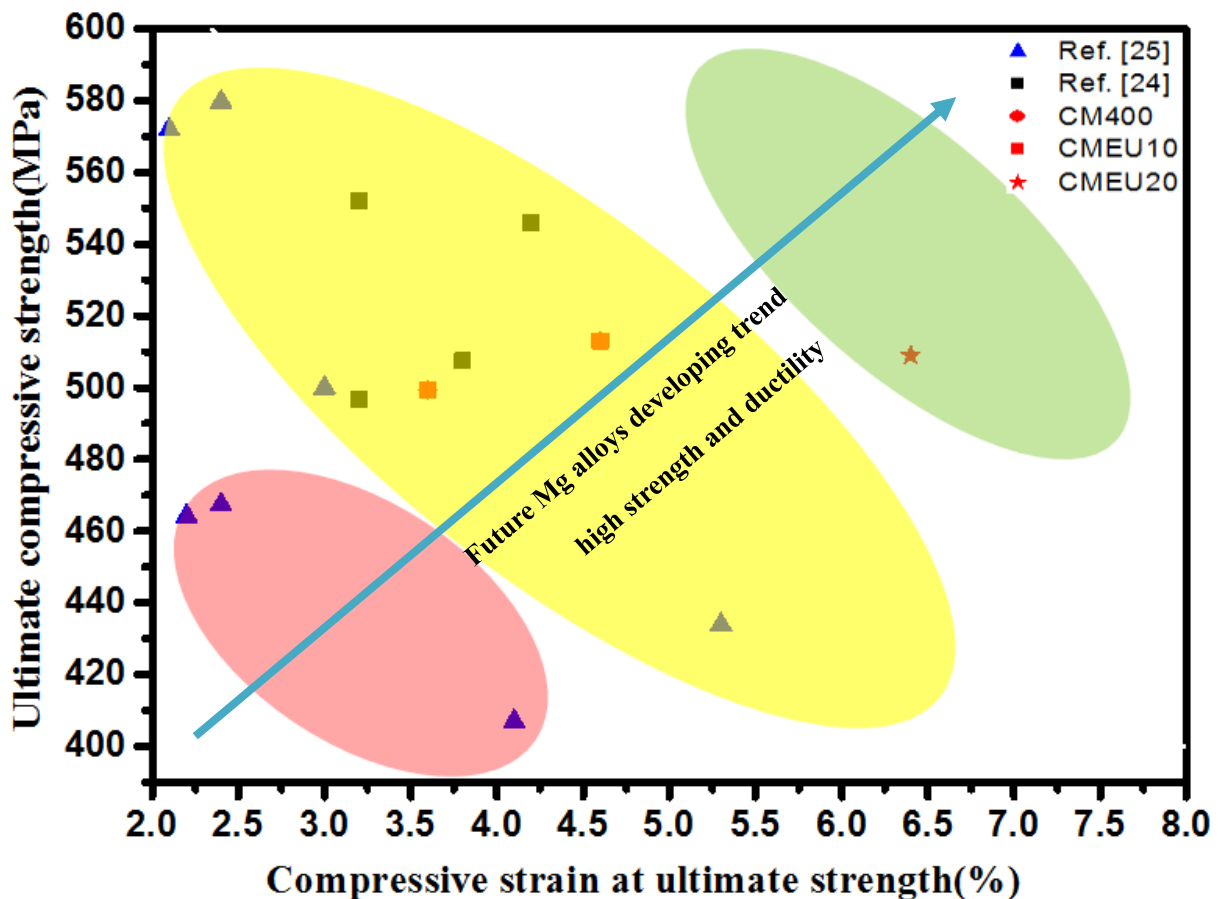
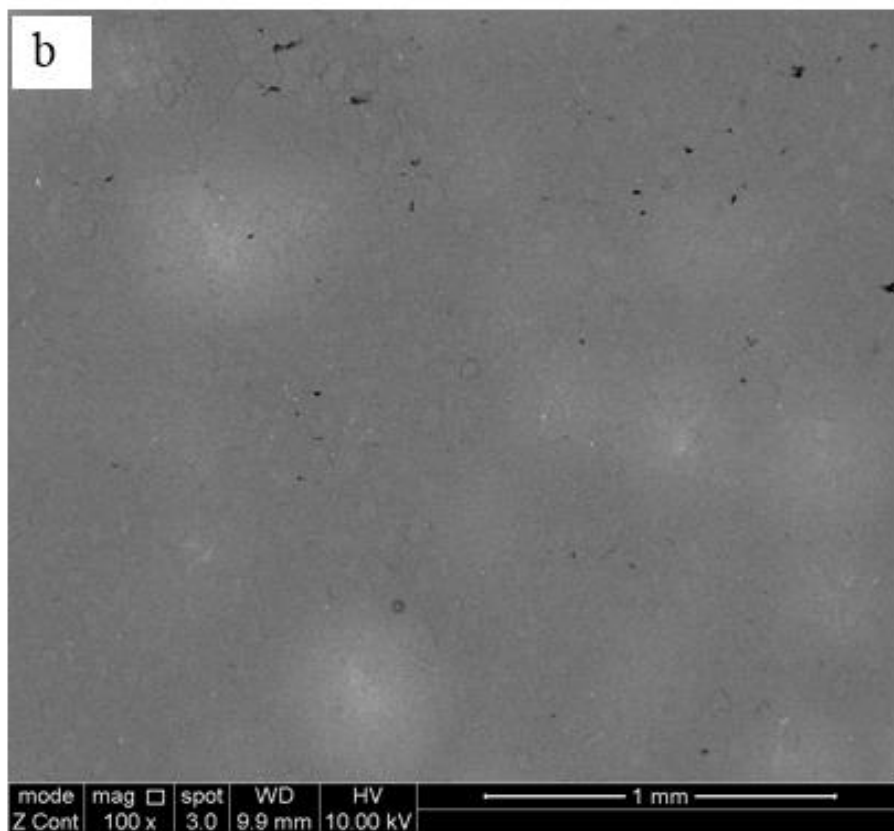
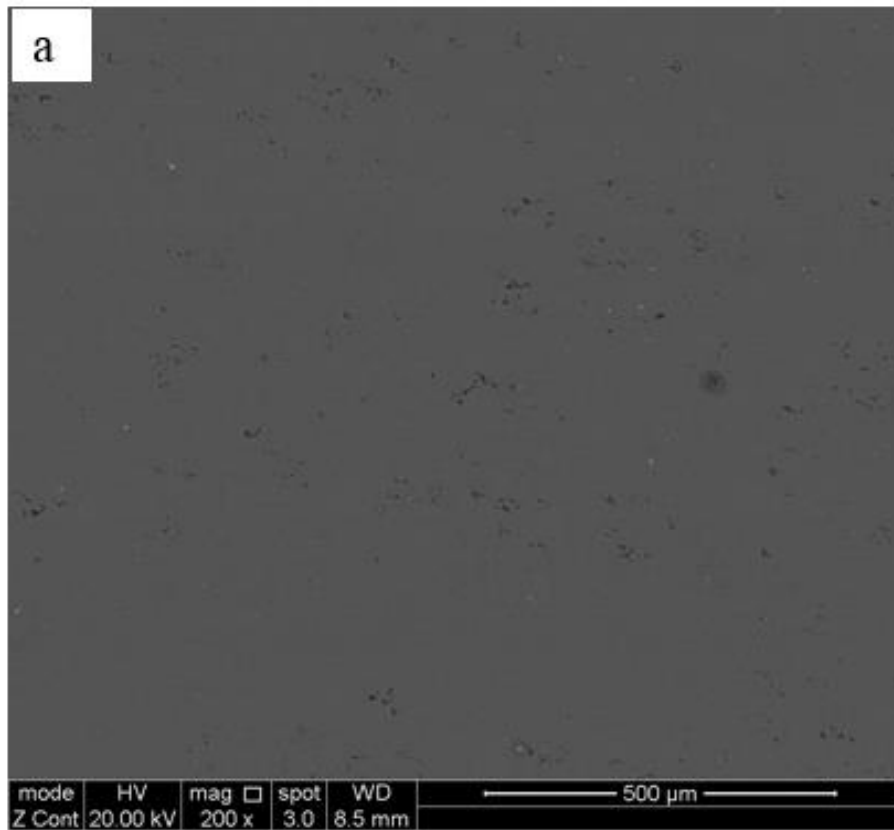


Figure 5.10 Ultimate strength versus strain of bulk NS Mg alloys.



**Figure 5.11** Back scattered electron SEM images of (a) CMEU0 and (b) CMEU5

Figure 5.11 shows typical back scattered electron SEM images of sample CMEU0 and CMEU5. Defects such as cracks and voids can be clearly observed in both samples due to incomplete sintering discussed in previous chapters. This explains why the compressive strain of CMEU5 was not significantly improved compared to CMEU0. In addition, several areas exhibiting bright contrast in sample CMEU5 can be seen, with a contrast gradient decreasing in a radial direction from the central bright spot. The brighter contrast was attributed to a locally higher Zn content, arising from the eutectic alloy powder, which had diffused into the nanocrystalline matrix.

Some large original eutectic alloy powder particles were observed in the microstructure (see Fig. 5.3). This shows that the short sintering SPS process was not enough to melt the eutectic and diffuse the Zn into the Mg matrix. Figure 5.12 presents a secondary electron SEM images showing residual Mg-Zn phases. It was distributed in the inter-junction region of the cryomilled particles and provided a connection between these particles without voids. The EDS result suggests the composition of this Mg-Zn phase was very close to the eutectic phase  $Mg_{51}Zn_{20}$ . In addition, the great majority of the phases exhibiting bright contrast were distributed in nano grains areas adjacent to this large residual Mg-Zn particle. This can be explained as follows: during sintering at higher temperature (e.g., 400 °C), the diffusion rate of Zn atoms was quicker than at room temperature. When the Zn atoms diffused to the nano grain boundaries with higher internal energy, the Zn segregated along the boundaries when the sample cooled down to room temperature.

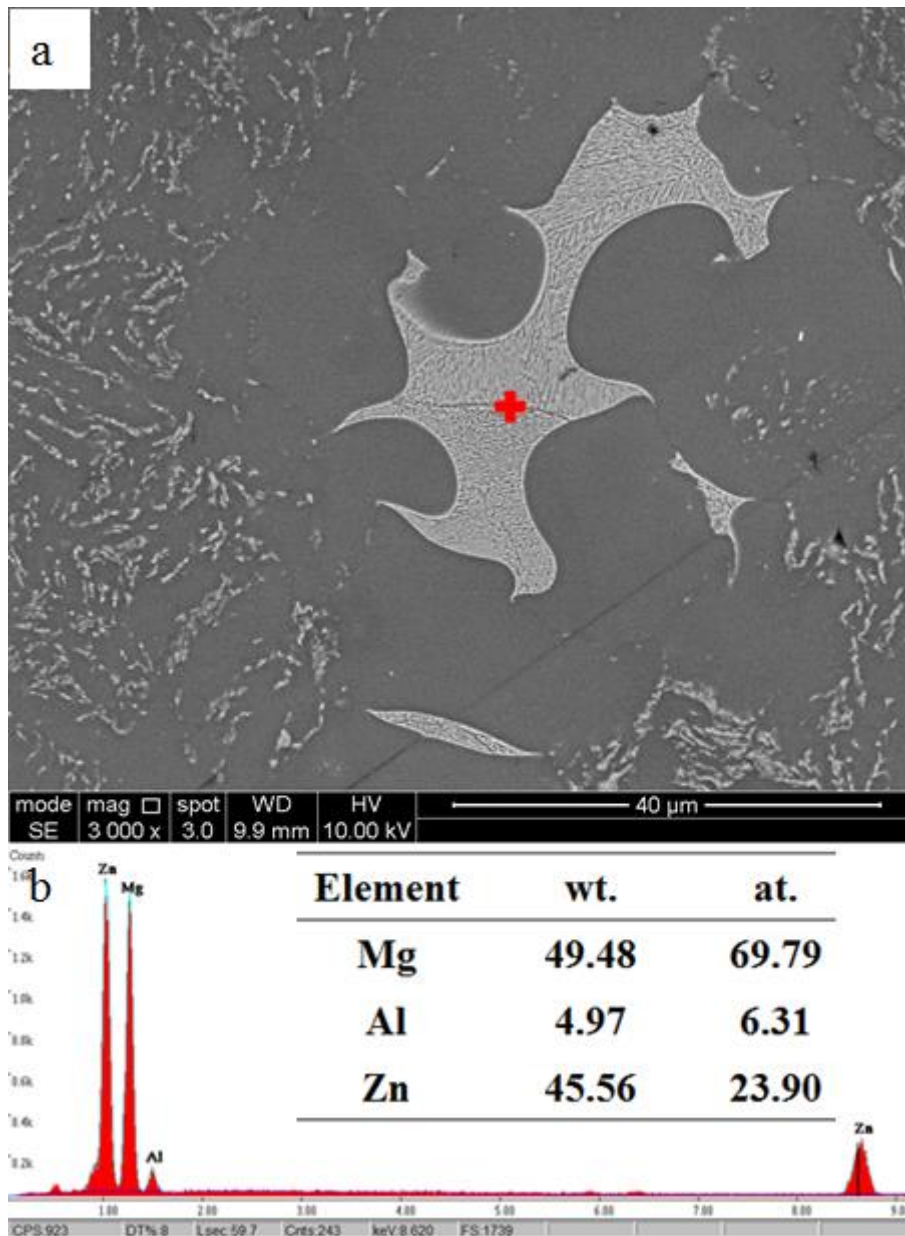


**Figure 5.12 (a)** a second electron SEM image of CMEU5, (b) EDS spectra and quantitative values (inset) from the marked eutectic phase.

Overall, it can be concluded the Zn rich phases were not distributed homogeneously, which caused heterogeneities in the microstructure for this sample. This explains why the mechanical test results of CMEU10 and CMEU5 varied with samples cut from different places (see Fig. 5.9 (b)).

When the weight fraction of eutectic alloy powder exceeded 10%, the distribution of Zn enriched phases became more homogeneous. Figure 5.13 shows back scattered electron images, which shows difference between samples CMEU10 and CMEU20. The corresponding SEM images of CMEU0 are provided for comparison. After carefully polishing, defects such as porosity, either introduced by consolidation process or particle pull-out during polishing because of insufficient inter-particle bonding, can be clearly seen in bulk sample CMEU0 as well as CMEU5 (Fig. 5.11 and Fig. 5.13 (a)). However, these defects almost disappeared in sample CMEU10 (Fig. 5.13 (b)), and no sign of defects could be found in sample CMEU20 (Fig. 5.13 (c)). The reason can be found in figure 5.7. It shows additional piston movement around 320-330 °C only in samples with additions of eutectic alloy powder, and the speed was much higher in samples CMEU10 and CMEU20 than in samples CMEU5. Thus, the extent of piston movement correlated with the amount of Mg-Zn eutectic alloy powder. It should be noted that a few Mg particles were “wrapped” by other particles and had not been broken up during cryomilling due to cold welding, as discussed in chapter 4. The molten liquid phase present during SPS easily flowed between the solid NC Mg particles and filled potential voids or gaps during compact by SPS, which was beneficial for consolidating a full dense sample after cooling down.

Comparing CMEU20 to CMEU10, the bright Zn enriched phases were distributed homogeneously throughout sample CMEU20, but did not evenly distributed in sample CMEU10. However, since some of the Mg-Zn phases were beyond the resolution of SEM, TEM would be required to fully determine the variations. Some Mg-Zn phases existed as fine precipitates in all samples with eutectic alloy powder, but due to the fine scale, this required TEM to characterize. In addition, Mg-Zn phases were not only found in the nano grain areas (Fig. 5.13 (b) and (c)), but also in the coarse grain areas, which will be investigated by TEM in following sections.

The difference between samples CMEU10 and CMEU20 was considered to be the density of precipitates and the extent of segregation phases, but no difference in phase constitution. Accordingly, only CMEU20 was investigated by TEM images. Figure 5.14 (a) shows representative bright-field TEM micrographs and selected area electron diffraction (SAED) pattern of the bulk sample CMEU20. Figure 5.14 (b) shows the equiaxed grains with a size range from 10 to 80 nm. The grain size was measured to be 37 nm based on more than 200 grains. Coarse grains were also observed among NC grains, but these coarse grains are different from the larger grains that arose from powder particles that had not been broken down during cryomilling, figure 5.13. The formation of these coarse grains was probably due to the absence of pinning particles, allowing rapid grain growth, but may have also been due to localized higher temperature and stress at points of contact area between initially separate particles during SPS process [100,224,225]. For comparison, these grains were similar in size to the bulk sample CMEU0 (see Fig. 4.14).

A high density of fine precipitates can be observed in CMEU20 sample. The precipitates were not only observed in coarse grains (e.g., introduced by SPS process and from unprocessed particles), but also NC grains, as shown in figures 5.15. Figure 5.16 gives TEM images from a coarse area in sample CMEU20. According to the diffraction pattern, most of these precipitates have a base-centred monoclinic structure ( $a = 2.596$  nm,  $b = 1.428$  nm,  $c = 0.524$  nm,  $\gamma = 102.5^\circ$ ) and an orientation relationship with matrix was  $[0\ 0\ 1]_p // [0\ 0\ 0\ 1]_\alpha$  and  $(6\ 3\ 0)_p // [0\ 1\ -1\ 0]_\alpha$ . The crystal structure, shape and orientation of these precipitates are consistent with  $\beta_1'$  strengthening phase that occurs in the Mg-Zn alloy system [226]. In addition, some blocky precipitates can be also observed in figures 5.15 and 5.16 and were expected to be  $\beta_2'$  phase based on their shape and orientation [226,227]. The existence of this high density of precipitates can be fully explained by classical casting theory. The solubility difference of Zn in Mg between room temperature and 400 °C is considerable (Fig.5.2). Most of the Zn atoms

in the liquid dissolved and then diffused into the surrounding solid Mg particles between 350 and 400 °C. Finally, the oversaturated solid solution decomposed as high dense fine precipitates while cooling down to room temperature (Fig.5.1).

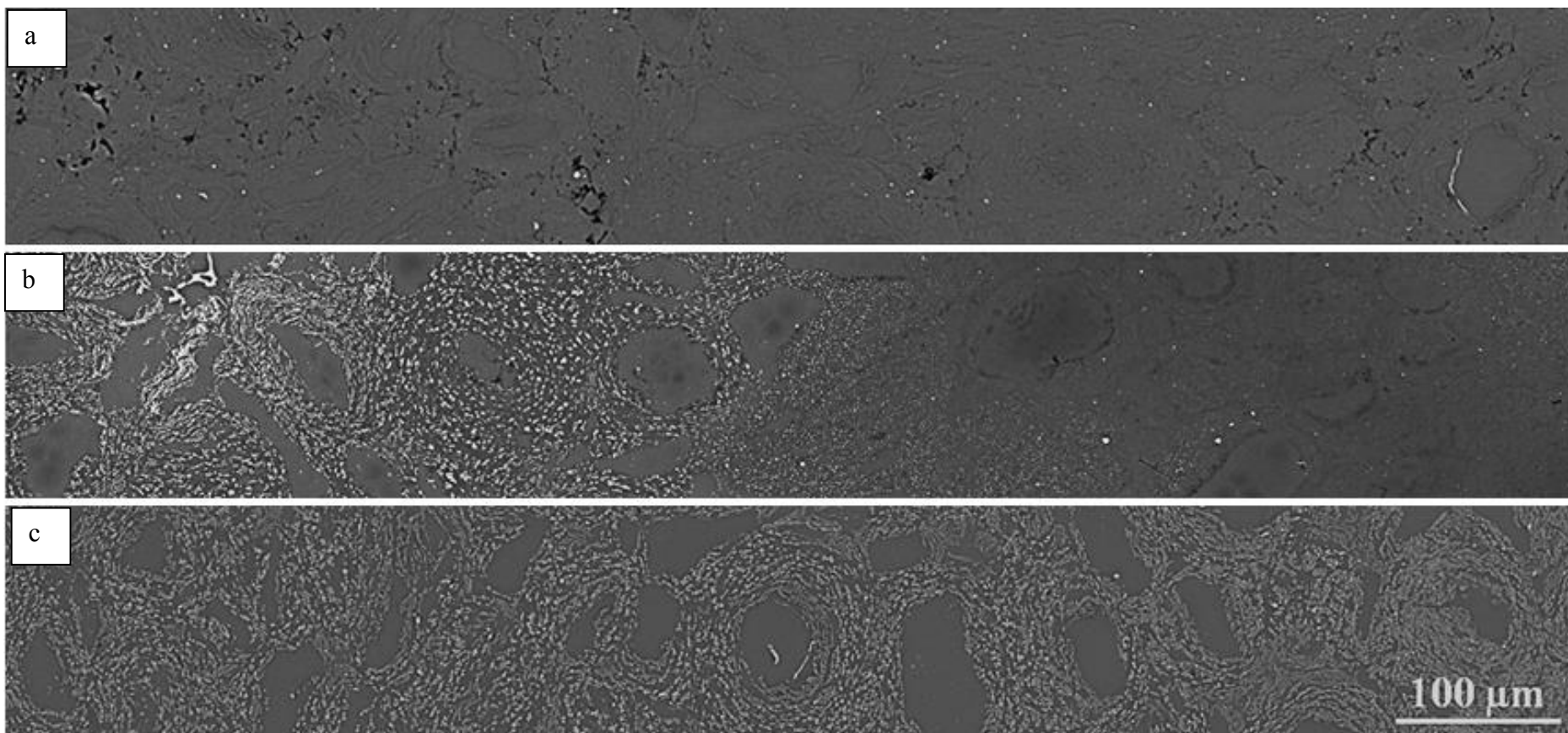


**Figure 5.13** Representative back scattered SEM images of samples (a) CMEU0, (b) CMEU10 and (c) CMEU20 showing the internal morphology after polishing

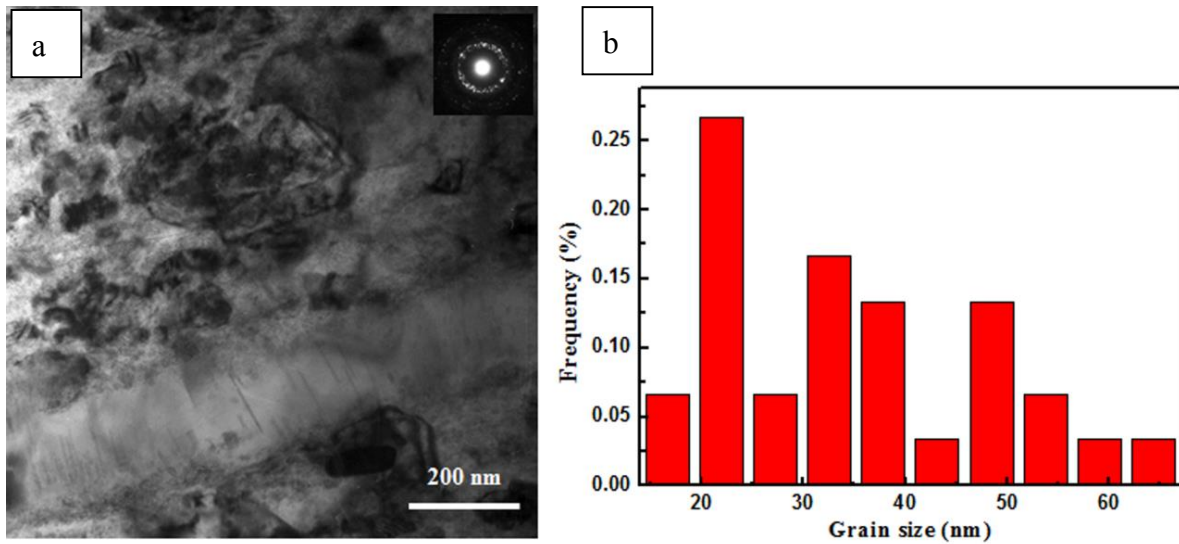


**Figure 5.14** a) A representative bright-field TEM image of sample CMEU20; the upper right inset shows the selected-area electron diffraction pattern, b) statistical grain size distribution

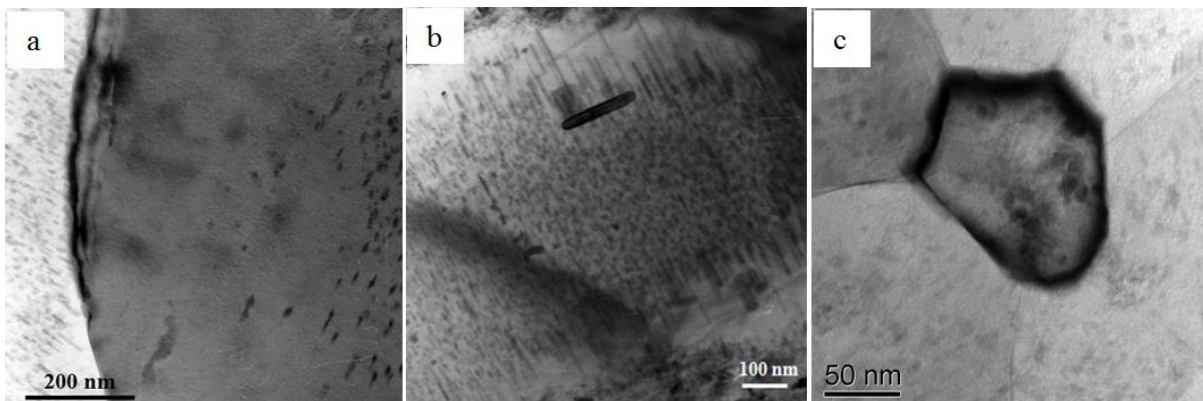


**Figure 5.15** BF TEM images showing precipitates in a) coarse grains in unprocessed particles during cryomilling, b) a big grain introduced by local heating during SPS and c) several NC grains of sample CMEU20

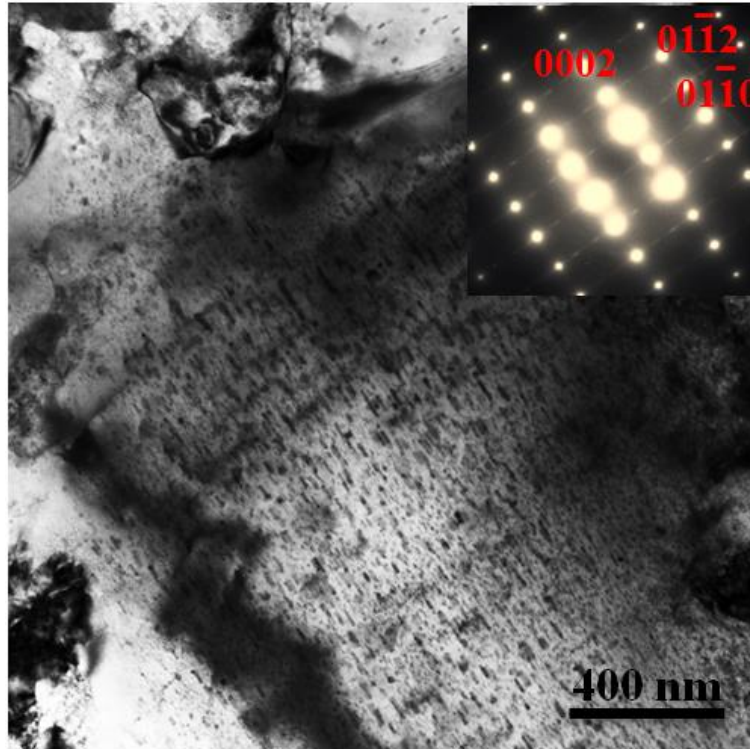


**Figure 5.16** TEM image and SADP of sample CMEU20

As mentioned previously, high strength and poor ductility is the common feature of NC materials [48-50,54,133]. It is now well recognized that low ductility of bulk NS materials is caused by either extrinsic defects such as porosity, insufficient inter-particle bonding or intrinsic microstructures with low strain hardening/dislocation storage capacity [182]. The improved ductility without sacrificing the strength of bulk CMEU10 and CMEU20 samples can be due to the considerably decrease processing defects and the formation of dense precipitates. The porosity or voids present in CMEU0 sample (Fig. 5.13) were filled by liquid Mg-Zn phase during sintering and “welded” those particles during cooling, leading to an improved inter-particle bonding of CMEU samples. Figure 5.17(a) shows a BF TEM image of CMEU20 of one of these regions, which exhibits a fine grain structure, with Mg-Zn phases.

The EDS result shown in figure 5.17(b) suggests the composition of this Mg-Zn phase was very close to the eutectic phase  $Mg_{51}Zn_{20}$  as well. The copper and oxygen were introduced during TEM sample preparation and the signal of aluminum was from adjacent matrix.

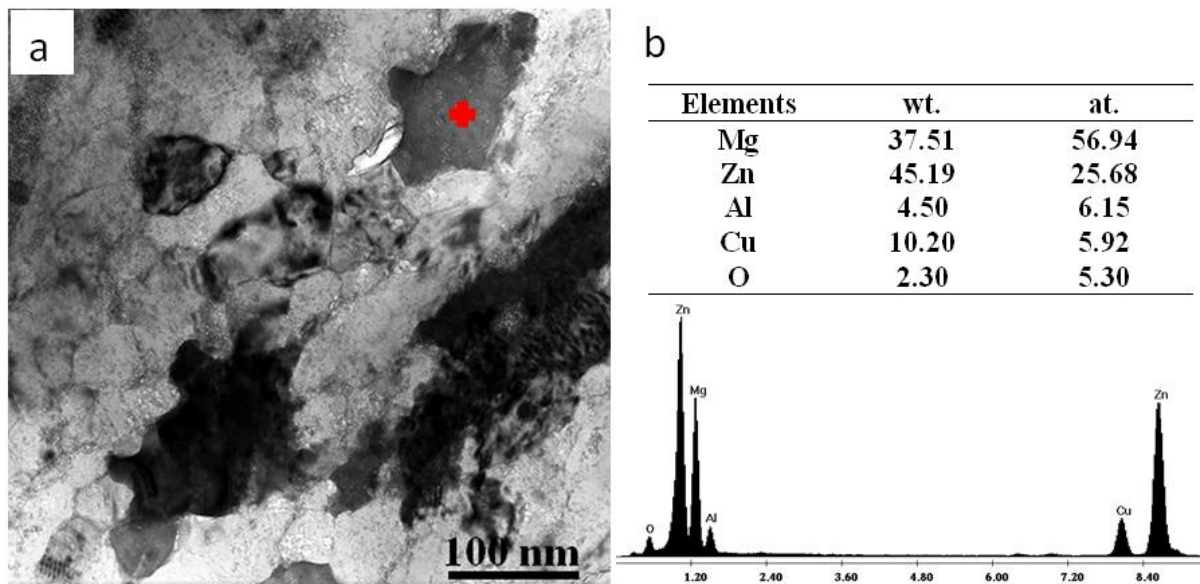


**Figure 5.17 (a)** A BF TEM image of sample CMEU20 showing the Mg-Zn eutectic phase connecting adjacent solid Mg particles, (b) EDS spectra and quantitative values (inset) from the marked eutectic phase

Figure 5.18 shows narrow bands of very small NC grains (<20 nm) present in some coarse grained regions from samples with additions of eutectic alloy powder. High resolution TEM (HRTEM) microscope was used for characterization. Figure 5.19 (a) shows images of one narrow band. The corresponding energy dispersive spectroscopy (EDS) and inset HRTEM image in figure 5.19 (b) demonstrated that the fine grains were Mg. For some small Mg-Zn

eutectic alloy particles, the Zn concentration became very low if we treat this isolated particle (or melt at high temperature) and the surrounding Mg particles as a whole. The majority of the Zn atoms in the melt diffused into adjacent Mg particles because of the strong concentration gradient, leaving the former eutectic region depleted of Zn. In this case, the depletion appears to be been complete, leaving a narrow band of polycrystalline Mg with low level of Zn between two Mg particles that contain a dispersion of precipitates.

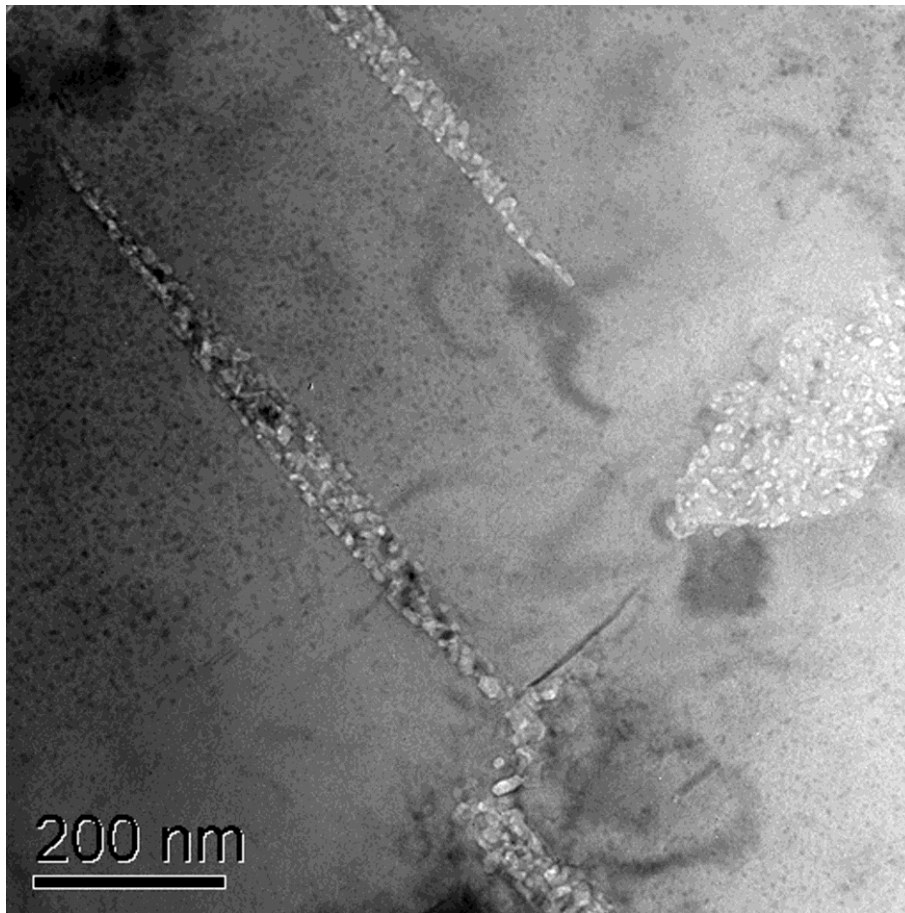


**Figure 5.18** A BF TEM image of an area in sample CMEU20 showing narrow bands of NC Mg grains

Strain hardening is another critical factor related to the ductility of bulk NS materials [50]. Compared to the true stress-strain curves of bulk sample CMEU0 (Fig. 4.12), strain hardening was observed, especially in sample CMEU20 (Fig. 5.9). This can be explained by the appearance of a high density of precipitates within grains, which restricted dislocation movement, whether by shearing or Orowan by-passing. The precipitation hardening more than offset the expected loss in strength by substituting 20 wt.% of hard cryomilled NC Mg particles with the coarse grained eutectic in the CMEU20 samples; Figure 5.9 (c) shows the strength was slightly enhanced rather than incurred a noticeable loss. In addition, the solid solution strengthening and hard Mg-Zn phases (Fig. 5.17) will have also made contributions to the increase in strength.

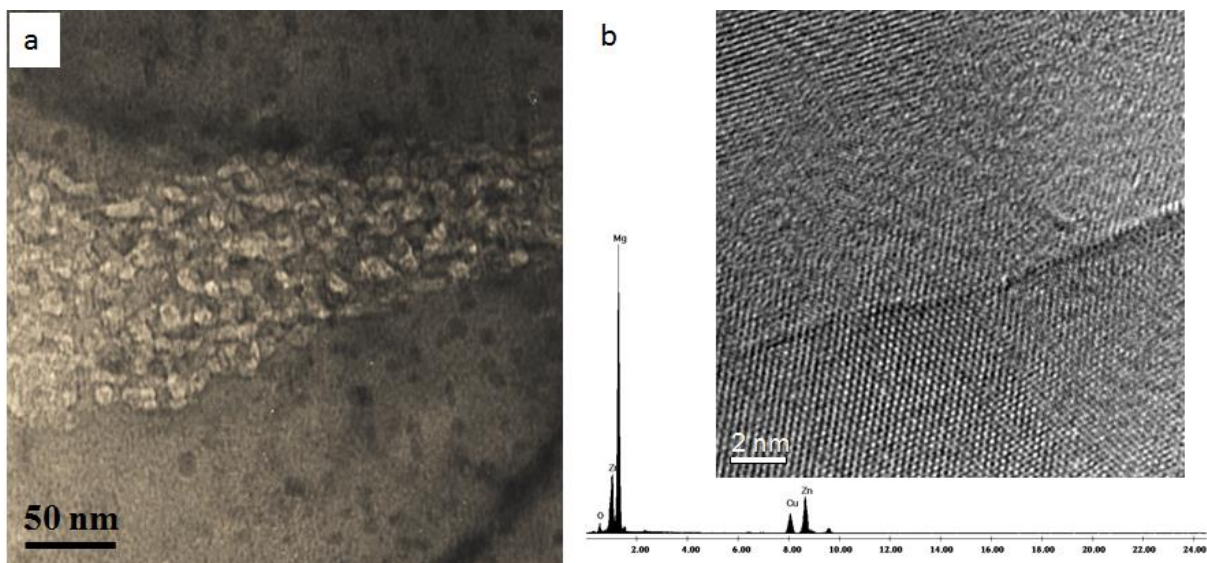


**Figure 5.19** a) HRTEM image of sample CMEU20 showing a narrow band of NC grains, (b) the corresponding energy dispersive spectroscopy (EDS) and inset HRTEM image proving they are Mg

## 5.4 Conclusions

In summary, a facile strategy for the *in situ* powder casting during SPS has been developed to enhance the ductility without loss of strength. The *in situ* powder casting simultaneously significantly removed the artifacts such as porosity, enhanced the inter-particle bonding between nanostructured Mg particles and introduced very small dense precipitates into bulk NS Mg alloy. The mechanical properties had a strong correlation with the weight fraction of eutectic alloy powder. When the amount of eutectic powder was only 5%, internal defects were still found, the Zn enriched phases were not evenly distributed and the compressive strain was slightly improved. However, when the amount increased to 10% and 20%, the compressive strain was significantly enhanced. The main reason for this was that the voids in CMEU0 and CMEU5 were refilled by Mg-Zn phases. The precipitates formed during *in situ* casting also made a contribution to the improved compressive strain as well as the strength. The improved mechanical behavior could also be ascribed to solid solution strengthening and hard Mg-Zn  $\beta_1'$  strengthening phase. Overall, sample CMEU20 exhibited the best combination of ductility (6.6%) and ultimate strength (509 MPa) among all samples, which is superior to the published properties for most conventional Mg alloys.

This strategy can be also extended to other alloy systems which contain intermetallic with low melting temperatures. For example, 10% (wt.%) pure Zn (melting temperature: 419.5 °C) powder was added to cryomilled AZ31 powder and sintered at 430 °C. Figure 5.20 shows the compressive strain and strength of these samples with addition of Zn were improved

simultaneously compared to the pure cryomilled samples sintered at 425 °C. Furthermore, the cryomilling and SPS used in this project could be modified to existing industrial process or extended to other consolidation techniques, and has the potential for large-scale application of bulk dense NS materials produced by “two step” approach. If the experimental parameters are optimized (i.e., dissolve all the Zn from residual brittle Mg-Zn phase into Mg matrix), the ductility may be further enhanced while simultaneously improve the strength.

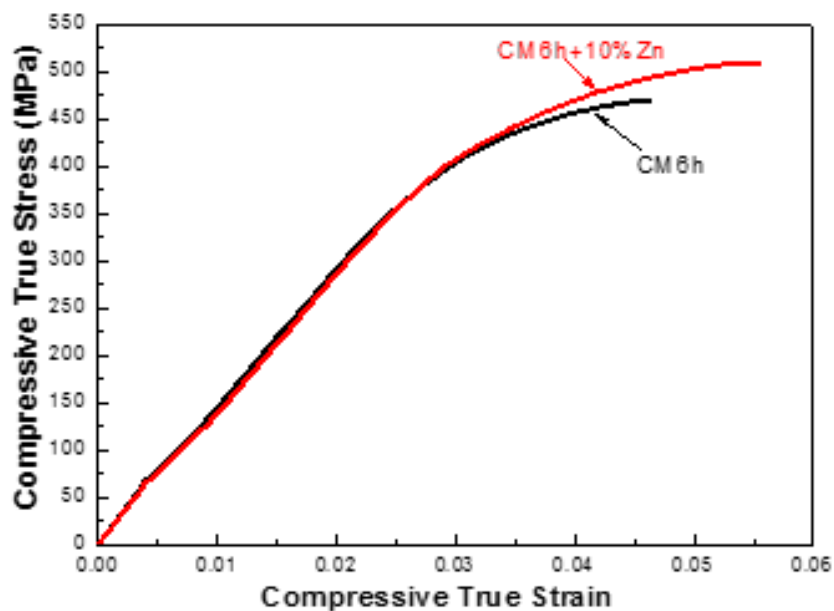


**Figure 5.20** Compressive true stress–strain curves of CM6h sintered at 425 °C and CM6h+10%Zn sintered at 430 °C

## 6 Conclusions

Nanocrystalline AZ31 powder was produced by cryomilling in this study. The particles undergo cold welding and fracture and its average size dropped to approximately 26 $\mu$ m after cryomilling 6 hours. The chemical analysis results indicated contamination introduced from cryomilling was not significant. The levels of contamination were small compared to other studies relating to cryomilling. A minimum average grain size of about 26 nm for the powder can be reached for a cryomilling time of 6 hours or longer. The corresponding hardness of the 6 hours cryomilled powder had a highest value of approximately 160 HV among all the cryomilled powders from 0.5 hours to 8 hours. Therefore, it can be concluded that 6 hours cryomilling can reach the minimum grain size in this study based on the investigations of XRD and TEM. It also should be noted a few particles were agglomerated by other particles and cannot be processed by cryomilling due to cold welding.

The NC AZ31 powder prepared by cryomilling exhibits excellent thermal stability during short anneals at 350-450°C. There were two separate growth stages with a transition point at around 400 °C. More specifically, between 350 and 400 °C, NC Mg grains were stable at approximately 32 nm, even after 1h annealing. At 450 °C, the nano grains grew to 37 nm in the first 5 minutes and grew quickly to approximately 60 nm after 15 minutes. However, the grain growth was limited when the annealing time was increased to 60 minutes. Some submicrometer scale (>200 nm) particles can be also observed in some areas when the powder was annealed at 450 °C. Nevertheless, the average grain size remained stable less than

approximately 60 nm even after long anneals at temperatures as high as 450 °C(0.78 T/TM), indicating an outstanding degree of grain size stability. This excellent thermal stability can be attributed to solute drag, Zener pinning, and micro porosity. In addition, the results of micro hardness of these annealed powders agreed fairly well with the grain size changes.

A bulk NS AZ31 alloy with exceptionally high strength can be produced by cryomilling and SPS. All the bulk samples consolidated from cryomilled powders exhibited a bimodal microstructure. Sample CM400 showed the highest yield strength of 408.7 MPa and ultimate strength of 504.0 MPa with acceptable compressive strain of 0.036. The mean grain size of the material cryomilled for 6h followed by spark plasma sintering consolidation was about 35 nm. The high strength of sample was generally ascribed to the grain refinement strengthening, oxide dispersion and solid solution strengthening. The low compressive strain of this alloy is due to limited work hardening, rare twinning behavior and pores located between particle boundaries.

The density of SPSed samples increased with increase in sintering temperature. More specifically, the density was improved significantly from 350 to 400 °C while it was slightly enhanced from 425 to 450 °C. Higher sintering temperature (425-450 °C) improved compressive strain at the sacrifice of strength. In contrast, samples consolidated at 350 °C displayed brittle behaviour with low strength. Generally, bulk NS materials usually have high strength but poor ductility. For example, true compressive strains were all less than 0.06 at true ultimate compressive strength in this study.

Based on the results of micro hardness and grain size distributions, it indicated the sintering temperature 400 °C is a transition point. Below this temperature, the grain growth and

decrease of hardness during short sintering was limited; but at higher temperature, grain growth and drop of hardness became prominent, even for a 3 minute dwell time. However, the changes between samples sintered at 425 and 450 °C can be ignored. This is the reason that sample CM450 with higher density owned good compressive behavior compared to CM425, although it was sintered at higher temperature.

A facile strategy for the *in situ* powder casting during SPS has been developed to enhance the ductility without loss of strength. The *in situ* powder casting simultaneously significantly removed the artifacts such as porosity, enhanced the inter-particle bonding between nanostructured Mg particles and introduced very small dense precipitates into bulk NS Mg alloy. The mechanical properties had a strong correlation with the weight fraction of eutectic alloy powder. When the amount of eutectic powder was only 5%, internal defects were still found, the Zn enriched phases were not evenly distributed and the compressive strain was slightly improved. However, when the amount increased to 10% and 20%, the compressive strain was significantly enhanced. The main reason for this was that the voids in CMEU0 and CMEU5 were refilled by Mg-Zn phases. The precipitates formed during *in situ* casting also made a contribution to the improved compressive strain as well as the strength. The improved mechanical behavior could also be ascribed to solid solution strengthening and hard Mg-Zn  $\beta_1'$  strengthening phase. Overall, sample CMEU20 exhibited the best combination of ductility (6.6%) and ultimate strength (509 MPa) among all samples, which is superior to the published properties for most conventional Mg alloys.

## 7 Future work

Systematic annealing studies can be conducted to investigate the thermal stability of cryomilled Mg powders. Microstructural investigations should focus on locating the oxides. Because second phases were distributed intragranularly and at grain boundaries, the thermal stability mechanisms of bulk NS samples will be also worth investigating using advance electron microscopes.

The SPS processing parameters for sintering cryomilled Mg powder with eutectic alloy Mg-Zn powders could be optimized to obtain bulk NS defect free samples with higher density of precipitates by reducing residual Mg-Zn phases. Therefore, the strength and ductility of bulk sintered samples may be improved simultaneously. In addition, in order to characterize the precipitates, high resolution TEM needs to be employed to examine more detailed microstructure via using scanning transmission electron microscopy (STEM), high angle annular dark field (HAADF), energy-dispersive spectroscopy (EDS) and electron energy loss (EELS).

To produce specimens for tensile tests, disk shaped samples of 40 or 60 mm in diameter should be produced by SPS. Furthermore, mechanical tests including tensile and compressive tests can be conducted at elevated temperatures to study its corresponding mechanical behaviour.

Other alloy systems (e.g., Ti-Al system) which possess intermetallic with low melting temperatures can be used to try to produce defect free bulk sample via *in situ* casting strategy. Furthermore, the cryomilling and SPS used in this study may be replaced by other consolidation

techniques (e.g., HIP) to produce large-scale size bulk dense NS metallic alloys by “two step” approach.

## 8 References

- 1 K. U. Kainer, "Magnesium alloys and technology", DGM. 2003
- 2 H. E. Friedrich and B. L. Mordike, "Magnesium Technology: Metallurgy, Design Data, Applications", Springer. 2010 64
- 3 I. J. Polmear, "Light Alloys: From Traditional Alloys to Nanocrystals", Elsevier/Butterworth-Heinemann. 2006
- 4 S. R. Agnew and J. F. Nie, "Preface to the viewpoint set on: The current state of magnesium alloy science and technology", *Scr. Mater.* , 2010, 63, 671-673
- 5 W. Hume-Rothery and G. V. Raynor, "The structure of metals and alloys", Institute of Metals. 1962
- 6 M. M. Avedesian, H. Baker and A. I. H. Committee, "Magnesium and magnesium alloys", ASM International. 1999
- 7 L. R. Gill, G. Lorimer and U. o. M. S. o. Materials, "Microstructure/property relationships of four Mg-RE-Zn-Zr alloys", University of Manchester. 2005
- 8 R. V. Mises, "Mechanics of Plastic Deformation of Crystals", *ZAMM - Journal of Applied Mathematics and Mechanics / Zeitschrift für Angewandte Mathematik und Mechanik*, 1928, 8, 161-185
- 9 R. Gehrman, M. M. Frommert and G. Gottstein, "Texture effects on plastic deformation of magnesium", *Mater. Sci. Eng. A*, 2005, 395, 338-349
- 10 M. Barnett, "A taylor model based description of the proof stress of magnesium AZ31 during hot working", *Metall. Mater. Trans. A*, 2003, 34, 1799-1806
- 11 A. Akhtar and E. Teghtsoonian, "Solid solution strengthening of magnesium single crystals—I alloying behaviour in basal slip", *Acta Metall.* , 1969, 17, 1339-1349
- 12 J. Koike, T. Kobayashi, T. Mukai, H. Watanabe, M. Suzuki, K. Maruyama and K. Higashi, "The activity of non-basal slip systems and dynamic recovery at room temperature in fine-grained AZ31B magnesium alloys", *Acta Mater.* , 2003, 51, 2055-2065
- 13 A. Akhtar and E. Teghtsoonian, "Solid solution strengthening of magnesium single crystals—ii the effect of solute on the ease of prismatic slip", *Acta Metall.* , 1969, 17, 1351-1356
- 14 M. R. Barnett, "Twinning and the ductility of magnesium alloys: Part I: "Tension" twins", *Mater. Sci. Eng. A*, 2007, 464, 1-7
- 15 M. R. Barnett, "Twinning and the ductility of magnesium alloys: Part II. "Contraction" twins", *Mater. Sci. Eng. A*, 2007, 464, 8-16
- 16 J. D. Robson, N. Stanford and M. R. Barnett, "Effect of precipitate shape on slip and twinning in magnesium alloys", *Acta Mater.* , 2011, 59, 1945-1956
- 17 A. Staroselsky and L. Anand, "A constitutive model for hcp materials deforming by slip and twinning: application to magnesium alloy AZ31B", *Int. J. Plast.* , 2003, 19, 1843-1864

- 18 J. Koike, "Enhanced deformation mechanisms by anisotropic plasticity in polycrystalline Mg alloys at room temperature", *Metall. Mater. Trans. A*, 2005, 36, 1689-1696
- 19 M. D. Nave and M. R. Barnett, "Microstructures and textures of pure magnesium deformed in plane-strain compression", *Scr. Mater.* , 2004, 51, 881-885
- 20 S. R. Agnew and Ö. Duygulu, "Plastic anisotropy and the role of non-basal slip in magnesium alloy AZ31B", *Int. J. Plast.* , 2005, 21, 1161-1193
- 21 D. W. Brown, S. R. Agnew, M. A. M. Bourke, T. M. Holden, S. C. Vogel and C. N. Tomé, "Internal strain and texture evolution during deformation twinning in magnesium", *Mater. Sci. Eng. A*, 2005, 399, 1-12
- 22 S. R. Agnew, M. H. Yoo and C. N. Tomé, "Application of texture simulation to understanding mechanical behavior of Mg and solid solution alloys containing Li or Y", *Acta Mater.* , 2001, 49, 4277-4289
- 23 S. E. Ion, F. J. Humphreys and S. H. White, "Dynamic recrystallisation and the development of microstructure during the high temperature deformation of magnesium", *Acta Metall.* , 1982, 30, 1909-1919
- 24 T. Obara, H. Yoshinga and S. Morozumi, "{1122} <1123> Slip system in magnesium", *Acta Metall.* , 1973, 21, 845-853
- 25 W. D. Callister, "Materials science and engineering: an introduction", John Wiley & Sons. 2007
- 26 J. F. Nie, "Preface to viewpoint set on: phase transformations and deformation in magnesium alloys", *Scr. Mater.* , 2003, 48, 981-984
- 27 B. L. Mordike and T. Ebert, "Magnesium: Properties — applications — potential", *Mater. Sci. Eng. A*, 2001, 302, 37-45
- 28 R. Zhu, Y. J. Wu, W. Q. Ji and J. T. Wang, "Cyclic softening of ultrafine-grained AZ31 magnesium alloy processed by equal-channel angular pressing", *Mater. Lett.* , 2011, 65, 3593-3596
- 29 G. Wan, B. L. Wu, Y. H. Zhao, Y. D. Zhang and C. Esling, "Strain-rate sensitivity of textured Mg–3.0Al–1.0Zn alloy (AZ31) under impact deformation", *Scr. Mater.* , 2011, 65, 461-464
- 30 N. Stanford, K. Sotoudeh and P. S. Bate, "Deformation mechanisms and plastic anisotropy in magnesium alloy AZ31", *Acta Mater.* , 2011, 59, 4866-4874
- 31 J. Oddershede, B. Camin, S. Schmidt, L. P. Mikkelsen, H. O. Sørensen, U. Lienert, H. F. Poulsen and W. Reimers, "Measuring the stress field around an evolving crack in tensile deformed Mg AZ31 using three-dimensional X-ray diffraction", *Acta Mater.* , 2012, 60, 3570-3580
- 32 J. R. Luo, A. Godfrey, W. Liu and Q. Liu, "Twinning behavior of a strongly basal textured AZ31 Mg alloy during warm rolling", *Acta Mater.* , 2012, 60, 1986-1998
- 33 W. J. Kim, Y. G. Lee, M. J. Lee, J. Y. Wang and Y. B. Park, "Exceptionally high strength in Mg–3Al–1Zn alloy processed by high-ratio differential speed rolling", *Scr. Mater.* , 2011, 65, 1105-1108

- 34 D.-G. Kim, K.-M. Lee, J.-S. Lee, Y.-O. Yoon and H.-T. Son, "Evolution of microstructures and textures in magnesium AZ31 alloys deformed by normal and cross-roll rolling", *Mater. Lett.* , 2012, 75, 122-125
- 35 N. V. Dudamell, I. Ulacia, F. Gálvez, S. Yi, J. Bohlen, D. Letzig, I. Hurtado and M. T. Pérez-Prado, "Twinning and grain subdivision during dynamic deformation of a Mg AZ31 sheet alloy at room temperature", *Acta Mater.* , 2011, 59, 6949-6962
- 36 Z. Zhang, M.-p. Wang, N. Jiang and S.-m. Li, "Orientation analyses for twinning behavior in small-strain hot-rolling process of twin-roll cast AZ31B sheet", *Mater. Sci. Eng. A*, 2010, 527, 6467-6473
- 37 X. Zhang, G. Yuan and Z. Wang, "Mechanical properties and biocorrosion resistance of Mg-Nd-Zn-Zr alloy improved by cyclic extrusion and compression", *Mater. Lett.* , 2012, 74, 128-131
- 38 G. Riontino, M. Massazza, D. Lussana, P. Mengucci, G. Barucca and R. Ferragut, "A novel thermal treatment on a Mg-4.2Y-2.3Nd-0.6Zr (WE43) alloy", *Mater. Sci. Eng. A*, 2008, 494, 445-448
- 39 P. Mengucci, G. Barucca, G. Riontino, D. Lussana, M. Massazza, R. Ferragut and E. H. Aly, "Structure evolution of a WE43 Mg alloy submitted to different thermal treatments", *Mater. Sci. Eng. A*, 2008, 479, 37-44
- 40 B. L. Mordike, "Creep-resistant magnesium alloys", *Mater. Sci. Eng. A*, 2002, 324, 103-112
- 41 C. Antion, P. Donnadiou, F. Perrard, A. Deschamps, C. Tassin and A. Pisch, "Hardening precipitation in a Mg-4Y-3RE alloy", *Acta Mater.* , 2003, 51, 5335-5348
- 42 D. Orlov, G. Raab, T. T. Lamark, M. Popov and Y. Estrin, "Improvement of mechanical properties of magnesium alloy ZK60 by integrated extrusion and equal channel angular pressing", *Acta Mater.* , 2011, 59, 375-385
- 43 M. Shahzad and L. Wagner, "Microstructure development during extrusion in a wrought Mg-Zn-Zr alloy", *Scr. Mater.* , 2009, 60, 536-538
- 44 S. Q. Zhu, H. G. Yan, J. H. Chen, Y. Z. Wu, J. Z. Liu and J. Tian, "Effect of twinning and dynamic recrystallization on the high strain rate rolling process", *Scr. Mater.* , 2010, 63, 985-988
- 45 H. Gjestland, G. Nussbaum, G. Regazzoni, O. Lohne and Ø. Bauger, "Stress-relaxation and creep behaviour of some rapidly solidified magnesium alloys", *Mater. Sci. Eng. A*, 1991, 134, 1197-1200
- 46 R. Valiev, "Nanostructuring of metals by severe plastic deformation for advanced properties", *Nat. Mater.* , 2004, 3, 511-516
- 47 R. Z. Valiev and T. G. Langdon, "Principles of equal-channel angular pressing as a processing tool for grain refinement", *Prog. Mater. Sci.* , 2006, 51, 881-981
- 48 X. Huang, N. Hansen and N. Tsuji, "Hardening by Annealing and Softening by Deformation in Nanostructured Metals", *Science*, 2006, 312, 249-251
- 49 Y. Wang, M. Chen, F. Zhou and E. Ma, "High tensile ductility in a nanostructured metal", *Nature*, 2002, 419, 912-915
- 50 Y. T. Zhu and X. Liao, "Nanostructured metals: Retaining ductility", *Nat. Mater.* , 2004, 3, 351-352

- 51 H. Gleiter, "Nanocrystalline materials", *Prog. Mater. Sci.* , 1989, 33, 223-315
- 52 H. Gleiter, "Nanostructured materials: basic concepts and microstructure", *Acta Mater.* , 2000, 48, 1-29
- 53 C. Koch, "Optimization of strength and ductility in nanocrystalline and ultrafine grained metals", *Scr. Mater.* , 2003, 49, 657-662
- 54 C. C. Koch, D. G. Morris, K. Lu and A. Inoue, "Ductility of nanostructured materials", *MRS Bull.* , 1999, 24, 54-58
- 55 L. Lu, Y. Shen, X. Chen, L. Qian and K. Lu, "Ultrahigh Strength and High Electrical Conductivity in Copper", *Science*, 2004, 304, 422-426
- 56 L. Lu, R. Schwaiger, Z. W. Shan, M. Dao, K. Lu and S. Suresh, "Nano-sized twins induce high rate sensitivity of flow stress in pure copper", *Acta Mater.* , 2005, 53, 2169-2179
- 57 K. S. Kumar, S. Suresh, M. F. Chisholm, J. A. Horton and P. Wang, "Deformation of electrodeposited nanocrystalline nickel", *Acta Mater.* , 2003, 51, 387-405
- 58 M. A. Meyers, A. Mishra and D. J. Benson, "Mechanical properties of nanocrystalline materials", *Prog. Mater. Sci.* , 2006, 51, 427-556
- 59 J. Gil Sevillano, P. van Houtte and E. Aernoudt, "Large strain work hardening and textures", *Prog. Mater. Sci.* , 1980, 25, 69-134
- 60 R. Z. Valiev, R. K. Islamgaliev and I. V. Alexandrov, "Bulk nanostructured materials from severe plastic deformation", *Prog. Mater. Sci.* , 2000, 45, 103-189
- 61 R. Z. Valiev, N. A. Krasilnikov and N. K. Tsenev, "Plastic deformation of alloys with submicron-grained structure", *Mater. Sci. Eng. A*, 1991, 137, 35-40
- 62 V. M. Segal, "Materials processing by simple shear", *Mater. Sci. Eng. A*, 1995, 197, 157-164
- 63 M. Furui, H. Kitamura, H. Anada and T. G. Langdon, "Influence of preliminary extrusion conditions on the superplastic properties of a magnesium alloy processed by ECAP", *Acta Mater.* , 2007, 55, 1083-1091
- 64 P. Berbon, M. Furukawa, Z. Horita, M. Nemoto and T. Langdon, "Influence of pressing speed on microstructural development in equal-channel angular pressing", *Metall. Mater. Trans. A*, 1999, 30, 1989-1997
- 65 R. Z. Valiev, A. V. Korznikov and R. R. Mulyukov, "Structure and properties of ultrafine-grained materials produced by severe plastic deformation", *Mater. Sci. Eng. A*, 1993, 168, 141-148
- 66 S. X. Ding, W. T. Lee, C. P. Chang, L. W. Chang and P. W. Kao, "Improvement of strength of magnesium alloy processed by equal channel angular extrusion", *Scr. Mater.* , 2008, 59, 1006-1009
- 67 O. V. Mishin, V. Y. Gertsman, R. Z. Valiev and G. Gottstein, "Grain boundary distribution and texture in ultrafine-grained copper produced by severe plastic deformation", *Scr. Mater.* , 1996, 35, 873-878
- 68 J. H. Gao, S. K. Guan, Z. W. Ren, Y. F. Sun, S. J. Zhu and B. Wang, "Homogeneous corrosion of high pressure torsion treated Mg–Zn–Ca alloy in simulated body fluid", *Mater. Lett.* , 2011, 65, 691-693

- 69 M. Kai, Z. Horita and T. G. Langdon, "Developing grain refinement and superplasticity in a magnesium alloy processed by high-pressure torsion", *Mater. Sci. Eng. A*, 2008, 488, 117-124
- 70 K. Edalati, A. Yamamoto, Z. Horita and T. Ishihara, "High-pressure torsion of pure magnesium: Evolution of mechanical properties, microstructures and hydrogen storage capacity with equivalent strain", *Scr. Mater.* , 2011, 64, 880-883
- 71 P. Serre, R. B. Figueiredo, N. Gao and T. G. Langdon, "Influence of strain rate on the characteristics of a magnesium alloy processed by high-pressure torsion", *Mater. Sci. Eng. A*, 2011, 528, 3601-3608
- 72 R. B. Figueiredo and T. G. Langdon, "Development of structural heterogeneities in a magnesium alloy processed by high-pressure torsion", *Mater. Sci. Eng. A*, 2011, 528, 4500-4506
- 73 H. Miura, G. Yu and X. Yang, "Multi-directional forging of AZ61Mg alloy under decreasing temperature conditions and improvement of its mechanical properties", *Mater. Sci. Eng. A*, 2011, 528, 6981-6992
- 74 G. A. Salishchev, O. R. Valiakhmetov and R. M. Galeev, "Formation of submicrocrystalline structure in the titanium alloy VT8 and its influence on mechanical properties", *J. Mater. Sci.*, 1993, 28, 2898-2902
- 75 R. M. Imayev, V. M. Imayev and G. A. Salishchev, "Formation of submicrocrystalline structure in TiAl intermetallic compound", *J. Mater. Sci.*, 1992, 27, 4465-4471
- 76 J. Xing, H. Soda, X. Yang, H. Miura and T. Sakai, "Ultra-Fine Grain Development in an AZ31 Magnesium Alloy during Multi-Directional Forging under Decreasing Temperature Conditions", *Mater. Trans.*, 2005, 46, 1646-1650
- 77 S. Biswas and S. Suwas, "Evolution of sub-micron grain size and weak texture in magnesium alloy Mg-3Al-0.4Mn by a modified multi-axial forging process", *Scr. Mater.* , 2012, 66, 89-92
- 78 G. W. Nieman, J. R. Weertman and R. W. Siegel, "Microhardness of nanocrystalline palladium and copper produced by inert-gas condensation", *Scr. Metall.* , 1989, 23, 2013-2018
- 79 C. C. Koch, "Synthesis of nanostructured materials by mechanical milling: problems and opportunities", *Nanostruct. Mater.* , 1997, 9, 13-22
- 80 C. Suryanarayana, "Mechanical alloying and milling", *Prog. Mater Sci.* , 2001, 46, 1-184
- 81 D. B. Witkin and E. J. Lavernia, "Synthesis and mechanical behavior of nanostructured materials via cryomilling", *Prog. Mater Sci.* , 2006, 51, 1-60
- 82 H. J. Fecht, "Nanostructure formation by mechanical attrition", *Nanostruct. Mater.* , 1995, 6, 33-42
- 83 M. Pozuelo, C. Melnyk, W. H. Kao and J.-M. Yang, "Cryomilling and spark plasma sintering of nanocrystalline magnesium-based alloy", *J. Mater. Res.* , 2011, 26, 904-911
- 84 F. Sun, P. Rojas, A. Zúñiga and E. J. Lavernia, "Nanostructure in a Ti alloy processed using a cryomilling technique", *Mater. Sci. Eng. A*, 2006, 430, 90-97

- 85 R. S. Herrick, J. R. Weertman, R. Petkovic-Luton and M. J. Luton, "Dislocation/particle interactions in an oxide dispersion strengthened alloy", *Scr. Metall.* , 1988, 22, 1879-1884
- 86 J. H. He and E. J. Lavernia, "Development of nanocrystalline structure during cryomilling of Inconel 625", *J. Mater. Res.* , 2001, 16, 2724-2732
- 87 B. Yang, J. Fan, B. Hao, X. Tian, J. Cheng and J. Zhang, "Synthesis and characterization of nanocrystalline Ni produced by cryomilling in liquid nitrogen", *Rare Met.* , 2007, 26, 147-151
- 88 Y. S. Park, K. H. Chung, N. J. Kim and E. J. Lavernia, "Microstructural investigation of nanocrystalline bulk Al–Mg alloy fabricated by cryomilling and extrusion", *Mater. Sci. Eng. A*, 2004, 374, 211-216
- 89 J. Ye, L. Ajdelsztajn and J. Schoenung, "Bulk nanocrystalline aluminum 5083 alloy fabricated by a novel technique: Cryomilling and spark plasma sintering", *Metall. Mater. Trans. A*, 2006, 37, 2569-2579
- 90 J. Ye, B. Q. Han, Z. Lee, B. Ahn, S. R. Nutt and J. M. Schoenung, "A tri-modal aluminum based composite with super-high strength", *Scr. Mater.* , 2005, 53, 481-486
- 91 R. Vintila, A. Charest, R. A. L. Drew and M. Brochu, "Synthesis and consolidation via spark plasma sintering of nanostructured Al-5356/B4C composite", *Mater. Sci. Eng. A*, 2011, 528, 4395-4407
- 92 F. Zhou, X. Z. Liao, Y. T. Zhu, S. Dallek and E. J. Lavernia, "Microstructural evolution during recovery and recrystallization of a nanocrystalline Al-Mg alloy prepared by cryogenic ball milling", *Acta Mater.* , 2003, 51, 2777-2791
- 93 F. Zhou, J. Lee, S. Dallek and E. J. Lavernia, "High grain size stability of nanocrystalline Al prepared by mechanical attrition", *J. Mater. Res.* , 2001, 16, 3451-3458
- 94 B. Huang, R. J. Perez and E. J. Lavernia, "Grain growth of nanocrystalline Fe–Al alloys produced by cryomilling in liquid argon and nitrogen", *Mater. Sci. Eng. A*, 1998, 255, 124-132
- 95 Y. Xun, F. Mohamed and E. Lavernia, "Synthesis of nanocrystalline Zn-22 Pct Al using cryomilling", *Metall. Mater. Trans. A*, 2004, 35, 573-581
- 96 O. Ertorer, A. Zúñiga, T. Topping, W. Moss and E. Lavernia, "Mechanical Behavior of Cryomilled CP-Ti Consolidated & Quasi-Isostatic Forging", *Metall. Mater. Trans. A*, 2009, 40, 91-103
- 97 S. Deledda, B. C. Hauback and H. Fjellvåg, "H-sorption behaviour of mechanically activated Mg–Zn powders", *J. Alloys Compd.* , 2007, 446–447, 173-177
- 98 C. W. Su, L. Lu and M. O. Lai, "A model for the grain refinement mechanism in equal channel angular pressing of Mg alloy from microstructural studies", *Mater. Sci. Eng. A*, 2006, 434, 227-236
- 99 A. J. Maisano, "Cryomilling of Aluminum-based and Magnesium-based Metal Powders", Virginia Tech. 2006
- 100 B. Zheng, O. Ertorer, Y. Li, Y. Zhou, S. N. Mathaudhu, C. Y. A. Tsao and E. J. Lavernia, "High strength, nano-structured Mg-Al-Zn alloy", *Mater. Sci. Eng. A*, 2011, 528, 2180-2191

- 101 F. Zhou, D. Witkin, S. R. Nutt and E. J. Lavernia, "Formation of nanostructure in Al produced by a low-energy ball milling at cryogenic temperature", *Mater. Sci. Eng. A*, 2004, 375–377, 917-921
- 102 M. D. Riktor, S. Deledda, M. Herrich, O. Gutfleisch, H. Fjellvåg and B. C. Hauback, "Hydride formation in ball-milled and cryomilled Mg–Fe powder mixtures", *Mater. Sci. Eng. B*, 2009, 158, 19-25
- 103 A. V. Borissova, S. Deledda and B. C. Hauback, "Synthesis and hydrogen sorption properties of Mg–Ti–Ni composite, produced by mechanical milling at liquid nitrogen temperature", *J. Alloys Compd.*, 2009, 481, L24-L26
- 104 B. Han, F. Mohamed, Z. Lee, S. Nutt and E. Lavernia, "Mechanical properties of an ultrafine-grained Al-7.5 Pct Mg alloy", *Metall. Mater. Trans. A*, 2003, 34, 603-613
- 105 R. Orrù, R. Licheri, A. M. Locci, A. Cincotti and G. Cao, "Consolidation/synthesis of materials by electric current activated/assisted sintering", *Mater. Sci. Eng. R*, 2009, 63, 127-287
- 106 Z. Munir, U. Anselmi-Tamburini and M. Ohyanagi, "The effect of electric field and pressure on the synthesis and consolidation of materials: A review of the spark plasma sintering method", *J. Mater. Sci.*, 2006, 41, 763-777
- 107 J. E. Garay, "Current-Activated, Pressure-Assisted Densification of Materials", *Annual Review of Materials Research*, 2010, 40, 445-468
- 108 J. Langer, M. J. Hoffmann and O. Guillon, "Direct comparison between hot pressing and electric field-assisted sintering of submicron alumina", *Acta Mater.*, 2009, 57, 5454-5465
- 109 T. Holland, D. Hulbert, U. Anselmi-Tamburini and A. Mukherjee, "Functionally graded boron carbide and aluminum composites with tubular geometries using pulsed electric current sintering", *Mater. Sci. Eng. A*, 2010, 527, 4543-4545
- 110 R. S. Mishra and A. K. Mukherjee, "Electric pulse assisted rapid consolidation of ultrafine grained alumina matrix composites", *Mater. Sci. Eng. A*, 2000, 287, 178-182
- 111 J. A. Schneider, A. K. Mukherjee, K. Yamazaki and K. Shoda, "Mechanisms of plasma assisted sintering in the Si<sub>3</sub>N<sub>4</sub> ceramic system", *Mater. Lett.*, 1995, 25, 101-104
- 112 K. A. Khor, L. G. Yu, O. Andersen and G. Stephani, "Effect of spark plasma sintering (SPS) on the microstructure and mechanical properties of randomly packed hollow sphere (RHS) cell wall", *Mater. Sci. Eng. A*, 2003, 356, 130-135
- 113 J. Zhao, J. E. Garay, U. Anselmi-Tamburini and Z. A. Munir, "Directional electromigration-enhanced interdiffusion in the Cu-Ni system", *J. Appl. Phys.*, 2007, 102
- 114 J. E. Garay, S. C. Glade, U. Anselmi-Tamburini, P. Asoka-Kumar and Z. A. Munir, "Electric current enhanced defect mobility in Ni<sub>3</sub>Ti intermetallics", *Appl. Phys. Lett.*, 2004, 85, 573-575
- 115 J. E. Garay, U. Anselmi-Tamburini and Z. A. Munir, "Enhanced growth of intermetallic phases in the Ni–Ti system by current effects", *Acta Mater.*, 2003, 51, 4487-4495
- 116 U. Anselmi-Tamburini, J. E. Garay and Z. A. Munir, "Fundamental investigations on the spark plasma sintering/synthesis process: III. Current effect on reactivity", *Mater. Sci. Eng. A*, 2005, 407, 24-30

- 117 D. M. Hulbert, A. Anders, D. V. Dudina, J. Andersson, D. Jiang, C. Unuvar, U. Anselmi-Tamburini, E. J. Lavernia and A. K. Mukherjee, "The absence of plasma in "spark plasma sintering"", *J. Appl. Phys.* , 2008, 104
- 118 D. M. Hulbert, A. Anders, J. Andersson, E. J. Lavernia and A. K. Mukherjee, "A discussion on the absence of plasma in spark plasma sintering", *Scr. Mater.* , 2009, 60, 835-838
- 119 K. Y. Sastry, L. Froyen, J. Vleugels, O. Van der Biest, R. Schattevoy and J. Hennicke, "Mechanical milling and field assisted sintering consolidation of nanocrystalline Al-Si-Fe-X alloy powder", *Reviews on Advanced Materials Science*, 2004, 8, 27-32
- 120 T. Nishio, K. Kobayashi, A. Matsumoto and K. Ozaki, "Semi-solid consolidation processing of rapidly solidified powders for fabrication of high strength AZ91 magnesium alloys", *Mater. Trans.*, 2002, 43, 2110-2114
- 121 H. Okumura, K. Watanabe, S. Kamado and Y. Kojima, "Fabrication of Porous Magnesium Alloys by Pulse Electric Current Sintering Process Using Machined Chips", *Mater. Trans.*, 2003, 44, 595-600
- 122 F. O. Mear, G. Xie, D. V. Louzguine-Luzgin and A. Inoue, "Spark Plasma Sintering of Mg-Based Amorphous Ball-Milled Powders", *Mater. Trans.*, 2009, 50, 588-591
- 123 E. Ayman, U. Junko and K. Katsuyoshi, "Application of rapid solidification powder metallurgy to the fabrication of high-strength, high-ductility Mg-Al-Zn-Ca-La alloy through hot extrusion", *Acta Mater.* , 2011, 59, 273-282
- 124 A. Elsayed, K. Kondoh, H. Imai and J. Umeda, "Microstructure and mechanical properties of hot extruded Mg–Al–Mn–Ca alloy produced by rapid solidification powder metallurgy", *Mater. Des.* , 2010, 31, 2444-2453
- 125 G. Straffelini, A. P. Nogueira, P. Muterlle and C. Menapace, "Spark plasma sintering and hot compression behaviour of AZ91 Mg alloy", *Mater. Sci. Technol.* , 2011, 27, 1582-1587
- 126 W. N. A. W. Muhammad, Z. Sajuri, Y. Mutoh and Y. Miyashita, "Microstructure and mechanical properties of magnesium composites prepared by spark plasma sintering technology", *J. Alloys Compd.* , 2011, 509, 6021-6029
- 127 M. Kubota and B. P. Wynne, "Electron backscattering diffraction analysis of mechanically milled and spark plasma sintered pure aluminium", *Scr. Mater.* , 2007, 57, 719-722
- 128 B. Akinrinlola, R. Gauvin and M. Brochu, "Improving the mechanical reliability of cryomilled Al–Mg alloy using a two-stage spark plasma sintering cycle", *Scr. Mater.* , 2012, 66, 455-458
- 129 T. T. Sasaki, T. Ohkubo and K. Hono, "Microstructure and mechanical properties of bulk nanocrystalline Al–Fe alloy processed by mechanical alloying and spark plasma sintering", *Acta Mater.* , 2009, 57, 3529-3538
- 130 Z. Lee, V. Radmilovic, B. Ahn, E. Lavernia and S. Nutt, "Tensile Deformation and Fracture Mechanism of Bulk Bimodal Ultrafine-Grained Al-Mg Alloy", *Metall. Mater. Trans. A*, 2010, 41, 795-801
- 131 K. S. Kumar, H. Van Swygenhoven and S. Suresh, "Mechanical behavior of nanocrystalline metals and alloys", *Acta Mater.* , 2003, 51, 5743-5774

- 132 K. Lu, L. Lu and S. Suresh, "Strengthening Materials by Engineering Coherent Internal Boundaries at the Nanoscale", *Science*, 2009, 324, 349-352
- 133 Y. H. Zhao, X. Z. Liao, S. Cheng, E. Ma and Y. T. Zhu, "Simultaneously Increasing the Ductility and Strength of Nanostructured Alloys", *Adv. Mater.* , 2006, 18, 2280-2283
- 134 L. Balogh, T. Ungár, Y. Zhao, Y. T. Zhu, Z. Horita, C. Xu and T. G. Langdon, "Influence of stacking-fault energy on microstructural characteristics of ultrafine-grain copper and copper–zinc alloys", *Acta Mater.* , 2008, 56, 809-820
- 135 S. Ni, Y. B. Wang, X. Z. Liao, S. N. Alhajeri, H. Q. Li, Y. H. Zhao, E. J. Lavernia, S. P. Ringer, T. G. Langdon and Y. T. Zhu, "Grain growth and dislocation density evolution in a nanocrystalline Ni–Fe alloy induced by high-pressure torsion", *Scr. Mater.* , 2011, 64, 327-330
- 136 H. Wen, T. D. Topping, D. Isheim, D. N. Seidman and E. J. Lavernia, "Strengthening mechanisms in a high-strength bulk nanostructured Cu–Zn–Al alloy processed via cryomilling and spark plasma sintering", *Acta Mater.* , 2013, 61, 2769-2782
- 137 S. Cheng, Y. Zhao, Y. Guo, Y. Li, Q. Wei, X.-L. Wang, Y. Ren, P. K. Liaw, H. Choo and E. J. Lavernia, "High Plasticity and Substantial Deformation in Nanocrystalline NiFe Alloys Under Dynamic Loading", *Adv. Mater.* , 2009, 21, 5001-5004
- 138 R. Z. Valiev, V. Y. Gertsman and O. A. Kaibyshev, "Grain boundary structure and properties under external influences", *physica status solidi (a)*, 1986, 97, 11-56
- 139 T. H. Courtney, "Mechanical Behavior of Materials", Second edn, McGraw-Hill Higher Education. 2000
- 140 B. Li, S. P. Joshi, O. Almagri, Q. Ma, K. T. Ramesh and T. Mukai, "Rate-dependent hardening due to twinning in an ultrafine-grained magnesium alloy", *Acta Mater.* , 2012, 60, 1818-1826
- 141 H. Van Swygenhoven, "Grain Boundaries and Dislocations", *Science*, 2002, 296, 66-67
- 142 J. Schiøtz and K. W. Jacobsen, "A Maximum in the Strength of Nanocrystalline Copper", *Science*, 2003, 301, 1357-1359
- 143 V. Yamakov, D. Wolf, S. R. Phillpot and H. Gleiter, "Grain-boundary diffusion creep in nanocrystalline palladium by molecular-dynamics simulation", *Acta Mater.* , 2002, 50, 61-73
- 144 H. Van Swygenhoven and P. M. Derlet, "Grain-boundary sliding in nanocrystalline fcc metals", *Physical Review B*, 2001, 64, 224105
- 145 H. Van Swygenhoven and A. Caro, "Plastic behavior of nanophase Ni: A molecular dynamics computer simulation", *Appl. Phys. Lett.* , 1997, 71, 1652-1654
- 146 S. P. Joshi and K. T. Ramesh, "Rotational diffusion and grain size dependent shear instability in nanostructured materials", *Acta Mater.* , 2008, 56, 282-291
- 147 B. N. Kim, K. Hiraga and K. Morita, "Viscous grain-boundary sliding and grain rotation accommodated by grain-boundary diffusion", *Acta Mater.* , 2005, 53, 1791-1798
- 148 D. Moldovan, D. Wolf and S. R. Phillpot, "Theory of diffusion-accommodated grain rotation in columnar polycrystalline microstructures", *Acta Mater.* , 2001, 49, 3521-3532

- 149 H. Van Swygenhoven, P. M. Derlet and A. G. Frøseth, "Nucleation and propagation of dislocations in nanocrystalline fcc metals", *Acta Mater.* , 2006, 54, 1975-1983
- 150 V. Yamakov, D. Wolf, M. Salazar, S. R. Phillpot and H. Gleiter, "Length-scale effects in the nucleation of extended dislocations in nanocrystalline Al by molecular-dynamics simulation", *Acta Mater.* , 2001, 49, 2713-2722
- 151 D. Wolf, V. Yamakov, S. R. Phillpot, A. Mukherjee and H. Gleiter, "Deformation of nanocrystalline materials by molecular-dynamics simulation: relationship to experiments?", *Acta Mater.* , 2005, 53, 1-40
- 152 H. Van Swygenhoven, P. M. Derlet and A. G. Froseth, "Stacking fault energies and slip in nanocrystalline metals", *Nat. Mater.* , 2004, 3, 399-403
- 153 X. Z. Liao, Y. H. Zhao, S. G. Srinivasan, Y. T. Zhu, R. Z. Valiev and D. V. Gunderov, "Deformation twinning in nanocrystalline copper at room temperature and low strain rate", *Appl. Phys. Lett.* , 2004, 84, 592-594
- 154 X. L. Wu, Y. T. Zhu, Y. G. Wei and Q. Wei, "Strong Strain Hardening in Nanocrystalline Nickel", *Phys. Rev. Lett.* , 2009, 103, 205504
- 155 H. J. Choi, Y. Kim, J. H. Shin and D. H. Bae, "Deformation behavior of magnesium in the grain size spectrum from nano- to micrometer", *Mater. Sci. Eng. A*, 2010, 527, 1565-1570
- 156 Y. T. Zhu, X. Z. Liao and X. L. Wu, "Deformation twinning in nanocrystalline materials", *Prog. Mater. Sci.* , 2012, 57, 1-62
- 157 M. R. Barnett, Z. Keshavarz, A. G. Beer and D. Atwell, "Influence of grain size on the compressive deformation of wrought Mg–3Al–1Zn", *Acta Mater.* , 2004, 52, 5093-5103
- 158 V. Yamakov, D. Wolf, S. R. Phillpot and H. Gleiter, "Deformation twinning in nanocrystalline Al by molecular-dynamics simulation", *Acta Mater.* , 2002, 50, 5005-5020
- 159 M. R. Barnett, M. D. Nave and A. Ghaderi, "Yield point elongation due to twinning in a magnesium alloy", *Acta Mater.* , 2012, 60, 1433-1443
- 160 M. A. Meyers, O. Vöhringer and V. A. Lubarda, "The onset of twinning in metals: a constitutive description", *Acta Mater.* , 2001, 49, 4025-4039
- 161 Q. Yang and A. K. Ghosh, "Deformation behavior of ultrafine-grain (UFG) AZ31B Mg alloy at room temperature", *Acta Mater.* , 2006, 54, 5159-5170
- 162 Q. Yang and A. K. Ghosh, "Production of ultrafine-grain microstructure in Mg alloy by alternate biaxial reverse corrugation", *Acta Mater.* , 2006, 54, 5147-5158
- 163 M. R. Barnett, "A rationale for the strong dependence of mechanical twinning on grain size", *Scr. Mater.* , 2008, 59, 696-698
- 164 H. H. Fu, D. J. Benson and M. A. Meyers, "Analytical and computational description of effect of grain size on yield stress of metals", *Acta Mater.* , 2001, 49, 2567-2582
- 165 M. Pozuelo, Y. W. Chang and J. M. Yang, "Enhanced compressive strength of an extruded nanostructured Mg–10Al alloy", *Mater. Sci. Eng. A*, 2014, 594, 203-211
- 166 M. Pozuelo, S. N. Mathaudhu, S. Kim, B. Li, W. H. Kao and J. M. Yang, "Nanotwins in nanocrystalline Mg–Al alloys: an insight from high-resolution TEM and molecular dynamics simulation", *Philos. Mag. Lett.* , 2013, 93, 640-647

- 167 B. Zheng, Y. Li, W. Xu, Y. Zhou, S. N. Mathaudhu, Y. Zhu and E. J. Lavernia, "Twinning in cryomilled nanocrystalline Mg powder", *Philos. Mag. Lett.* , 2013, 1-8
- 168 F. Sansoz and V. Dupont, "Grain growth behavior at absolute zero during nanocrystalline metal indentation", *Appl. Phys. Lett.* , 2006, 89, -
- 169 J. W. Cahn, Y. Mishin and A. Suzuki, "Coupling grain boundary motion to shear deformation", *Acta Mater.* , 2006, 54, 4953-4975
- 170 M. Legros, D. S. Gianola and K. J. Hemker, "In situ TEM observations of fast grain-boundary motion in stressed nanocrystalline aluminum films", *Acta Mater.* , 2008, 56, 3380-3393
- 171 T. J. Rupert, D. S. Gianola, Y. Gan and K. J. Hemker, "Experimental Observations of Stress-Driven Grain Boundary Migration", *Science*, 2009, 326, 1686-1690
- 172 G. Saada and T. Kruml, "Deformation mechanisms of nanograined metallic polycrystals", *Acta Mater.* , 2011, 59, 2565-2574
- 173 E. O. Hall, "The Deformation and Ageing of Mild Steel: III Discussion of Results", "Proc. Phys. Soc. London, Sect. B ", 1951, 64, 747
- 174 Y. Zhao, T. Topping, Y. Li and E. J. Lavernia, "Strength and Ductility of Bi-Modal Cu", *Adv. Eng. Mater.* , 2011, 13, 865-871
- 175 Y. Zhao, Y. Zhu and E. J. Lavernia, "Strategies for Improving Tensile Ductility of Bulk Nanostructured Materials", *Adv. Eng. Mater.* , 2010, 12, 769-778
- 176 Z. Budrovic, H. Van Swygenhoven, P. M. Derlet, S. Van Petegem and B. Schmitt, "Plastic Deformation with Reversible Peak Broadening in Nanocrystalline Nickel", *Science*, 2004, 304, 273-276
- 177 D. Jia, Y. M. Wang, K. T. Ramesh, E. Ma, Y. T. Zhu and R. Z. Valiev, "Deformation behavior and plastic instabilities of ultrafine-grained titanium", *Appl. Phys. Lett.* , 2001, 79, 611-613
- 178 Y. S. Li, Y. Zhang, N. R. Tao and K. Lu, "Effect of thermal annealing on mechanical properties of a nanostructured copper prepared by means of dynamic plastic deformation", *Scr. Mater.* , 2008, 59, 475-478
- 179 Y. Zhao, T. Topping, J. F. Bingert, J. J. Thornton, A. M. Dangelewicz, Y. Li, W. Liu, Y. Zhu, Y. Zhou and E. J. Lavernia, "High Tensile Ductility and Strength in Bulk Nanostructured Nickel", *Adv. Mater.* , 2008, 20, 3028-3033
- 180 L. Lu, X. Chen, X. Huang and K. Lu, "Revealing the Maximum Strength in Nanotwinned Copper", *Science*, 2009, 323, 607-610
- 181 W. S. Zhao, N. R. Tao, J. Y. Guo, Q. H. Lu and K. Lu, "High density nano-scale twins in Cu induced by dynamic plastic deformation", *Scr. Mater.* , 2005, 53, 745-749
- 182 Y. H. Zhao, J. F. Bingert, Y. T. Zhu, X. Z. Liao, R. Z. Valiev, Z. Horita, T. G. Langdon, Y. Z. Zhou and E. J. Lavernia, "Tougher ultrafine grain Cu via high-angle grain boundaries and low dislocation density", *Appl. Phys. Lett.* , 2008, 92, -
- 183 T. Hu, K. Ma, T. D. Topping, B. Saller, A. Yousefiani, J. M. Schoenung and E. J. Lavernia, "Improving the tensile ductility and uniform elongation of high-strength ultrafine-grained Al alloys by lowering the grain boundary misorientation angle", *Scr. Mater.* , 2014, 78-79, 25-28

- 184 K. Tao, H. Choo, H. Li, B. Clausen, J.-E. Jin and Y.-K. Lee, "Transformation-induced plasticity in an ultrafine-grained steel: An in situ neutron diffraction study", *Appl. Phys. Lett.* , 2007, 90, -
- 185 M. Pozuelo, W. H. Kao and J.-M. Yang, "High-resolution TEM characterization of SiC nanowires as reinforcements in a nanocrystalline Mg-matrix", *Mater. Charact.* , 2013, 77, 81-88
- 186 E. J. Lavernia, B. Q. Han and J. M. Schoenung, "Cryomilled nanostructured materials: Processing and properties", *Mater. Sci. Eng. A*, 2008, 493, 207-214
- 187 M. S. Khoshkhou, S. Scudino, J. Thomas, K. B. Surreddi and J. Eckert, "Grain and crystallite size evaluation of cryomilled pure copper", *J. Alloys Compd.* , 2011, 509, Supplement 1, S343-S347
- 188 O. Ertorer. *Processing, Microstructure and Mechanical Behavior of Cryomilled Commercially Pure Titanium* 3456819 thesis, University of California, Davis, (2011).
- 189 H. Wen. *Processing, microstructure, mechanical behavior and deformation mechanisms of bulk nanostructured copper and copper alloys* 3544819 thesis, University of California, Davis, (2012).
- 190 C. C. Koch, "Nanostructured Materials: Processing, Properties and Applications", Elsevier Science. 2006
- 191 H. J. Höfler and R. S. Averbach, "Grain growth in nanocrystalline TiO<sub>2</sub> and its relation to vickers hardness and fracture toughness", *Scripta Metallurgica et Materialia*, 1990, 24, 2401-2406
- 192 T. Chookajorn and C. A. Schuh, "Nanoscale segregation behavior and high-temperature stability of nanocrystalline W-20% Ti", *Acta Mater.* , 2014, 73, 128-138
- 193 P. Cao, L. Lu and M. O. Lai, "Grain growth and kinetics for nanocrystalline magnesium alloy produced by mechanical alloying", *Mater. Res. Bull.* , 2001, 36, 981-988
- 194 K. A. Darling, R. N. Chan, P. Z. Wong, J. E. Semones, R. O. Scattergood and C. C. Koch, "Grain-size stabilization in nanocrystalline FeZr alloys", *Scr. Mater.* , 2008, 59, 530-533
- 195 G. D. Hibbard, K. T. Aust and U. Erb, "The effect of starting nanostructure on the thermal stability of electrodeposited nanocrystalline Co", *Acta Mater.* , 2006, 54, 2501-2510
- 196 C. Saldana, T. G. Murthy, M. R. Shankar, E. A. Stach and S. Chandrasekar, "Stabilizing nanostructured materials by coherent nanotwins and their grain boundary triple junction drag", *Appl. Phys. Lett.* , 2009, 94, 021910-021913
- 197 C. Bansal, Z. Q. Gao and B. Fultz, "Grain growth and chemical ordering in (Fe,Mn)<sub>3</sub>Si", *Nanostruct. Mater.* , 1995, 5, 327-336
- 198 I. Roy, M. Chauhan, F. Mohamed and E. Lavernia, "Thermal stability in bulk cryomilled ultrafine-grained 5083 Al alloy", *Metall. Mater. Trans. A*, 2006, 37, 721-730
- 199 B. Q. Han, Z. Zhang and E. J. Lavernia, "Creep behaviour and thermal stability of cryomilled Al alloy", *Philos. Mag. Lett.* , 2005, 85, 97-108
- 200 K. Chung, R. Rodriguez, E. Lavernia and J. Lee, "Grain growth behavior of cryomilled INCONEL 625 powder during isothermal heat treatment", *Metall. Mater. Trans. A*, 2002, 33, 125-134

- 201 J. Lee, F. Zhou, K. H. Chung, E. J. Lavernia and N. J. Kim, "Grain growth of nanocrystalline Ni powders prepared by cryomilling", *Metall. Mater. Trans. A*, 2001, 32, 3109-3115
- 202 W.-b. Fang, W. Fang and H.-f. Sun, "Preparation of high-strength Mg–3Al–Zn alloy with ultrafine-grained microstructure by powder metallurgy", *Powder Technol.* , 2011, 212, 161-165
- 203 S. M. Razavi, D. C. Foley, I. Karaman, K. T. Hartwig, O. Duygulu, L. J. Kecskes, S. N. Mathaudhu and V. H. Hammond, "Effect of grain size on prismatic slip in Mg–3Al–1Zn alloy", *Scr. Mater.* , 2012, 67, 439-442
- 204 W. J. Kim, M. J. Lee, B. H. Lee and Y. B. Park, "A strategy for creating ultrafine-grained microstructure in magnesium alloy sheets", *Mater. Lett.* , 2010, 64, 647-649
- 205 C. J. Lee, J. C. Huang and P. J. Hsieh, "Mg based nano-composites fabricated by friction stir processing", *Scr. Mater.* , 2006, 54, 1415-1420
- 206 Y. Morisada, H. Fujii, T. Nagaoka and M. Fukusumi, "Nanocrystallized magnesium alloy – uniform dispersion of C60 molecules", *Scr. Mater.* , 2006, 55, 1067-1070
- 207 C. I. Chang, X. H. Du and J. C. Huang, "Producing nanograined microstructure in Mg–Al–Zn alloy by two-step friction stir processing", *Scr. Mater.* , 2008, 59, 356-359
- 208 C. I. Chang, X. H. Du and J. C. Huang, "Achieving ultrafine grain size in Mg–Al–Zn alloy by friction stir processing", *Scr. Mater.* , 2007, 57, 209-212
- 209 H.-f. Sun, W. Fang and W.-b. Fang, "Producing nanocrystalline bulk Mg–3Al–Zn alloy by powder metallurgy assisted hydriding–dehydriding", *J. Alloys Compd.* , 2011, 509, 8171-8175
- 210 D. Liu, Y. Xiong, T. Topping, Y. Zhou, C. Haines, J. Paras, D. Martin, D. Kapoor, J. Schoenung and E. Lavernia, "Spark Plasma Sintering of Cryomilled Nanocrystalline Al Alloy - Part II: Influence of Processing Conditions on Densification and Properties", *Metall. Mater. Trans. A*, 2012, 43, 340-350
- 211 H. Wen and E. J. Lavernia, "Twins in cryomilled and spark plasma sintered Cu–Zn–Al", *Scr. Mater.* , 2012, 67, 245-248
- 212 Y. Xiong, D. Liu, Y. Li, B. Zheng, C. Haines, J. Paras, D. Martin, D. Kapoor, E. Lavernia and J. Schoenung, "Spark Plasma Sintering of Cryomilled Nanocrystalline Al Alloy - Part I: Microstructure Evolution", *Metall. Mater. Trans. A*, 2012, 43, 327-339
- 213 Z. Zhang, B. Q. Han, J. Y. Huang, Y. H. Han, Y. Zhou, K. Kakegawa and E. J. Lavernia, "Mechanical Behavior of Cryomilled Ni Superalloy by Spark Plasma Sintering", *Metall. Mater. Trans. A*, 2009, 40, 2023-2029
- 214 S. R. Kalidindi, A. Abusafieh and E. El-Danaf, "Accurate characterization of machine compliance for simple compression testing", *Exp. Mech.* , 1997, 37, 210-215
- 215 Q. Yu, Z.-W. Shan, J. Li, X. Huang, L. Xiao, J. Sun and E. Ma, "Strong crystal size effect on deformation twinning", *Nature*, 2010, 463, 335-338
- 216 B. Srinivasarao, K. Oh-ishi, T. Ohkubo and K. Hono, "Bimodally grained high-strength Fe fabricated by mechanical alloying and spark plasma sintering", *Acta Mater.* , 2009, 57, 3277-3286

- 217 C. C. Koch, K. M. Youssef, R. O. Scattergood and K. L. Murty, "Breakthroughs in Optimization of Mechanical Properties of Nanostructured Metals and Alloys", *Adv. Eng. Mater.* , 2005, 7, 787-794
- 218 Y. H. Zhao, J. F. Bingert, X. Z. Liao, B. Z. Cui, K. Han, A. V. Sergueeva, A. K. Mukherjee, R. Z. Valiev, T. G. Langdon and Y. T. Zhu, "Simultaneously Increasing the Ductility and Strength of Ultra-Fine-Grained Pure Copper", *Adv. Mater.* , 2006, 18, 2949-2953
- 219 Z. Horita, K. Ohashi, T. Fujita, K. Kaneko and T. G. Langdon, "Achieving High Strength and High Ductility in Precipitation-Hardened Alloys", *Adv. Mater.* , 2005, 17, 1599-1602
- 220 P. G. Sanders, G. E. Fougere, L. J. Thompson, J. A. Eastman and J. R. Weertman, "IMPROVEMENTS IN THE SYNTHESIS AND COMPACTION OF NANOCRYSTALLINE MATERIALS", *Nanostruct. Mater.* , 1997, 8, 243-252
- 221 K. M. Youssef, R. O. Scattergood, K. L. Murty, J. A. Horton and C. C. Koch, "Ultrahigh strength and high ductility of bulk nanocrystalline copper", *Appl. Phys. Lett.* , 2005, 87, 091904-091903
- 222 X. L. Wu, K. M. Youssef, C. C. Koch, S. N. Mathaudhu, L. J. Kecskés and Y. T. Zhu, "Deformation twinning in a nanocrystalline hcp Mg alloy", *Scr. Mater.* , 2011, 64, 213-216
- 223 Y. Zhu, X. Liao and X. Wu, "Deformation twinning in bulk nanocrystalline metals: Experimental observations", *JOM* 2008, 60, 60-64
- 224 F. R. N. Nabarro, "Stress-driven grain growth", *Scr. Mater.* , 1998, 39, 1681-1683
- 225 A. J. Haslam, D. Moldovan, V. Yamakov, D. Wolf, S. R. Phillpot and H. Gleiter, "Stress-enhanced grain growth in a nanocrystalline material by molecular-dynamics simulation", *Acta Mater.* , 2003, 51, 2097-2112
- 226 X. Gao and J. F. Nie, "Characterization of strengthening precipitate phases in a Mg–Zn alloy", *Scr. Mater.* , 2007, 56, 645-648
- 227 D. Orlov, D. Pelliccia, X. Fang, L. Bourgeois, N. Kirby, A. Y. Nikulin, K. Ameyama and Y. Estrin, "Particle evolution in Mg–Zn–Zr alloy processed by integrated extrusion and equal channel angular pressing: Evaluation by electron microscopy and synchrotron small-angle X-ray scattering", *Acta Mater.* , 2014, 72, 110-124